# A Measurement of the Temperature and Polarization Anisotropies in the Cosmic Microwave Background Radiation

Thesis by

William C. Jones

In Partial Fulfillment of the Requirements

for the Degree of

Doctor of Philosophy

California Institute of Technology

Pasadena, California

2005

(Submitted May 10, 2005)

© 2005
William C. Jones
All Rights Reserved

# Acknowledgements

Many thanks to everyone who has contributed in one way or another to the completion of this project, especially Molly, who is no doubt pleased that I will soon leave my mistress behind; and my family, all of whom have been very supportive. I am indebted to Andrew Lange, who has not only provided an outstanding environment in which to perform research, but also has been a very generous and supportive mentor over the last $N$ years. If Andrew taught me everything I know about *how* experimental physics gets done, then Byron Philhour and Marcus Runyan have, between them, taught me most of what I know about *doing* experimental physics. There is no question in my mind that BOOMERANG would never have flown (and therefore I would never have graduated) were it not for the organizational and financial genius of Kathy Deniston. It has been a pleasure and an honor to be able to work with such talented people along the way, including Tom Montroy, Ted Kisner, Carrie MacTavish, Carlo Contaldi, Eric Hivon, Andrew Lange, John Ruhl, and Barth Netterfield. Of course, many thanks are also due to Lyman Page, Dave Wilkinson, and Jim Peebles who, between them, got me into this mess.

# The BOOMERANG Collaboration

**California Institute of Technology** V. V. Hristov, W. C. Jones, A. E. Lange

**Case Western Reserve University** T. Kisner, T. Montroy, J. Ruhl

**University of Toronto** C. MacTavish, C. B. Netterfield, E. Pascale

**Universita' di Roma La Sapienza** P. de Bernardis, S. Masi, F. Piacentini, G. Polenta, A. Iacoangeli

**IPAC** B. P. Crill, K. Ganga, E. Hivon

**CITA** D. Bond, C. Contaldi

**JPL** J. J. Bock

**Cardiff University** P. Ade, P. Mauskopf

**IROE** A. Boscaleri

**ING** G. Romeo, G. di Stefano

**LBNL, UC Berkeley** J. Borrill

# Abstract

We describe the design and performance of the BOOMERANG experiment, and report on measurements of the temperature and polarization anisotropies of the Cosmic Microwave Background (CMB) obtained during the January 2003 flight of BOOMERANG (B2K). To enable these studies, we have developed a bolometric detector which is intrinsically sensitive to linear polarization. The receiver consists of a pair of colocated silicon nitride micromesh absorbers that couple anisotropically to linearly polarized radiation through a corrugated waveguide structure. This system allows simultaneous background limited measurements of the Stokes $I$ and $Q$ parameters over $\sim 30\%$ bandwidths at frequencies from $\sim 60$ to 400 GHz.

The science results reported here are derived from 195 hours of observation with four 145 GHz Polarization Sensitive Bolometer (PSB) pairs [83]. The data include 75 hours of observations distributed over 1.8% of the sky with an additional 120 hours concentrated on the central portion of the field, itself representing 0.22% of the full sky. The B2K data improve significantly on existing measurements of the CMB temperature power spectrum at angular scales of $500 \lesssim \ell \lesssim 1100$. In addition, we have measured a spectrum of curl-free polarization anisotropies that, in the context of the most simple adiabatic inflationary models, are consistent with the predictions of the currently favored $\Lambda$CDM cosmology.

# Contents

**Acknowledgements** **iii**

**Abstract** **v**

**1 Introduction** **1**

1.1 Modern cosmology . . . . . 2

1.1.1 Isotropy and the metric . . . . . 4

1.1.2 Expansion . . . . . 6

1.1.3 The "Hot Big Bang" scenario . . . . . 8

1.1.4 Structure formation . . . . . 11

1.1.5 Inflation . . . . . 12

1.2 The microwave background anisotropies . . . . . 14

1.2.1 Temperature . . . . . 14

1.2.2 Polarization . . . . . 16

1.2.3 Observations . . . . . 18

**2 The BOOMERANG Experiment** **21**

2.1 Experimental approach . . . . . 23

2.2 Gondola and flight systems . . . . . 29

2.3 Focal plane . . . . . 37

2.3.1 Polarization sensitive bolometers . . . . . 37

2.3.2 Photometers . . . . . 58

2.3.3 Optical filtering . . . . . 59

2.3.4 Detectors . . . . . 62

2.3.5 Readout electronics . . . . . 63
2.4 Optics . . . . . 66
2.4.1 Telescope . . . . . 66
2.4.2 Feeds . . . . . 76

**3 Instrument Performance** **87**
3.1 Preflight characterization . . . . . 87
3.1.1 System checks . . . . . 87
3.1.2 System characterization . . . . . 89
3.2 In-flight performance . . . . . 93
3.2.1 Calibration . . . . . 95
3.2.2 Beams . . . . . 100

**4 Low Level Analysis** **107**
4.1 Pointing reconstruction . . . . . 108
4.1.1 Sensors . . . . . 109
4.1.2 Attitude reconstruction . . . . . 111
4.2 Signal processing . . . . . 113

**5 Science Analysis** **116**
5.1 An introduction to mapmaking . . . . . 116
5.1.1 Signal estimation . . . . . 121
5.1.2 Polarization formalisms . . . . . 124
5.1.3 Polarized beams . . . . . 127
5.1.4 Polarized mapmaking . . . . . 130
5.1.5 Direct differences . . . . . 131
5.1.6 Noise estimation . . . . . 134
5.2 CMB power spectrum estimation . . . . . 141
5.2.1 Formalism . . . . . 141
5.2.2 The likelihood . . . . . 144
5.2.3 Monte Carlo methods . . . . . 147

5.2.4 Practical considerations . . . . . 150

**6 Primary Science and Discussion** **156**

6.1 CMB maps . . . . . 156

6.2 Spectra . . . . . 163

6.2.1 Temperature . . . . . 164

6.2.2 Polarization . . . . . 172

6.3 Conclusion . . . . . 175

**Bibliography** **178**

**A Galactic Plane Maps** **201**

**B Numerical Modeling of Bolometric Receivers** **209**

B.1 Bolometers 101 . . . . . 209

B.1.1 Semiconductor bolometers . . . . . 210

B.1.2 TES bolometers . . . . . 214

B.2 Bolometer parameter estimation . . . . . 219

B.3 Noise in bolometric receivers . . . . . 221

**C Numerical Procedures** **230**

C.1 The Newton-Raphson method . . . . . 230

C.2 The Jacobi method . . . . . 232

**D The BOOMERANG Readout** **235**

# List of Figures

1.1 Leavitt and Hubble . . . 3
1.2 Generation of local quadrupole . . . 17

2.1 Foreground spectra . . . 22
2.2 The BOOMERANG bands . . . 24
2.3 Stratospheric long duration balloon . . . 25
2.4 The BOOMERANG target regions . . . 27
2.5 Scan crosslinking . . . 28
2.6 BOOMERANG sky coverage . . . 29
2.7 Atmospheric temperature profiles . . . 30
2.8 The BOOMERANG gondola . . . 33
2.9 BOOMERANG prior to launch . . . 36
2.10 Power coupling in a PSB . . . 39
2.11 Corrugation geometry of the PSB feed . . . 40
2.12 Photograph of a PSB . . . 41
2.13 Poynting flux through the absorbers . . . 42
2.14 Absorber coupling efficiency . . . 45
2.15 PSB thermal properties . . . 47
2.16 The spectrum of polarization leakage . . . 49
2.17 Assembly drawing of the PSB pixel . . . 54
2.18 Atmospheric fluctuations, time domain . . . 56
2.19 Atmospheric fluctuations, frequency domain . . . 57
2.20 Assembly drawing of the photometer pixel . . . 59
2.21 Bolometer optimization for optical loading . . . 62

2.22 Overview of the BOOMERANG optics . . . . . 67
2.23 Physical optics reflector illumination . . . . . 69
2.24 Physical optics beams on the sky . . . . . 70
2.25 Comparison of physical optics beam with data . . . . . 71
2.26 Physical optics near sidelobe structure . . . . . 72
2.27 Physical optics intermediate sidelobe structure . . . . . 75
2.28 Mode diagram for BOOMERANG feeds . . . . . 77
2.29 Corrugation geometry of the 2K PSB feed . . . . . 79
2.30 Corrugation geometry of the 2K photometer feed . . . . . 80
2.31 Feed antenna radiation patterns . . . . . 81
2.32 Waveguide high-pass edge . . . . . 83

3.1 Polarization calibration . . . . . 90
3.2 Spectral integrals . . . . . 92
3.3 BOOMERANG flight track . . . . . 94
3.4 Altitude drift . . . . . 95
3.5 Calibration drift . . . . . 97
3.6 CMB Dipole . . . . . 98
3.7 Histogram of pixel errors . . . . . 99
3.8 Extragalactic sources . . . . . 104
3.9 (PKS)0537-441 . . . . . 105
3.10 (PKS)0537-441 . . . . . 105
3.11 (PKS)0518-45 . . . . . 105
3.12 (PKS)0454-46 . . . . . 105
3.13 (PKS)0402-362 . . . . . 106
3.14 (PKS)0521-36 . . . . . 106
3.15 Beam window functions . . . . . 106

4.1 Transfer functions . . . . . 114

5.1 Striping removal with GLS maps . . . . . 119

5.2 Convergence of iterative GLS mapmaker . . . . . 122
5.3 Convergence of iterative GLS mapmaker . . . . . 123
5.4 Beam pattern, copolar and crosspolar . . . . . 128
5.5 Comparison of direct and differencing methods . . . . . 133
5.6 Noise-stationary subset lengths. . . . . 135
5.7 Noise PSD and bias . . . . . 139
5.8 Noise sonogram . . . . . 140
5.9 CMB power spectra . . . . . 142
5.10 Raw B2K pseudo-power spectra . . . . . 152

6.1 WMAP/BOOMERANG map comparison . . . . . 157
6.2 Wiener-filtered CMB polarization map . . . . . 159
6.3 Jackknife pixel histograms . . . . . 159
6.4 Deep field map, 145 GHz . . . . . 160
6.5 Deep field map, 245 GHz . . . . . 161
6.6 Deep field map, 345 GHz . . . . . 162
6.7 The B2K $\langle TT \rangle$ spectrum . . . . . 165
6.8 Peak/Valley likelihoods . . . . . 167
6.9 B98/B2K comparison . . . . . 169
6.10 The B2K $\langle TT \rangle$ window functions . . . . . 169
6.11 Features in the $\langle TT \rangle$ spectrum . . . . . 170
6.12 Comparison of $\langle TT \rangle$ results . . . . . 171
6.13 The B2K $\langle TE \rangle$ spectrum . . . . . 172
6.14 Amplitude/Phase likelihoods for polarization . . . . . 173
6.15 The B2K $\langle EE \rangle$ spectrum . . . . . 174
6.16 The B2K $\langle BB \rangle$ spectrum . . . . . 175
6.17 The B2K $\langle EE(BB) \rangle$ window functions . . . . . 176
6.18 Summary of CMB observational results . . . . . 177

A.1 Galactic emission, 145 GHz . . . . . 202
A.2 Galactic emission, 245 GHz . . . . . 203

A.3 Galactic emission, 345 GHz . . . . . 204
A.4 Galactic emission, 100 $\mu$m . . . . . 205
A.5 Polarized galactic emission, 145 GHz . . . . . 206
A.6 Polarized galactic emission, 245 GHz . . . . . 207
A.7 Polarized galactic emission, 345 GHz . . . . . 208

B.1 Semiconductor bolometer bridge circuit . . . . . 210
B.2 TES bolometer readout circuit . . . . . 215
B.3 R(T) for NTDGe and TES bolometers . . . . . 215
B.4 TES bolometer response . . . . . 217
B.5 NTDGe bolometer parameter degeneracy . . . . . 220
B.6 PSB Scattering matrix . . . . . 225
B.7 NTDGe receiver model . . . . . 227
B.8 TES receiver model . . . . . 228

# List of Tables


2.1 Material emissivities . . . . . 32
2.2 System temperature ranges . . . . . 35
2.3 PSB design parameters . . . . . 53
2.4 Optical filters . . . . . 61
2.5 Bolometer parameters . . . . . 64
2.6 Reflector design parameters . . . . . 68
2.7 Physical beam summary . . . . . 73
2.8 Tertiary edge tapers . . . . . 82
2.9 Feed design parameters . . . . . 85

3.1 Polarization calibration . . . . . 91
3.2 Cryogenic temperature ranges . . . . . 96
3.3 Calibration summary . . . . . 101
3.4 In-flight receiver performance . . . . . 102
3.5 Extragalactic source observations . . . . . 104

6.1 Temperature spectra and consistency tests . . . . . 168
6.2 Features in the $\langle TT \rangle$ power spectrum . . . . . 170

# Chapter 1

# Introduction

> "As a result of this discussion, a most interesting question arises for astronomers and physicists, and that is whether the universe in which we live is infinite, or whether it is finite in the manner of the spherical universe. Our experience is far from being sufficient to enable us to answer this question."
>
> –Albert Einstein, 1916, *The Special and General Theory*

The twentieth century has been an impressive period of discovery in both the theoretical and observational realms of cosmology. The torrent of observational data, probing vastly different scales and independent phenomena, have failed to expose fundamental inconsistencies with the theoretical framework established at the beginning of the century. Significantly, this failure is due neither to the ambiguity of the theorists, nor to a lack of observational opportunity.

The remarkable progress of the past century has led some prominent cosmologists to declare the achievement of "cosmic concordance", and others to make the bold public claim of "cosmology solved" [30, 162]. Despite this progress, we nevertheless find ourselves at the beginning of a new century with more questions than we began the last. We may at least find comfort in the fact that our questions are now better posed than they were. In this chapter, we briefly survey the current state of our knowledge; what has become generally accepted as the standard model of cosmology.

## 1.1 Modern cosmology

The revolution in our understanding of the structure and evolution of our Universe since the beginnings of the twentieth century can hardly be exaggerated. While Einstein, Hilbert, and others were developing the framework required for a self-consistent mathematical description of the Universe, astronomers had only just begun to provide the data needed to relate the theory to observation.[1]

Indeed, the degree homogeneity on the largest scales and the existence of a hierarchy of smaller scale structure in the Universe were topics of much debate. The prevailing assumption was that the Universe was filled with stars at roughly the same density as that observed in the vicinity of our solar system. Prior to Edwin Hubble's estimate of the distance to the Andromeda Nebula, Einstein wrote [40],

> "If we ponder over the question as to how the Universe, considered as a whole, is to be regarded, the first answer that suggests itself to us is surely this: As regards space (and time) the universe is infinite. There are stars everywhere, so that the density of matter, although very variable in detail, is nevertheless on the average everywhere the same. In other words: However far we might travel through space, we should find everywhere an attenuated swarm of fixed stars of approximately the same kind and density."

It is something of a remarkable coincidence that the formulation of the General Theory and the first identification of galaxies distant from our own occurred within such a short period of time. This observational triumph was a direct result of the insight of one Henrietta Leavitt, a staff member at the Harvard Observatory studying a class of pulsating stars, known as Cepheid variables, in the Small Magellanic Cloud. Ms. Leavitt systematically combed through thousands of photographic plates, measuring the variations in time of the flux of a number of stars.

By 1912, Leavitt had compiled enough data to accurately measure the periods of 25 stars. Making the reasonable assumption that all the Cepheids in the SMC were

[1] I borrow heavily from the excellent and very readable history by Hoskin [70].

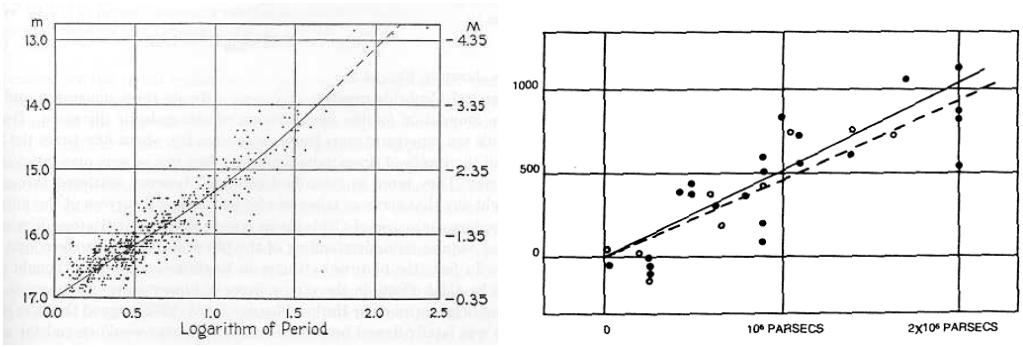


Figure 1.1: On the left, the original data from which Henrietta Leavitt derived the period-luminosity relation for Cepheid variable type stars. These stellar objects were, and are, invaluable tools in the determination of the distance scales in our Universe. The abscissa indicates the logarithm of the period of brightness fluctuations, while the ordinate shows the logarithm of the intrinsic luminosity. The right panel shows Hubble's original survey showing evidence for the expansion. Due to the limited depth of Hubble's survey, peculiar velocities contribute significantly to the uncertainty in the original estimate of the slope. Modern surveys, extending to much larger distances, provide measurements of $H$ that are accurate to $\sim 10$ %.

equally distant, she was the first to discover the correlation between the period of these stars and their intrinsic luminosity [98, 167].[2]

The period–luminosity relation, calibrated more accurately by the observations of Harlow Shapley, allowed the determination of the distance to a Cepheid simply by measuring the average flux and period of the star. Not suffering from the fundamental angular resolution requirements that limit parallax measurements, the Cepheids expanded by a factor of $\sim 10^5$ the distance scales that could be probed by standard astronomical observations.

Nevertheless, lively debate regarding the nature and the extent of the Galaxy persisted until 1923, when Edwin Hubble found a Cepheid variable star in the Andromeda Nebula. Applying Ms. Leavitt's period-luminosity relation, Hubble was able to establish an accurate distance to the Andromeda Nebula, which was well in excess

[2]This perhaps understates how remarkable an individual Ms. Leavitt must have been–as a deaf woman in the late nineteenth century, she yet managed to become the head of the Photometry Department at the Observatory. Ms. Leavitt, having provided an invaluable tool for cosmological observations, was thereafter sidelined by the more commanding personalities of Shapley and Hubble. Over ninety years later, similar distance measurements using Cepheids (as part of the HST Key project) have provided the most accurate estimate of the Hubble parameter to date [45].

of the largest estimates of the size of the Galaxy. Eventually, Hubble's measurements went on to show that our Galaxy is one of many such bodies, initiating the dawn of modern observational cosmology.

### 1.1.1 Isotropy and the metric

The advent of Einstein's "theory of invariants" initiated a transformational period for human understanding of the large scale structure and evolution of the Universe. General Relativity is an extremely rich discipline; we make no attempt at rigor, preferring to focus on the conceptual connection to observations. In this regard, we follow the extremely readable reviews by R. H. Sanders and by Liddle and Lyth [150, 108].

Coupled with the essentially Copernican assumption that the Universe is homogeneous and isotropic on the largest scales (the "cosmological principle"), General Relativity permits a particular family of solutions that are embodied in the Friedmann-Robertson-Walker line element:[3]

$$ds^2 = c^2dt^2 - a(t)^2\left(\frac{dr^2}{1-r^2/R_0^2} + r^2d\theta^2 + r^2\sin^2\theta d\phi^2\right) \ . \tag{1.1}$$

The FRW metric defines the coordinate-independent method of measuring time and space in an isotropic Universe. Our particular Universe is distinguished from other possible universes by the scale factor, $a(t)$, and the curvature parameter $R_0$. The scale parameter describes the time evolution of physical distances, whereas the curvature parameter determines the geometrical properties of the Universe.

The field equations determine the relationship between the mass-energy content and the geometry of the Universe; the latter determines how the former evolves in space and time. Under the assumption that the contents of the Universe may be treated as an ideal fluid (Weyl's postulate), the field equations of General Relativity (in particular the time-time component of the field equations) relate the scale

[3]Although both spellings are found in the literature, I use the most common anglicized version of Aleksandr Aleksandrovich Friedmann's last name, though the need for the second "n" is unclear to me.

parameter, $a(t)$, to the mass/energy distribution through the differential equation

$$\frac{\ddot{a}}{a} = -\frac{4\pi G}{3}\left(\rho + 3p/c^2\right) + \frac{\Lambda}{3} \ . \tag{1.2}$$

This is about what one might expect from Newtonian gravity, with the exception that the gravitational force is sourced not only by the distribution of mass, but also by the fluid's *pressure*, and possibly by some constant term, $\Lambda$. Energy conservation requires $d(\rho V) = -pdV/c^2$. Therefore, if you assume $p = w\rho c^2$ then $\rho \propto a^{-1(1+w)}$. If $w < -1/3$, then we have acceleration. The space-like components of the Einstein equation, combined with Equation 1.1, relate the mass-energy contents to the expansion parameter,

$$\left(\frac{H}{H_0}\right)^2 = -\left(\frac{r_H}{aR_0}\right)^2 + \frac{8\pi G}{3H_0^2}\sum_i \rho_i \ a^{-3(1+w_i)} \ , \tag{1.3}$$

where $H \equiv \dot{a}/a$, $r_H \equiv c/H_0$. The evolution of the density parameters has been explicitly included, such that the $\rho_i$ above are to be evaluated at the present epoch. The equation of state for nonrelativistic species such as baryons or cold dark matter gives $w = 0$. Relativistic species, such as neutrinos or radiation, will have $w = 1/3$. A cosmological constant, $\Lambda$, is defined by $w = -1$. The dark energy (or "Quintessence"), defined by $-1 < w < -1/3$, is simply anything that is less strongly damped by expansion than the curvature term. The contributions from each component are generally expressed in terms of the fraction of their critical density,

$$\Omega_i = \frac{8\pi G}{3H_0^2}\ \rho_i \ .$$

As has become conventional, the Hubble parameter is expressed in terms of $h$, defined by $H_0 = h \cdot 100$ [km s$^{-1}$ Mpc$^{-1}$]. For most observational tests, the density and Hubble parameters are degenerate, leading observational teams to report limits on the quantities $\{\Omega_i h^2\}$.

Evaluated at present, where we have defined $a \equiv 1$, Equation 1.3 can be written

in units of the critical density

$$1 - \sum_i \Omega_i = \Omega_k \ , \tag{1.4}$$

where we have made the definition $\Omega_k \equiv -(r_H/R_0)^2$. Clearly, if the left hand side of Equation 1.4 vanishes, $\Omega_k = 0$, or $R_0 \to \infty$ in Equation 1.1. In this case, the metric corresponds to a Euclidean (or flat) geometry. The measurement of a small but nonzero curvature term would require extremely precise fine-tuning of initial conditions due to the evolution of the density contributions described in Equation 1.3. At early times ($a \to 0$) the relative contribution of the curvature term will be negligible, whereas at late times ($a \to \infty$) either the $\Omega_k$ or $\Omega_\Lambda$ terms will dominate. A considerable degree of fine-tuning is required for the curvature term to remain subdominant if it is not precisely zero.

### 1.1.2 Expansion

The Friedmann equation (Equation 1.2, sometimes called the Friedmann-Lemaître Equation) implies the natural dynamism of cosmological distance scales; unless the parameter $\Lambda$ is tuned to *exactly* cancel the fluid density and pressure, a net acceleration of the scale parameter will result. Therefore, the metric (Equation 1.1) and the existence of matter imply that the proper separation of coordinates is generally a time dependent quantity, proportional to the expansion parameter, $l(t) = a(t)l_0$. Taking the derivative with time, we obtain the expression that defines the Hubble parameter [104, 105],

$$\dot{l} = \dot{a}(t)l_0 = \frac{\dot{a}(t)}{a(t)} l \equiv H(t)l \ . \tag{1.5}$$

Hubble's constant, $H_0 = H(t_0)$, is defined to be the value of the Hubble parameter evaluated at the present epoch. Like all physical distances, the wavelength of radiation propagating over cosmological distances is scaled by the ratio of the value of the scale

parameter between the emission and observation,

$$\frac{\lambda_{obs}}{\lambda_{emit}} = \frac{a_{obs}}{a_{emit}} \equiv (1+z) \ ,$$

where we have introduced the definition of the redshift, $z$, which serves as a convenient evolution parameter. An important distinction must be made between expansion of the sort described by Equation 1.5 and the sort of relative velocities we experience daily; they are fundamentally different phenomena.

The concept of an intrinsic "grid" of space-time points is fundamental to the workings of General Relativity. Coordinate positions on this grid indicate the separation of objects, just as the coordinates on a street map indicate the location (among other things) of the corner market. If you want to estimate the "proper distance" to the market, you must first find the relative positions of yourself and the market on the grid (say, three centimeters). In the notation of Equation 1.5, this "coordinate distance" corresponds to the quantity $l_0$, *not* $l$. Once you have measured $l_0$, it is necessary to refer to the map's scale to convert that into a "proper distance" (say, three kilometers). This conversion is exactly equivalent to multiplication by the scale parameter, $a$. Our daily experience with velocity is a rate of change of $l_0$ rather than a change in the scale of a map, and the two must not be confused. The cosmic expansion is of the latter sort; a change in the way we are to interpret proper distances rather than motion with regard to the grid.

Unless the $\Lambda$ term is tuned to exactly cancel the density and pressure terms, Equation 1.2 suggests that a universe containing any amount of matter or energy density will tend to evolve, with $\ddot{a} \neq 0$.[4] The implications of this dynamic space-time were not lost on Einstein and, in fact, it greatly displeased him (and others) on aesthetic grounds. While by no means required by the field equations, Einstein explicitly included the cosmological constant, $\Lambda$, in the solution in order to achieve a "more natural" static solution. In his own words (from the appendix of [40], circa 1935),

[4]The importance of this "fine-tuning" problem cannot be overstated, and is a topic to which we will return in the context of Inflation.

> "That the radius of space is independent of time appeared unavoidable to me at the time, since I thought that one would get into bottomless speculations if one departed from it."

Einstein was half correct. Shortly after the publication of the Special and General Theory, an analysis of Hubble's survey of distant (extragalactic) Cepheids provided the first observational evidence for a positive correlation between the redshift and the distance to objects that are not gravitationally bound. Interpreted as a positive value of $H_0$, the observational evidence that the Universe was indeed expanding (see Figure 1.1) led Einstein to abandon his cosmological constant, $\Lambda$, and to accept the notion of a dynamic Universe. Thus began an era of bottomless, if not fascinating, speculation.

### 1.1.3 The "Hot Big Bang" scenario

The most straightforward interpretation of the observed expansion is that at some earlier epoch the Universe must have been more dense and therefore more energetic than it is today. This hot and dense initial state is the origin of the "Hot Big Bang" theory (originally referred to as the Gamow theory), which postulates that the observable Universe has evolved from an initially hot and dense state into its current relatively cool and diffuse state [47, 48].

A philosophical prejudice toward the concept of a dynamic Universe persisted well into the 1960's with the advent of the steady-state theories of Bondi, Gold, and Hoyle (which postulated the spontaneous creation of energy to support the expansion), as well as the more fundamental modifications to relativity theory suggested by Milne and Dirac. Objections to the direct application of Einstein's General Theory to cosmological distances were not unreasonable; the only independent tests of the theory probed gravity on the scale of our solar system, making the application of the theory to cosmological scales an unprecedented extrapolation. Indeed, it was not until 1965, with the detection of the cosmic microwave background, that the hot big bang scenario came into nearly universal acceptance [136, 36].

Nevertheless, prior to discovery of the CMB, a great deal of theoretical progress was made on various aspects of the theory. In particular, physicists immediately recognized the potential of the hot initial phase as a laboratory for nuclear and particle physics. By the early 1950s, physicists had established the basic relationships between the baryon to photon ratio and the relative abundance of the elements created through thermonuclear reactions in the early Universe. The theory of Big Bang Nucleosynthesis (BBN) resulted in precise and testable predictions of the relative abundances of the light elements, which depend sensitively on the validity of the Friedmann equation during the epoch of radiation domination [1, 47, 48].

A number of researchers (including one Arno Penzias, in 1973), would eventually go on to make observations of interstellar deuterium abundances that would allow direct comparisons with the theory of nucleosynthesis. Similar observations would eventually provide a stunning confirmation of the validity of the BBN scenario, placing extremely strong constraints on deviations from the FRW cosmology during the epoch of radiation domination [168, 163].[5]

Prior to 1965, several independent observations pointed to the existence of an isotropic background at approximately the level expected from the cosmological background [48, 39]. In particular, it was known to various groups studying interstellar molecular line emission (in particular, the hyperfine lines of molecular Carbon) that the temperature of space was in excess of 2 Kelvin [63].[6] In 1961, during the commissioning of the Bell Labs receiver at Holmdel, Ohm reported a sky temperature of $2.3 \pm 0.2$K, while others at the same site reported similar contributions to the system temperature that were *"not otherwise accounted for"* [129]. However, it was the detection in 1965 of a uniform background emission by Arno Penzias and Robert Wilson that was positively identified by Dicke, Peebles, Roll and Wilkinson as the

[5]When combined with the temperature of the background radiation (which determines the photon number, or $\rho_\gamma$ in Equation 1.3), these same observations require that baryons contribute no more than a few percent of the critical density.

[6]Recent measurements have verified the expected scaling with redshift of the CMB temperature through observations of high redshift molecular clouds. The measurements provide independent verification of the validity of the Friedmann Equation at moderate redshift [120].

primordial background radiation [136, 36].[7]

Following the initial detection of the background radiation, a series of dedicated observations not only revealed the spectrum to be consistent with that of a 3-Kelvin blackbody, as Gamow and others had predicted, but also indicated that the background emission was fairly isotropic [154, 171]. This presented something of a problem for cosmologists due to the fact that the horizon size at the epoch of last scattering subtended an angle on the order of a degree. Therefore, regions of the sky with angular separations larger than a degree could never have been in causal contact. The apparent isotropy of the CMB raised the question of how such causally disconnected regions of the Universe could possibly have achieved such close thermal equilibrium, which became known as the "horizon problem".

It was not until 1991 that the Far-Infrared Spectrometer (FIRAS) and the Differential Microwave Receiver (DMR) onboard the COBE spacecraft returned the first definitive measurements of the temperature and isotropy of the CMB. FIRAS measured, with unprecedented accuracy, the spectrum of the CMB to be that of a 2.728-Kelvin blackbody, while the DMR measured the large angular scale anisotropies of the CMB for the first time. The FIRAS measurement remains the most precise measurement of a thermal Planck spectrum ever made, while the DMR observations revealed the temperature of the CMB to be isotropic to a few parts in $10^5$ [116, 10].

Despite its many successes, the hot big bang scenario is itself incapable of providing a natural explanation for the horizon and flatness problems. Perhaps more problematic, the assumption of homogeneity in theory provides no mechanism for the formation of structure in the Universe, such as galaxies and clusters of galaxies. It is now believed that these three enigmas, the horizon problem, the flatness problem, and structure formation, may share a common solution, namely Inflation. Before moving on to this topic, we outline the basic approach to structure formation.

[7] These observations were made while at Bell Laboratories using a surplus maser amplifier, at a wavelength of 7-cm, and an antenna that had been renovated to test the first TELSTAR communication satellite shortly after the assassination of Malcolm X.

### 1.1.4 Structure formation

As early as the late 1940s, it was recognized that the formation of structure requires a departure from strict homogeneity at early times; a spectrum of primordial density perturbations is required to seed the growth of structure under gravitational instability. During the 1970s, a number of authors considered the evolution of these perturbations through the epochs of radiation and matter domination, beyond the surface of last scattering, and on to the nonlinear regime, which results in the formation of the observed galaxies and clusters of galaxies.

The two most commonly studied classes of perturbation to the FRW line element are curvature (scalar) perturbations, $\mathcal{R}_s(k)$, and metric (tensor) perturbations, $\mathcal{R}_t(k)$. Curvature perturbations can be expressed in terms of spatial variations in the amplitude of the curvature, $1/R_0$, appearing in Equation 1.1. Metric perturbations are gravity waves, which can be described as small spatial variations in the metric. Choosing a Cartesian coordinate system in which the perturbation is propagating in the $\hat{z}$ direction, this can be expressed as a strain $h_{ij} = h_+ \ \sigma_3 + h_- \ \sigma_1$, where the $\sigma_i$ are the usual Pauli matrices, and the statistical distributions of the $h_\pm$ are described by the tensor power spectrum $\mathcal{R}_t(k)$.

The most simple models consider the evolution of a scale-invariant spectrum of curvature fluctuations, with all particle species characterized by a common initial density contrast (the so called adiabatic initial condition), $\delta\rho_i/\rho_i = g_i(k,t)$. The initial conditions specify the relationship between the primordial power spectrum and the density perturbation, $g_i(k,t)$, for each particle species, $i$. Since the fluctuations are stipulated to be small, each spatial mode propagates independently of the others. Therefore, for a given cosmological model, it is possible to calculate the transfer function, $g_i(k,t) = T_i(k,t) \ \mathcal{R}(k)$, for each particle species in the Fourier domain, providing a description of the time evolution of each spatial mode.

Calculations of the matter and radiation transfer functions, assuming a scale-invariant spectrum of curvature fluctuations, led to the first testable cosmological predictions regarding the statistical properties of the distribution of the matter and

energy contents of our Universe. In particular, the solution to the Boltzmann (Euler) transport equation resulted in early estimates of the radiation (matter) power spectrum [155, 60, 135].

More recently, numerical tools (such as CMBFAST and CAMB) have been made available to the community that calculate these transfer functions to high accuracy over a wide range of scales [151, 106]. At the smallest scales, where the perturbations become nonlinear, the spectrum of fluctuations can be estimated via massive $N$-body simulations. The combination of measurements of the microwave background anisotropy, the distribution of galaxies [137, 159], and the redshift distribution of line absorption in molecular hydrogen (the so-called Lyman-$\alpha$ forest) [51], provide observational constraints on the power spectrum over physical scales spanning an impressive four orders of magnitude.

### 1.1.5 Inflation

The concept of inflation was proposed by Guth in 1981 as a modification of the expansion history of the Universe at early times, supplementing rather than replacing the hot big bang scenario [52]. While originally introduced to solve some problems relating to particle physics (copious production of magnetic monopoles), Inflation has come to provide a framework for understanding the origin and functional form of the primordial perturbations that seed the formation of structure, as well as a successful (if ad hoc) solution to the horizon and flatness problems.

Inflation simply postulates a period, prior to the onset of nucleosynthesis (radiation domination), during which the acceleration of the scale parameter remains positive. As can be seen in Equation 1.2, this condition is satisfied during any period in which the matter/energy content of the Universe is characterized by an equation of state more negative than $w = -1/3$. The result is a period of rapid (usually, but not necessarily, exponential) expansion, in which the smallest physical scales are stretched to well beyond the particle horizon.

According to the scale dependence of the terms on the right hand side of Equation

1.3, the rapid growth of the scale parameter decreases the contribution of all particle species (*including* the curvature component) relative to the term driving inflation. This introduces a natural insensitivity to the initial curvature and geometry of space-time, and explains how causally disconnected regions of the present day Universe have achieved the observed degree of uniformity.

The most simple inflationary model, termed "slow roll" inflation, consists of a single scalar field, $\phi(r,t)$ evolving through a potential, $V(\phi)$. From the Lagrangian of the scalar field, one can show the pressure and density terms to be of the form [108]

$$\begin{aligned} \rho\, c^2 &= \tfrac{1}{2}\dot{\phi}^2 + V(\phi) \\ P &= \tfrac{1}{2}\dot{\phi}^2 - V(\phi)\ , \end{aligned} \tag{1.6}$$

The term "slow roll" derives from the condition for inflation, $\rho\, c^2 + 3P < 0$, which implies that the kinetic term be small compared to the potential, $\dot{\phi}^2 < V(\phi)$. It is assumed that the energy content of the Universe is dominated by the dynamics of the scalar field, which evolves to a minimum of the potential by the time inflation comes to an end.

Quantum fluctuations of the inflaton field result in spatial perturbations, $\phi(\vec{x}) = \phi_0 + \delta\phi(\vec{x})$, to the fields appearing in Equation 1.6. The relationship between the scalar and tensor perturbations, $\mathcal{R}(k)$, and those of the inflaton field, $\delta\phi$, is obtained by inserting the perturbed equations 1.6 into equations 1.2 and 1.1, and then equating the perturbations $\mathcal{R}$ with those of the inflaton field $\delta\phi(\vec{x})$. The form of the inflaton potential, $V(\phi)$, determines the spectrum of the primordial perturbations through its relation to the scale parameter, $k = aH/c$. The physical scale of quantum fluctuations in the scalar field is accelerated beyond the horizon during inflation. After the end of inflation, as the spatial fluctuations re-enter the horizon, they serve as a common source of the inhomogeneities in the distribution of the matter and radiation density [132, 92].

The most simple models generically predict a nearly scale invariant spectrum of adiabatic curvature and tensor perturbations whose relative amplitudes depend on the

detailed shape of the potential, $V(\phi)$.[8] More complicated inflationary models, usually involving more than one scalar field, are generally motivated by supersymmetric extensions to particle physics. These models are capable of producing more general initial conditions, including an admixture of isocurvature and adiabatic modes, each with their own primordial spectrum of perturbations. Field driven inflation represents a tantalizing connection between fundamental particle physics and cosmology [108, 37].

Until recently, nearly all cosmological parameter estimation has been performed under the assumption of a scale invariant spectrum of adiabatic perturbations, as is expected from slow roll inflation. As observations become more precise, especially observations of the CMB, it is important to keep in mind that relaxing these assumptions can dramatically *decrease* the significance of the determination of the various cosmological parameters. More optimistically, the quality of contemporary observational data is beginning to allow cosmologists to test the validity of the models themselves by directly probing the primordial power spectrum.

## 1.2 The microwave background anisotropies

The origin and basic statistical properties of the CMB temperature fluctuations have been understood for over thirty-five years [135, 155]. In this section, we briefly summarize the physics behind the observed anisotropies. Rigorous treatments may be found in [71, 73, 93, 72].

### 1.2.1 Temperature

The CMB photons observed today last interacted with matter approximately 13.5 billion years ago. As the Universe expanded and cooled, the primordial plasma even-

[8] Isocurvature initial conditions assume that the density fluctuations ($\delta\rho$, not $\delta\rho/\rho$) of each particle species add to zero. These modes are often referred to as entropy perturbations since they represent fluctuation in the number density of the species relative to radiation, $S_i = \delta n_i/n_i - \delta n_\gamma/\gamma$. In the most simple models, isocurvature modes are suppressed relative to adiabatic modes while beyond the horizon scale.

tually became optically thin as protons (preceded by a few helium nuclei) formed bound states with the free electrons to form a neutral gas, a process confusingly termed "recombination". The decoupling of baryonic matter and radiation allowed each species to evolve largely independently of one another. Since that epoch, the background radiation has continued to adiabatically cool as the photon wavelengths are increased by the cosmic expansion. The temperature of the background is measured by FIRAS to be 2.728 Kelvin [116], suggesting that the last scattering of CMB photons occurred at a redshift of $\sim 1300$.

On scales corresponding to physical distances larger than the particle horizon at the epoch of last scattering, causal physics could not have played any part in the formation of the observed anisotropies in the CMB. The anisotropies on scales larger than two degrees are therefore a direct probe of the unprocessed primordial spectrum of scalar fluctuations. This primordial component, referred to as the Sachs-Wolfe plateau, dominates the power spectrum at $\ell \lesssim 100$

At smaller scales, which correspond to causally connected regions of the Universe, the dominant features derive from the relatively simple physics describing small perturbations evolving in an isotropically expanding plasma. As the primordial fluctuations enter the horizon, their gravitational collapse is resisted by radiation pressure. The tight coupling between the photons and baryons results in gravitationally driven oscillations in which the density and peculiar velocity fields are coherent and out of phase, almost exactly like a harmonic oscillator.

As the Universe expands and cools, the transition from a fully ionized plasma to a neutral gas happens relatively quickly. The observed anisotropies are sourced by the two-dimensional projection of the inhomogeneities in the photon-baryon fluid on the sphere defined by the redshift of recombination. The oscillations in the photon-baryon fluid result in the well-known series of acoustic peaks in the power spectrum, the fundamental frequency being determined by the acoustic horizon scale at the surface of last scattering. Doppler shifts resulting from the peculiar velocity of the oscillating fluid fill in the regions between the compression and expansion peaks.

As expansion causes the plasma to become optically thin, the mean free path of

photons defines a characteristic length scale. Photons will have a tendency to diffuse out of density perturbations smaller than this scale, dragging baryons and electrons with them through Coulomb interactions. This causes the small scale oscillations in the fluid to be damped, a process known as "Silk Damping". This characteristic diffusion scale is precisely that which determines the thickness of the surface of last scattering. Since the observed anisotropies are sourced by the projection of the oscillations on the sphere, there will be many fluctuations with a wavelength smaller than the diffusion scale along any line of sight, resulting in a further suppression of CMB power on small scales. The diffusion scale corresponds to a comoving length of $\sim 80$ Mpc, or a multipole of $\ell \simeq 900$.

### 1.2.2 Polarization

A free charge in the presence of an incoherent and unpolarized radiation field with finite quadrupole anisotropy generates a net polarization due to Thompson scattering. The Thompson scattering cross section is proportional to the square of the scalar product of the incident and scattered photon polarizations. As a result all other multipole components of the radiation field will average to zero, making the polarization of the CMB sensitive only to the quadrupole seen by the free electrons.

Within the photon-baryon fluid, density perturbations result in velocity gradients in the frame of free-streaming electrons as the plasma undergoes acoustic oscillations. The acceleration of electrons flowing towards overdensities (cold spots) produces a quadrupole in the local frame of the scatterer, resulting in net polarization aligned in the direction of motion. Likewise, the deceleration of electrons flowing towards underdensities (hot spots) results in a net polarization aligned perpendicular to the flow (see Figure 1.2).

Generally speaking, the acoustic oscillations result in subhorizon polarization patterns that align radially with regard to cold spots, and parallel to the gradient surrounding hot spots in the temperature anisotropy field. At large angular scales, which correspond to distances comparable to the horizon size at the epoch of last scatter-

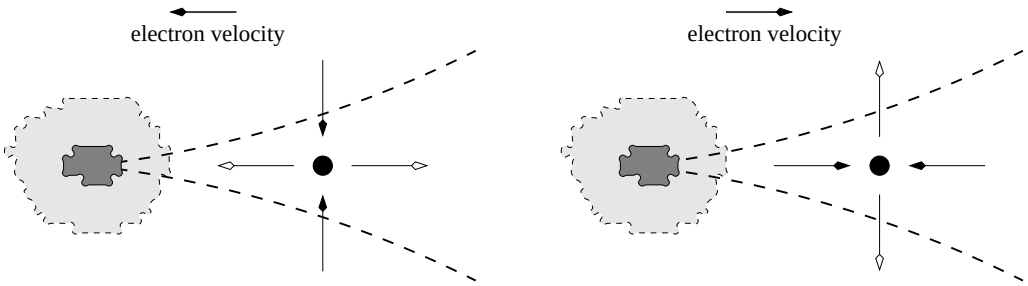


Figure 1.2: Velocity gradients during the epoch of last scattering generate quadrupole anisotropies in the frame of the scatterers. The figure is adapted from Kaplan and Delabrouille [86, 35].

ing, the CMB polarization reflects the properties of the unprocessed primordial power spectra.

In the tight thermal equilibrium characterizing the primordial plasma, repeated scatterings randomize the polarization. Only once the mean free path of photons is significantly larger than the rate of scattering of an average electron does the Thompson scattering result in a net polarization. Therefore, the subhorizon scale polarization of the CMB results from the scattering of CMB photons during the final stages of recombination, when the mean free path of photons was large and yet the density of free electrons remains finite. The restrictive requirements on the rarefied plasma are the origin of the relatively small amplitude of the polarization signature relative to the temperature anisotropies.

Inflationary theories generally predict a stochastic background of gravitational waves. During the epoch of last scattering, the propagation of these gravitational waves through the optically thin plasma will contribute to the local quadrupole of scatterers, and therefore to the generation of polarized emission. Unlike the anisotropy sourced by scalar density perturbations, gravitational waves are tensorial and therefore capable of generating both E- and B-mode signatures in the CMB polarization. In most inflationary scenarios, the amplitude of the gravitational-wave contribution is proportional to the fourth power of the energy scale of inflation. Therefore, a detection of a cosmological B-mode signal would be a direct probe of the physics of the epoch of inflation.

The physics of the surface of last scattering and of inflation are not the sole sources of CMB polarization. The energy injection resulting from the first generation of fusion burning objects reionized the neutral hydrogen in the Universe. The quadrupole anisotropy present at the epoch of reionization, which is generally thought to have occurred at redshifts $10 \lesssim z_{reion} \lesssim 30$, results in polarized scattering of CMB photons in a way exactly analogous to that which occurs at the surface of (almost) last scattering. Due to the expansion of the particle horizon between the epochs of recombination and reionization, the scattering at this later period results in an increase in the large angular scale E-mode polarization signal.

At smaller angular scales, the distribution of matter along the line of sight to the surface of last scattering results in a gravitational distortion of the CMB . This weak gravitational lensing effect results in conversion between the E- and B-mode signals, and represents a fundamental limit to the ability to detect any primordial gravitational wave signal through measurements of the B-mode power spectrum.

### 1.2.3 Observations

The wealth of cosmological information encoded in the statistical properties of the Cosmic Microwave Background Radiation (CMB) has motivated a highly successful observational effort to determine the angular power spectrum of the CMB temperature anisotropies. The experimental effort has been broad-based, with teams reporting results from interferometric and single dish observations spanning a decade in frequency and more than three decades in angular scale. The recent success of these observations, coupled with the predictive power of accurate theoretical modeling, has contributed to the transformation of cosmology into a quantitative, precise and, more importantly, an increasingly accurate science.

The COBE-DMR instrument was the first to detect the large angular scale fluctuations in the CMB, which are believed to result from the unprocessed primordial curvature perturbations, of the variety expected from inflation [10]. In the decade that followed, numerous experimental teams detected the first of the (much antic-

ipated) series of peaks in the angular power spectrum of the CMB resulting from acoustic oscillations of the photon-baryon fluid prior to the epoch of last scattering [127, 117, 119].

The 1998 flights of the BOOMERANG and MAXIMA suborbital payloads resulted in the first wide area images of the CMB enjoying high signal-to-noise at moderate ($\simeq 10'$) angular resolution. These observations resulted in an unambiguous measurement of the first and second peaks of the the angular power spectrum [34, 126, 145, 99, 55]. Soon thereafter, ground based single dish and interferometric observations confirmed these results and extended the characterization of the power spectrum to smaller angular scales [53, 113, 50, 95].

When combined with independent measurements of the Hubble parameter [45] and the large scale distribution of galaxies [137, 159], the CMB data tightly constrain the spatial curvature of the unperturbed metric to be consistent with a Euclidean geometry [96, 74, 13, 152]. The observations of primordial fluctuations and the negligible contribution of space-time curvature each lent further support to the emerging paradigm of inflationary cosmology.

It had long been known, from measurements of the rotation curves of galaxies and clusters of galaxies, that the gravitational influence on dynamics appeared to be much greater than could be accounted for by luminous matter alone [149]. Furthermore, the light element abundances indicate that the density of baryons is far less than the critical density [163].

In early 2003, the WMAP satellite returned its first images of the CMB, covering nearly the whole sky with modest signal-to-noise at degree angular scales [11, 12]. These measurements provide a sample variance limited measurement of the CMB power spectrum at angular scales ranging from the dipole to $\ell \lesssim 400$. The WMAP data confirmed the findings of the earlier experiments, while providing the tightest constraints reported on the cosmological parameters within the context of the most simple adiabatic inflationary models [65, 152, 130].

The first statistical detection of CMB polarization was announced by the DASI team a few months prior to the WMAP release [94]. The 30 GHz interferometer re-

ported a statistically significant detection of a polarized signal at an angular scale of about a half degree. In the release of the first year data, the WMAP team reported a very high signal-to-noise measurement of the spatial correlation between the temperature and polarization anisotropies at angular scales on the order of one degree [130]. In late 2004, the DASI and WMAP findings were confirmed by the CBI, another 30 GHz interferometer.

The field of CMB polarization is at a stage of development similar to that of the temperature anisotropy measurements of the late 1980s. Statistical detections are beginning to emerge, but definitive measurements with high signal-to-noise over a large area are still a number of years away.

# Conclusion

Cosmology is far from solved. The formulation of an appropriate set of questions is often more difficult than finding their solution, and in that sense the field may be passing the most difficult of a series of hurdles. A consensus has emerged that the basic theoretical framework of Inflationary Cosmology is the one that appears to describe our Cosmos. More specifically, a number of independent observations indicate that our particular Universe appears to be Euclidean (from observations of the CMB), and dominated by a combination of dark energy (the CMB and observations of distant supernovas [138, 143]) and dark matter (the CMB, BBN [163], large scale structure [137, 159], and dynamics [149]). Observations have not only become sensitive enough to probe the parameter space of these models, but also to probe the consistency of the theory itself [23, 24, 25, 175, 8, 78, 134, 165, 41]. The evidence for Inflation, while compelling, remains purely circumstantial; the search for direct evidence of Inflation remains one of the primary pursuits in the field of observational cosmology.

# Chapter 2

# The BOOMERANG Experiment

> "Duct tape is like the Force. It has a light side, a dark side, and it holds the Universe together."
>
> –Carl Zwanzig

After over five years of development BOOMERANG made its first long duration balloon flight above Antarctica in 1998. The 1998 instrument consisted of sixteen unpolarized detectors that operated at four wavelengths. At the time of its release, the data from this flight were of unprecedented quality. While a number of other experiments indicated the presence of a rise in power at degree angular scales, the BOOMERANG instrument's sensitivity, frequency coverage, and angular resolution allowed the unambiguous measurement of temperature fluctuations in the cosmic microwave background over a broad range of angular scales [31, 32].

The basic scientific result of this mission was the determination that the Universe is very close to being geometrically flat [34, 33, 126, 145].[1] One of the major implications of this result is that we have only a very dim understanding of what the Universe is made of; baryonic matter contributes a small fraction of the critical density, the energy density required to achieve a flat space-time geometry [163, 96]. The release of the WMAP data in 2003 confirmed the cosmological results of the BOOMERANG98 data

[1] My own involvement in the collaboration began in 2000, with the development of the physical optics package that was used to determine the instrument's window functions for the Netterfield and Ruhl, et al., releases [126, 145].

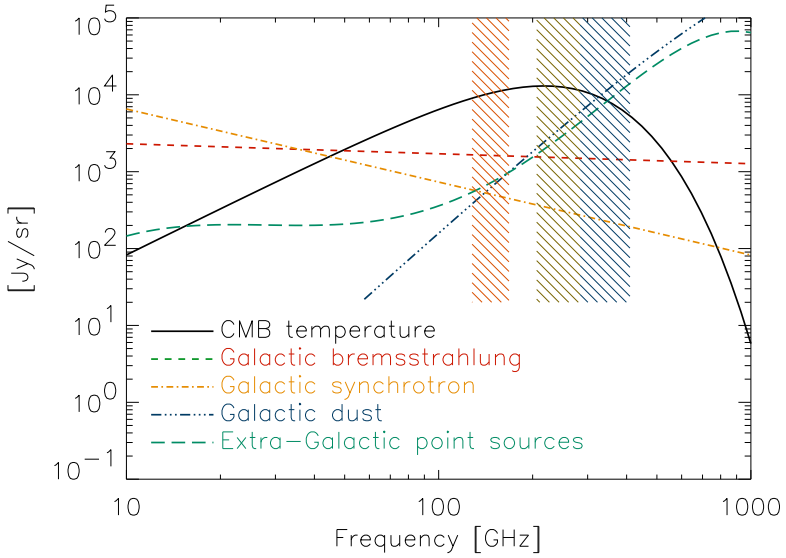


Figure 2.1: The frequency spectra of the signal and foregrounds. Galactic synchrotron and bremsstrahlung radiation are characterized by falling spectra, while the thermal emission of galactic dust is steeply rising. Synchrotron radiation is expected to be highly polarized, whereas the polarization fraction of the dust emission is not well known. The levels of emission shown are typical of the mid-galactic latitudes, $|b| \simeq 25°$. BOOMERANG's bands are highlighted for comparison. The extragalactic point source brightness model comes from [49], and assumes a $10'$ FWHMbeam.

and provided a much improved measurement of the large angular scale temperature fluctuations [12, 65, 152].

Since the 1998 flight, we have completely redesigned the focal plane of the instrument to study the polarization as well as the temperature anisotropy of the CMB. Analysis of the statistical properties of the CMB polarization allows a direct probe of the surface of last scattering, breaking degeneracies in the temperature data and providing a check on the initial conditions imposed on the primordial fluctuations.

In addition to the study of the CMB, B2K has provided the most sensitive survey to date of the intensity, spectrum, and polarization of galactic emission at millimeter wavelengths. Very little is known about the polarization properties of the diffuse emission from the Galaxy at these frequencies. These data will aid in our understanding of the physics of the interstellar medium. While scientifically interesting in

its own right, knowledge of the nature of galactic emission is also necessary in guiding the design of the next generation of CMB polarimeters.

BOOMERANG is an international consortium with funding from national agencies in Canada, Italy, the United Kingdom, and the U. S. Within the U. S., the payload development and flight are each supported by NASA and by NSF. Additional support for the development of the detector system has been provided by Caltech and JPL.

In this chapter, we describe the conceptual and technical design of the experiment. Section 2.1 describes the overall strategy, Section 2.2 reviews the gondola and flight systems, Section 2.3 describes the design of the focal plane and detectors, and Section 2.4 covers the design and analysis of the optical system.

## 2.1 Experimental approach

The primary science goal is to estimate, from a limited sample of the full sky, the underlying statistical distribution of the temperature and polarization anisotropies of the CMB of a wide range of angular scales. In addition to the extremely small amplitude of the signal relative to the background, measurements of the power spectra are complicated by foreground emission from non-cosmological astrophysical sources, interference from the atmosphere, and systematic effects introduced by the instrument.

Our approach is to produce high fidelity images of the Stokes **I**, **Q**, and **U** parameters over a modest portion of the sky in three distinct frequency bands. These images are then combined to separately produce the best estimates of the CMB anisotropies and of the foreground emission. From this image of the CMB, we estimate the underlying power spectrum of fluctuations from which the observed anisotropies are drawn. In this section, we present an overview of the BOOMERANG experiment, describing the rationale behind the basic aspects of the approach.

### Frequency coverage

The choice of frequency bands is determined by the spectrum of the cosmological signal, the spectra of the various non-cosmological foregrounds (galactic and extra-

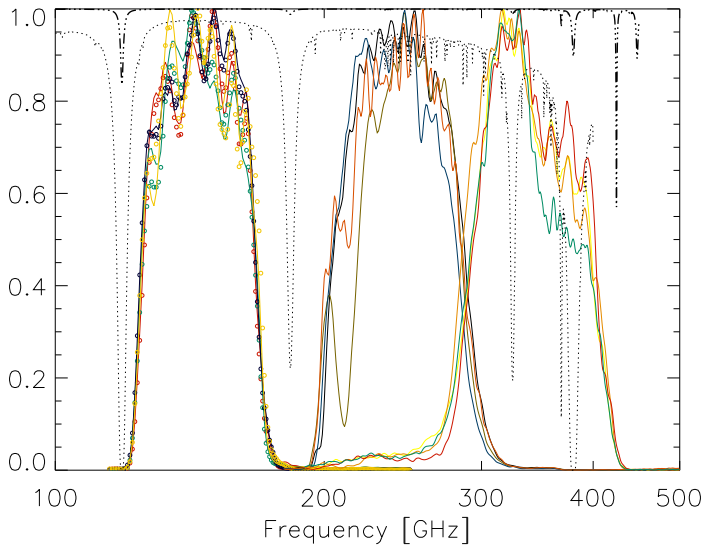


Figure 2.2: The BOOMERANG bands as measured prior to launch. The broken lines are an atmospheric model describing the transmission of the atmosphere from *terrestrial* sites, the dotted line representing Mauna Kea, Hawaii, and the darker dashed line representing conditions typical of the South Pole winter. The atmospheric transmission is of course much better at the stratospheric altitudes. The fine-structure lines of molecular oxygen ($O_2$) appear at 60, 119, 370 and 425 GHz. Water vapor, which is present in the troposphere, results in the absorption lines at 183 and 325 GHz as well as the continuum, which dominates the terrestrial spectra above $\sim$ 300 GHz [164].

galactic), the presence of atmospheric absorption and emission lines, as well as angular resolution requirements. For a given primary aperture, angular resolution scales inversely with frequency, favoring higher frequencies. The spectrum of the CMB and typical foreground spectra are illustrated in Figure 2.1. The normalization of the galactic spectra corresponds to middle galactic latitudes, however it is important to note that the brightness, spectrum, and polarization fraction of the foregrounds are spatially variable and subject to a large degree of uncertainty [91, 21, 43].

The spectra of the foregrounds and the CMB define an optimal bandwidth for CMB observations ranging from $\sim$ 50 GHz to $\sim$ 300 GHz. BOOMERANG operates in three bands centered near 150, 240 and 340 GHz (2 mm, 1.25 mm, and 880 $\mu$m, respectively), allowing for good discrimination between CMB emission and that of galactic dust. We rely on observations at lower frequencies to estimate the degree of contamination resulting from galactic synchrotron and bremsstrahlung emission.

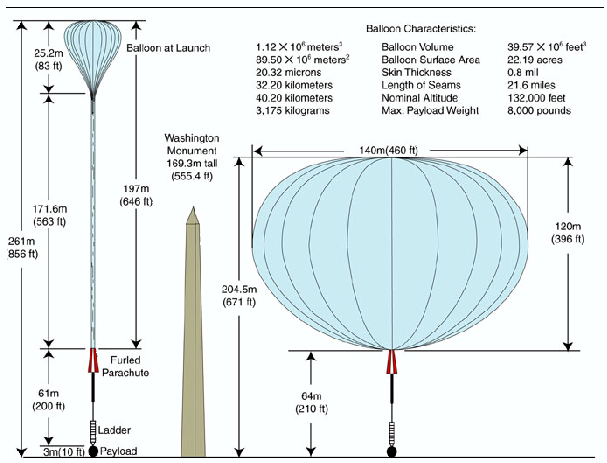


Figure 2.3: A schematic drawing illustrating the size of the balloon at sea level (left) and at a float altitude (right), with Washington monument for scale. The parachute, flight train, and payload can be seen suspended below the balloon. Image courtesy of the NSBF.

At millimeter and submillimeter wavelengths, atmospheric continuum and molecular line emission and absorption represent a very significant limitation for terrestrial telescopes. The detailed shape of the BOOMERANG bands are shown in Figure 2.2, together with typical atmospheric transmission spectra from good terrestrial sites (Mauna Kea, Hawaii, and the South Pole).

The presence of the atmosphere degrades the performance of millimeter-wave observations in a number of ways: absorption attenuates the astrophysical signals, the emission contributes to optical background level, and spatial and temporal atmospheric brightness fluctuations produce spurious (although largely unpolarized) signals. Above 180 GHz, atmospheric emission (largely line emission from molecular oxygen) contributes significantly to the background, even at an altitude of $\sim 35$km. The desire to minimize systematic effects and the need to make sensitive, wide-bandwidth observations at frequencies up to 400 GHz, makes observing from above the atmosphere a necessity.

## Long duration ballooning

The Antarctic Long Duration Balloon (LDB) Program is operated by the National Scientific Balloon Facility (NSBF) and supported by NASA's Office of Space Science and NSF's Office of Polar Programs. The LDB platform is a low-cost alternative to an orbital mission, carrying an $\sim$ 1700-kg science payload to an altitude of roughly 35 km for approximately twenty days. At this altitude, the atmospheric pressure is typically below $\sim$ 10 mbar ($\sim$ 7.5 torr), providing an excellent platform for millimeter-wave observations. The National Scientific Balloon Facility maintains a seasonal launch site at William's Field, about 10 km from McMurdo Station, Antarctica. The flights occur during the Austral summer to coincide with the onset of the southern polar vortex. This is a favorable high-altitude wind pattern that tends to carry payloads launched from William's Field at roughly constant latitude, returning to the vicinity of McMurdo Station after one or two trips around the pole.

The NSBF typically supports two Antarctic science payloads a season. Each LDB is flown with an NSBF-supplied Support Integration Payload (SIP), which provides low-bandwidth telemetry via the TDRSS communications network. Bandwidth and reliability considerations require that the science payload be autonomous and have provision for on-board data storage. The launch window typically opens around the end of December, and closes by mid-January, leaving about three months for preflight integration and testing of the payload. Launching an LDB is a prolonged procedure requiring in excess of six hours of very mild ($\lesssim$ 5 knots) low level winds. Weather in Antarctica is highly unpredictable and rarely favorable for ballooning; there are few launch opportunities per season. The outstanding observing platform comes at the cost of a high level of risk, complicated logistics, complex systems, and difficult working conditions.

## Sky coverage

The launch date and location constrain the portion of sky accessible to an LDB platform. During the Austral summer, the antisolar direction falls in the vicinity of

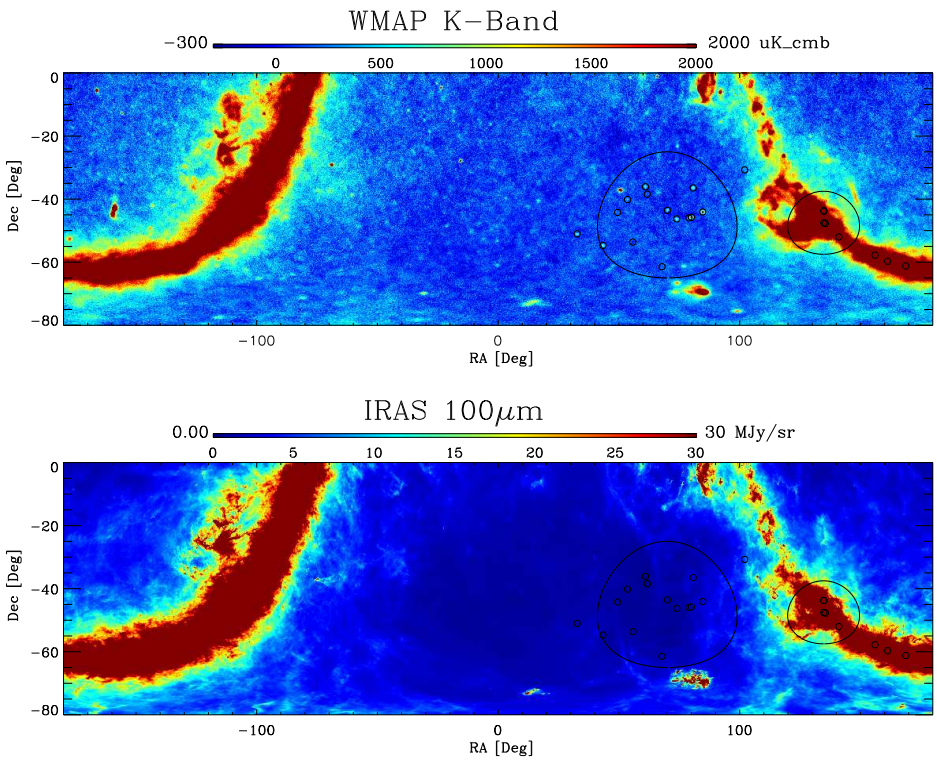


Figure 2.4: The BOOMERANG target fields overlaid on the WMAP K-Band (22 GHz) map of the southern sky. Quasars and compact galactic sources are marked with small circles. The main BOOMERANG field was chosen to minimize galactic emission under the constraints imposed by the Sun, balloon, and horizon.

RA (J2000) $\simeq 70°$. galactic emission is significant over much of the sky, so care must be taken to target regions relatively free of foreground contamination. The Wilkinson Microwave Anisotropy Probe (WMAP) has produced all-sky images of microwave emission at 22 GHz [12]. These data provide a sensitive survey of galactic synchrotron radiation, which is useful for selecting fields that are relatively free of contamination. The BOOMERANG fields were chosen to minimize galactic contamination, subject to the constraints imposed by the LDB flight parameters. Figure 2.4 shows the WMAP K-Band image of the southern sky, with the BOOMERANG target fields overlaid. A section of the galactic plane was targeted for calibration purposes, as well as to achieve our secondary science goals.

The BOOMERANG telescope is an Alt-Az mount, which is scanned at constant velocity in azimuth. Torque considerations, discussed in more detail in Section 2.2

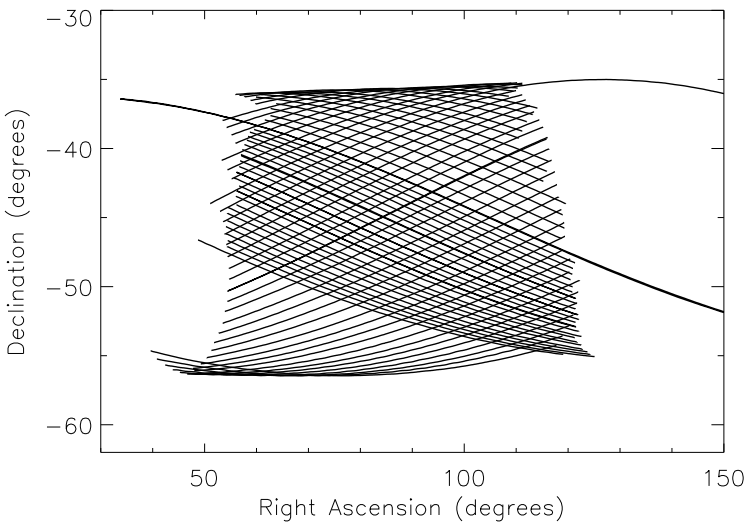


Figure 2.5: An illustration of BOOMERANG's cross linking resulting from sky rotation. Depending on the latitude of the flight track, the projection of the scan on the sky is modulated by $\sim 20^\circ$ every 24 hour period.

limit the minimum peak-to-peak scan amplitude to approximately 15°. The telescope elevation is adjusted on $\sim$ one hour time scales. The earth's rotation provides about 20° of cross linking between scans, which aids in the analysis. During the meridians, when the sky rotation is minimal, our scans were redirected to a nearby portion of the galactic plane, thereby gaining valuable calibration and secondary science data with minimal impact to our primary science. Figure 2.5 illustrates the projection of our scans on the sky over the course of a 24 hour period.

For a fixed amount of observing time, one must balance the competing demands of maximal sky coverage and integration time per resolution element. When attempting to measure the power spectrum, mapping the sky with a signal-to-noise ratio of a few is a good compromise between sample variance, instrumental noise, and control of systematics. For the CMB polarization, the signal level is sufficiently low to require BOOMERANG to concentrate as much integration time as possible in as small a region as possible. However, the desire to make high fidelity measurements of (the relatively large amplitude) unpolarized temperature fluctuations in addition to the polarization measurements led to a two-tiered scan strategy.

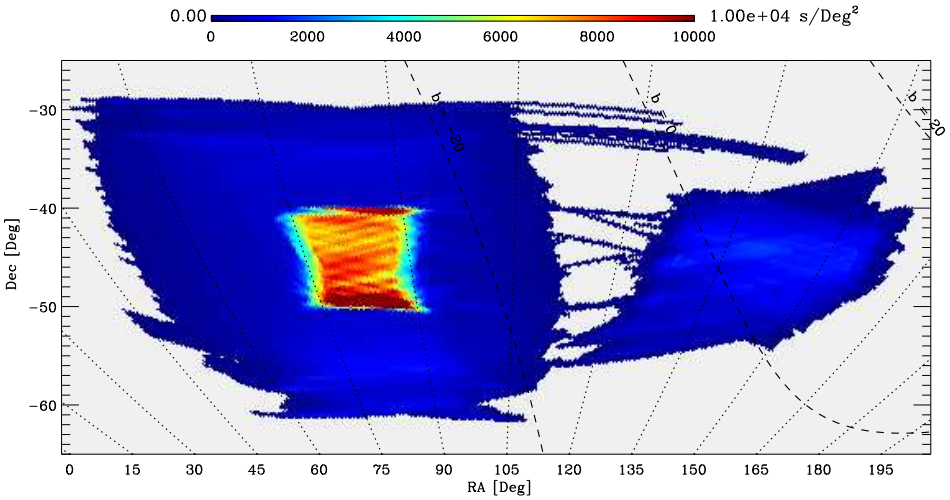


Figure 2.6: The distribution of BOOMERANG's integration time on the sky. The galactic equator and $b = \pm 20°$ contours are drawn for reference.

Roughly one quarter of the flight was spent observing a modest fraction ($\sim 3\%$) of the sky, while the remainder of the flight was spent on a region centered on the larger field. This smaller field constitutes roughly $\sim 0.3\%$ of the sky. Due to weather related delays, BOOMERANG launched about two weeks later than anticipated. In order to mitigate risk, the schedule file for observations was not updated to reflect the later launch date. As a result, our actual sky coverage shifted approximately 14° in the ecliptic, bringing our fields closer to the galactic plane than originally planned. The actual distribution of integration time on the sky is shown in Figure 2.6.

## 2.2 Gondola and flight systems

The BOOMERANG payload has been described extensively in the literature [19, 111, 112, 31, 32, 122, 121]. We summarize the various support subsystems here, with an emphasis on the details that have been added or significantly changed since the 1998 flight. The focal plane and optics are described separately in sections 2.3 and 2.4.

An Antarctic LDB payload operates in an environment very similar to that of a spacecraft. The low ambient pressure and constant sunlight result in large ($\sim 100°$

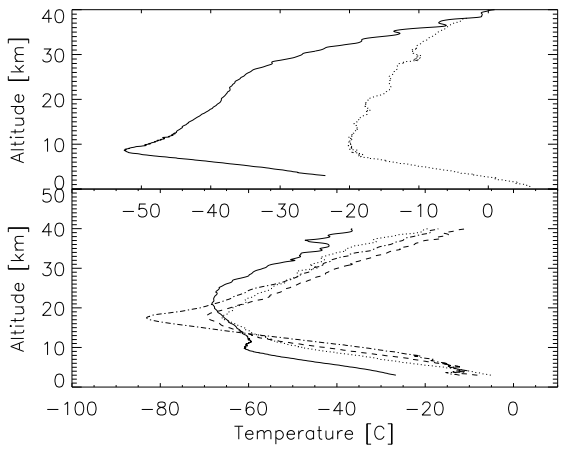


Figure 2.7: CHAMP measurements of the atmospheric temperature profile. The top panel shows the average of temperature profiles measured in the vicinity of the BOOMERANG payload during the flight (solid line), and the temperature of the gondola during ascent (dotted line). The bottom panel shows the temperature profile over the north pole (solid line), the equator (dot-dashed line), and at $\pm 33^\circ$ latitudes (dotted and dashed lines). At polar latitudes the tropopause is $\sim 20^\circ$ C warmer and occurs at roughly half the altitude of that at middle latitudes. The temperature data are accurate to $\sim 0.5^\circ$ C while the vertical resolution is $\sim$ 1km [169].

C) thermal gradients and exposure to intense radiation. During ascent, the payload passes through the troposphere, where the ambient temperature drops to well below $-50^\circ$ C. Due to the remoteness of the flight path, communication with the payload must rely on intermittent low-bandwidth links via relay satellites. The payload must be robust, self sufficient, and autonomous.

The BOOMERANG gondola, shown in Figure 2.8, has flown on two Antarctic LDB missions. The gondola itself is constructed from a welded aluminum frame, with a balanced inner frame that supports the primary mirror and the cryostat. The suspended mass of the instrument is 2156 kg, with the science payload contributing 1656 kg.

The payload must be designed to survive the thermal environment encountered during the ascent to float altitude. In February 2001, the CHAMP satellite began continuously monitoring the global atmospheric temperature profile using the GPS-based limb sounding method developed by the GPS/MET mission in 1996. The GPS radio occultation technique directly measures the variation of the atmospheric refrac-

tive index with altitude. The temperature profile can be derived from this data with sub-Kelvin accuracy. CHAMP provides approximately 230 globally distributed vertical profiles of atmospheric parameters each day. Accurate temperature profiles are obtained at altitudes from $\sim$ 1–50km, at $\sim$ 1km vertical resolution. The measurement probes spatial scales of several hundred kilometers [169, 3, 144].

Numerous temperature profiles were measured by CHAMP in the vicinity of the BOOMERANG payload during the month of January 2003. The average temperature profile during the two week flight is shown in the upper panel of Figure 2.7. At altitudes between a few hundred meters and $\sim$ ten kilometers, the atmospheric temperature drops steadily with altitude to a minimum (well below $-50^\circ$ C), which defines the tropopause. The precise altitude and temperature of the tropopause vary with season and latitude. Above the tropopause, the temperature steadily rises through the stratosphere. The bottom panel of Figure 2.7 shows the temperature profiles for the tropical latitudes (broken lines) and for the northern polar latitudes (solid line) coincident with the BOOMERANG flight. The troposphere occurs at a significantly lower altitude over the south polar cap than it does at higher latitudes. Convective heat transport is still efficient at these altitudes, and extensive insulation of the motors and electronics is required to protect them from the extreme cold during ascent.

The continuous solar exposure and the high albedo of the polar ice cap produce a large radiative load on the gondola. At float altitudes, the low ambient pressure makes convective heat transport negligible, and thermal equilibrium is reached through radiative coupling to space. To protect the instrument, panels of expanded foam insulation are secured to the outer frame. These panels are covered with 50$\mu$m mylar sheet coated with a 25$\mu$m aluminized layer.

The mylar outer-layer is essentially transparent to the solar flux (which peaks near 0.5$\mu$m) and, unlike aluminum, is highly emissive in the infrared. Sun shields, made from the same material stretched on a PVC frame, extend out from both sides of the gondola. All panel joints are sealed with aluminum tape to prevent light leaks into the telescope. Prior to launch, all the remaining bare aluminum is sprayed with white paint. The ratio of 10$\mu$m to 0.5$\mu$m emissivity is similar for white paint and aluminized

Material Emissivities

| | $\epsilon_{10\mu m}$ | $\epsilon_{0.5\mu m}$ | ratio |
|---|---|---|---|
| Pure Al .... | 0.02 | 0.05 | 0.4 |
| $Al_2O_3$ ..... | 0.02 | 0.12 | 0.1 |
| Mylar..... | 0.40 | trans. | – |
| Alum. Mylar | 0.40 | 0.05 | 8.0 |
| $TiO_2^{\dagger}$ ..... | 0.92 | 0.1 | 9.2 |

Table 2.1: The emissivity of several materials used on the exterior coating of the payload. The ratio of emissivities between $10\mu$m, where the thermal emission of objects at ambient temperature is at a maximum, and the emissivity at $0.5\mu$m, where the solar irradiance peaks, determines the equilibrium temperature of the surface. $^{\dagger}$Titanium oxide is the primary pigment in white paint.

Mylar (see Table 2.1). Therefore, both provide for efficient radiative cooling to space while keeping the absorption of solar radiation to a minimum.

Two independent power systems supply the attitude control system and the data acquisition system. The batteries were kept charged by two arrays of solar panels mounted on wings at the rear of the gondola. Each array delivered $\sim$ 700 W to the charge controllers at normal incidence to the Sun. The cryostat, receiver, and DAS are powered by a 300 W system, while the attitude control system and data storage run off a 750 W power system.

Two torque motors control the gondola azimuth. The primary motor torques against a massive flywheel located just below the flight train pivot, while the secondary motor torques against the steel cables securing the gondola to the flight train. The elevation axis of the balanced inner frame is driven with a DC motor, coupled to a worm gear.

The telescope motors are controlled by a pair of redundant 386 computers, which servo the motor currents off of the data read from the pointing sensors. The primary sensors used in this loop are the azimuth gyro, which provides velocity feedback, and the fixed sun sensor, which provides absolute pointing data to the flight computers. In the event of sensor failure, the DGPS and star camera can be used to reference the center and limits of the azimuth scans. In the event of a reboot of either flight computer, a watchdog circuit ensures the switching of telescope control to the redundant

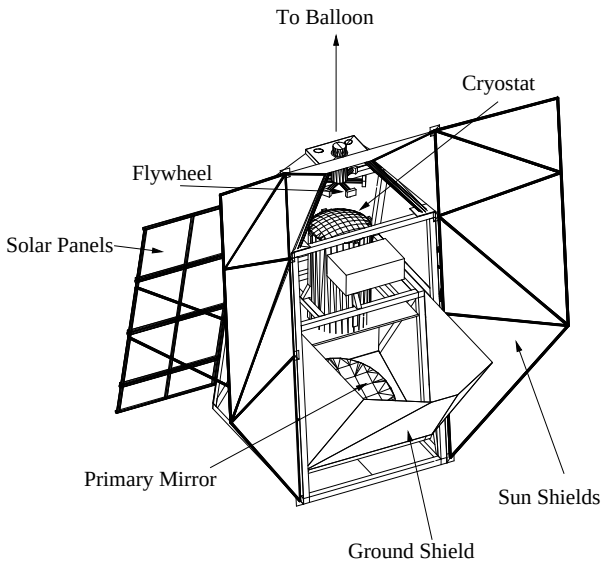


Figure 2.8: A schematic of the BOOMERANG gondola, shown at an oblique angle to the telescope. The upper edge of the primary can be seen from behind the telescope baffle. The cryostat, warm readout electronics, and fly-wheel are shown on the interior. The sun-shields extend to either side of the gondola, and above the cryostat. One of the two Solar arrays is visible at the rear.

CPU in $\sim 300$ ms.

The attitude control system (ACS) and pointing reconstruction rely on a variety of sensors. Because of the extreme latitude of the flight path, magnetic sensors are of limited use as a primary sensor. The B2K payload carried a pointed star tracker, a pointed sun sensor, a fixed sun sensor, a three-axis laser-ring gyroscope, and a differential Global Positioning Satellite (DGPS) receiver. An absolute encoder on the elevation drive of the inner frame determined the orientation of the telescope boresight with respect to the gondola. Prior to flight, the gondola was balanced to minimize the equilibrium pitch and roll of the payload.

BOOMERANG uses a pointed star camera, mounted on the outer frame of the gondola. The star camera employed a Cohu 4920 monochrome CCD camera coupled to an f/5.6 Rubinar Maksutov lens with a 500 mm focal length. The camera was coupled to a Matrox METEOR frame grabber. The camera and lens provided a half degree field of view. The spectral response was limited to a band extending from

roughly 715 nm to 1000 nm, with the long wavelength response determined by the roll off of the CCD sensor performance. In this band, the (daytime) sky brightness at $\sim$ 35-km altitude was found to be roughly 4.5 magnitude. The camera was capable of locking on to mag-4 stars, although during most of the flight mag-2 stars were available. The camera position was controlled by two Servo-systems AMP HT17-075 stepper motors and monitored with two Gurly model A25S absolute encoders.

The required $\sim 1^\circ$ in-flight pointing accuracy was achieved with the fixed sun sensor, the elevation encoder, and the DGPS coordinates (time, latitude, and longitude) and the assumption of zero pitch and roll of the gondola. The post-flight pointing reconstruction incorporated all available sensors, and achieved an accuracy of $\lesssim 3'$ full width half maximum (FWHM).

The 16-bit DAS is constructed entirely from discrete CMOS logic, with the data frame defined by a UV-EPROM. The 38-kbps bi-phase output is sent to a line-of-sight transmitter, then on to the data system. The line of sight transmitter can support a bandwidth up to 275 kbs, allowing the full data stream to be relayed to the launch site for the first $\sim$ 24 hours of the flight.

A pressure vessel houses two commercial grade, single board computers (one a Celeron 333, and the other a 486/99) that handle the processing and storage of the signal and housekeeping data. The data streams are stored on a 10 GB EIDE drive as well as a Hewlett-Packard DDS2 digital audio tape. The vessel is slightly overpressured prior to launch to protect the operation of the hard drives. These computers handle the processing of the star camera frames, and compress the data for return over the TDRSS link. The data compression involves the boxcar averaging of a buffered data stream over three samples, then passing the average of two subsequent samples to the transmit stream. This results in a factor of two compression over the raw time streams. The compressed stream is returned over the TDRSS (Tracking and Data Relay Satellite) S band multiple access downlink (2.29 GHz). The newer TDRSS-H, -I and -J satellites offer a high bandwidth Ka band link offering 800 Mbs data rates through a pointed high gain antenna.

The BOOMERANG cryostat is a simple system using expendable cryogens to pro-

System Temperature Ranges

| Subsystem | Low | High |
|---|---|---|
| DAS/ACS power controllers | 0 | 25 |
| ACS backup battery ..... | -5 | 15 |
| PV/ACS CPUs ..... | 24 | 38 |
| Readout electronics ..... | 8 | 25 |
| Cryostat vacuum jacket .... | -16 | 0 |
| Primary mirror ..... | -25 | -5 |
| Gondola frame ..... | 5 | 26 |
| Outer insulation ..... | 25 | 45 |
| Star camera ..... | 0 | 15 |
| Sun sensor ..... | 30 | 50 |
| Telescope baffle ..... | -50 | -20 |
| Elevation encoder ..... | -15 | 4 |

Table 2.2: The BOOMERANG payload was heavily instrumented. The temperature ranges (in Celsius) of some critical systems are shown. Most of the variation was diurnal due to the variation in sun elevation, however some of the variation tracked the altitude, which dropped steadily over the flight. As the altitude dropped, convective heat transport became progressively more important.

vide ample cooling power at a working temperature of 1.4 K for periods in excess of two weeks. The outer stage consists of a toroidal 65-liter tank of liquid nitrogen. A second toroidal tank, concentric to the nitrogen tank, holds 60 liters of liquid $^4$He. Mechanical support and thermal isolation of the two tanks are provided by tensioned 1.6-mm diameter Kevlar cord. The outer nitrogen stage is insulated with layered aluminized Mylar sheeting to reduce the radiative load from the ambient temperature vacuum canister. Thermal radiation from the nitrogen stage is intercepted by a helium vapor cooled shield that surrounds the helium tank. The $^4$He tank provides a 60 liter working volume in which are mounted the cold reimaging optics and the sub-Kelvin bolometric receiver.

In operation, the $^4$He bath is pumped to reduce the vapor pressure to a few millibar, which drops the temperature to $\sim$ 1.4K, well below the $^3$He condensation point. A closed cycle sorption cooler containing $\sim$ 48 STP liters of $^3$He provides $\sim 30\mu$W of cooling power at 270 mK. This system maintains the focal plane at 270 mK for fourteen days after an $\sim$ nine hour cycle. The ability to cycle the fridge

Figure 2.9: BOOMERANG ready to launch.

in flight was added to prevent the fridge from limiting the effective lifetime of the telescope.

BOOMERANG is launched with a cold focal plane. Prior to launch, the $^4$He bath is mechanically pumped to $\sim 6$ millibar, and the $^3$He fridge is cycled to cool the receiver. The nitrogen tank is left at ambient pressure. At launch, the $^4$He bath is valved off, and the pump removed. Once the payload reaches float altitude a motorized valve opens, dropping the $^4$He vapor pressure to $\lesssim 10$ millibar. The $LN_2$ vapor pressure is held at $\sim 150$ millibar. At this pressure, the nitrogen is mixture of ice and liquid at a temperature of $\sim 60$K.

The cold launch requirement imposes a significant constraint on the launch window. The liquid cryogens must be topped off as close to the launch date as possible in order to maximize the hold-time of the cryostat; however a minimum of 24 hours is required between the end of the fill and the launch in order to allow time to pump down the $^4$He bath and cycle the $^3$He fridge. Once the cryogenic cycle is completed,

any launch delay represents a significant impact on the science operations due to the limited hold-time of the cryostat and the duty cycle of the fridge.

## 2.3 Focal plane

BOOMERANG's focal plane consists of eight optically active bolometric receivers, two dark bolometers, and a fixed resistor, all of which operate from a 300 mK base temperature. The optically inactive channels are read out as a check against systematic effects. The focal plane is split equally between two types of receivers: four (dual-polarized) polarization sensitive bolometer pixels operating at 150 GHz, and four (single-polarization) two-color photometers operating at 245 and 345 GHz. To monitor the gain stability of the detectors, BOOMERANG relies on a calibration lamp installed in the 1-cm diameter hole located in the center of the tertiary mirror. The lamp consists of a thermistor on a NiCr-coated sapphire chip supplied with a periodic current pulse ($\sim$ 15 minute period). In the following we describe in detail the design of the polarization sensitive bolometers, the photometers, the optical filtering, and the detectors.

### 2.3.1 Polarization sensitive bolometers

Over the last twenty years, nearly all published efforts to detect polarization in the CMB have used coherent receivers.[2] Heterodyne and homodyne, quasi-total power and correlation receivers with low noise RF front-end amplifier blocks based on HEMTs are mature technologies at millimeter wavelengths. The fundamental design principles of these receivers are well-established and have been used to construct polarimeters at radio to mm-wave frequencies for many years [153, 128, 5, 103, 142]. Although cryogenic bolometric receivers achieve higher instantaneous sensitivities over wider bandwidths than their coherent analogs, the intrinsic polarization sensitivity of coherent systems has made them the choice of the first generation of CMB

[2] To the author's knowledge, the pioneering efforts of Caderni, et al., are the only published CMB polarization limits set by a bolometric system [27].

polarization experiments.

In this section we describe a new bolometric system that combines the sensitivity, bandwidth, and stability of a cryogenic bolometer with the intrinsic polarization capability traditionally associated with coherent systems [83]. In addition, the design obviates the need for orthogonal mode transducers (OMTs), hybrid tee networks, waveguide plumbing, or quasi-optical beam splitters whose size and weight make fabrication of large format arrays impractical. Finally, unlike OMTs or other waveguide devices, these systems can be relatively easily scaled to $\sim 600$ GHz, limited at high frequencies only by the ability to reliably manufacture sufficiently small single-moded corrugated structures. Polarization sensitive bolometers (PSBs) are fabricated using the proven photolithographic techniques used to produce "spider web" bolometers, and enjoy the same benefits of reduced heat capacity, negligible cross section to cosmic rays, and structural rigidity [118].

Polarization sensitivity is achieved by controlling the vector surface current distribution on the absorber, and thus the efficiency of the ohmic dissipation of incident Poynting flux. This approach requires that the optics, filtering, and coupling structure preserve the sense of polarization of the incident radiation with high fidelity. A multi-stage corrugated feed structure and coupling cavity has been designed that achieves polarization sensitivity over a 33% bandwidth. A next generation of suborbital, ground based, and orbital bolometric CMB polarization experiments, including Boomerang, BICEP, QUEST, and the *Planck* HFI are based on the PSB concept.

The PSB design has been driven by the desire to minimize systematic contributions to the polarized signal. Both senses of linearly polarized radiation propagate through a single optical path and filter stack prior to detection, thereby assuring both detectors have identical spectral passbands and quantum efficiencies. This results in nearly identical background loading and closely matched responsivities between the two detectors. Two orthogonal free-standing lossy grids, which are separated by $\sim 60\mu$m and both thermally and electrically isolated, are impedance-matched to terminate a corrugated waveguide structure. The physical proximity of the two detectors assures that both devices operate in identical RF and thermal environments. A printed circuit

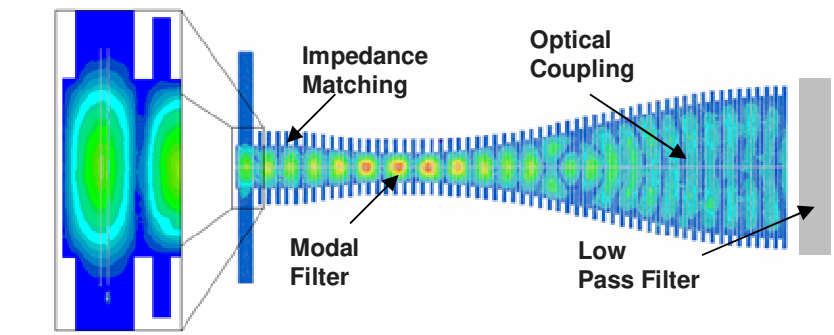


Figure 2.10: An instantaneous image of the field distribution in BOOMERANG's corrugated coupling feed. The radiation is incident from the right where low-pass filters and, in some applications, additional optical elements are located. The two bolometers are symmetrically spaced at $\lambda_g/4 \ +(-)\ 30\mu$m from the backshort in order to maximize coupling efficiency. Similar feed structures have been designed for *Planck*, QUEST and BICEP at 100, 150, 217, and 350 GHz.

board attached to the module accommodates load resistors and RF filtering on the leads entering the cavity. The post-detection electronics consist of a highly stable AC readout with a system $1/f$ knee below 100 mHz. Unlike coherent systems, this low frequency stability is attained without phase switching the RF signal.

We have designed the optical elements, including the feed antenna and detector assembly, to preserve sky polarization and minimize instrumental polarization of unpolarized light. To this end, the detector has been designed as an integral part of the optical feed structure.

Corrugated feeds couple radiation from the telescope to the detector assembly. Corrugated horns are the favored feed element for high performance polarized reflector systems due to their superior beam symmetry, large bandwidth, and low sidelobe levels. In addition, cylindrical corrugated feeds and waveguides preserve the orientation of polarized fields with higher fidelity than do their smooth-walled counterparts.

The coupling structure, which is cooled to 300 mK, consists of a profiled corrugated horn, a modal filter, and an impedance-matching section that allows efficient coupling to the polarization sensitive bolometer (see figures 2.11 and 2.10). In addition to a reduction in the physical length of the structure, the profiled horn provides a nearly uniform phase front that couples well to the other filters and optical elements in

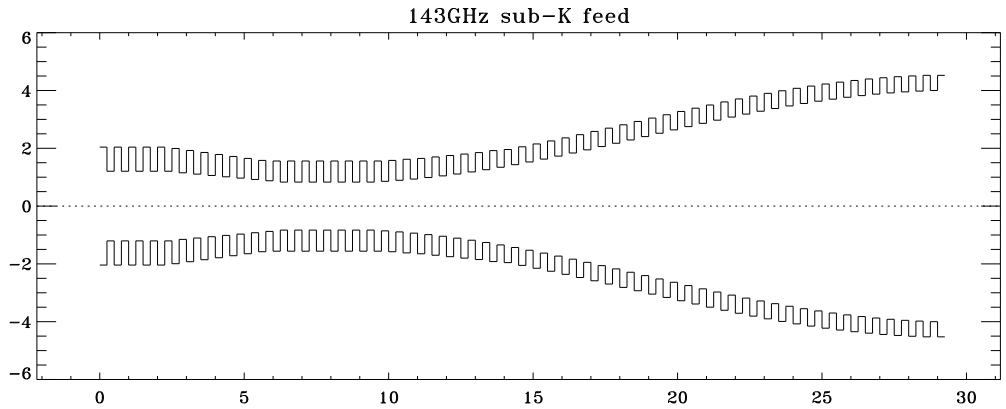


Figure 2.11: The corrugation geometry of the BOOMERANG PSB feeds, with dimensions in millimeters. The radiating aperture is on the right hand side, while the PSB module would be seated on the left.

the system. The modal filter isolates the detectors from any unwanted higher order modes that may be excited in the thermal break. Equivalently, this filter completely separates the design of the bolometer cavity from that of the feed, which couples to the optics. The impedance-matching section (the reexpansion at the left side of Figure 2.10) produces a uniform vector field distribution with a well-defined guide wavelength[3] and characteristic impedance over a large ($\sim 33\%$) bandwidth.

The detector assembly is a corrugated waveguide terminated with impedance-matched loads that have a weak thermal link to the temperature bath. An electric field drives currents through the absorber surfaces, which result in ohmic power dissipation. This power is detected as a temperature rise measured by means of matched Neutron Transmutation Doped Germanium thermistors (NTDGe) [9]. The bolometers each couple to a single (mutually orthogonal) linear polarization by properly matching each absorber geometry to the vector field of the coupling structure. The coupling structure has been tailored to ensure that the field distribution at the location of the bolometer resulting from a polarized source is highly linear. The detector assembly forms an RF tight Faraday cage around the bolometers, and both the signal and bias lines are buffered by onboard RF filters.

[3]The guide wavelength, $\lambda_g$, is typically 20% larger than free space, and $\mathrm{d}\log(\lambda_g)/\mathrm{d}\log(\nu)$ remains small over the entire range of operation.

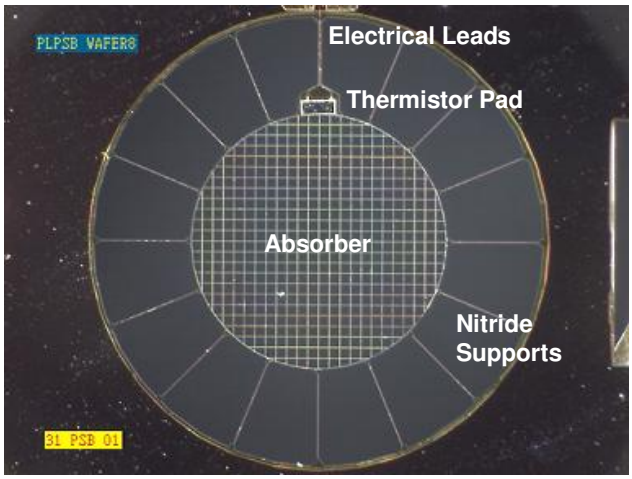


Figure 2.12: A photograph of a 145 GHz BOOMERANG PSB absorber. The diameter of the grid is 2.6 mm, while the absorber leg spacing, $g$, is 108 $\mu$m. Each leg is 3$\mu$m wide. This device is sensitive to incident radiation polarized in the vertical direction due to the metallization of the $Si_3N_4$ mesh in that direction. The horizontal $Si_3N_4$ beams evident in the photo are not metallized, and provide structural support for the device. The thermal conductivity between the absorber and the heat sink is dominated by the metallic leads running to the thermistor chip.

Because the absorber geometry influences the field distribution within the coupling structure, a treatment of the bolometer cavity as a black-body is in general *not* valid. An important consequence of this fact is that any attempt to model an analogous multimoded optical system will have to carefully consider interference terms between modes when calculating coupling efficiencies or simply trying to predict radiation patterns. The amplitude and phase of any higher order modes capable of propagating to the bolometer depend on the details of both the excitation and structure. Therefore, any numerical calculation would be susceptible to a large number of uncertainties associated with the appropriate boundary conditions at the bolometer, while an accurate analytic solution would be exceedingly difficult. For this reason, it may prove difficult to extend the general single mode PSB design to a multimoded application without sacrificing crosspolar performance.

Each bolometer consists of a linear absorber geometry designed to couple independently to a single linear polarization. PSBs are made using fabrication techniques originally developed for the successful "spider-web" bolometers developed at

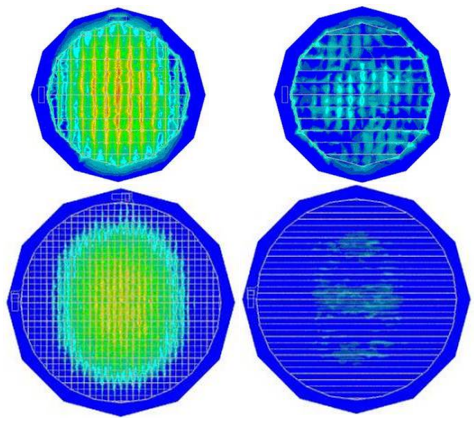

Figure 2.13: An illustration of the Poynting flux through the surface of the bolometer for the BOOMERANG PSBs (top) and the 143 GHz PSBs designed for the *Planck* HFI (bottom). For each type of detector, the leftmost plot corresponds to the copolar device, while the rightmost plot is the crosspolar device. The source polarization is vertical. The intensity and physical scale is the same for all four plots. The superior cross polar performance of the *Planck* device is visually evident in the reduced crosspolar Poynting flux. Integration of the component of the Poynting vector normal to a surface completely inclosing each of the bolometers provides a numerical estimate of the polarization efficiency, $\varpi = 1 - \epsilon$. For the devices shown above the results are shown in Figure 2.16, and correspond to crosspolar leakages, $\epsilon$, of about 5% (prototype) and 1.5% (*Planck*) across the band. Color, animated versions of the above figures, and others, are available from the author upon request.

JPL [174]. The lithographic technique used to fabricate these devices has become fairly routine, and is practiced by several independent groups. The detectors are fabricated from $4''$ commercial silicon-on-insulator (SOI) wafers, which consist of a 2 $\mu$m Si layer, a 1 $\mu$m insulating $SiO_2$ layer, and a 350 $\mu$m "backside" Si layer. The layer thickness are accurate to $\sim 10\%$. Care must be taken that variations of this magnitude do not compromise the mechanical or electrical design of the PSB housing.

The wafers are cleaned using the industry standard RCA procedure, which involves sequential application of $H_2O_2/NH_4OH$, HF, and $H_2O_2/HCl$ solutions. A $\sim 1\mu$m layer of $Si_3N_4$ (nitride) is deposited on both sides of the SOI wafer via a low-pressure chemical vapor deposition process. Because the nitride will eventually form a mechanically large structure, care must be taken in the deposition process to minimize the internal stresses and defects that may cause the free standing mesh to break. Next, separate Ti-Au metal films are deposited using a lift-off technique for both the absorber and

the electrical leads. For our devices, the absorber layer consists of a $\sim 2$ nm layer of Ti and a $\sim 12$ nm layer of Au. The thickness of the absorber layer plays a critical role in the efficiency of the optical coupling, as described below. The lead layer thickness determines the thermal conductance of the device to the bath, and typically consists of an $\sim 20$ nm layer of Au. The electrical contacts constitute a third layer, typically $\sim 500$ nm thick.

At this point, the wafer is patterned with a mask, and an Ar reactive ion etch (RIE) is used to remove the absorber layer. This is followed by a $CF_4/O_2$ RIE to remove the topside nitride layer. A similar process removes the backside nitride layer, defining the extent of the Si frame.

The thermistor pad is located at the edge of the absorbing mesh, well into the groove of the corrugations, in order to minimize its effect on the optical coupling and to maximize the thermal efficiency of the device (see Figure 2.12). A 15 $\mu$m x 40 $_\mu$m Nickel-Indium bump ($\sim 40$ nm and $\sim 3\mu$m thick, respectively) is deposited on the contact pads patterned on the nitride layer.

The Haller-Beeman NTDGe thermistors are manufactured from a single slab of NTDGe p-doped with a $4.53 \cdot 10^{16}$/cc concentration of Ga and a $1.29 \cdot 10^{16}$/cc concentration of As. The faces of the chip are Boron implanted, and a metal bilayer of Ti-Au is deposited, forming the electrical contacts [9]. Ni-In bumps are applied to the thermistor contacts, and the chips are diced with a diamond saw and an $HF/HNO_3$ rinse, resulting in a 300 $\mu$m x 50 $\mu$m x 25 $\mu$m chip with 100 $\mu$m x 50 $\mu$m contacts separated by 200$\mu$m. The chips are bump bonded to the wafer with $\sim 10$ g.

At this stage, the front side of the wafer is covered in wax to protect the thermistor and bump bonds from the Si wet etch. A deep trench reactive ion etch (DRIE) is applied to the backside of the wafer. The $SiO_2$ layer stops the etch, which is removed in a subsequent liquid etches. The individual devices are then sliced from the wafer, and they are extensively cleaned. They are then individually recoated, and a final wet etch removes the upper Si layer from behind. A final cleaning completes the microlithographic process.

Optimal coupling efficiency requires careful impedance-matching of the PSB to the

coupling structure. For a given absorber geometry, impedance-matching is achieved by controlling the thickness of the absorber metallization and therefore the cold surface impedance of the device. The surface impedance resulting in the highest power coupling efficiency is dependent not only on the geometry of the coupling structure and the frequency of operation, but also on the geometry of the absorber.

This fact can be understood in terms of classical transmission line theory. For an idealized transmission line of characteristic impedance $Z_0$ terminated in a load with impedance $Z_{\rm load}$ one expects a reflection amplitude ($S_{11}$, normalized to input) of

$$| S_{11}| = \left| \frac{Z_0 - Z_{\rm load}}{Z_0 + Z_{\rm load}} \right| \ . \tag{2.1}$$

In the limit that the characteristic spacing of the absorber grid is much less than a wavelength, the transmission line model is applicable to the PSB coupling. In order to parameterize the power coupling efficiency as a function of bolometer surface impedance, we use the functional form suggested by transmission line theory,

$$\eta \left( Z_{\rm abs} \right) = f \times \left[ 1 - \left( \frac{Z_0 - Z_{\rm abs}}{Z_0 + Z_{\rm abs}} \right)^2 \right] \ , \tag{2.2}$$

where $f$ and $Z_0$ are free parameters, while $Z_{\rm abs}$ is determined by the processing of the absorber.

In order to determine the optimal absorber impedance for our devices, numerical computations of $\eta \left( Z_{\rm abs} \right)$ were made for discrete values of $Z_{\rm abs}$ using the Ansoft HFSS package. These results were used to determine $f$ and $Z_0$ for each of six device geometries at the center frequency of our band. The geometries included a solid sheet, a "spider-web" bolometer, and four types of PSBs, all of which were found to be well fit by the functional form of Equation 2.2. The results of the numerical procedure for two of the devices, a solid sheet and the PSB design chosen for BOOMERANG, are shown at the left and right of Figure 2.14, respectively. The best-fit surface impedances ranged from 470 $\Omega$/square for the solid sheet to nearly 5 $\Omega$/square for the device with the finest absorber leg widths.

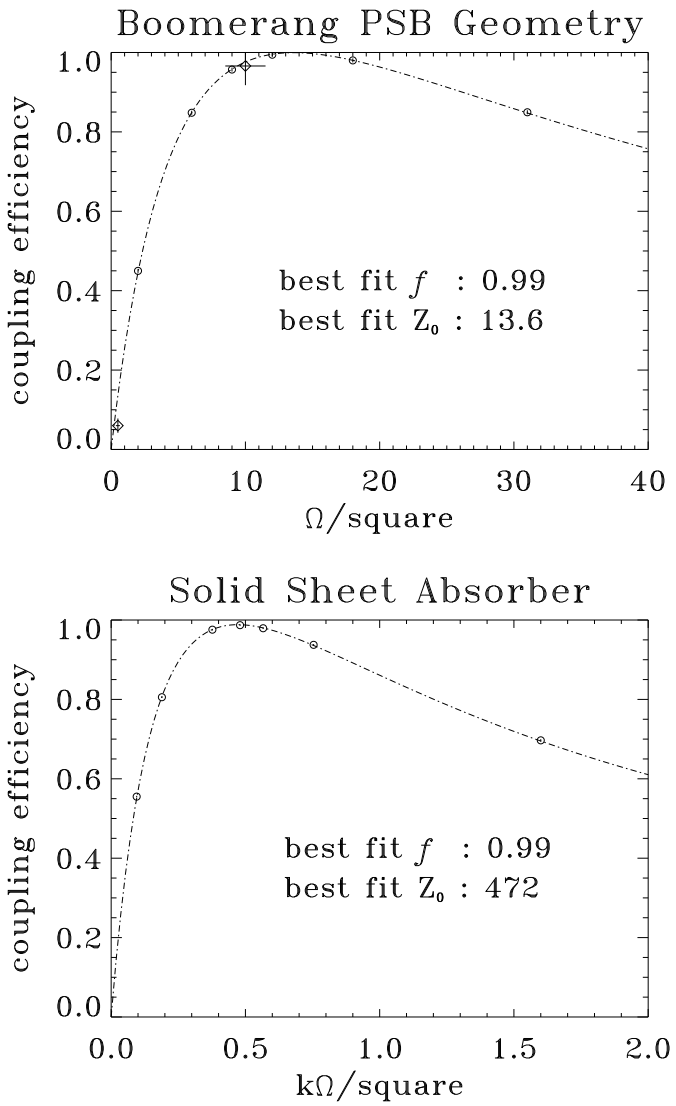


Figure 2.14: The upper panel shows the numerically determined coupling efficiency, $\eta(Z_{\rm abs})$, for the geometry of the BOOMERANG PSBs. The open circles are the numerical results. A function of the form of Equation 2.2 is fit to the points to determine the peak coupling efficiency and characteristic impedance of the structure at the center frequency of the operational band. The lower panel shows the same numerical procedure performed for a solid sheet of uniform surface impedance mounted in a PSB coupling structure. Note the change in scale of the abscissa, from Ω to kΩ, which can be understood in terms of the filling factor of the PSB absorber (see Equation 2.3). For the BOOMERANG geometry, two absorber metallizations were fabricated and tested, corresponding to approximately 0.5 Ω/square and 10 Ω/square. The measured coupling efficiency of the two types of devices are indicated by the open diamonds, and are in excellent agreement with the numerical result. The error bars represent the uncertainty in the cold impedance of the metallization layer and the transmission of the window material and optical filters.

In order to validate both the numerical procedure and the application of transmission line theory to the PSB coupling, optical efficiency measurements of devices with physical surface impedances of $\sim 0.5\ \Omega$/square and $\sim 10\ \Omega$/square were made. The numerical, theoretical, and measured efficiencies are compared in Figure 2.14 at right. The well-matched devices showed optical efficiencies nearly a factor of four higher than the low impedance devices, and validate the applicability of transmission line theory to the PSB coupling structure.

Similar numerical simulations were made of a smooth-walled conical feed exiting into an integrating cavity. This structure was found to deviate significantly from the transmission line theory and showed little dependence on the details of the absorber geometry, presumably because the abrupt discontinuity in the boundary conditions at the entrance to the cavity dominates the return loss.

The results of the numerical computations suggest that it is not possible, in principal, to analytically calculate the optimal absorber surface impedance for an arbitrary geometry due to the fact that the characteristic impedance of the structure, $Z_0$, is itself dependent on the web geometry. However, in the limit that the absorber geometry approaches a solid resistive sheet, the optimal characteristic impedance of the PSB coupling structure approaches $Z_0 \rightarrow 470\Omega$. This numerically determined characteristic impedance is greater than that of free space (377 $\Omega$), as is to be expected for an electrically small structure.

An approximate relationship for the optimal target surface impedance of a given absorber geometry can then be obtained in the following way. Imagine making $N$ infinitesimally thin slices through a solid sheet absorber of this surface impedance. Clearly $Z_0$, the optimal surface impedance of a solid sheet, is still the appropriate target impedance. If one then reduces the width, $w$, of each of the $N+1$ legs of the absorber without adjusting the physical surface impedance from $Z_0$, the *optically* active area will no longer have the same characteristic impedance. For a given absorber diameter $D$ and center to center leg spacing $g = \frac{D}{N+1}$, each leg will be acting for an optical area that is fixed $(g \times L)$, while its geometric area $(w \times L)$ is clearly not. Therefore, one would expect that the optimal target surface impedance would

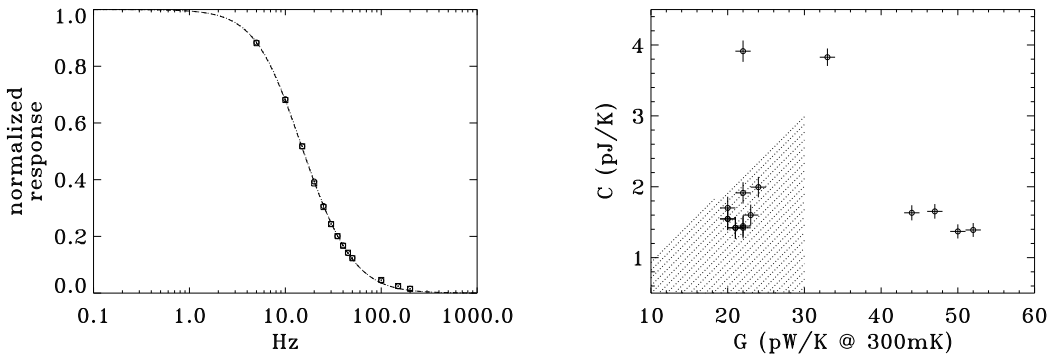


Figure 2.15: The thermal properties of the prototype PSBs. At left, the measured response of a PSB pair to a chopped optical source. The two devices, which are overplotted, are very well-matched in $\tau$ and therefore well-matched in both heat capacity and thermal conductivity. At right, a plot of the measured heat capacity versus thermal conductivity for a variety of PSB devices at 300mK. The region is the region of parameter space acceptable for BOOMERANG's 150 GHz PSBs is crosshatched.

scale as the ratio of geometric area to optical area,

$$Z_{\rm abs} \approx Z_0 \frac{w}{g} = Z_0 \frac{w(N+1)}{D} \ , \tag{2.3}$$

so that in the limit that the filling factor approaches unity the surface impedance, $Z_{\rm abs}$, approaches $Z_0$. For $g \lesssim \lambda/5$, we have found good agreement between this approximate relation and numerical calculations of the optimal surface impedance of a given absorber geometry. For reference, the BOOMERANG devices have twenty-three absorber legs of width $w \simeq 3\mu$m, and a 2.6-mm absorber diameter (see Table 2.3). Using the $Z_0$ determined from a solid sheet absorber, application of Equation 2.3 yields an optimal impedance of 12.5 $\Omega$/square, versus the numerically determined value of 13.6.

The bolometer design must ensure that the power deposited on the absorber is efficiently detected by the thermistor. The parasitic thermal conductivity of the $Si_3N_4$ supports and inefficient heat transport across the absorber can potentially result in a loss of detector efficiency if a significant fraction of the optical power dissipated in the absorber does not result in a temperature rise of the thermistor. For this reason,

several features were built into the PSB design to ensure sufficient thermal efficiency.

The electrical leads constitute the dominant thermal path from the bolometer to the temperature bath. The thermistor is located on a pad that is heat sunk to both the leads and the absorber via a thermally conductive ring surrounding the absorber. For the extremely low background bolometers with thermal conductivities below 30 pW/K, the $Si_3N_4$ beam supporting the leads has been found to be a significant contribution to the total thermal conductivity. The scaling of the thermal conductance with temperature for these devices is consistent with a $T^3$ dependence, as described in Holmes, et al. [68].

A finite element thermal model of the bolometer design was implemented in order to analyze the thermal efficiency of the bolometer design. The thermal conductance and heat capacity of the metallization and $Si_3N_4$ structures used by the model were obtained empirically in independent analysis of similar structures [68]. The thermal model allows the calculation of the temperature rise at the thermistor resulting from power (DC and AC) dissipated on the absorber, the bolometer response to a transient pulse of power deposited on the absorber (similar to a cosmic ray hit), and the ratio of power flow through the thermistor to the total power deposited on the bolometer.

The response of the device to a chopped source was measured over a $\sim$ 1 kHz bandwidth. The measured bolometer response agrees very well with the finite element model. The calculated ratio of rise time to relaxation time for a transient pulse is $\sim$ 10% at 400 mK, which indicates that the crossing time for temperature fluctuations across the absorber is much less than the thermal time constant of the bolometer. Finally, the results of the thermal analysis indicate that the ratio of power flow through the thermistor to the total power deposited on the mesh is 0.97 for the prototype devices.

The two bolometers in a PSB pair can be read out either in a bridge circuit or individually. A bridge circuit has the advantage of measuring the difference signal directly through a single amplifier chain, however it requires close matching of the thermistor properties and does not provide a precise measurement of the Stokes $I$ parameter. For the study of the cosmic background radiation, it is highly advantageous

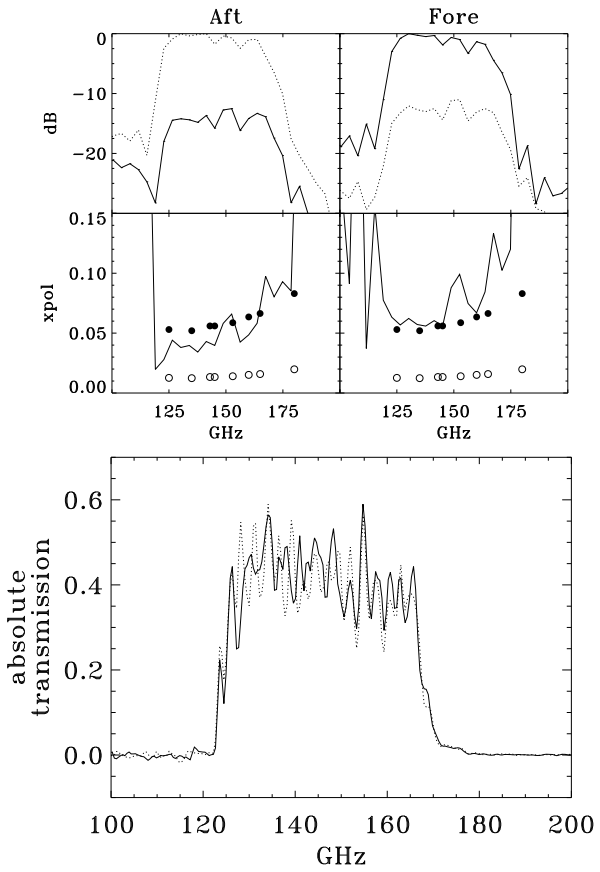


Figure 2.16: The upper panel displays the measured crosspolar performance of a prototype (Type 04, see Table 2.3) PSB in the BOOMERANG test bed. The upper panels show the measured spectra in the two orthogonal directions defined by the PSB pair. Below, the measured crosspolar leakage, $\epsilon_i$, as a function of frequency for a PSB pair. The spectral resolution of the measurement is 4 GHz and the signal to noise is only significant within the passband, from 124 to 168 GHz. The filled circles indicate the single frequency results of the HFSS simulations. The open circles are the simulation results for the device geometry designed for *Planck*. In the bottom panel, the measured optical efficiency of the BOOMERANG PSBs. The spectra are taken with a Fourier transform spectrometer at 500 MHz resolution. The spectral normalization is obtained by measuring the electrical power difference at constant resistance with 77K, 90K, 273K, and 300K beam filling loads. The spectra for the two bolometers in a PSB pair are shown, one with a solid line, the other with a dotted line.

to measure both the polarized and unpolarized components simultaneously. In the remainder of this chapter we will consider the signals received by the bolometers individually. An analysis of the individual readout illustrates the fundamental properties of the PSBs and how they can be interpreted in terms of the Stokes parameters.

A completely general analysis of the signals is presented in Section 5.1.3. In the following discussion, we take a somewhat simplified approach; in a suitably defined coordinate system the measured signal voltage is given by the integral over electromagnetic frequency,

$$v_i = \frac{s_i}{2} \int d\nu \lambda^2 \; F_\nu \; \left[ (1+\epsilon) \; \mathbf{I} + \; (1-\epsilon) \; ( \; \mathbf{Q} \cos 2\psi_i + \; \mathbf{U} \sin 2\psi_i) \right] , \tag{2.4}$$

where $s$ is the voltage responsivity of the bolometer, $\lambda^2$ is the throughput ($A\Omega$) of the system, and $F_\nu$ is the absolute spectral transmission. The crosspolar leakage, $\epsilon_i$, the quantity measured in Figure 2.16, is the response of a device to a 100% linearly polarized source oriented perpendicular to the design axis of sensitivity.[4] Equivalently, one may define a polarization efficiency of the detector, $\eta \equiv 1 - \epsilon$, which, as is shown below, enters as a multiplicative factor in the overall efficiency of the system to polarized radiation. The alignment angle, $\psi_i$, is the orientation of the bolometer in the coordinate system that defines $Q$ and $U$. The bolometer voltage responsivities, $s_i$, are dependent on the total background power, the temperature of the bath, the thermal conductance, and the thermistor properties.

Ideally, the two bolometers would have $\epsilon = 0$ and would be oriented exactly 90° with respect to one another; however, in practice the two devices exhibit crosspolar response at the few percent level and are typically orthogonal to within 1.5°. It is important to note that a single PSB cannot fully characterize the polarization of the signal without some method of rotating $Q$ into $U$, or vice versa. Ideally one would modulate the polarized component of the radiation, as with a wave-plate or Faraday rotator, in order to unambiguously measure both the Stokes $Q$ and $U$ parameters from a single feed. In practice, instruments such as BOOMERANG and *Planck* will rely on

[4] As shown in Section 5.1.2, the leakage $\epsilon$ is simply the square of the ratio of the diagonal elements of the Jones matrix describing an imperfect polarizer.

scanning through several orientations on the sky in order to build up information on both $Q$ and $U$.

In a suitably defined coordinate system, $\psi_1 \simeq 0^\circ$ and $\psi_2 \simeq 90^\circ$. Therefore, so long as $\epsilon_i \ll 1$, a measurement of $I$ is obtained by summing the two signals while a measurement of $Q$ is obtained by taking the difference. For simplicity, we approximate Equation 2.4 by removing $I, Q$, and $U$ from the frequency integral and introducing the factor $\mathcal{F}_i \equiv \int d\nu\ \lambda^2\ \eta_i\ F_i(\nu)$. Taking the signal difference yields

$$(v_1 - v_2) = \gamma \cdot I + \delta \cdot Q\ , \tag{2.5}$$

where we have made the definitions

$$\gamma \equiv [S_1 \cdot \mathcal{F}_1 \cdot (1 + \epsilon_1)\ -\ S_2 \cdot \mathcal{F}_2 \cdot (1 + \epsilon_2)] \tag{2.6}$$

$$\delta \equiv [S_1 \cdot \mathcal{F}_1 \cdot (1 - \epsilon_1)\ +\ S_2 \cdot \mathcal{F}_2 \cdot (1 - \epsilon_2)]\ . \tag{2.7}$$

The parameter $\epsilon$ is identical to a degradation in sensitivity to polarization. The common mode rejection ratio (CMRR) of the PSB receiver depends crucially on the stability of the coefficient $\gamma$ in Equation 2.6. For studies of the CMB, the dominant unpolarized signal, $I$, will be that of the temperature anisotropy. For the currently favored $\Lambda$CDM cosmology, the ratio of the polarized to unpolarized power is expected to range from 2–6% over the angular scales of interest, which determines the level of stability required of the parameter $\gamma$.[5] Observational efforts to detect the (much smaller) imprint of tensor fluctuations on the CMB will require a correspondingly greater control of gain fluctuations. Analytical methods are addressed in more detail in Chapter 5.

From Equation 2.6, it is evident that the stability of $\gamma$ depends on the stability of both the crosspolar leakage and the calibration. The intrinsic polarization efficiency of a PSB is a property of the geometry of the absorber and coupling structure, the

[5]Specifically, $\langle EE \rangle / \langle TT \rangle$, the ratio of gradient mode polarization to temperature anisotropy band-powers over angular scales of $\sim 2^\circ$ to $10'$, or $\ell \simeq 400 - 2000$.

metallization of the absorber, and the spectral bandpass.[6] The numerical simulations provide some intuition about the origin of this crosspolar response. For a single frequency, one can integrate the component of the Poynting vector normal to two separate surfaces, each of which fully enclose one of the bolometers. The model used includes the detailed geometry of the absorber, the thermistor, the electrical leads, and all support structures. For a given source polarization, a comparison of the total integrated flux through these surfaces yields the ratio of power absorbed on each bolometer. The results of this numerical procedure for five PSB absorber geometries are presented in Table 2.3. In all cases, the surface impedance which provided the maximum polarization efficiency was found to coincide with the value yielding the peak power absorption. A deviation from optimal surface impedance of $\sim 20\%$ was found to result in a degradation of the polarization leakage by $\sim 12\%$ (absolute).

Measurements of the cross polarization are in good agreement with the numerically determined values. Two methods were used to measure the crosspolar response of the system. A polarized Fourier transform spectrometer (FTS) was used to measure the spectral dependence of the polarization efficiency. The left panel of Figure 2.16 shows the measured spectrum of the crosspolar response for a prototype PSB installed in the BOOMERANG testbed at 4 GHz resolution. The filled circles represent single frequency results from numerically integrating the Poynting flux. A second test used a chopped thermal (Raleigh-Jeans) source and polarizing grid to measure the broadband response as a function of grid orientation. The latter measurement will generally result in a lower polarization efficiency than will result in a measurement of the CMB due to the relatively flat spectrum of the cosmological signal and the rising spectrum of the polarization leakage.

As is evident from Figure 2.13, a significant fraction of the crosspolar response of the prototype devices originates from power dissipation at the edge of the mesh. Another factor found to influence the crosspolar response is the line spacing, $g$. The

[6] Of course, the efficiency of a given instrument depends as well on the properties of optical arrangement, including the filters, feed elements, reflectors, and window material, etc. At the percent level, we have observed a degradation of polarization efficiency with increased thickness of the window material.

Bolometer Parameters

| | $d$ [ mm ] | $w$ [ $\mu$m ] | $g$ [ $\mu$m ] | $Z_0$ [ $\Omega$/square] | $\epsilon$ [ % ] |
|---|---|---|---|---|---|
| Type 01$^\dagger$ | 2.6 | 3 | 108 | 13.6 | 2.6 |
| Type 02$^\dagger$ | 2.6 | 5 | 108 | 22.5 | 2.3 |
| Type 03 | 2.6 | 3 | 325 | 4.9 | 5.6 |
| Type 04 | 2.6 | 3 | 217 | 6.8 | 5.4 |
| Type 05$^\ddagger$ | 3.2 | 3 | 100 | 15.4 | 1.3 |

Table 2.3: Bolometer design parameters for the four prototype device geometries (Types 01–04), and the *Planck* 143 GHz geometry (type 05). The values of $Z_0$ and $\epsilon$ quoted in the last two columns represent the numerically determined values at 150 GHz. $^\S$ The polarization leakage, defined by Equation 2.4 is calculated at optimal absorber impedance. $^\dagger$ The device geometries used in BOOMERANG. $^\ddagger$ The device designed for *Planck* HFI's 143 GHz channels.

calculated crosspolar level generally declines with a more densely packed grid. In order to determine the effect, if any, of the $Si_3N_4$ mechanical supports running perpendicular to the absorbing legs on the cross polarization, the support legs of a prototype device were removed by laser oblation after optical testing. Retesting the device showed no change in the level of polarization leakage. The polarization leakage, $\epsilon$, is a material property of the device and is entirely stable.

An additional effect which can be important is the role of electrical crosstalk between readout channels. Electrical shielding of the bias and signal lines is required to minimize this effect, especially between the two devices within a pair. This crosstalk is indistinguishable from crosspolar leakage, $\epsilon$, and must be both carefully avoided and characterized.

We have shown that the stability of the relative calibration of the two polarization senses is critical in order to achieve an acceptably small systematic contribution to the signal. This situation is by no means unique to a PSB receiver. Coherent receivers are susceptible to large gain fluctuations and phase error in the front-end amplifiers, which are analogous, though typically far larger in amplitude, to fluctuations in the product $S_i \cdot \mathcal{F}_i$. For this reason most correlation receivers used in measurements of the CMB use some sort of synchronous demodulation of the signal at frequencies above that of the gain fluctuations. As we will see, the PSB architecture is designed

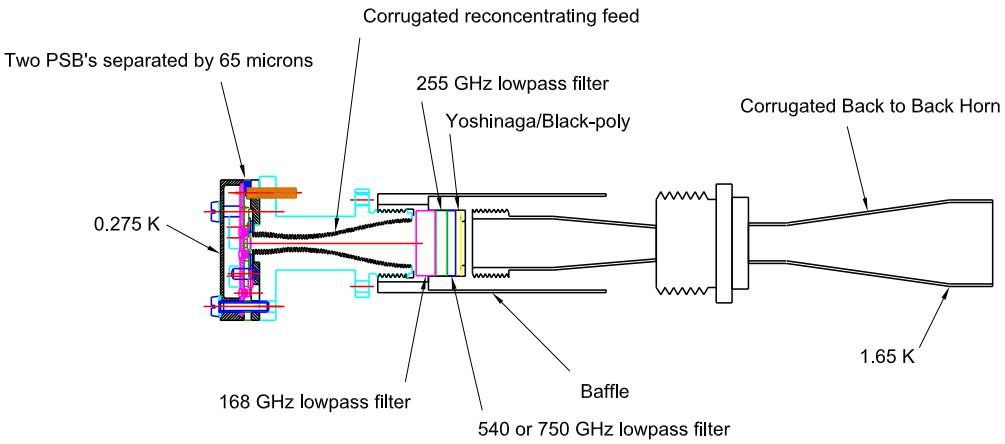


Figure 2.17: The BOOMERANG 150 GHz PSB feed assembly. The 2K feed, though not a necessary component of the PSB design, is a convenient method of including additional filtering and control of the beam without loss of performance. Both the 2K and sub-Kelvin feeds are fully corrugated and profiled to provide high fidelity transmission of the polarized signal, symmetric E and H plane beams, and relatively high gain in a compact system.

to realize stability in the relative calibration at frequencies as low as a few tens of milliHertz.

Fluctuations in the relative calibration arise from mismatched effective throughput, $\mathcal{F}_i$, as well as from drifts in the voltage responsivity, $S_i$. The lower panel of Figure 2.16 shows band-averaged optical efficiencies, essentially $d\mathcal{F}_i/d\nu$, of the BOOMERANG PSBs. The efficiencies are matched to within a few percent, while the band edges are matched to better than 0.2%. The edge of the band is determined by the wave guide cutoff of the feed, while the upper edge is defined by metal mesh resonant filters [164, 100]. Due to the fact that the optical path for each polarization sense is identical, the voltage responsivity will dominate variations in the calibration. As we will see, the great advantage of the PSB architecture is the fact that the factors that determine the relative responsivity are intrinsic to the physical arrangement, and are therefore extremely stable.

Any number of authors have discussed the theory of operation of bolometric receivers; the authoritative treatment is given in the series of papers by Mather, which borrows heavily on the early work of Jones [82, 114, 115]. It can be fairly easily

shown that the voltage responsivity of a bolometer under a given optical load is completely determined by five quantities, the spectral bandpass, the quantum efficiency, the temperature of the bath, the thermal conductance to the bath, and the properties of the thermistor material. We have discussed the first two items, and have shown them to be well matched and extremely stable. The physical proximity of the devices, separated by $< 60\mu$m on a beryllium copper housing, ensures that the two devices operate from a common bath temperature. The thermal conductance to the bath is determined by the uniformity of the metal deposition of the electrical leads, and is matched to within $\sim 10\%$ for the devices fabricated on a single wafer for the BOOMERANG PSBs. Better matching is possible for devices with higher thermal conductivity than those designed for BOOMERANG, $G \simeq 20$ pW/K at 300 mK. The final contribution to the difference in responsivity of devices within a PSB pair is the variation in the thermistor properties between the two devices. The NTD germanium thermistors used in this work have a resistance versus temperature well described by

$$R(T) = R_0 e^{\sqrt{\frac{\Delta}{T}}} \ .$$

Variation in the parameter $\Delta$, which is a property of the doping of the germanium, is found to be much smaller than the variation in $R_0$, which is dependent on the geometry of the chip. However, both parameters are intrinsic to the chip, and likewise are entirely stable.

As an illustration of the CMRR of a working PSB, Figure 2.18 shows the raw output of one of the BOOMERANG PSB pairs while observing through the atmospheric column from sealevel prior to the Antarctic LDB flight. The two upper panels show the traces from each of the individual detectors, while their difference is shown in the third panel. The power spectrum of the sum and difference time streams is shown in Figure 2.19. The power spectrum of the difference signal is consistent with the expected noise level of the receiver alone, putting a limit on the CMRR of better than $-26$ dB at 10 mHz.

The experimental results reported in this work are primarily the results of the

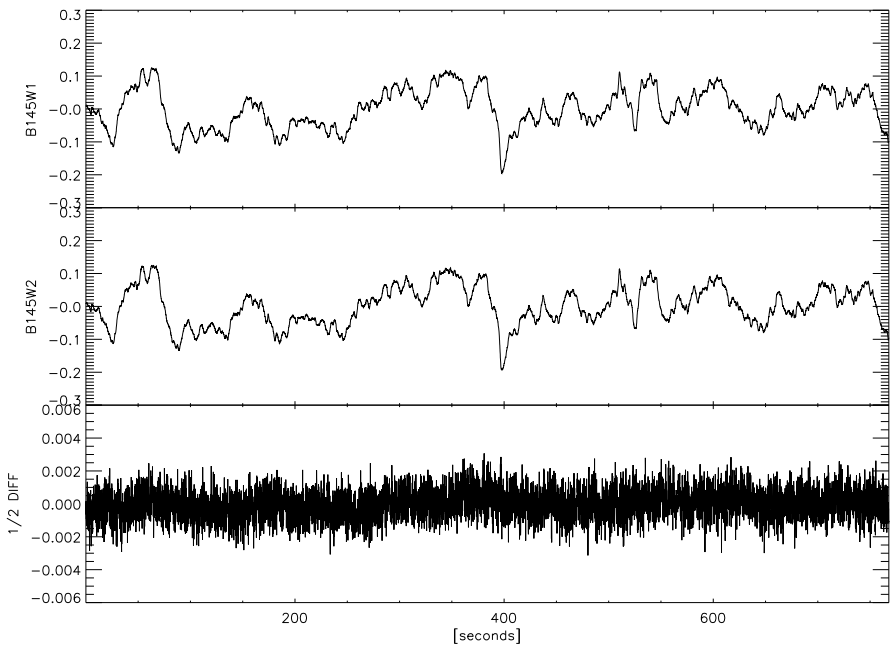


Figure 2.18: Atmospheric brightness fluctuations in the time domain. These bolometer traces were obtained while staring at a 45° zenith angle from the Ross Ice Shelf prior to launch. While not typical of the atmospheric noise at good observing sites, the data are indicative of the common mode rejection achieved with a PSB. The top two panels are the signals (scaled by a relative calibration factor) from a PSB pair. The bottom panel is the difference time stream.

development program for the new BOOMERANG focal plane. The BOOMERANG receiver is a prototype of the *Planck* HFI 143 GHz polarized receiver. We include for completeness the details of this system, so that the data may be interpreted in the proper context.

In addition to the feed element described in Section 2.4, the prototype optical system consists of a profiled, corrugated back-to-back feed that is cooled to 2 K. This feed defines the lower edge of the operational band, and couples to the reflector system. The high-pass edge of the sub-Kelvin assembly is designed to be $\sim$ 10% below that of the 2 K feed in order to assure that both the throughput and beam definition are provided by the 2 K feed element. Two different 2 K feeds were designed and tested, each of which is corrugated in both the front and back sections. Neither of these feeds were found to contribute to the cross polarization or to degrade the

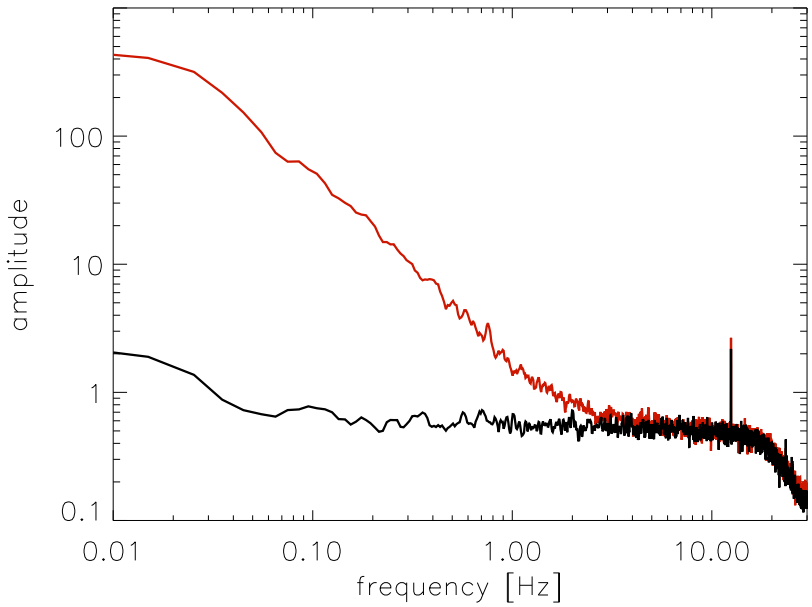


Figure 2.19: The power spectrum of the atmospheric fluctuations, and that of the difference between the two signals from a PSB pair. CMRRs were obtained in excess of −26 dB at frequencies down to 10 mHz. The difference signal is consistent with the noise power spectrum of the readout electronics alone. For terrestrial telescopes, the atmospheric fluctuations allow a precise determination of the relative calibration of devices within a PSB pair over very short timescales.

optical efficiency when properly configured. However, replacing the sub-Kelvin feed with a smooth-walled but otherwise identical feed resulted in a two-fold increase (roughly 5%, absolute) in the crosspolar response, $\epsilon$, of a PSB receiver tested in the BOOMERANG focal plane.

The system has achieved high end-to-end efficiency in lab testing. A band-average efficiency of nearly 40% is measured by calculating the power difference observed between beam-filling loads that are controlled at temperatures of 273 and 300 K, as well as 77 K and 90 K. The right panel of Figure 2.16 shows the normalized transmission of the system measured as integrated in the BOOMERANG cryostat. This efficiency is not corrected for any loss in the vacuum window material, the blocking filters at 80 K and 2 K, or the sub-Kelvin or 2 K feeds.

We have demonstrated a 300 mK bolometric receiver that is intrinsically sen-

sitive to linear polarization over a 33% bandwidth. The general design is scalable from $\sim 60 - -600$ GHz. This design benefits from reduced susceptibility to systematic effects due to the common filtering, matched beams on the sky, matched time constants, stable relative responsivities, and matched end-to-end efficiencies of each sense of linear polarization. Unlike coherent correlation polarimeters, this receiver simultaneously measures the polarized and unpolarized components of the signal with comparable sensitivity. The design minimizes the size and weight of the receiver, making it especially appropriate for orbital and suborbital compact feed-horn arrays. A general method of reliably calculating the optimal absorber impedance for a bolometric detector is presented. The measured performance of the system is well understood theoretically and is in good agreement with the results of the numerical modeling. The system has been realized at 100, 143, 217 and 353 GHz in the *Planck* HFI.

### 2.3.2 Photometers

The two-color photometer is an evolutionary development of the photometers originally designed for MAX [44], and used subsequently by the SuZIE [69], the FIRP instrument on the IRTS [97], and the BOOMERANG98 CMB experiments [122]. The BOOMERANG photometer has been optimized for only two frequencies, and has been made polarization sensitive by the fitting of a polarizing grid to the feed aperture. The detectors are all similar, if not identical, to the detectors flown on BOOMERANG98. The BOOMERANG feed design, described in Section 2.4.2, is significantly advanced relative to earlier versions of the photometer.

The photometer body is fed with a feed antenna designed to operate at frequencies from $\sim$ 200 GHz to 400 GHz. The radiation is coupled through a 420 GHz low-pass filter into the 12.7 mm diameter photometer body. A dichroic filter, oriented at 45° with respect to the optical axis, directs radiation at frequencies above 295 GHz to the 345 GHz detector module while passing the all lower frequencies to the 245 GHz detector module. The detector modules are thermally isolated from the

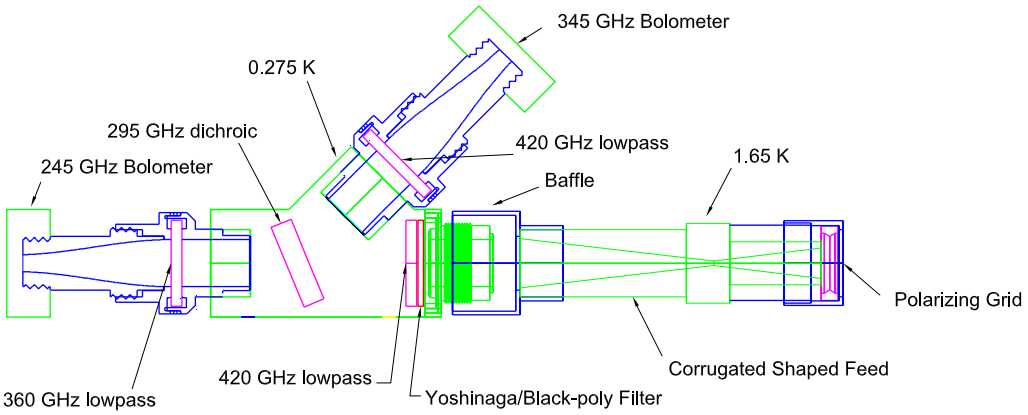


Figure 2.20: An assembly drawing of the two-color photometer. The radiating aperture, which couples to the telescope, is to the right. A polarizing grid is attached to the radiating aperture to provide sensitivity to polarization. The 2K feed is fully corrugated, while the sub-Kelvin feeds are smooth-walled. The sub-K feeds are oversized to maximize coupling efficiency, therefore the throat of the corrugated feed determines the high-pass edge for the 245 GHz.

photometer body, which is held near 2K, by a $\sim$ 5-mm gap. The photometer sub-Kelvin feeds are smooth walled with an exit aperture matched to the geometric area of the absorber. Corrugated feeds are not necessary, as the polarization discrimination and beam forming is determined by the 2-Kelvin feed antenna. In order to preserve beam symmetry, the ideal location for the polarizing grid is on the *photometer* side of the feed antenna. Unfortunately, due to mode conversion in the photometer body this resulted in unacceptably high polarization leakage. As a result, the grid was moved to the radiating aperture.[7]

### 2.3.3 Optical filtering

Optical filtering is of critical importance to a bolometric receiver; in addition to defining the optical passband, care must be taken to ensure that the detector is shielded

[7] At least, for the case of single-moded operation. The photometer feed will be discussed in more detail in Section 2.4.2.

from out-of-band radiation originating from within the cryostat. The optical filters also play a significant role in the determination of the end-to-end optical efficiency of the system. Finally, the optical filtering must reduce the radiative loading on the various stages of the cryogenic system to acceptable levels.

The window of the BOOMERANG cryostat consists of a $50-\mu$m polypropylene film stretched on an elliptical aluminum frame. The window has excellent transmission at all three wavelengths but is exceedingly fragile, requiring replacement after each run of the cryostat.[8]

Far infrared filters typically consist of layered capacitive and inductive meshes deposited on polyethylene, polypropylene, or Mylar substrates. Polyethylene is used least often since it lacks the rigidity of the other plastics, which are largely self-supporting. A familiar example of an inductive mesh is the thick-grill high-pass filter of the sort often seen on the glass of a microwave-oven door. Wavelengths longer than the hole spacing (microwaves) see a perfectly conducting surface, whereas shorter wavelength radiation (visible light) passes through freely. Capacitive meshes are the negative of the inductive geometry. Capacitive coupling between the elements of the mesh make the surface reflective (or lossy) at short wavelengths, while transmitting longer wavelengths. An example of this sort of filter is the type of foil through which you might observe a solar eclipse. Pop-Tart wrappers work admirably well for just this purpose.

BOOMERANG uses neither microwave-oven doors nor Pop-Tart wrappers in its optical chain, although it would be fascinating to try the latter. Most of the filters used in BOOMERANG consist of layers of patterned meshes deposited on polypropylene substrates.[9] The layers are hot-pressed to form a single self-supporting filter. Some of the thicker hot-pressed filters are antireflection coated with a tuned layer of PTFE

[8] When under vacuum, the $\sim 20$ cm window bows inward by nearly 2 cm, and retains this shape even when brought to neutral pressure. This is an exceedingly frightening sight for an experimentalist.

[9] The dichroic beam-splitter used in the photometer body is the sole exception. That filter is an air-gap filter. The inductive layers are deposited on a thin Mylar substrate and stretched on an aluminum frame. The polarizing grids used on the photometer and in laboratory testing, and the neutral-density filter, are made in a similar fashion. Instead of inductive or capacitive grids, a linear pattern is used for the polarizer, while a uniform lossy coating is used for the NDF.

Optical Filters

| Temp. | 145 GHz | 245 GHz | 345 GHz |
|---|---|---|---|
| 77 K | $\sim 100\mu$m IR blocker | | |
| ⋮ | 540 GHz AR-coated LPF | | |
| 2 K | $\sim 100\mu$m IR blocker | | |
| ⋮ | 450 GHz AR-coated LPF | | |
| ⋮ | Removable NDF† | | |
| ⋮ | | Polarizing Grid | |
| ⋮ | | 420 GHz LPF | |
| ⋮ | | 180$\mu$m BP/Yosh LPF‡ | |
| ⋮ | | 295 GHz dichroic LPF | 295 GHz dichroic HPF |
| 0.3 K | 180$\mu$m BP/Yosh LPF‡ | 360 GHz LPF | 410 GHz LPF |
| ⋮ | 255 GHz LPF | | |
| ⋮ | 540 GHz LPF | | |
| ⋮ | 168 GHz LPF | | |

† The neutral density filter can be mechanically rotated in and out of the beam while the system is cooled down.

‡ A black-poly Yoshinaga filter is an absorptive filter consisting of a thallium salt deposited on a black polyethylene substrate, the thickness of which is tuned to minimize reflections [173].

Table 2.4: The optical filtering scheme employed by BOOMERANG. In order to take advantage of the low backgrounds available at float altitudes, much care must be taken to reduce the background originating from within the cryostat. While the metal mesh filters, which consist of bonded layers of polyethylene, exhibit in-band emissivities at the percent level, the PTFE antireflection coating is several times more emissive. It is crucial that these filters remain well heat-sunk and protected from infrared emission from the warmer stages.

(Teflon). At normal incidence to a dielectric boundary, a $\lambda_n/4$ layer of material with an index equal to the geometric mean of the two media minimizes the reflected amplitude.

PTFE has an index of refraction close to the square root of that of the polypropylene material in the hot-pressed filters. However, the PTFE has high infrared emissivity, which resulted in excessive heating of the BOOMERANG filters as well as a large thermal load on the $LN_2$ and $^4$He stages. In addition, the heating of the filters led to a significant increase in background loading of the detectors resulting from

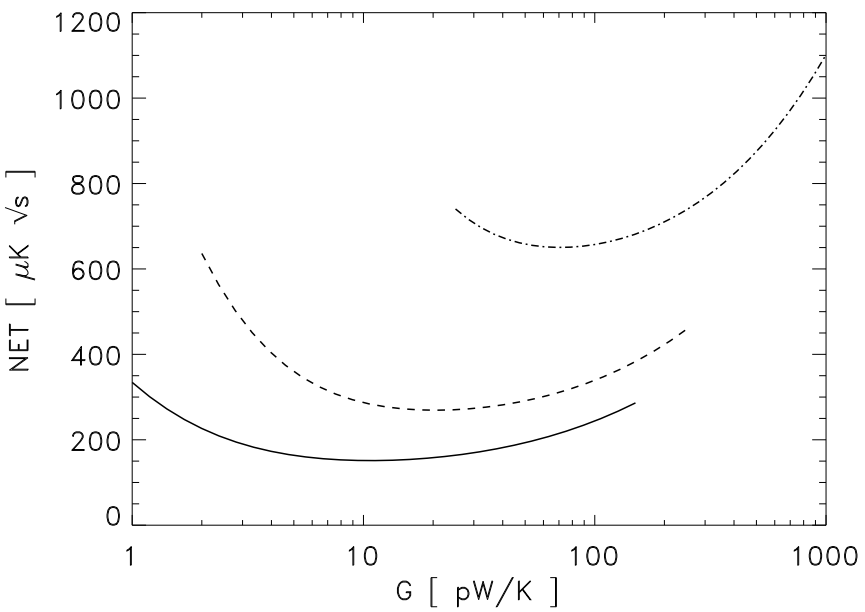


Figure 2.21: The dependence of receiver sensitivity to bolometer thermal conductance, $G_0$. The sensitivity curves for all three BOOMERANG frequency bands are shown, the lowest NET being the 145GHz PSBs, and the highest corresponding to the 345GHz photometer channel. A detailed explanation of the receiver model can be found in Appendix B. The calculations depend on accurate modeling of the in-flight background loading conditions.

in-band thermal emission. To ameliorate this problem, large-format, composite IR blockers were fitted in front of the 77K and 2K filters. These filters have high in-band transmission and reflect radiation at wavelengths shortward of $\sim 100\mu$m.

### 2.3.4 Detectors

A model of the in-flight optical loading accounted for the expected contributions from the CMB, the atmosphere, and the internal components of the cryostat, based on the detailed transmission spectrum of each channel. This estimate of optical background was fed into the bolometer model described in Appendix B. The optimal bolometer design parameters are found by minimizing the raw sensitivity. The dependence of the sensitivity on the thermal conductance, $G_0$, is shown in Figure 2.21.

Because of the sharp decline in responsivity at low impedance, the degradation in sensitivity is more gradual at higher $G$ than it is at lower $G$, the targets were chosen

slightly higher than the optimal value. With the current fabrication techniques, there is considerable ($\sim$ 30–50%) variation between the achieved and target thermal conductivity, especially at the extremely low $G$s required for BOOMERANG's 145 GHz PSBs. This is another reason to aim high when setting a thermal conductivity specification.

Based on these considerations, the PSB $G$s were all targeted to $\sim$30 pW/K at 300 mK. Prior to BOOMERANG, no bolometers had been operated with such low thermal conductance. For the photometer channels, the optimal $G$ range was perfectly suited to the existing BOOMERANG98 "spider-web" devices. Several more detectors of the same type were fabricated and mounted in modules as spares. One of the devices flown in BOOMERANG98 (B220A1) developed an open circuit and was replaced. The types and properties of the bolometers flown on BOOMERANG are given in Table 2.5. All 145 GHz devices are prototypes of the *Planck* HFI detectors. The designations for the 245 and 345 detectors refer to their original use in the BOOMERANG98 focal plane.

### 2.3.5 Readout electronics

In order to achieve the required low frequency stability, the bolometers are sine-wave biased and square-wave demodulated. Phase shift compensation is applied at the demodulator. Cold (120 K) front end JFETs (IR Labs TIA JFET amplifiers) act as unity-gain differential impedance transformers for the high impedance wiring. A bias frequency of 144 Hz, nearly three times lower than originally planned, was chosen in order to minimize susceptibility to parasitic capacitance and noise. In particular, lowering the bias frequency decreases the amplitude of the signal/reference phase shift and places the noise lines resulting from beat frequencies outside our signal bandwidth. Beat frequencies are observed with both the DAS sample rate and the system's microphonic resonant frequencies.[10] The bias frequency must be kept sufficiently high to be above the $\sim$ 10 Hz $1/f$ knee of the JFETs, as well as to

[10]Indeed, monitoring of these resonances allows one to track, with very high precision, the frequency stability of the bias generator.

Bolometer Parameters

| channel | device | $G_0$ | $\beta$ | $\Delta Q_{(90-77)}{}^{\dagger}$ | $\eta^{\ddagger}$ | $R_{300K}$ |
|---|---|---|---|---|---|---|
| b145w1 | HFI-10R | 23 | 1.3 | 1.90 | 0.33 | 5.00 |
| b145w2 | HFI-10L | 17 | 1.3 | 1.93 | 0.36 | 6.27 |
| b145x1 | HFI-09R | 17 | 1.4 | 2.01 | 0.39 | 5.75 |
| b145x2 | HFI-09L | 22 | 1.3 | 1.83 | 0.31 | 5.92 |
| b145y1 | HFI-03L | 17 | 1.4 | 2.09 | 0.39 | 6.98 |
| b145y2 | HFI-03R | 20 | 1.3 | 2.24 | 0.46 | 5.36 |
| b145z1 | HFI-07L | 20 | 1.4 | 1.44 | 0.27 | 5.41 |
| b145z2 | HFI-07R | 24 | 1.2 | 1.07 | 0.23 | 6.07 |
| b245w | B150B1 | 55 | 1.0 | 4.15 | 0.37 | 1.56 |
| b245x | B150A | 56 | 1.0 | 3.54 | 0.37 | 1.65 |
| b245y | DarkB | 54 | 1.0 | 3.35 | 0.34 | 1.52 |
| b245z | B150B2 | 66 | 1.0 | 3.51 | 0.36 | 1.46 |
| b345w | B220A2 | 150 | 1.0 | 12.9 | 0.77 | 1.05 |
| b345x | B220B2 | 142 | 1.0 | 14.2 | 0.90 | 1.13 |
| b345y | M1-10 | 174 | 1.0 | 13.4 | 0.88 | 0.71 |
| b345z | B220B1 | 161 | 1.0 | 12.5 | 0.88 | 1.14 |

Table 2.5: The characteristics of the bolometers flown on B2K. The 145 GHz bandpass provides 0.51 pW/K$_{RJ}$, assuming perfect efficiency. The integrated spectral transmissions of the PSB pairs differ by less than 2% for all pixels. The column labeled $R_{300\mathrm{K}}$ indicates the warm lead impedances. The Weideman-Franz conductivity ($2.5 \cdot 10^{-8}$ W$\Omega$/K$^2$), after scaling the impedance of the thin film to the operating temperature (the impedance drops by a factor of 1.8) gives a lower bound on the thermal conductance of about 3 pW/K for the BOOMERANG PSBs.$^{\dagger}$ Power differences are accurate to $\pm$0.25 pW. $^{\ddagger}$ Assuming single moded throughput. The 345 GHz channels are slightly overmoded.

provide constant power dissipation in the bolometers. Sine-wave biasing at frequencies below or near the thermal time constant of the detectors results in a degradation of sensitivity.

The JFETs dominate the voltage noise of the system, contributing 8–10 nV/$\sqrt{\mathrm{Hz}}$ with a 1/f knee near 10 Hz. The JFETs feed a low noise differential preamplifier (gain about 375), which is followed by a $\sim$ 40 Hz bandwidth bi-quad bandpass filter centered at the bias frequency. This limits the voltage noise contribution from the JFETs to the postdetection bandwidth centered at the bias frequency. The warm electronics contribute an additional $\sim$ 6 nV/$\sqrt{\mathrm{Hz}}$ of noise to the system. The trimpots used to set the center frequency of the bandpass filter were the source of considerable popcorn noise, and were replaced prior to flight with fixed metal film resistors.

The signal from the bandpass filter is multiplied by the square wave reference, and is passed through a four-pole Butterworth low-pass filter with a cutoff of 20 Hz. The (bit noise limited) Butterworth output is sampled at 5 Hz, and is passed on to a high-pass 5.6-mHz HP filter with in-band gain of 100. This AC-coupled signal is sampled at 60 Hz.

The demodulator output is a rectified sine wave characterized by a dominant Fourier component at $2f_{bias}$. While heavily attenuated by the antialiasing filter, this signal at $2f_{bias}$ is still present with high signal-to-noise. This is a distinct disadvantage of lowering the bias frequency given a fixed postdetection bandwidth. Beating of $2f_{bias}$ with the fifth harmonic of the DAS sample rate produces our prominent 12-Hz line (see Figure 2.19). A more detailed description of the readout and its quirks can be found in Appendix D.

It is extremely important that the bias generator and biquad bandpass filters be very stable over long ($\sim$ hour) periods; thermal variations in these components contribute to fluctuations in the low frequency noise properties over these time periods, which would violate the assumption of piecewise noise stationarity required for the analysis. Therefore, all of the capacitors in the bias generator and bandpass filter were replaced with either low TC NPO or Polycarbonate film components. The stability of the bias generator was monitored in-flight both by directly demodulating and sampling the reference, and by monitoring a cold (sub-Kelvin) resistor. The low frequency of the AC-coupling filter required high capacitance Tantalum capacitors, which have a relatively high temperature coefficient. The current leakage in the capacitors results in a DC offset. The severity of the low frequency noise was found to be well-correlated with the DC offset level, indicating that the coupling capacitors on the output stage of the demodulation circuit dominate the low frequency noise in the electronics.

### RF and microphonics

The high impedance of the semiconductor bolometers makes them susceptible to RF and microphonic interference. The PSB modules incorporate onboard LC filters that

attenuate RF at frequencies above a few tens of MHz. From the modules, the high impedance wiring runs through shielded twisted pair wires that are tightly secured to the sub-Kelvin plate with wire ties and silicone tape. As they exit the 2K Faraday cage, the signal and bias lines are run through an Eccosorb filter consisting of bare copper wires cast in Eccosorb. RF currents flowing on the wires are isolated to the outer skin depth of the conductor, where they are attenuated due to the proximity of the lossy Eccosorb. These filters form an effective (although massive and bulky) RF filter that is microphonically robust. The signals enter the JFET box directly from the Eccosorb filters. Finally, in-line filters buffer the lines running from the cryostat to the warm electronics box, which is sealed with conductive tape prior to launch.

## 2.4 Optics

### 2.4.1 Telescope

The BOOMERANG telescope is an off-axis Gregorian system consisting of an ambient temperature 1.3-meter primary and cooled (2K) secondary and tertiary mirrors. The tertiary is illuminated by an array of eight profiled, corrugated feed horns. The telescope was designed in the geometrical optics limit to produce an image of the primary at the tertiary mirror. There is a 1-cm diameter hole bored through the center of the tertiary mirror to accommodate a calibration lamp. In retrospect, there is no justification for placing the calibration lamp in the center of the optical system. An off-axis source could provide a calibration reference with more than enough signal-to-noise, and would not degrade the beam quality or throughput of the telescope.

The secondary and tertiary have effective focal lengths of 20 cm and 33 cm, respectively. The surface shapes of these mirrors were designed using the Code V ray-tracing software to provide diffraction limited performance at 1-mm wavelengths over a $2^\circ \times 5^\circ$ field of view. The surfaces of the primary, secondary, and tertiary

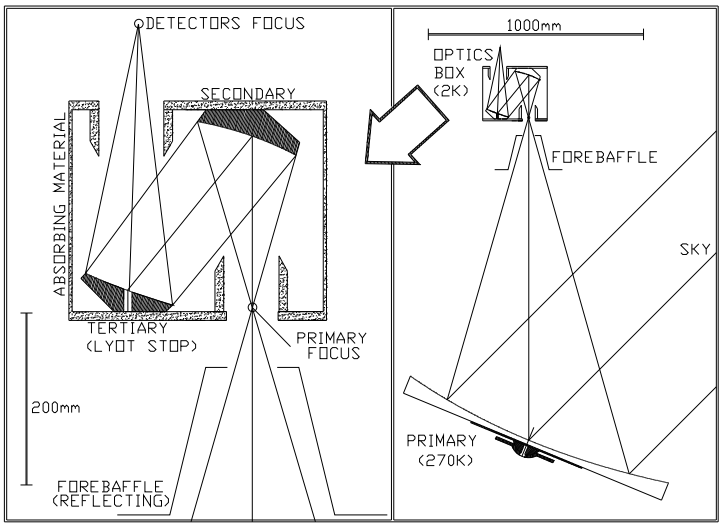


Figure 2.22: An overview of the BOOMERANG optics. Radiation from the primary reflects off the secondary, to the tertiary, and then to the focal plane. The secondary and tertiary correct aberrations induced by the primary. They are kept at 1.65 K in a box coated with absorbing material. The tertiary acts as the Lyot stop for the system, controlling the illumination of the primary. Spillover off the edge of the tertiary sees a 1.65-K blackbody.

mirrors are designed to the specification

$$z(r) = \frac{r^2}{R\left[1+\sqrt{1-(1+k)\frac{r^2}{R^2}}\right]} + Ar^4 + Br^6 \ , \tag{2.8}$$

with parameters $R$, $k$, $A$, $B$ as in Table 2.6.

The secondary and tertiary mirrors are housed in an optically sealed enclosure that is cooled to $\sim 2$ K. The interior of the optics box surrounding the tertiary and secondary reflectors is treated with a high emissivity coating. The undersized tertiary therefore defines a 2K Lyot stop, truncating the primary illumination at roughly 3/4 the radius (see Figure 2.23).

The introduction of a cold stop to the optical system represents a critical design trade-off between near and far-sidelobe levels. The presence of the Lyot stop results in a very large (nearly $-100$ dB) edge taper on the primary, which limits the diffractive contribution to the wide angle response. However, the abrupt truncation of the

Reflector Design Parameters

| Mirror | $R$ (mm) | $k$ | $A$ (mm$^{-3}$) | $B$ (mm$^{-5}$) |
|---|---|---|---|---|
| Primary | 2560 | -1.0 | 0.0 | 0.0 |
| Secondary | 363.83041 | -0.88279 | $1.36411\times10^{-9}$ | $1.86915\times10^{-15}$ |
| Tertiary | 545.74548 | -1.0 | $4.39086\times10^{-10}$ | $-3.26054\times10^{-15}$ |

Table 2.6: The design parameters for the BOOMERANG telescope (Equation 2.8). The reflectors are machined from bulk aluminum, and the surface is hand polished. The accuracy of the surface finish is not well known.

primary illumination results in relatively high near-sidelobe levels.

The original beam calculations were performed using ray-tracing methods supplemented by the diffractive analysis of the commercial Zemax package. The impact of the off-axis response of the telescope on the window function and calibration of the instrument motivated the interest in performing a more rigorous calculation of the telescope's radiation pattern.

In order to accurately model the off-axis response of the telescope, a physical optics calculation was performed for each of the 145 GHz and 245 GHz channels on the instrument. Physical optics is the analysis of the electrical currents flowing on all conductive surfaces that would be induced by power radiated from a feed horn located in the focal plane. The three-dimensional surface currents, $\mathbf{J}_s$ are determined by tangential magnetic field $H$ at the location of the conductor,

$$\mathbf{J}_s = 2\hat{\mathbf{n}} \times \mathbf{H}(\mathbf{r}_s).$$

In the limit that the grid spacing is sufficiently small that the surface is locally flat, the radiated field is determined by the integral over the individual contributions of the discretised surface currents,

$$\mathbf{H}(\hat{r}) = -\frac{1}{4\pi} \int\int d\mathbf{s}' \left(ik + \frac{1}{r}\right) \frac{e^{-ikr}}{r} \hat{\mathbf{r}} \times \mathbf{J}_s(s') \ .$$

Accurate modeling of an optical system requires a detailed treatment of the feed element; *a well designed telescope is only as good as its feed.* Therefore, the radiation

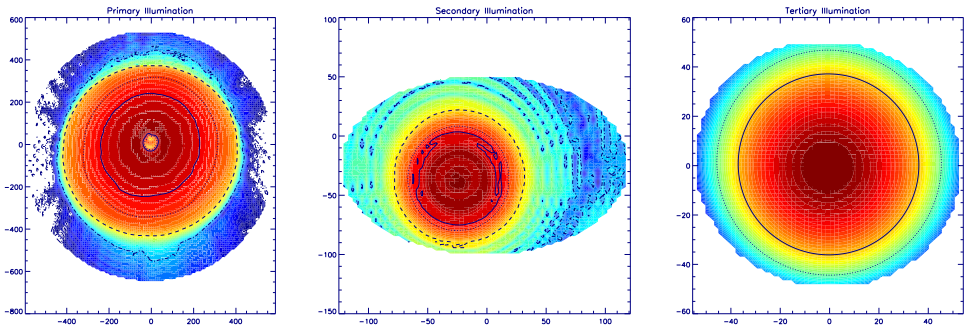


Figure 2.23: The power illumination of the primary (left), secondary (middle) and tertiary (right) mirrors for the B145W pixel, which is located on the edge of the BOOMERANG focal plane. The secondary and tertiary mirrors are cooled to 2 K, and are surrounded by absorbing material to control the primary illumination. There is a 1-cm diameter hole in the center of the tertiary to accommodate a calibration lamp. The impact of the hole is visible in the illumination pattern of the primary.

patterns of the feed horns are calculated by means of a modal-matching algorithm. This method, which is easily applicable to single-moded, azimuthally symmetric geometries, is an exact numerical solution for the vector field distribution within the feed element. The feed design and analysis will be discussed in detail in Section 2.4.2.

The aperture field distribution of the feed is propagated to the tertiary mirror, where the induced surface currents are calculated on a $1/2\ \lambda$ grid. The radiated (complex) field amplitude at the grid positions on the secondary are calculated by integrating over the individual contributions of the currents on the tertiary.

This process is repeated to reproduce the surface current distribution on the primary. The power illumination of each of the reflectors for one of the 145 GHz channels is illustrated in Figure 2.23. It is assumed that the system is linear in the field amplitudes; that is, that the back reaction of induced currents on the source conductor current distribution is of negligible amplitude. This assumption is checked through direct calculation and, as one would expect, is found to be valid for BOOMERANG's reflector geometry at millimeter wavelengths. The exit aperture of the 4-K optics box is coated with millimeter-wave absorbing material, which significantly limits the contribution of induced currents in the vicinity of the window to the source currents on the reflectors.

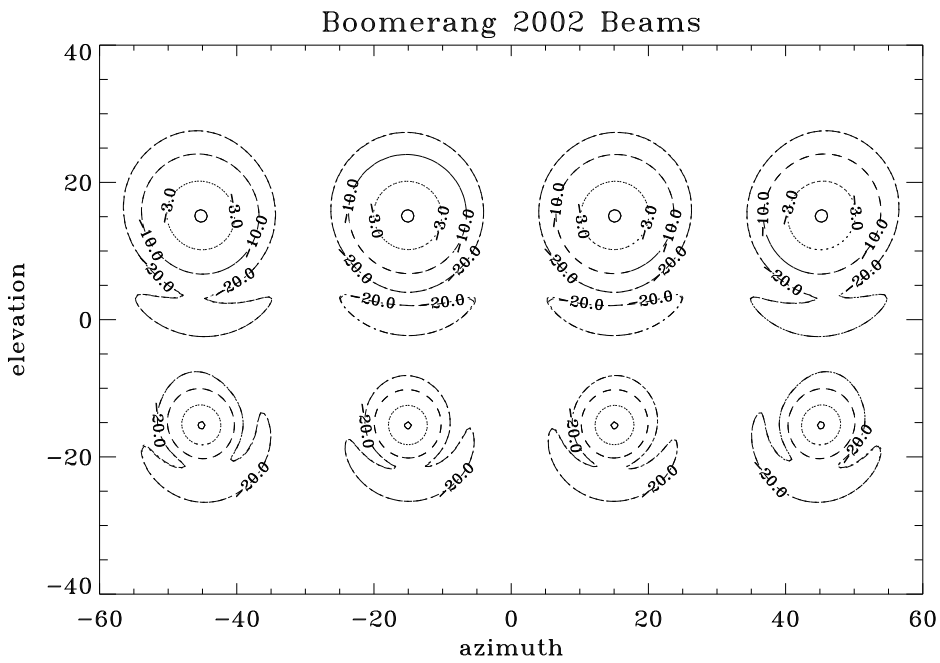


Figure 2.24: The physical optics prediction of the projection of the beams on the sky. Both the beam centroids and shape are in good agreement with measurements.

The primary illumination was calculated with several grid densities to check the numerical convergence. Once the primary illumination is determined, the radiated field can be computed at an arbitrary field point by performing a similar integration over the surface current distribution. This procedure results in a fully polarized prediction of the telescope response. Within one degree of the boresight the solution was found to have converged with a $4\lambda$ grid. To calculate the radiated fields at large angles, a higher grid density is required.

While extremely accurate, the physical optics technique is computationally intensive. The calculation scales as $\nu^4$, with a large prefactor that depends on the number and arrangement of the optical system. This scaling has restricted the common application of the technique to electrically small structures. With a few notable exceptions, full scale physical optics calculations at high frequencies ($> 100$ GHz) and for electrically large structures ($D \geq 600\lambda$) are seldom found in the literature.

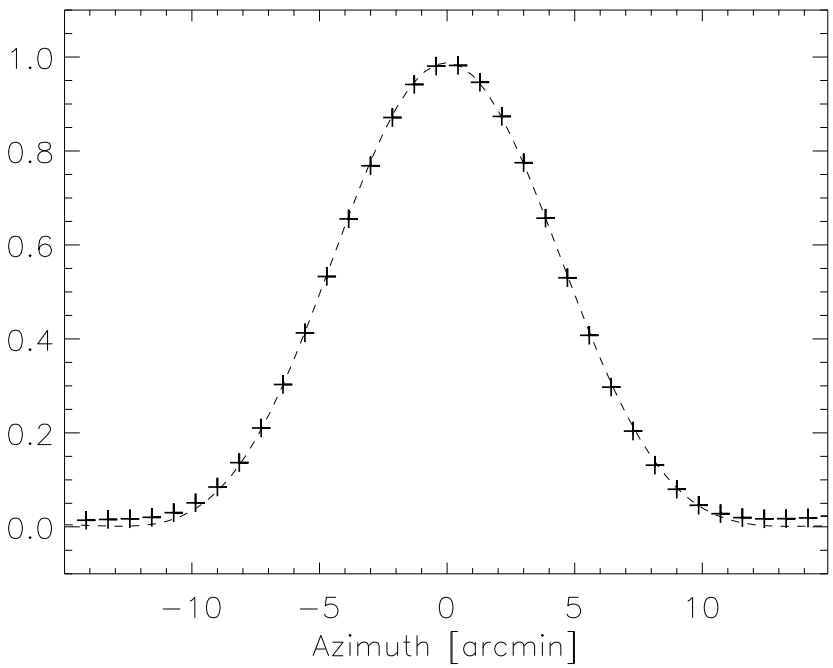


Figure 2.25: The physical optics model of the near sidelobe structure of the 145GHz beam (dashed line) and measurements of a thermal source (crosses). Measurement errors are comparable to the size of the plot symbol. Deviations from the model at low amplitudes are due to nonstationary atmospheric noise. The measured beam size is $9.72 \pm 0.05'$ FWHM, in good agreement with the physical optics model.

For BOOMERANG's three-reflector optical system, the computation time scales as

$$\tau \propto \; N_\nu \; N_{\rm pol} \; \left[ a_t \; \rho_t \nu^2 + \left( a_t a_s \; \rho_t \rho_s + a_s a_p \; \rho_s \rho_p + a_p a_f \; \rho_p \rho_f \right) \nu^4 \; \right] \; ,$$

where the $\rho_i$ (for $i = t, s, p$ or $f$, for the tertiary, secondary, primary, or field) are the gridding densities of the reflector or field surfaces, and the $a_i$ scale as the area of the surface. The $\rho_i$ depend on the size, shape, and relative orientations of the various reflectors, and must be optimized for a balance between accuracy and efficiency.

The computational problem is exacerbated by BOOMERANG's large dual-polarized bandwidth. For an accuracy of $\sim 5\%$, BOOMERANG requires a calculation of the beam at $N_\nu \gtrsim 5$ frequencies in each band. The large bandwidth also implies that the beam size is generally dependent on the spectrum of the observed source. Therefore, frequency weighted beams must be produced independently for each required source

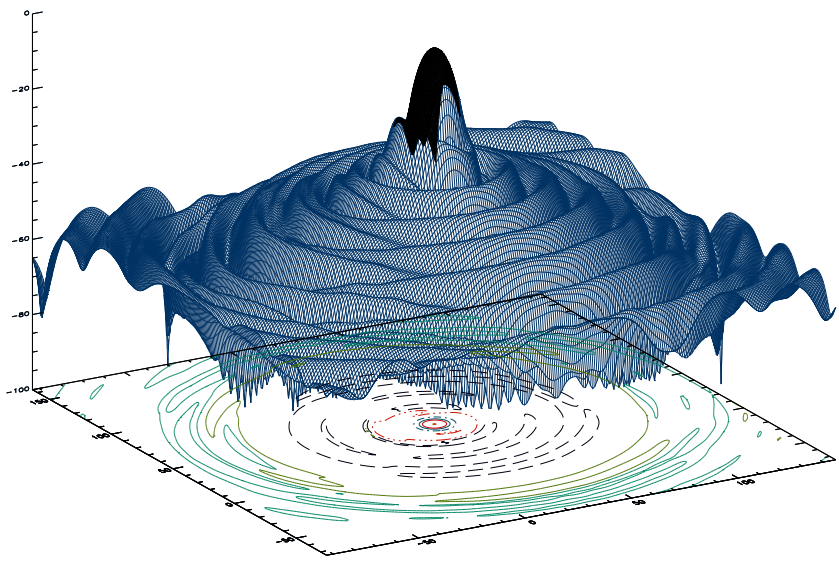

Figure 2.26: The physical optics model of the near sidelobe structure of the 145 GHz beam.

spectrum–the two of interest for the present work are that of the CMB anisotropies and of a Rayleigh-Jeans spectrum.

Fortunately, the problem is maximally parallelizable; each element's surface integral may be accomplished independently. Furthermore, the frequency integrals are assumed to be independent, allowing averaging of the radiated beam. For the analysis of the BOOMERANG telescope, an eleven-node Beowulf cluster of 800 MHz P4s running under Linux accomplished the task for each 145 GHz channel in approximately 72 hours.

In this way, polarization and bandpass-averaged far-field radiation patterns are calculated, producing beam centroid positions and two-degree-square beam patterns for each of the eight 145 GHz and four 245 GHz channels, as illustrated in Figure 2.24. The beam maps are generated at half-arcminute resolution. The two-dimensional radiation pattern of one of the pixels is illustrated in Figure 2.26. An azimuthal cut through the beam center of B145X is shown in Figure 2.27. The two-dimensional frequency and polarization averaged radiation patterns are then used to generate window functions for each channel.

To check the precision of the model calculations, a comparison with beam map

Physical Beam Summary

| Channel | $Az_{cent}$ | $El_{cent}$ | $Az_{fwhm}$ | $El_{fwhm}$ | major | minor | angle |
|---|---|---|---|---|---|---|---|
| B145W1 | 45.25 | 15.19 | 9.76 | 9.92 | 10.08 | 9.62 | -34 |
| B145W2 | 45.25 | 15.19 | 9.76 | 9.92 | 10.09 | 9.61 | -34 |
| B145X1 | 15.09 | 15.19 | 9.75 | 9.88 | 9.93 | 9.71 | -23 |
| B145X2 | 15.09 | 15.19 | 9.78 | 9.88 | 9.95 | 9.72 | -30 |
| B145Y1 | -15.09 | 15.19 | 9.78 | 9.87 | 9.85 | 9.80 | 66 |
| B145Y2 | -15.09 | 15.19 | 9.75 | 9.88 | 9.93 | 9.71 | 24 |
| B145Z1 | -45.25 | 15.19 | 9.75 | 9.92 | 10.08 | 9.61 | 33 |
| B145Z2 | -45.25 | 15.19 | 9.78 | 9.92 | 10.08 | 9.63 | 35 |
| B245W | 45.17 | -15.32 | 5.51 | 5.69 | 5.69 | 5.32 | -29 |
| B245X | 15.06 | -15.34 | 5.49 | 5.61 | 5.52 | 5.38 | -15 |
| B245Y | -15.06 | -15.34 | 5.50 | 5.60 | 5.52 | 5.37 | 21 |
| B245Z | -45.17 | -15.32 | 5.51 | 5.71 | 5.68 | 5.34 | 25 |

Table 2.7: The physical beam parameters, for a source with CMB spectrum.

data was made. The telescope beams were measured down to the $\approx -20$ dB level with high signal-to-noise using an ambient temperature Eccosorb ball suspended by a helium filled dirigible $\sim 1.4$ kilometers from the telescope. The calculated beams compare well with the beam map data down to the noise floor of the data, as shown in Figure 2.25. The observed FWHM derived from the field QSOs are consistent with the calculated far-field beam shapes, convolved with the error in the pointing reconstruction.

The accuracy of the sidelobe model within a degree of the boresight is limited by the effect of window materials and optical filters on the beam. However, because of their proximity to the prime-focus and the truncation of power due to the cold stop, the impact of the filters and windows will be minimal.

The BOOMERANG telescope is heavily shielded from sun and earthshine. Two large sun shields located on either side of the gondola ensure that the entire face of the gondola remains shaded throughout the flight. A baffle, fixed with respect to the telescope, provides further shielding from Earthshine and diffracted solar emission.

While the current distribution on the primary mirror determines the structure in the near sidelobes, the far-sidelobe response is dominated by the phase errors associated with surface imperfections and by diffraction around the edges of the shields

and the gondola structure. The effect of the former is well understood, at least for a known power spectrum of Gaussian distributed surface deformations. The presence of the cold Lyot stop serves to mitigate the latter.

Phase errors in the aperture plane of the optical system give rise to a degradation in forward gain and redistribution of that power to large solid angles. These phase errors may arise from misalignment of the feed antennas or optics, imperfections in the surfaces of the reflectors, or from thermal or gravitational deformation of the surface shape. Because the physical optics approach works with equal efficiency (or lack thereof) on arbitrary geometries, the procedure described above is naturally suited to treat the effects of surface imperfections on scales larger than the grid spacing. Given a measurement or calculation of the surface errors, their effect on the beam is directly calculable. Accurate modeling of error tolerances is one of the most valuable aspects of the physical optics approach.

Physical optics is as time-consuming as it is flexible; fortunately, an approximate analytical treatment of surface errors illustrates the most important impacts of the resultant phase error on the beam. Ruze has investigated the impact of a uniform distribution of Gaussian aperture-plane phase errors on the primary beam, and found an analytical solution that is in good agreement with controlled measurements [148]. Ruze scattering is an efficient way to approximate the effect of Gaussian random surface errors on the beam.

For an *rms* surface error $\sigma_l$ with a correlation length $l$, the beam pattern $P(\hat{r})$ is degraded according to the Ruze theory,

$$P'(\hat{r}) = P(\hat{r})\, e^{-\rho_l^2} + \left(2\pi\frac{l}{\lambda}\right)^2 \; e^{-\rho_l^2} \; \sum_i^{\infty} \frac{\rho^{2i}}{(i\; i!)}\; e^{-\frac{1}{i}\left(\frac{\pi l \sin\theta}{\lambda}\right)^2}\;, \tag{2.9}$$

where $\rho_l \equiv 4\pi\sigma_l/\lambda$. Ruze scattering redistributes power from the main lobe into a broad, azimuthally symmetric shoulder, whose solid angle is determined by the correlation length.

Given the power spectrum of the surface errors, the Ruze approach may be applied to each spatial mode independently to synthesize the resultant beam. Although no

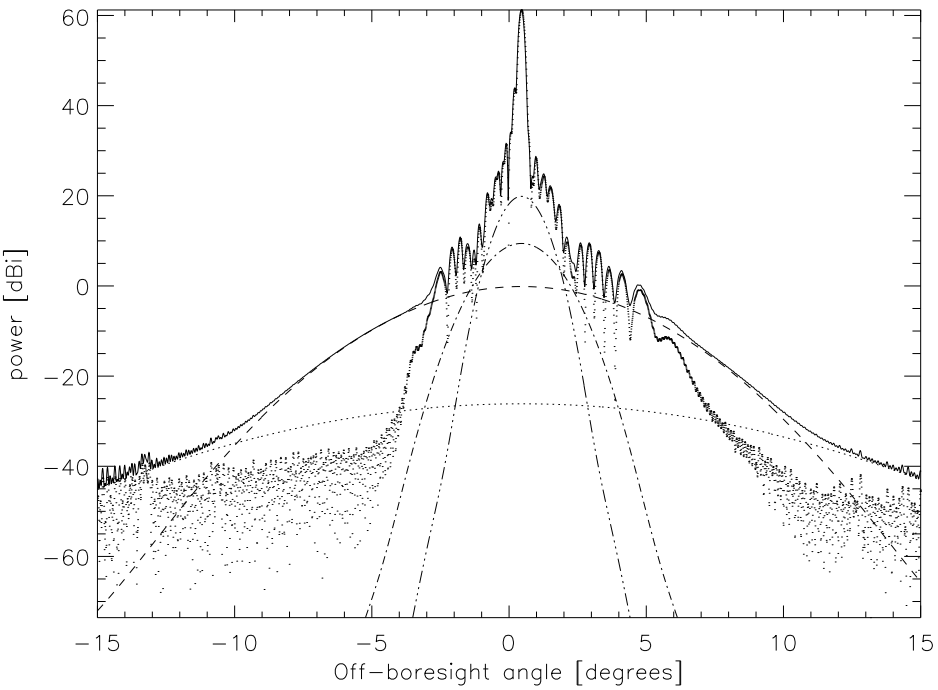


Figure 2.27: The physical optics model of the intermediate sidelobe structure, including the effects of phase error (Ruze scattering). The series of broken lines indicate the contribution of surface errors on 5-, 10-, 30- and 50-mm scales. The narrowest features result from the largest scale errors. The points represent the beam pattern for a perfect surface shape. The effect of the cold stop is evident in the sharp decrease in power beyond $\sim 6^\circ$.

surface accuracy measurement has been performed on the BOOMERANG telescope, a rough estimate of the power spectrum of surface errors may be inferred from that typical of polished bulk aluminum.[11] To first order, the phase errors of each reflector will add in quadrature. The physical optics beam with Ruze scattering corrections for one of BOOMERANG's 145 GHz channels is shown in Figure 2.27. The two-dimensional beam patterns resulting from this procedure are used to calculate BOOMERANG's window functions.

[11]Bulk aluminum 6061 can be hand polished to a surface accuracy of 0.1–0.2 $\mu$m *rms* [131].

### 2.4.2 Feeds

A back-to-back feed design is used to couple radiation from the sub-Kelvin optics to the telescope. In order to isolate the radiated field distribution from the sub-Kelvin detectors and filters, the throat region of the back-to-back feeds are designed to be single moded, and define the high-pass edge of the system. The design of the two halves of the feed are therefore separable; the radiating feed must couple well to the telescope optics whereas the back side of the feed must couple to the sub-Kelvin optics and filters.

BOOMERANG's focal plane contains two types of corrugated, profiled feed horns. Corrugated feeds provide excellent beam symmetry and extremely low crosspolar response over wide bandwidths. They are also less susceptible to the instrumental polarization that can result from manufacturing asymmetries in circular waveguide.

#### Corrugated feeds

Motivated by the desire to make use of dual polarizations in communication antennas, corrugated feeds were first investigated in the early 1960s. Forty years later, corrugated feeds are widely used in commercial, military, and astrophysical applications requiring selective polarization, beam symmetry, high efficiency, and wide operational bandwidth. Since the 1960s, the increase in available computational power has enabled feed designers to tailor the performance of the feeds through highly accurate numerical simulations. Zhang has published an excellent review of the theory of operation of corrugated waveguides [179]. Here we briefly summarize the topics needed to describe the BOOMERANG feed design; a complete treatment may be found in the referenced literature.

Corrugated waveguide structures (circular or otherwise) consist of a series–several dozen to many hundreds–of adjacent hollow conductors with alternating crosssectional area. The longitudinal length of each segment is much less than the smallest operational wavelength.

BOOMERANG's feeds are azimuthally symmetric in order to support both polariza-

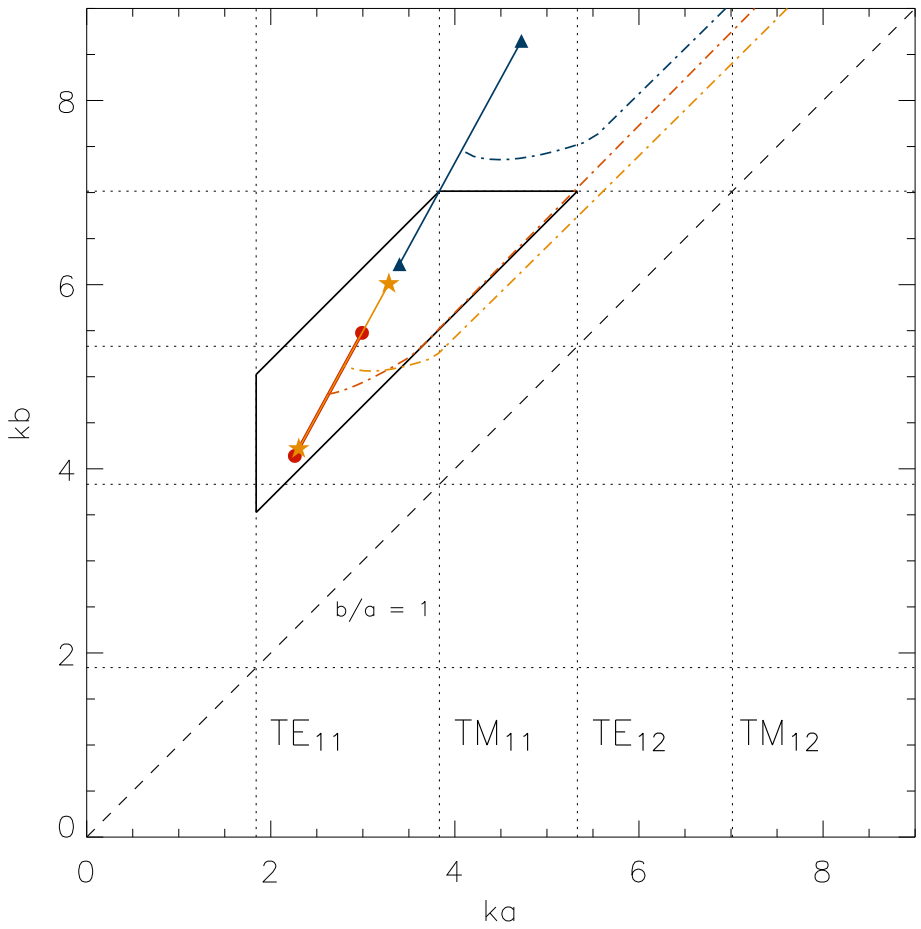


Figure 2.28: A mode diagram illustrating the design philosophy of the BOOMERANG feeds. The normalized corrugation depths, $ka$ and $kb$, are the radii of the inner and outer corrugations, respectively. Here $k$ is the free-space wave number, $k = 2\pi\nu/c$. The outlined area illustrates the region phase space that supports only the desired $HE_{11}$ mode. The solid lines indicate the full operational bandwidth of each of BOOMERANG's three channels *in the throat section* of the feed. The broken lines running from the center of the band illustrate the evolution of the corrugation geometry as a function of the axial distance along the feed. That is, the lines indicate the operational point in the $ka$-$kb$ phase space along the length of the feed, at the center frequency of each band. The red lines marked with filled circles indicate the 145 GHz band and feed. The orange lines marked with stars are the 245 GHz band and photometer feed, while the blue lines with triangles indicate the photometer's 345 GHz band. The modal cut-on frequencies are shown and labeled for the lowest four circular waveguide modes. The 345 GHz channel is clearly multimoded, as is confirmed by the channel's throughput ($A\Omega > \lambda^2$).

tion senses; the structures consist of a series of cylindrical conductors of alternating radius. Within each segment, the radius and azimuthal symmetry define a set of orthogonal basis functions; namely, the familiar $TE_{1i}$ and $TM_{1i}$ circular waveguide modes. These modes, like any solutions for a hollow conductor, are determined entirely by the longitudinal components of the $E$ (TM) or $B$ (TE) fields. An arbitrary azimuthally symmetric field distribution may be expressed as a linear combination of these basis functions.

The boundary conditions for a perfect conductor require the tangential component of the electric field and the normal component of the magnetic field to vanish at the surface of the conductor. This implies,

$$\left.\frac{\partial B_z}{\partial r}\right|_{r=a} = 0 \quad \text{(TE)} \qquad \text{and} \qquad \left.E_z\right|_{r=a} = 0 \quad \text{(TM)} \ , \tag{2.10}$$

For a cylindrical geometry, the longitudinal field has the form $B_z \propto J_1(\kappa a)\, e^{i\kappa z}$. The TE boundary condition imposed by the waveguide of radius, $a$, determines the propagation constant, $\beta$, for the ground state $TE_{11}$ mode. The solution to the Helmholtz equation gives

$$\kappa^2 + \beta^2 = k^2 \ ,$$

where $k = 2\pi/\lambda_0$, is the free-space wavenumber. The propagation constant for this mode vanishes when $\kappa a = ka = 1.841$, the lowest order solution to the boundary condition $dJ_1(\kappa r)/dr\big|_{r=a} = 0$. Wavelengths longer than this cutoff (and higher order modes at this wavelength) are exponentially damped with $z$ as the propagation constant, $\beta$, becomes imaginary.

Assuming there are a large number of grooves per wavelength, the surface of the corrugated waveguide can be described by an effective boundary condition in which the axial components of *both* the $E$ and $H$ fields must vanish. Intuitively, this must result due to the fact that a nonzero $H_z$ field component *within* a groove would be normal to the conductive face of the adjacent ridges. This results in a symmetric boundary condition for the TE and TM modes. As for smooth-walled guides the TE

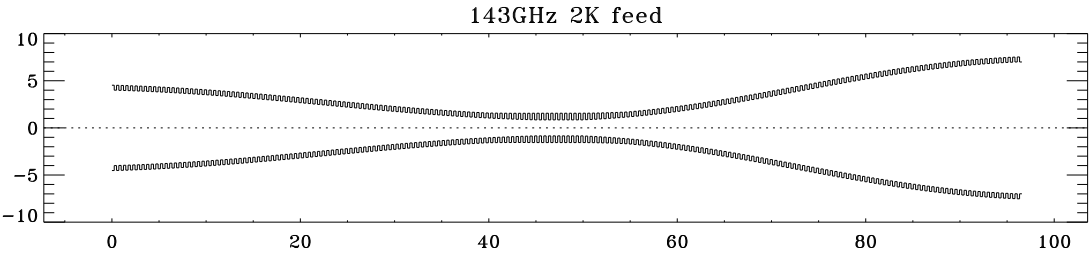


Figure 2.29: The corrugation geometry of BOOMERANG's 2K PSB feeds. The radiating aperture, which couples to the telescope, is on the right hand side, dimensions are millimeters.

boundary condition is

$$\left.\frac{\partial B_z}{\partial r}\right|_{r=a} \sim B_z|_{r=a} \approx 0 \qquad \text{(TE)} ,$$

whereas the corrugated guide imposes a symmetric TM boundary condition,

$$\left.\frac{\partial E_z}{\partial r}\right|_{r=a} \sim E_z|_{r=a} \approx 0 \qquad \text{(TM)} ,$$

where it is worth noting that the above TM condition holds only when $H_\phi \simeq E_z$, which is equivalent to the "balanced hybrid condition". The "balanced hybrid" condition results in TE and TM modes that are characterized by the same group velocities, which is not the case for a smooth-walled waveguide. The $HE_{1i}$ and $EH_{1i}$ families of modes are linear combinations of the familiar TE and TM states, which exhibit a coherent phase relationship.[12]

The corrugation geometry is defined by the inner and outer radii of the segments, $a$ and $b$, respectively. These dimensions determine which of the hybrid modes may propagate in a corrugated waveguide structure. The outlined region in Figure 2.28 illustrates the region of phase space in which only the desirable $HE_{11}$ mode may propagate with minimal attenuation. The importance of the throat, or mode-launching,

[12]To be specific, the HE family of modes consist of in-phase linear combinations, while the EH family consists of out-of-phase combinations of the general cylindrical TE and TM modes.

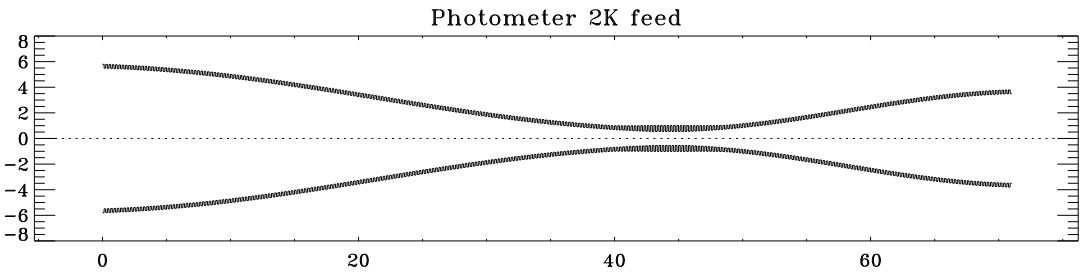


Figure 2.30: The corrugation geometry of BOOMERANG's 2K photometer feeds. The radiating aperture, which couples to the telescope, is on the right hand side. The dimensions are indicated in millimeters.

portion of the feed cannot be overstated; it is here that the radiating modes and the high-pass edge are determined. The only role of the rest of the feed is to produce the desired beam size and phase center, with minimal power conversion from the desired mode.

The discussion in the preceding paragraph suggests a powerful approach to the analysis of corrugated waveguide structures. For a given segment of the waveguide, we have a complete and orthogonal set of basis functions in the standard cylindrical-waveguide TE and TM modes. Furthermore, in the set of Equations 2.10, we have the well-known boundary conditions for each class of solution.

Starting at the throat of the feed, we assume an initial set of complex (amplitude and phase) mode coefficients corresponding to the field distribution at the input. The resultant field distribution is then propagated to the next annular section. Because of the difference in radii of the two segments, the propagation constants for each mode differ on either side of the boundary. At the boundary between the two segments, the field distribution is decomposed into the new set of basis functions, which are appropriate for the geometry of the following section. The amplitudes and phases that result are used to propagate the fields to the next boundary, and so on, until one obtains the field distribution at the aperture of the feed. This procedure, termed "modal matching", provides an efficient and exact analysis of the vector electromagnetic field at the aperture of a feed or waveguide. Once the aperture field distribution

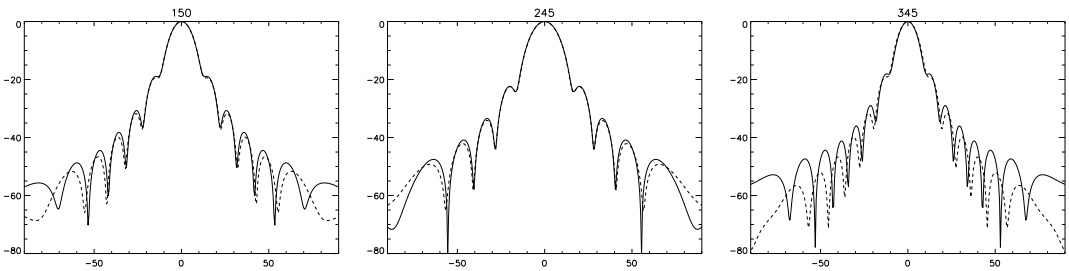


Figure 2.31: From the left, the radiation patterns of the 145, 245 and 345 GHz feed antennas. Both the E- and H-plane patterns are plotted, in solid and dashed lines, respectively.

as been calculated, the radiated fields may be obtained via spherical wave expansion (for the near field) or, more efficiently, via direct Fourier transform of the aperture fields (as is appropriate for the far field).

The only free parameters in the analysis are the complex amplitudes used for the input modes. In practice, most designs are completely insensitive to the details of the input because the throat region is single moded; the input field distribution has no effect on the radiated beam pattern. The power that couples to the higher order modes is simply not transmitted beyond the throat region. However, in order to accurately model the return loss of the system, one typically inserts an adiabatic transition from a smooth-walled waveguide supporting a pure $TE_{11}$ input to the corrugation geometry of the throat region. If the impedance-matching section is sufficiently well-designed, this allows a complete accounting of the input power and therefore an accurate calculation of the return loss of the corrugated feed. The modal-matching technique allows for rapid and cost effective prototyping of arbitrarily complex feed geometries, greatly easing the optimization of the feed profile and corrugation design.[13]

For multimoded feeds, the analysis is significantly more complicated since the aperture field distribution is strongly coupled to the amplitudes *and phases* of the *input* mixture of modes. Current electromagnetic modeling of these structures, for instance that of the submillimeter channels of the *Planck* HFI, relies on the assump-

[13]The WMAP feed horns are an example of the kind of highly optimized designs that are possible as a result of the numerical modeling techniques. The WMAP feeds were designed to place a pattern null on the edge of the secondary mirror, reducing the diffractive straylight contribution of the secondary by several orders of magnitude [6].

| PSB | | | Photometer | | |
|---|---|---|---|---|---|
| Freq. [ GHz ] | E.T.† [ dB ] | AΩ‡ [ $\lambda^2$ ] | Freq. [ GHz ] | E.T.† [ dB ] | AΩ‡ [ $\lambda^2$ ] |
| 120 | -6.4 | 0.00 | 200 | -4.3 | 0.14 |
| 130 | -7.8 | 0.82 | 210 | -4.7 | 0.67 |
| 140 | -9.4 | 0.85 | 220 | -5.3 | 0.71 |
| 150 | -11.1 | 0.83 | 230 | -5.8 | 0.75 |
| 160 | -12.6 | 0.81 | 240 | -6.5 | 0.79 |
| 170 | -14.0 | 0.81 | 250 | -7.2 | 0.81 |
| | | | 260 | -8.0 | 0.84 |
| | | | 270 | -8.8 | 0.85 |
| | | | 280 | -9.5 | 0.87 |
| | | | 340 | -15.0 | 0.91 |

†Edge taper on the tertiary mirror.

‡Effective throughput due to spillover on the cold stop.

Table 2.8: The edge taper as a function of frequency for the PSB and photometer feeds. The tertiary is an image of the primary, and therefore defines the edge taper on the Lyot stop. A higher edge taper results in suppressed sidelobe levels and a marginally broader main lobe.

tion that the input of the multimode feeds is terminated in a perfect blackbody, and that the allowed *hybrid* HE and EH modes radiate incoherently. In reality, the TE and TM modes excited in the throat of the feed interact coherently throughout the structure, with initial amplitudes and phases dependent on the details of fields at the input of the feed.

### The BOOMERANG feed designs

The BOOMERANG feeds are optimized for large bandwidth, beam symmetry, and maximal forward gain given a fixed aperture size. High gain feeds maximize the throughput and edge taper on the tertiary, resulting in increased sensitivity and lower near-sidelobe amplitudes. Although more purely Gaussian beams may be obtained via a flaring of the aperture, this does not result in the maximum gain given constraints on the aperture diameter. Furthermore, the cold Lyot stop intercepts the generally undesirable sidelobes, preventing the spillover commonly associated with off-axis systems of this type from reaching the sky or even warm ($T > 2$ K) elements

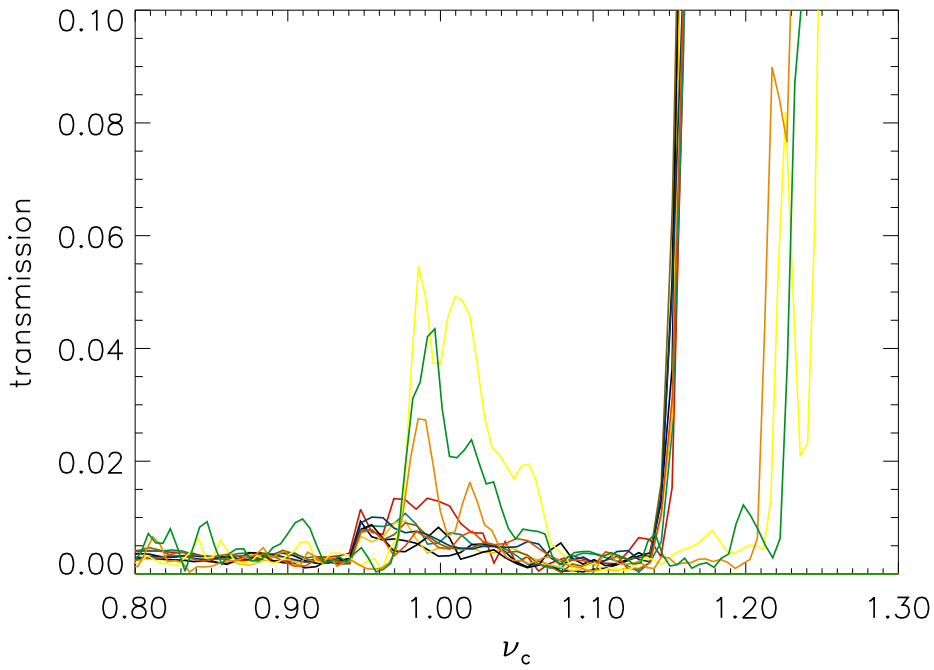


Figure 2.32: The high-pass cut-on of the BOOMERANG feeds, plotted against frequency normalized to the equivalent smooth-walled waveguide cutoff frequency, $\nu_c$ , as described in Equation 2.11. Note the slight increase in response in the vicinity of $\nu_c$. For the 143 GHz band, the molecular oxygen line falls close to a normalized frequency of 1.1.

within the cryostat. The shaped profile was adopted in order to achieve focus positions compatible with mechanical constraints. Moving the phase center of the feed nearer to the aperture flattens the phase front and minimizes the defocusing effect over a large bandwidth.

In most applications a corrugated feed must impedance-match with a smooth-walled waveguide, or transition to a (singly-polarized) rectangular guide. An adiabatic transformation of the corrugation geometry is achieved by gradually narrowing and deepening the grooves until a smooth waveguide wall results. This impedance-matching aspect of the design is not a consideration for the back-to-back feeds of the type developed for BOOMERANG. Unlike the corrugated feeds used in coherent receivers, there is never a need to transition to smooth-walled waveguide.

The lack of such a transition changes the approach to the design of the throat

section, both in terms of the corrugation geometry and the design of the high-pass edge. Although the corrugation geometry of the impedance matching design is more complicated when used in conjunction with smooth-walled waveguide, the design of the high-pass edge is decidedly simpler. For a single-moded system the high-pass edge is trivially determined by Equation 2.10; even an electrically short segment of waveguide of radius $a$ will strongly attenuate the transmission of frequencies lower than the implied cutoff,

$$\nu_c = \frac{1.841}{2\pi}\frac{c}{a}. \tag{2.11}$$

For a fully corrugated waveguide, the cutoff criterion is considerably more complicated. The location and shape of the edge is not easily treated analytically due to the subtle effects of the corrugation geometry and profile. Generally speaking, the cutoff is neither as sharp nor as monotonic as that of a circular waveguide of equal inner radius, $a$, and the effective edge occurs at a frequency well above $\nu_c$.

The problem is a serious one, as one usually is trying to maximize bandwidth while also ensuring rejection of certain atmospheric lines in the vicinity of the cutoff. In particular, the lower edge of BOOMERANG's 145 GHz channel is very close to the 119 GHz molecular oxygen line. Given these considerations, it is necessary to design the high-pass edge of the feed to better than 1% accuracy.

Fortunately, the details of the waveguide cutoff can be tailored with high accuracy through numerical simulation. The numerical analysis described above allows one to treat the corrugation geometry, the electrical length of the throat, and the details of the profiled expansion in a self-consistent fashion.

One must also consider the impact of manufacturing tolerances, which translates into an uncertainty in the location of the high-pass edge. For a smooth-walled waveguide, a radial tolerance, $\delta a$, results in a band-edge uncertainty, $\sigma_\nu$, of

$$\sigma_\nu \approx \delta a \frac{\partial \nu}{\partial a} = -\delta a \frac{1.841}{2\pi}\frac{c}{a^2} ,$$

Feed Design Parameters

| Feed type | $r_{in}$ | $r_{out}$ | $A$ | $p$ | $b/a$ |
|---|---|---|---|---|---|
| PSB, sub-K, back | 0.83 | 2.25 | 0.7 | 0.25 | 1.831 |
| PSB, sub-K, front | 0.83 | 4.00 | 0.7 | 0.25 | 1.831 |
| PSB, 2K, back | 0.85 | 4.00 | 0.6 | 0.245 | 1.831 |
| PSB, 2K, front | 0.85 | 7.00 | 0.7 | 0.245 | 1.831 |
| Phot., 2K, back | 0.55 | 5.50 | 0.7 | 0.128 | 1.818 |
| Phot., 2K, front | 0.55 | 3.50 | 0.7 | 0.128 | 1.818 |

Table 2.9: The feed design parameters, as in Equation 2.12.

therefore,

$$\frac{\Delta\nu}{\nu_c} = \quad - \frac{\delta a}{a} \, .$$

BOOMERANG's feeds were manufactured with an estimated tolerance of $10\mu$m on the corrugation geometry of the throat. This translates into a band-edge uncertainty of 1(2)% for the 145 (245) GHz high-pass edge. As illustrated in Figure 2.32, all of the BOOMERANG feeds achieved the design high-pass edge to this accuracy.

The details of the profile affect the gain, sidelobe structure, and Gaussianity of the main lobe. If, at any point in the feed, the flare angle becomes overly large ($\gtrsim 25^\circ$), one runs the risk of converting power from the $HE_{11}$ mode to higher order EH modes. In this regard, the design of the flare can impact beam symmetry, which is equivalent to crosspolarization.

That said, any smoothly varying parameterization is roughly as good as another, and the optimization is achieved through numerical analysis. The flare of the BOOMERANG feeds is given by the functional form

$$r(x) = r_{in} + (r_{out} - r_{in}) \cdot \left( (1 - A) \cdot \left( 1 - \frac{x}{L} \right) + A \sin^2 \left[ \frac{\pi}{2} \left( 1 - \frac{x}{L} \right) \right] \right) \qquad (2.12)$$

The addition of a flare to the aperture of the feed can extend the Gaussianity of the beam to well below $-30$ dB. However, due to the gain and aperture size requirements, the BOOMERANG feed profiles do not incorporate this design feature. A convenient flare that has been successfully implemented by the WMAP team, and others, is

parameterized by the form [6]

$$r(x) = r_{out} \cdot \sqrt{1 + \left(\frac{x\lambda}{\pi \eta r_{out}^2}\right)^2} \ . \tag{2.13}$$

While the flare results in very low sidelobe levels, it does not provide the largest gain for a given aperture size. In the BOOMERANG optical system, a 2K Lyot stop intercepts these sidelobes, making the gain requirement relatively more important than control over the throughput represented by the integrated power of the sidelobe structure.

# Chapter 3

# Instrument Performance

> "There are some observations which are not worth a damn, and others which are not worth a damn, and in my opinion the two damns are not better than one damn."
>
> –Heber Curtis, to the National Academy of Science, 1920

## 3.1 Preflight characterization

The preflight characterization of the focal plane instrument may be divided into two broad categories: those measurements required to confirm the operational status of the system, and those required to determine the parameters necessary to execute the science analysis of the data. We discuss each in turn, with an emphasis on the latter.

### 3.1.1 System checks

The realities of Antarctic logistics are such that, rather than meeting your assembled instrument on the launch pad, you arrive in McMurdo only to find a number of poorly labeled crates filled to the brim with parts, spares, tools and frozen PB&J sandwiches. With the exception of very few components, the entire instrument must be disassembled and rebuilt between the last run in the laboratory and the launch at Willy Field. This greatly complicates the execution of an Antarctic LDB flight, and makes it absolutely critical that thorough preflight systems checks are performed.

The situation is compounded by the fact that in order to verify the successful integration of the BOOMERANG receiver, you must cool it to 300 mK, a process which can take a week. Once the receiver is operating at 300 mK, you must systematically check that nothing is wrong with the optical efficiency, the background loading, the noise properties, the transmission spectra (including checking for out-of-band leaks, using thick grill filters [160]) and the beams before concluding that you do not need to take the entire thing apart to fix the receiver. In addition, the base temperature, cryogen consumption, and the $LN_2$/LHe hold times must be measured to ensure that the cryogenic system is functioning normally. These are the diagnostic tests that must be run to determine the functional health of the instrument.

For the 2002 campaign, we were fortunate that almost everything *cold* checked out on the first cooldown. All channels were operational, and the receiver parameters were within the expected range, with the exception of the Z PSBs, whose optical efficiency was abnormally low, and the B345Z channel, which exhibited popcorn noise typical of poorly made cold solder joints. The decision was made to accept the low efficiency of the Z PSB rather than risk warming and opening the cryostat. The origin of the low efficiency is thought to be due to contamination of the 2K feed.

Unfortunately, the successful cooldown used up every last drop of the team's good Karma; we subsequently had to rebuild the warm electronics. This operation included (but was not limited to) changing the bolometer bias frequency from $\sim$ 400 Hz to 143 Hz, due to the presence of microphonic lines and large parasitic capacitance, and fixing the ailing analog-to-digital converter. The parasitic capacitance resulted in a channel dependent phase shift between the signal and reference. While the problem was both severe and interesting, it is also unique to instruments using NTDGe bolometers coupled to an analog demodulation circuit, and is therefore neither of general interest nor likely to arise in any modern bolometric system. A discussion of the topic is therefore relegated to Appendix D.

### 3.1.2 System characterization

A thorough preflight characterization is required due to the lack of any polarized astrophysical sources that are both well-characterized at millimeter wavelengths on $10'$ scales *and* are within our range of observation. It is of vital importance that accurate measurements of the polarization efficiencies, absolute channel orientations, transmission spectra, and physical beam patterns be obtained prior to launch. [1] Furthermore, the instrument lacks a calibration source capable of accurately measuring the in-flight transfer functions. The strong dependence of the bolometer time constant on the optical background requires that the system transfer function be carefully measured under background conditions that are similar to those encountered in-flight.

It is instructive to consider an ideal (uncorrelated) sample from the time ordered data (TOD) of a given detector in a PSB pair. As is shown in detail in Section 5.1.3, each channel is sensitive to a linear combination of the Stokes I, Q, and U parameters on the sky, integrated over the frequency response, $F_\nu$ and the (two-dimensional) copolar and crosspolar beam patterns, $P_\parallel$ and $P_\perp$, respectively.

$$d_i = \frac{s}{2}\int d\nu \frac{\lambda^2}{\Omega_b} F_\nu \int d\Omega \left[ \mathbf{I} + \gamma\, \mathcal{P}\, \left( \mathbf{Q}\cos 2\psi_i + \mathbf{U}\sin 2\psi_i \right) \right] , \tag{3.1}$$

where we have defined the beam and polarization efficiencies,

$$\mathcal{P}(\hat{n}) \equiv \frac{P_\parallel - P_\perp}{P_\parallel + P_\perp} \qquad \gamma \equiv \frac{1-\epsilon}{1+\epsilon} \quad . \tag{3.2}$$

The polarization leakage parameter, $\epsilon$, is simply defined as the ratio of the square of the diagonal elements of the Jones matrix describing an imperfect polarizer.

$$\mathbf{J} = \begin{pmatrix} \eta & 0 \\ 0 & \delta \end{pmatrix}$$

with $\epsilon \equiv \delta^2/\eta^2$.

[1] By absolute we mean referenced to the gondola, whose attitude must be determined in flight to derive the projection of each channel on the sky.

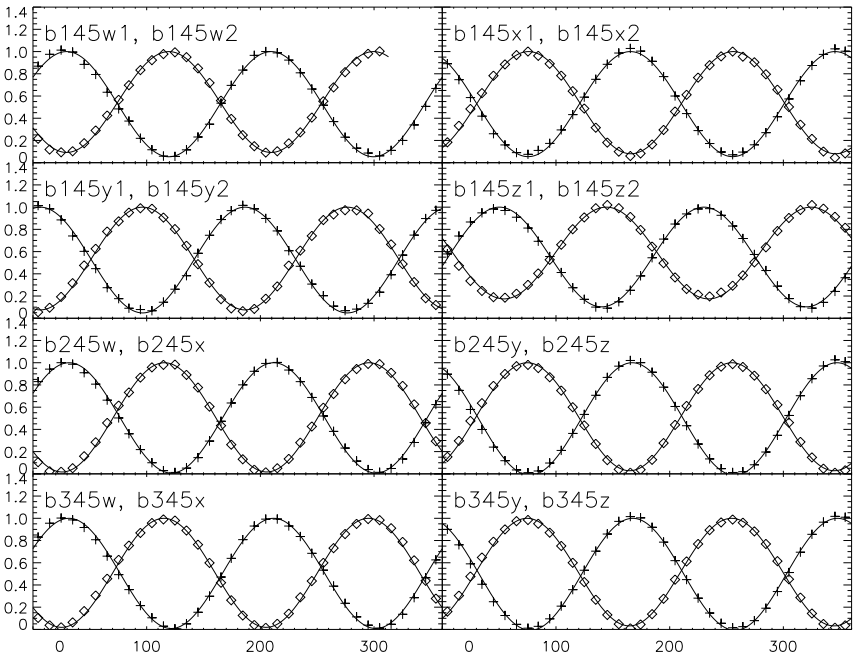


Figure 3.1: The calibration data for the polarization angles and efficiencies of all sixteen channels. These measurements were made at the prime focus, and are consistent with those obtained in the far-field of the feed horns.

We measure the polarization angles, $\psi_i$, and efficiencies, $\epsilon_i$, of each channel using a modulated 100% polarized thermal source. The orientation of the source polarization is rotated at a rate much slower than the source modulation. The signal is synchronously detected, allowing a high signal-to-noise measurement of the response as a function of source orientation. An example of these calibration data are shown in Figure 3.1. The parameters derived from these measurements are presented in Table 3.1.

The distinction between the polarization efficiency and the crosspolar beam is a critical one; one must be certain that the testing be designed to measure each effect independently. For most any optical system the crosspolar response, $P_\perp(\hat{n})$, is null on-axis. Therefore, a point-like source may be placed in the far-field of the optic to measure the leakage parameter $\epsilon$.

Performing these measurements with a beam-filling source, a source placed away from the beam center, or one that itself exhibits instrumental polarization will nec-

| channel | $1-\epsilon$ | $\sigma_\epsilon$ | $\psi$ | $\sigma_\psi$ | channel | $1-\epsilon$ | $\sigma_\epsilon$ | $\psi$ | $\sigma_\psi$ |
|---|---|---|---|---|---|---|---|---|---|
| b145w1 | 0.920 | 0.006 | 134.9 | 0.1 | b245w | 0.993 | 0.005 | 139.3 | 0.4 |
| b145w2 | 0.938 | 0.005 | 44.8 | 0.1 | b245x | 0.993 | 0.001 | 42.9 | 0.2 |
| b145x1 | 0.945 | 0.013 | 178.4 | 0.1 | b245y | 1.000 | 0.015 | 179.5 | 0.1 |
| b145x2 | 0.930 | 0.008 | 89.0 | 0.1 | b245z | 0.986 | 0.013 | 86.9 | 0.1 |
| b145y1 | 0.949 | 0.012 | 157.9 | 0.4 | b345w | 0.992 | 0.005 | 139.8 | 0.3 |
| b145y2 | 0.940 | 0.006 | 67.0 | 0.2 | b345x | 0.992 | 0.001 | 42.8 | 0.1 |
| b145z1 | 0.818 | 0.004 | 109.5 | 0.4 | b345y | 0.996 | 0.014 | 179.7 | 0.1 |
| b145z2 | 0.912 | 0.008 | 23.2 | 0.4 | b345z | 0.981 | 0.013 | 86.5 | 0.1 |

Table 3.1: The measured polarization efficiencies and angles, with the associated uncertainties. The relatively poor performance of the Z-channels is not fully understood, but is thought to derive from the 2K feeds.

essarily contaminate the measurement of the polarization leakage. The measurement must be carefully controlled to prevent overestimating the leakage parameter, $\epsilon$.

Measurements were performed both in the far-field of the feed, as well as through the cold optics at the prime focus of the telescope. The two measurements were in complete agreement. The relative polarization angles resulting from the optical measurement were referenced mechanically to the cryostat, and from the cryostat to the gondola.

Characterization of the beam was performed in the field using an ambient temperature thermal source suspended from a tethered dirigible. The dirigible was launched one kilometer from the telescope, and maintained at an altitude of one kilometer. The telescope was then raster scanned over the source to obtain a two-dimensional measurement of the (unpolarized) beam. These data were used to verify the predictions of the physical optics code, as reported in Figure 2.25 and Table 2.7.

We rely on the physical optics calculation for the estimate of the crosspolar beam. It is impossible to make a clean measurement of $P_\perp$ with an operational PSB due to the typical level ($\sim 5\%$) of the polarization leakage intrinsic to the device; the detected signal is completely dominated by the copolar beam response. One could measure the crosspolar beam of the system by inserting a section of rectangular waveguide into the throat of the 2K back-to-back feed.

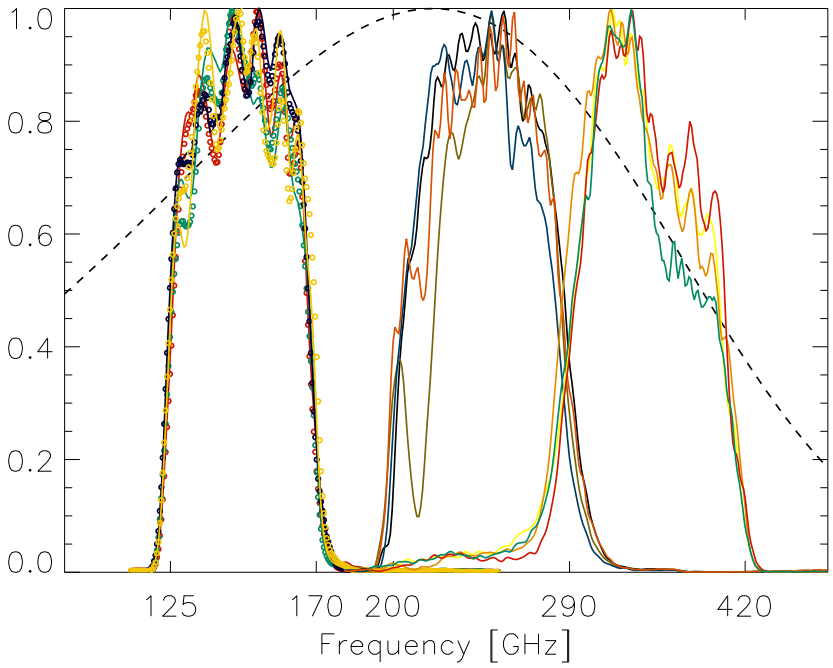


Figure 3.2: The measured transmission spectrum of each channel is shown along with the spectrum of the CMB anisotropies. These spectra are used to calculate the conversion factor between thermodynamic temperature and surface brightness units.

Given an accurate estimate of the in-flight loading conditions, it remains difficult to numerically determine the optimal *applied* in-flight bias because of parasitic capacitance in the wiring and JFETs. Coupled with the high bolometer impedance, some fraction of the applied AC bias current is shunted around the bolometer, making the relationship between the applied bias and the bias current through the bolometer very complicated. Therefore, the dependence of the signal-to-noise on the bias was determined empirically from the ratio of the amplitude of the calibration lamp pulse to the white noise level.

In order to accurately measure the detector time constants, measurements must be obtained over an $\sim$ 100 Hz bandwidth, which exceeds the bandwidth of the AC biased readout. Therefore, the detector and AC biased readout transfer functions were characterized independently. The bolometer transfer functions were measured optically, over a range of flightlike DC biases, while viewing a beam filling $LN_2$ load

through the 2K NDF. The transfer functions of the AC readout circuits were measured on the bench-top, using a custom built mixer.

The transmission spectra were measured extensively prior to deployment, and were checked again after integration in the field using a polarized Fourier transform spectrometer (FTS). The FTS is a Michelson interferometer using a thermal (77 K) load as a source. Using a traveling mirror to modulate the phase of one arm, one directly measures the Fourier transform of the spectral bandpass. The spectra as measured prior to launch are shown in Figure 3.2. As described below, BOOMERANG is calibrated directly on the CMB temperature anisotropy. This measurement provides the conversion from DAS voltages to an equivalent CMB temperature fluctuation. In order to convert from these thermodynamic temperature units, [$K_{cmb}$], to standard surface brightness units, [W/m$^2$ Hz sr], one must calculate the conversion factor from the band integrals over the (known) spectrum of the CMB anisotropies,

$$\frac{\int d\nu F_\nu \; \partial B_\nu(\mathrm{T}_{cmb})/\partial \mathrm{T}}{\int d\nu F_\nu}.$$

The conversion factors to surface brightness units for each BOOMERANG channel are given in Table 3.3.

## 3.2 In-flight performance

After a series of weather-related delays, BOOMERANG was launched on January 6, 2003 from the seasonal NSBF facility at Williams Field, Antarctica (77°51.63′ S. Latitude, 167°04.27′ E. Longitude). The launch site is situated on the Ross Ice Shelf, approximately ten kilometers from McMurdo Station, Antarctica. The launch was somewhat compromised due to unstable wind conditions, resulting in a rather violent release of the payload. Nevertheless, the release was successful. After a 3.5-hour ascent, the payload achieved a maximum altitude of 38.25 km. The flight was characterized by a steady drop in altitude and erratic high-altitude winds.

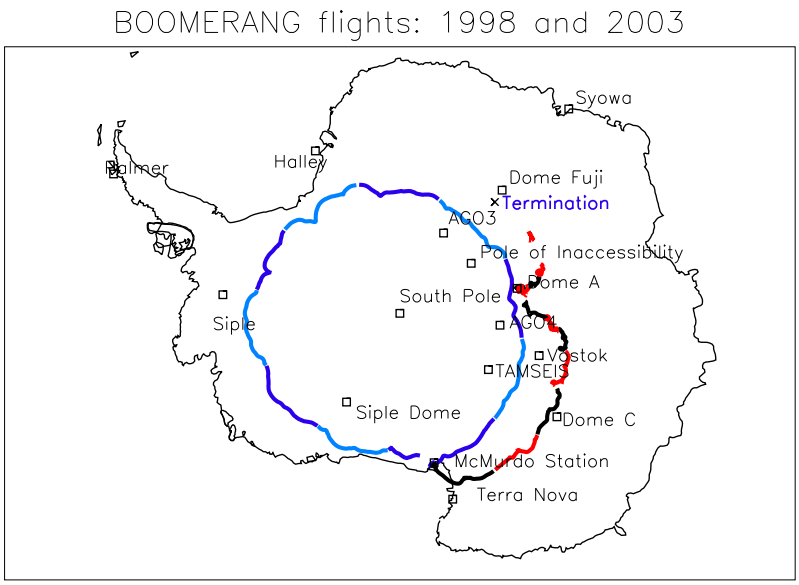


Figure 3.3: The flight trajectories of the BOOMERANG98 (blue) and B2K (black/red) payloads. The 2002 flight was suboptimal, stranding the payload on the Antarctic Plateau until recovery was possible the following Austral summer. However, NSF personnel recovered the data and flight computers immediately after termination.

BOOMERANG was launched with 171 kg of sand as ballast that was released in two controlled drops. In the first drop, which began on January 9, 22:30 UTC, 31.75 kg of ballast was released. The remaining 139.25 kg of ballast were released beginning at 00:00 UTC on January 11. The payload remained airborne for fifteen days before the flight was terminated on January 21.

During this time approximately 11.5 days of science data were obtained. At the end of day 13 the balloon altitude had dropped below 22 km, and the wind shear had increased to the point that we lost the ability to effectively control the gondola attitude. Although the instrument was shut down, the payload was not released until January 21 in order to facilitate recovery. A total of 257 hours of observations were obtained during the flight, including 75 hours spent observing the shallow CMB region, and 120 hours dedicated to the deep region (see Figure 2.6). While the pressure vessel containing the tape drives and hard disks was recovered from the payload on January 27, the rest of the gondola remained on the Plateau until the Austral summer of 2003–2004.

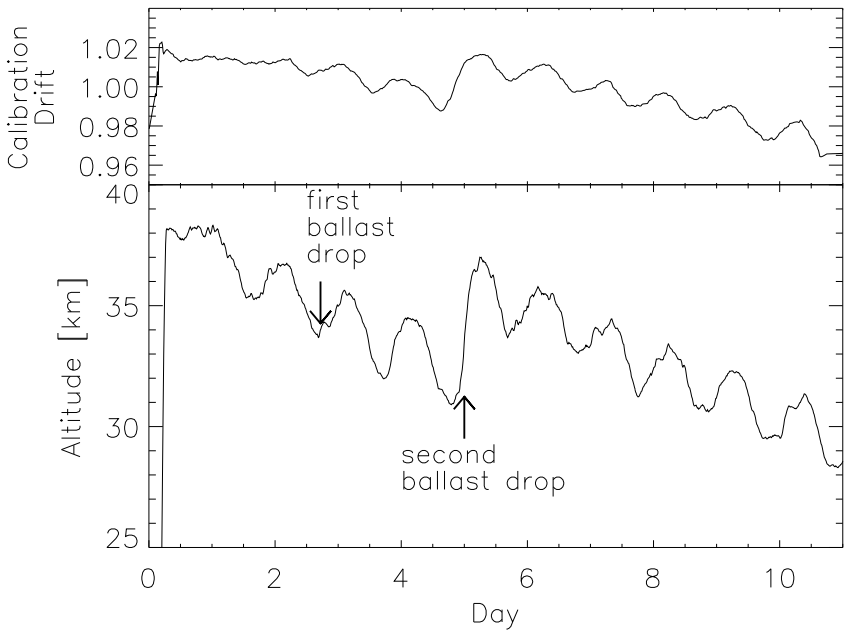


Figure 3.4: The drifts in calibration (top panel) and altitude (bottom panel) over the course of the flight. The decrease in responsivity of the PSBs was due primarily to an increase in the background. The backgrounds increased both from atmospheric emission and from emission within the cryostat as the system temperatures increased.

The flight profile was considerably worse than BOOMERANG's 1998 flight, both in terms of the altitude stability and the flight track. The diurnal variations and steady descent in altitude are illustrated in Figure 3.4. Figure 3.3 shows the flight track for each of the two flights, as well as the location of termination on January 21, 2003.

### 3.2.1 Calibration

Upon reaching float altitude, the signal-to-noise ratio was measured by stepping through the preset bias levels. The optimal (minimum NEP) bias is sensitive to the background loading at altitude (35 km), which we found to be equivalent to a $\lesssim$ 4.3-K Rayleigh-Jeans source at 150 GHz. In terms of total power, the receiver performance was consistent with a total optical background of 0.5 pW in our 143 GHz band. The loading estimates for the 245 and 345 GHz bands are more uncertain; however, their performance was consistent with backgrounds at float of 4 K (0.9 pW)

Cryostat Temperature Ranges

| Location | Low | High |
|---|---|---|
| Focal plane ..... | 0.292 | 0.298 |
| $^4$He cryopump ..... | 2.9 | 3.2 |
| $^4$He cold plate ..... | 1.6 | 1.9 |
| $^4$He radiation shield | 22 | 26 |
| $LN_2$ radiation shield | 60 | 62 |

Table 3.2: The extreme range of temperatures experienced over the duration of the B2K flight. All stages experienced temperature fluctuations that are well-correlated with the altitude.

and 16 K (6.2 pW), respectively.[2] More details regarding the in-flight performance of the receiver can be found in Table 3.4.

The large altitude fluctuations experienced throughout the flight resulted in variations in the optical background. While the base temperature of the bolometers remained stable, the optical background of the detectors fluctuated as a result of altitude dependent atmospheric emission as well as from thermal emission from the internal components of the cryostat, whose temperatures varied with altitude.

In the BOOMERANG cryostat, the vapor pressure above the cryogens is determined by the ambient pressure. Therefore, variations in altitude translate directly into variations of the system temperatures, albeit with very complicated phase relationships. The range of the temperature variations of the various cryogenic stages are given in Table 3.2.

The time variable backgrounds resulted in drifts of the bolometer responsivities, which were tracked throughout the flight using the calibration lamp. The calibration lamp pulsed every $\sim$ 15 minutes, allowing a precise measurement of the change in calibration on timescales longer than half an hour. The measured calibration drift over the course of the flight is shown for each band in Figure 3.5.

In order to verify that the calibration lamp provided an accurate measurement of the drift instead, say, of the drift in the calibration lamp brightness, the calibration

[2]Assuming a Rayleigh-Jeans source and single moded throughput, the BOOMERANG bands provide 0.5, 1.0, and 1.3 pW/K at 145, 245, and 345 GHz, respectively. The 345 GHz band is slightly overmoded.

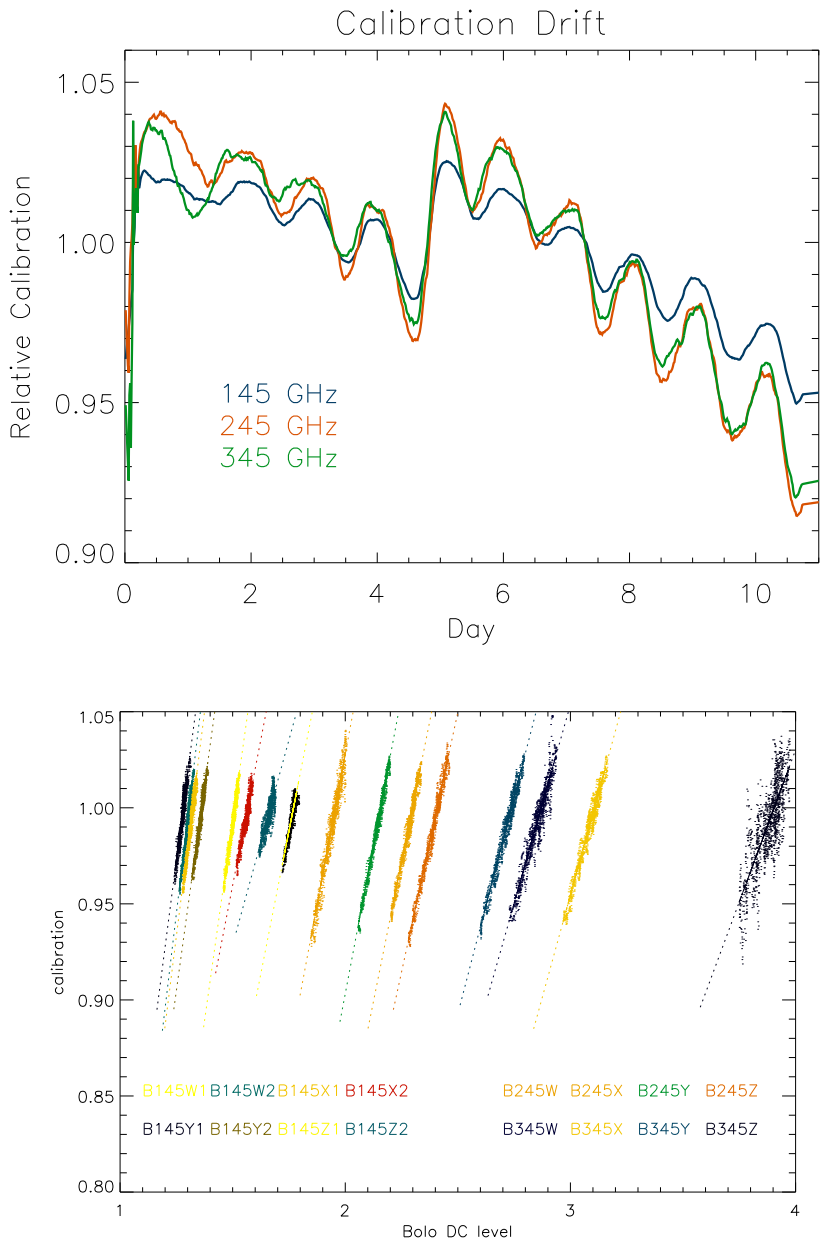


Figure 3.5: The top panel shows the calibration drift over the duration of the flight, averaged over each band. The high frequency channels are affected the most, indicating that much of the effect may be due to atmospheric loading. The lower panel shows the correlation between the calibration lamp pulse amplitude and the DC bolometer voltage (the DC voltage is proportional to bolometer resistance). The strong correlation is indicative that the drift in calibration lamp response is due to a change in bolometer responsivity rather than a drift in the calibration lamp current.

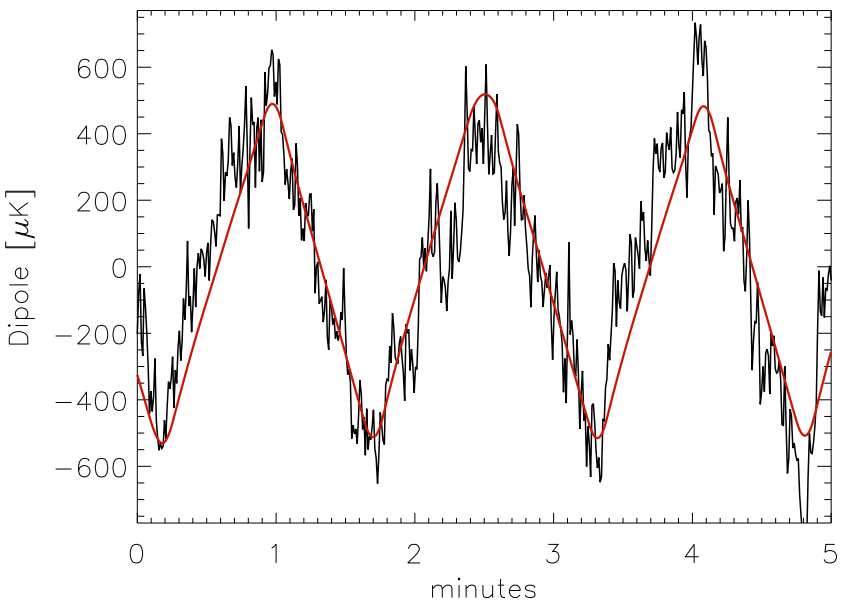


Figure 3.6: The CMB dipole as it appears in the time stream. The data and dipole signals are low-pass filtered and resampled at 1 Hz, for clarity. Much of the remaining "noise" originates from degree-angular scale fluctuations in the CMB.

drift was correlated with the DC coupled signal levels of the bolometers. The DC levels are proportional to the bolometer impedance, which itself is proportional to the voltage responsivity. A variation in the DC level necessarily leads to a variation in the voltage responsivity, as discussed in Appendix B. The DC levels were found not only to be well-correlated with the calibration drifts, but also were found to be perfectly in phase, consistent with a responsivity change due to a variation in the optical background. The correlation for each channel is shown in Figure 3.5.

The CMB represents an ideal calibration source for BOOMERANG since the spectrum of the calibration source is identical to that of the signal. In-flight absolute calibrations are obtained in two ways, both of which rely on the known properties of the CMB. The initial calibration was based on the CMB dipole, measured both in the time domain and by comparison with pixellized maps. The dipole is a prominent feature in the B2K time ordered data, as shown in Figure 3.6.

Due to the alignment of the CMB dipole with respect to the ecliptic plane and BOOMERANG's azimuthal scan strategy, the dipole appears in the time streams as

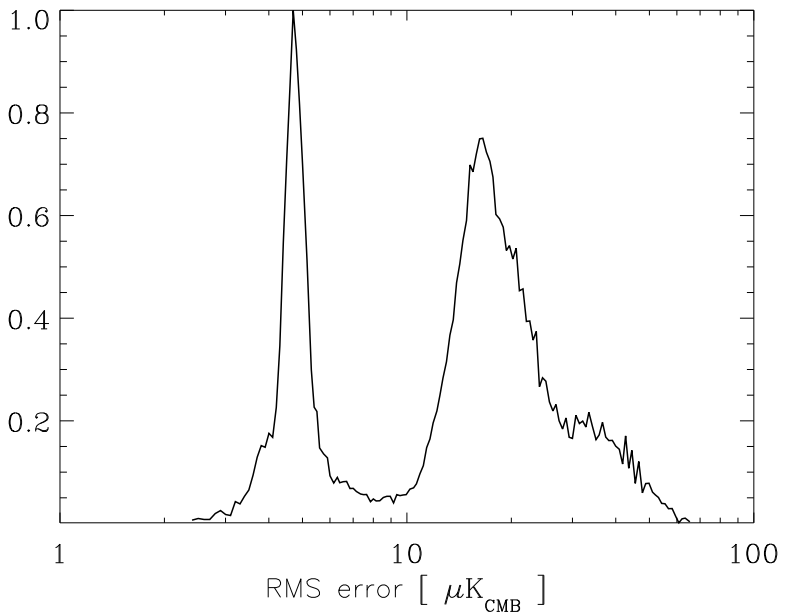


Figure 3.7: A histogram of the approximate noise per pixel, $\sqrt{\mathrm{diag}(\mathbf{C}_N)}$, for a $7'$ pixelization. The corresponding sky coverage is shown in Figure 2.6. In the deep region, B2K achieves approximately the same noise per pixel as that expected from *Planck*, while the shallow field enjoys a sensitivity roughly four times that of the first year WMAP data.

a triangle wave characterized by a fundamental frequency equal to that of the scan. This is problematic from the point of view of measuring the dipole due to the fact that there are many sources of noise at the scan frequency. The degeneracy of the dipole with the scan represents a fundamental limitation to the accuracy of the dipole calibration. The degeneracy is partially lifted by performing the calibration in the map domain, where the dipole is constant but the scan synchronous noise varies to some degree. The dipole provided the initial in-flight calibrations, but achieved an accuracy of $\sim 15\%$, which is far greater than the $\lesssim 5\%$ requirement.

We obtain our final calibrations from the amplitude of the degree-angular scale fluctuations in the CMB. These calibrations are obtained by cross-correlating the BOOMERANG maps from each channel with the published WMAP maps [12]. The accuracy of the calibrations obtained in this way are limited by the relatively low signal-to-noise of the WMAP data. The correlation is done in the Fourier domain rather than the pixel domain since systematic effects relating to the difference in the

scan strategy and beam size of the experiments are more easily handled in the Fourier domain. In order to eliminate any noise bias, absolute calibrations are obtained by observing the WMAP data with the boomerang scan strategy, filtering and coadding the resultant WMAP and B2K time ordered data identically, and finally calculating the cross-power spectra of the maps,

$$s_\ell^{\rm B2K} = \frac{\langle a_{\ell m}^{\rm WMAP\ W}\ a_{\ell m}^{*\ \rm WMAP\ V}\rangle}{\langle a_{\ell m}^{\rm WMAP\ W}\ a_{\ell m}^{*\ \rm B2K}\rangle}\ , \tag{3.3}$$

where W and V indicate different WMAP channels whose noise properties are presumably uncorrelated. This calculation provides an unbiased calibration as a function of $\ell$. The window functions of each experiment are used to correct for the effect of the beams on the cross spectra. The error on the measurement is determined by the scatter in the binned and decorrelated spectra.

As a cross-check, a similar calculation is made using the BOOMERANG98 map as a transfer calibrator,

$$s_\ell^{\rm B2K} = \frac{\langle a_{\ell m}^{\rm B98}\ a_{\ell m}^{*\ \rm WMAP\ W}\rangle}{\langle a_{\ell m}^{\rm B98}\ a_{\ell m}^{*\ \rm B2K}\rangle}\ . \tag{3.4}$$

Discrepancies between the two methods would indicate problems arising from the mismatched beam sizes of the WMAP and B2K instruments. No significant discrepancies are found.

The WMAP data are themselves calibrated with the CMB dipole with higher precision than the uncertainty in our estimate of the B2K/WMAP calibration [64]. The WMAP calibration error is nevertheless included in the estimate of the B2K calibration uncertainty. This procedure provides an absolute calibration [$\mu$K/Volt] for each BOOMERANG channel with an accuracy of 2%, as reported in Table 3.3.

### 3.2.2 Beams

In order to obtain unbiased estimates of the power spectrum, a correction must be applied to account for the window function of the experiment. Although the *physical* beam sizes were characterized prior to launch, the *effective* beam size on the sky must

Calibration Summary

| Channel | $\langle f \rangle$ | $\sigma_f^*$ | Calib,† | P.E.‡ | NET⋆ | S.I.≀ |
|---|---|---|---|---|---|---|
| B145W1 | 147.3 | 13.5 | 160200 | 0.920 | 140 | 388 |
| B145W2 | 146.7 | 12.4 | 170200 | 0.938 | 137 | 387 |
| B145X1 | 146.2 | 12.6 | 166900 | 0.945 | 156 | 386 |
| B145X2 | 146.6 | 12.4 | 218500 | 0.930 | 150 | 387 |
| B145Y1 | 147.0 | 12.8 | 172500 | 0.949 | 151 | 388 |
| B145Y2 | 146.8 | 12.7 | 179800 | 0.940 | 159 | 387 |
| B145Z1 | 147.0 | 12.6 | 238900 | 0.818 | 182 | 388 |
| B145Z2 | 147.1 | 13.1 | 384500 | 0.912 | 281 | 388 |
| B245W | 248.0 | 26.0 | 397900 | 0.993 | 281 | 461 |
| B245X | 250.7 | 24.7 | 505900 | 0.993 | 358 | 460 |
| B245Y | 244.0 | 24.6 | 446800 | 1.000 | 316 | 465 |
| B245Z | 247.6 | 26.5 | 468600 | 0.986 | 331 | 461 |
| B345W | 340.3 | 38.6 | 648800 | 0.992 | 459 | 321 |
| B345X | 338.9 | 38.9 | 599500 | 0.992 | 424 | 323 |
| B345Y | 344.1 | 37.6 | 876300 | 0.996 | 620 | 314 |
| B345Z | 337.8 | 38.7 | 436900 | 0.982 | 309 | 326 |

*The second moment of the transmission spectrum, $\sigma_f \equiv \sqrt{\langle f^2 \rangle - \langle f \rangle^2}$.
† Calibration in units of $[\mu \mathrm{K/V_{DAS}}]$
‡ P.E. is defined as $(1-\epsilon)$ where, $\epsilon = \delta^2/\eta^2$ and $\eta$, $\delta$ are the parameters of the PSB's Jones matrix.
⋆ NET in units of $[\ \mu \mathrm{K_{CMB}}\sqrt{\mathrm{s}}\ ]$
≀ Thermodynamic conversion factor for specific intensity, with units [MJy/sr per $\mathrm{K_{CMB}}$].

Table 3.3: The B2K calibration summary. The center frequency, bandwidth, absolute calibration, polarization efficiency, NET, and surface brightness conversion factor are given for each channel. Note that the bandwidth is expressed in terms of the second moment of the transmission spectrum, but that the spectrum is not a Gaussian in frequency.

be used to calculate the experimental window function. The effective beam differs from the physical beam due to errors in the pointing reconstruction, and therefore must be derived from in-flight observations of point sources.

Because of the limited signal-to-noise on these sources, we are able only to obtain a measurement of the FWHM of the effective beam. The pointing errors are assumed to be Gaussian, allowing an estimate of the *rms* pointing jitter by subtracting (in quadrature) the physical optics beamwidth from the measured effective beamwidth. The calculated physical optics beam, convolved with the Gaussian pointing jitter, is

Typical In-flight Receiver Performance

| | units | B145 | B245 | B345 |
|---|---|---|---|---|
| Center freq. | GHz | 146.1 | 248.0 | 340.0 |
| Bandwidth | GHz | 41.0 | 72.0 | 120.0 |
| Optical power | pW | 0.496 | 0.846 | 6.158 |
| CMB/total | % | 23.0 | 6.2 | 0.9 |
| Atmos./total | % | 4.1 | 32.6 | 64.7 |
| Refl./total | % | 21.4 | 17.2 | 10.0 |
| Internal/total | % | 51.5 | 44.0 | 24.4 |
| Elec. power | pW | 0.62 | 1.99 | 5.65 |
| Bias current | nA | 0.27 | 0.46 | 0.96 |
| Physical $G$ | pW/K | 22.9 | 59.5 | 173.3 |
| Effective $G$ | pW/K | 31.0 | 72.4 | 220.6 |
| Ratio | | 1.35 | 1.22 | 1.27 |
| Bolometer temp. | K | 0.326 | 0.322 | 0.347 |
| Bolo. impedance | MΩ | 8.63 | 9.28 | 6.17 |
| Responsivity | $10^8$ V/W | 7.23 | 4.56 | 2.07 |
| Opt. time constant | ms | 80.5 | 33.8 | 12.4 |
| $\mathrm{NEP_{total}}$ | $10^{-17}$ W/$\sqrt{\mathrm{Hz}}$ | 2.49 | 3.89 | 8.95 |
| $\mathrm{NEP_{photon}}$ | $10^{-17}$ W/$\sqrt{\mathrm{Hz}}$ | 0.99 | 1.64 | 5.31 |
| Bose term | % | 14.8 | 7.2 | 16.4 |
| $\mathrm{NEP_{phonon}}$ | $10^{-17}$ W/$\sqrt{\mathrm{Hz}}$ | 1.003 | 1.636 | 2.891 |
| $\mathrm{NEP_{johnson}}$ | $10^{-17}$ W/$\sqrt{\mathrm{Hz}}$ | 1.307 | 1.839 | 3.669 |
| $\mathrm{NEP_{amplifier}}$ | $10^{-17}$ W/$\sqrt{\mathrm{Hz}}$ | 1.578 | 2.518 | 5.494 |
| $\mathrm{NEP_{bolo}}$ / $\mathrm{NEP_{background}}$ | | 1.67 | 1.50 | 0.88 |
| NEFD | mJy/$\sqrt{\mathrm{Hz}}$ | 37 | 43 | 177 |
| $\mathrm{NET_{cmb}}$ | $\mu\mathrm{K_{CMB}}\sqrt{\mathrm{s}}$ | 151 | 341 | 551 |
| $\mathrm{NET_{RJ}}$ | $\mu\mathrm{K_{RJ}}\sqrt{\mathrm{s}}$ | 89 | 92 | 51 |
| $\mathrm{NET^{inst}_{cmb}}$ | $\mu\mathrm{K_{CMB}}\sqrt{\mathrm{s}}$ | 53 | 171 | 275 |
| Voltage noise | nV/$\sqrt{\mathrm{Hz}}$ | 18.0 | 17.7 | 18.5 |

Table 3.4: The receiver performance for a typical channel from each of the B2K bands, derived from the receiver model described in Appendix B and Figure B.7, using the observed in-flight loading conditions.

then used to generate the window functions for each channel.

There are five extragalactic point sources in our CMB field that are sufficiently bright to use for this purpose, all of which are radio-identified QSOs (see Table 3.5). We fit for the centroid and width of each source, and find the noise weighted average as well as the error on this estimate. In the deep region, the observations are confusion limited by $12'$ scale CMB fluctuations.

In order to minimize the confusion due to the background fluctuations, the source maps are filtered with a spatial bandpass filter (often referred to as a Mexican hat kernel) that is matched to the beamsize. The kernel width is chosen iteratively until the beamsize converges. It is at the same time remarkable and sad that B2K's pointing is determined by sources at a redshift of $\sim 1.5$, with the error on the pointing estimate limited primarily by confusion with CMB anisotropies at the level of a few $\mu$K.

The window functions generated using this procedure are shown in Figure 3.15. The deviation from a Gaussian, although most pronounced at higher multipoles, is also significant at scales corresponding to degree-angular scales. The difference is due primarily to the extended "wings" in the physical beam, evident in Figure 2.26.

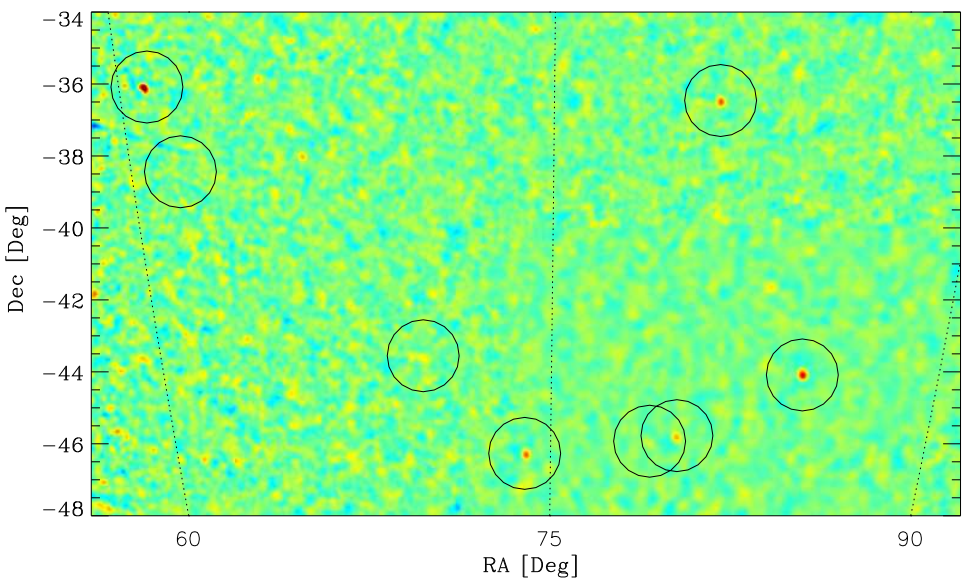


Figure 3.8: The B2K CMB field, filtered to highlight the extragalactic sources. The five brightest sources are used to estimate the effective beam size. Assuming that the pointing jitter is Gaussian, we derive the amplitude of the jitter from the (quadrature) difference between the best-fit effective beam FWHM and the physical optics beam FWHM. The window function is calculated from the physical optics beam pattern, convolved with the measured pointing jitter.

Extragalactic Source Observations

| Source Name | RA J2000 | Dec J2000 | $z$ | Flux[‡] [Jy] | RA FWHM | Dec FWHM | Radial FWHM | Error |
|---|---|---|---|---|---|---|---|---|
| (PKS)0537-441 | 84.68 | -44.11 | 0.89 | 2.9 (580) | 10.8 | 10.1 | 11.4 | ±0.5 |
| (PKS)0537-441[†] | ... | ... | 0.89 | ... | 12.1 | 11.0 | 12.8 | ±0.5 |
| (PKS)0518-45 | 79.98 | -45.82 | 0.04 | 1.4 (293) | 11.9 | 11.0 | 11.6 | ±0.3 |
| (PKS)0454-46 | 73.98 | -46.32 | 0.86 | 1.9 (376) | 11.1 | 8.8 | 10.9 | ±1.1 |
| (PKS)0402-362 | 60.86 | -36.15 | 1.42 | 3.6 (729) | 9.2 | 10.5 | 10.3 | ±2.7 |
| (PKS)0521-36 | 80.73 | -36.52 | 0.06 | 2.0 (400) | 9.9 | 10.5 | 11.6 | ±1.3 |
| Effective Beam | — | — | — | — | 11.51 | 10.65 | 11.49 | ±0.23 |

Table 3.5: Fit values. [†]These are the values obtained without subtracting the CMB from the background. [‡]The total source flux [Jy], with the apparent temperature [$\mu K_{CMB}$] in parenthesis. The observed fluxes vary slightly from those observed in 1998 [28].

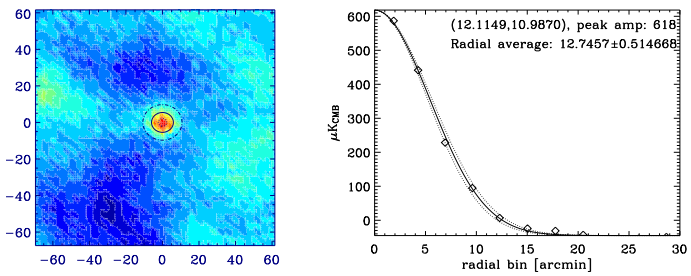


Figure 3.9: (PKS)0537-441, no background subtraction

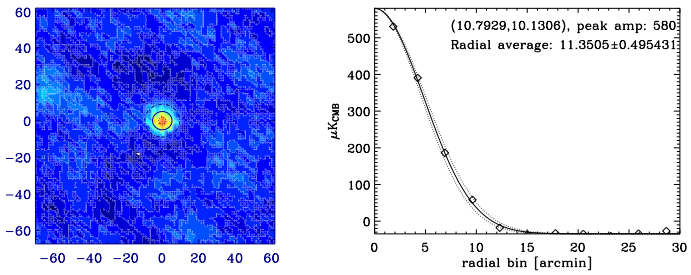


Figure 3.10: (PKS)0537-441, using background subtraction

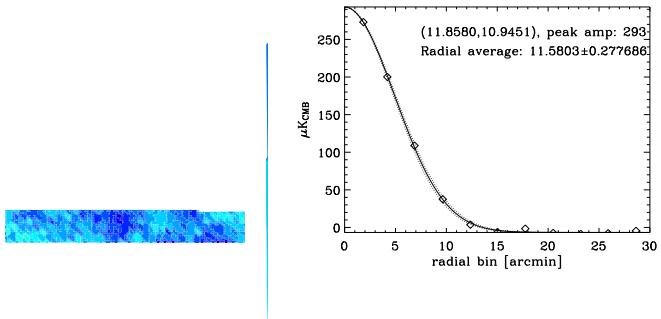


Figure 3.11: (PKS)0518-45

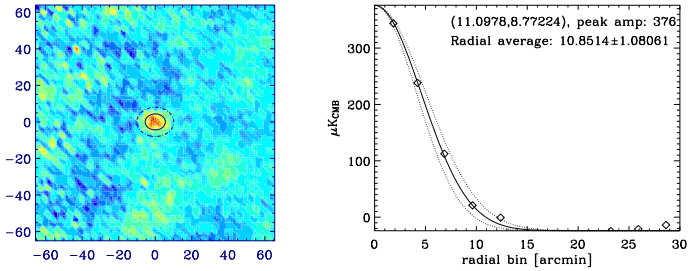


Figure 3.12: (PKS)0454-46

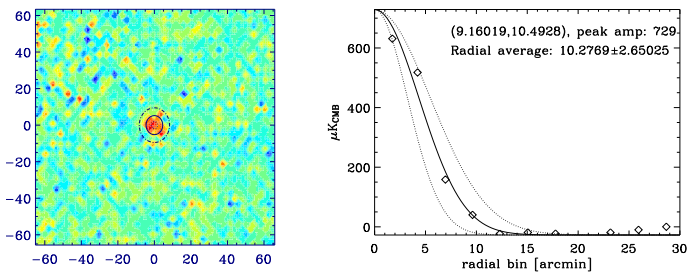


Figure 3.13: (PKS)0402-362

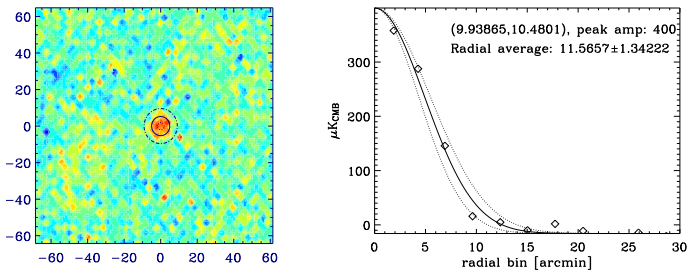


Figure 3.14: (PKS)0521-36

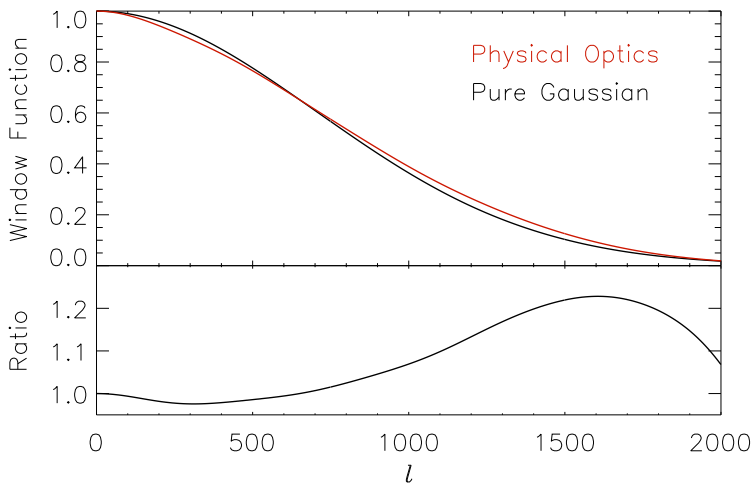


Figure 3.15: The actual B2K window function, compared with a Gaussian of equal width. The window function is the spherical harmonic transform of the (asymmetric) two dimensional beam pattern.

# Chapter 4

# Low Level Analysis

> "Few tasks are more like the torture of Sisyphus than housework, with its endless repetition: the clean becomes soiled, the soiled is made clean, over and over, day after day"
>
> –Simone de Beauvoir

Few tasks and few tortures, save the curse of data. Experimental data bears little resemblance to the idealistic musings of theorists which clog the literature. Data are a hard and cruel thing, not unlike a lover; an object of desire, an object one can no more resist than bear. This chapter describes the treatment of the raw data stream, the spinning of gold from straw.

Cosmology lives and dies by tedium; the lowest level processing of the time ordered data has, by far, more impact on the science return of a given experiment than does any of the subsequent analysis. The relative import of "optimal" methods, the generation of Weiner-filtered and foreground-marginalized maximum-likelihood maps, or any of the other myriad variations on the most naive analysis which one finds in the voluminous literature born of the analysis-mongers will pale in comparison to the lowly work of the experimentalist.

You will find no conferences in Aspen or Geneva dedicated to the development of algorithms to identify glitches in encoder data, nor to divine from an incomplete set of data the attitude of your gondola; the subdued classism of the scientific community would never permit (perhaps rightfully) the glorification of such priceless trivialities.

Without good data, careful low level analysis and heroic patience, one will never have a good science result no matter how sophisticated the top level analysis. This work is acknowledged as rarely as it is appreciated; the experimentalist's reward is having done a thing well.

## 4.1 Pointing reconstruction

Before anything interesting comes of the science data, you have to determine where the instrument happened to be pointed at any given time. This may seem like it shouldn't be that difficult, and in truth it need not be. For BOOMERANG, however, it is very difficult indeed.

The process begins with the de-glitching of the time ordered data coming from the attitude control system (ACS). The operational status of the sensors must be determined, often based on circumstantial evidence alone, and appropriately flagged. Without knowing what you are looking for, there is little one can do other than dig through the raw TOD, frame by frame, to familiarize yourself with the failure modes. Once you know your enemy, you may automate his destruction. For BOOMERANG, the process of identifying all of the subtle, but important, non-idealities in the data take much longer any of the subsequent analysis.

Once the ACS data are deglitched and cleaned, the (three - dimensional) gondola attitude is determined, providing the nominal pointing of the telescope boresight. Focal plane offsets are determined from observations of Galactic and extra-Galactic sources. This procedure gives the alt-az coordinates for each pixel, at each time sample. Combining this with the measured latitude, longitude, and UT allow one to calculate the RA/Dec and $\psi$ time-streams.

The basic approach is to determine the gondola attitude by measuring the vector to a guide star, and eliminating the remaining rotational degree of freedom by measuring the azimuth of the Sun. Quite often, simultaneous measurements were not available due to intermittent sensor failures or gaps in the calibrations. For much ($\sim 30\%$) of the flight we are left with no choice but to proceed in the face of absolute sensor

failure by dead-reckoning alone.

### 4.1.1 Sensors

The ACS data consists of the (two-axis) star position, the azimuth relative to the Sun (as measured by the fine Sun-sensor [FSS]), the azimuth, pitch and roll rate gyroscopes, the inner-frame elevation encoder, and the differential GPS data. The elevation encoder is the only sensor mounted directly to the inner-frame, which holds the telescope and cryostat.[1]

The DGPS provides measurements of the three-dimensional position, velocity, and attitude of the gondola, along with highly accurate timing information at a rate of approximately 1 Hz. The DGPS attitude determination is fairly course but, if averaged over a sufficiently long period, it enables the relative calibration of the other sensors to the required ∼arcminute accuracy. While not sufficient in itself for the pointing reconstruction, it was a fairly robust absolute sensor[2], which proved to be a rare commodity in flight.

When functional, the star camera returns a highly accurate two-axis measurement of the position of the guide star. However, the orientation of the star camera mount relative to the gondola frame was not known *a priori* with the required sub-arcminute accuracy. These Euler angles were obtained by comparison with the DGPS data over course of the entire flight.

On the fifth day of the flight, the star camera (quite literally) froze, remaining out of service for about 20 hours. During this period, we were forced to rely on the derivative of the DGPS velocity measurements to determine the pendulations of the gondola. We had no option but to assume the DC attitude of the gondola (the balance) remained fixed over this period of time.

In fact, it did not. The sharp decline in altitude required that in a ballast drop about 110 hours into the flight which, as luck would have it, was just after the star

[1] In addition to the sensors listed above, there was also a pointed Sun-sensor. However, it never really worked (or at least was not sufficiently well calibrated), and was only active for a few days of the flight due to a data handling error. We didn't end up using it for anything in the end.

[2] By absolute we mean both DC coupled and accurately calibrated

camera froze up. Since there were no operational sensors remaining with sufficient sensitivity to detect the $\sim 6'$ shift in the gondola balance, maps of the extra-Galactic sources generated from the data before and after the drop were used to characterize the shift which resulted from the ballast drop. The $\sim 3$ hour period during the ballast release, during which the gondola balance is shifting, are flagged and are not included in the subsequent analysis.

The FSS returns a signal indicative of (but not proportional to) the azimuth of the Sun relative to the back side of the gondola. Although the FSS proved very reliable[3], the calibration of this sensor depends in a complicated way on the Sun elevation. In practice, the FSS relies on the generation of a series of look-up tables which relate the signal to the Sun azimuth as a function of Sun elevation. The origin of the problem related to the uncertain radiative environment at float, and therefore is difficult to replicate on the ground. Therefore, the FSS relies on an in-flight calibration with the DGPS data. Unfortunately, however, the flight profile did not provide sufficient coverage of the Sun elevation-azimuth parameter space to fully calibrate the FSS to the required accuracy *outside* the CMB region. The failure of the FSS to meet the pointing requirement greatly complicates the analysis of the data covering the Galactic plane.

The integrated signals from the rate gyroscopes provide reliable and accurate ($\sim 6''$) azimuth, pitch, and roll information at frequencies from $\sim 50$ mHz to 5 Hz. However, these three sensors were neither perfectly calibrated on launch, nor completely orthogonal. During the course of the flight, the pitch and roll oscillations were both smaller in amplitude and at higher frequencies than the DGPS could measure. In one of the most stunning feats of this analysis, the calibration and decorrelation of the rate gyroscopes, in addition to the Euler angles which relate the DGPS frame to the frame of the gondola, were derived from the large amplitude pendulations which resulted from our exceedingly violent and nearly catastrophic launch.[4]

[3] What could possibly go wrong?

[4] This act of genius was by no means conceived or executed by this author, but rather by Carrie MacTavish and Brendan Crill.

### 4.1.2 Attitude reconstruction

Using the data from the absolute pointing sensors (the star camera, FSS, DGPS attitude, and DGPS velocities) we construct estimates of the gondola-guide star vector, $\hat{v}'_\star$, and the gondola-Sun vector, $\hat{v}'_\odot$, in the frame of reference of the gondola. The errors on each component are derived from the estimated sensor accuracy. For example the Sun elevation, which is not measured by any sensor, would be strongly down-weighted relative to the Sun azimuth, which is measured by the FSS. The Euler matrix, $M$, which transforms both $\hat{v}'_\star$, $\hat{v}'_\odot$ into the standard horizon (alt-az) coordinate system is found by minimizing the residual,

$$\chi^2 = \left( \hat{\sigma}_\star \, (\hat{v}_\star - M\hat{v}'_\star) \, \hat{\sigma}^\dagger_\star + \hat{\sigma}_\odot \, (\hat{v}_\odot - M\hat{v}'_\odot) \, \hat{\sigma}^\dagger_\odot \right)$$

A brute-force adaptive grid search algorithm is used to find the least squares solution, taking the trial solution from the result at the previous time domain sample. In this way we obtain an independent determination of the three-dimensional gondola attitude, parameterized by the three Euler angles entering $M$, for each sample of the ACS data. These azimuth, pitch, and roll time streams incorporate the noise properties of the absolute sensors; they are therefore very noisy at frequencies above $\sim 30$ mHz, and are riddled with gaps and spikes.

The next stage of the pointing pipeline incorporates the gyroscope data with the absolute sensor time-streams. The noise properties of the absolute sensors and gyroscopes are complementary in the frequency domain, which lends itself to analysis in the Fourier space. Before this can be done, the absolute time-streams must be despiked and made continuous. Short timescale ($< 40s$) gaps and glitches in the absolute fields are identified, flagged, and interpolated over. Long timescale gaps ($> 40s$) are flagged and filled with a noise weighted spline. The distinction between short and long is determined by the low frequency noise in the gyroscopes. At frequencies less than $\sim 25$ mHz the noise of the gyroscopes is comparable to that of the absolute sensors. The result is a well behaved and continuous time-stream which is amenable

to Fourier operations[5].

The cleaned absolute time-streams and the gyroscope data are filtered with a complementary kernel which, while preserving power at all frequencies, smoothly down-weights the absolute data at frequencies above $f_{low}$ and the gyroscope data at frequencies below $f_{high}$. The two time-streams are then added[6], providing a well behaved attitude determination at all frequencies. The values $(f_{low}, f_{high})$ used in the analysis were (0.06,0.08),(0.06,0.08), and (0.05,0.06), for the azimuth, pitch, and roll, respectively.

The initial focal plane offsets were determined from observations of compact Galactic sources (RCW38, and IRAS08576). However, the problems with the FSS calibration introduced an inconsistency between the offsets determined in the Galaxy and the centroids of the extra-Galactic sources in the CMB field. The final beam offsets were determined from (PKS)0537-441, a bright QSO at redshift $z = 0.9$.

The ACS data (with the exception of the GPS) are sampled at 10 Hz, and therefore must be interpolated to the 60 Hz bolometer sample rate. There is also a $\sim$ 300ms phase shift between the ACS data and the bolometer data, which is determined with high precision via the comparison of left and right-going Galactic point source crossings. The interpolation and phase shifting of the data is implemented in the calculation of the RA/Dec and $\psi$ time-streams. At the end of the process, we recover pointing information accurate to better than a few arcminutes for about 87% of the flight.

A complete library of astronomical pointing tools was written to allow fast calculation of RA/Dec and $\psi$ (the angle between the projection of the gondola $\hat{z}$-axis on the sky, and the local meridian in RA), from the gondola attitude, pointing offsets, and the GPS coordinates of the payload with sub-arcsecond accuracy. Extant codes either lack the required accuracy (the BOOMERANG98 code) or are prohibitively slow. The RA/Dec/$\psi$ calculation is fairly computationally intensive, taking about ten minutes per channel to process the whole flight (about as long as it takes to generate maps

[5]Now we're cooking with gas!

[6]Prior to combining the time-streams, they must be corrected for a pernicious relative phase which exists between the gyroscope data and the absolute pointing data

from the TOD). Although in principle it need only be calculated once, in practice the entire pipeline is run many times while iterating on a solution. Therefore, during the de-bugging process (which can last for years) fast turnaround is a necessity.

## 4.2 Signal processing

Relative to the the pointing data, the bolometer time streams are very well behaved. The primary (undesirable) features of the bolometer TOD, in order of increasing difficulty, are calibration lamp pulses, elevation changes, cosmic ray hits, and gyroscope-correlated vibrational signals. The raw bolometer signals must be deglitched, deconvolved, despiked, gap-filled, and corrected for responsivity drifts, roughly in that order. In this section we describe this process.

Hopelessly contaminated segments of the time-stream are flagged and gap-filled, a process which involves replacing the missing data with values that are both continuous and statistically consistent with the surrounding data. We use a constrained realization of the power spectrum of the neighboring time-stream for this purpose [170, 140].

As usual, the first step of the bolometer cleaning pipeline involves making the data suitable for the application of FFTs.[7] This requires flagging and gap-filling the data during the periods that the analog to digital converter is saturated.

Approximately 19.2% of the raw data are flagged based on the noise, the bulk of which occurs during the first day of the flight while the pendulations are large and the system temperatures are equilibrating. Also included in this figure are the data taken during the bias checks, and the fridge cycle toward the end of the flight. An additional 1.5% of the data are flagged in the vicinity of elevation changes, and 0.5% of the data are flagged from cosmic ray hits which rail the A/D converter.

Once these glitches are removed, the system transfer functions are deconvolved for each channel. It is preferable to deconvolve the transfer functions from the TOD *prior* to the removal of cosmic ray hits and the calibration lamp pulses in order to

[7] I am deeply indebted to Frigo and Johnson, who have provided the scientific community with FFTW, a beautifully executed package for the efficient calculation of discrete Fourier transforms [46].

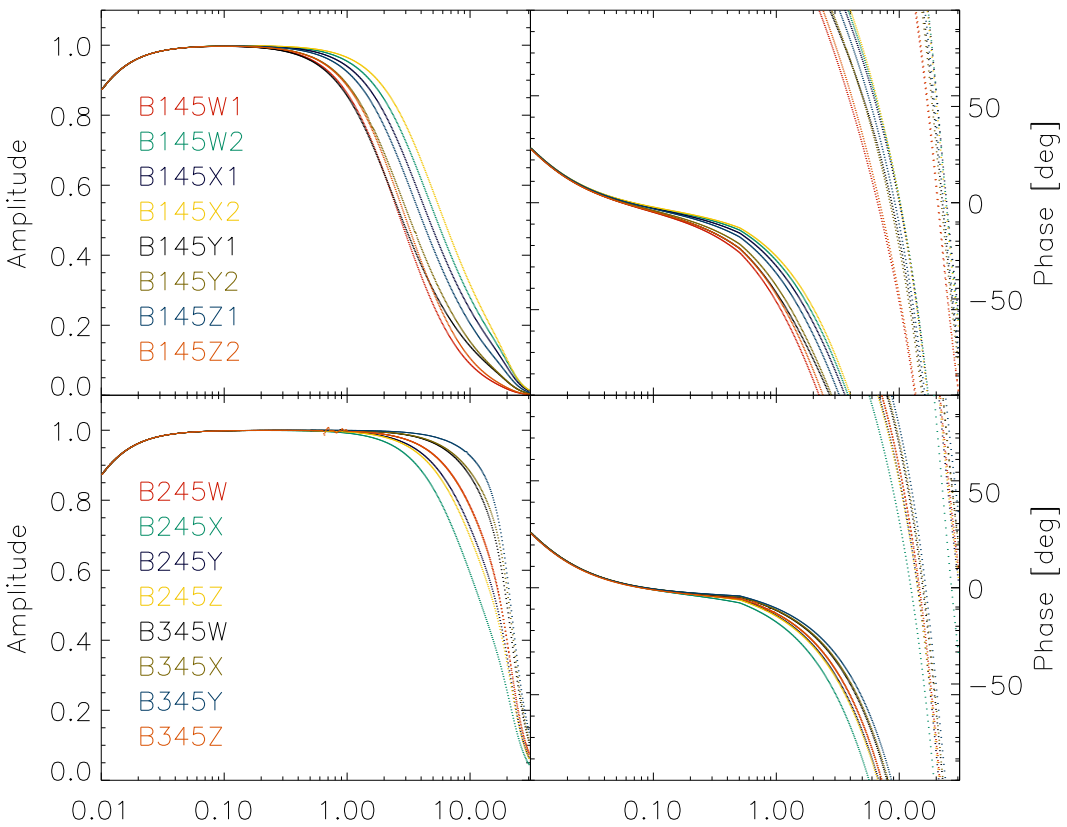


Figure 4.1: The measured system transfer functions for the PSBs (upper panels) and Photometers (lower panels). Both the amplitude and phase are displayed as a function of the the signal frequency [Hertz]. Above 100 mHz, the transfer functions are dominated by the bolometer response, which varies from channel-to-channel due to variations in thermal conductivity.

decorrelate the adjacent time stream. The transfer functions, shown in Figure 4.1, are deconvolved in the Fourier domain. In order to minimize the impact of edge-effects, the deconvolution of each channel is performed in a single operation over the entire time-stream.[8]

After completing the deconvolution, the calibration lamp pulses are flagged and a copy of the data are low-pass filtered and despiked using a three-point template in order to identify cosmic-ray hits. An iterative map-based despiking routine is used to aid in the despiking of the data near the Galactic plane. The deconvolved TODs are then flagged and gap-filled.

[8]The operation takes approximately 15 minutes and requires $\sim 2$ GB of RAM.

Of the 257 hours that were spent in observations of the CMB region, 195 hours (75.9%) survived the cuts based on pointing considerations. Of that data, and additional 6% of the data are flagged due to pointing, 6% are contaminated by cosmic ray hits, and 1.3% are cut due calibration lamp pulses. After all the cuts, the total observing efficiency is 66.2%, with the bulk of the cuts a result of pointing related problems.

A gyro-correlated signal is observed in the bolometer time-streams. The origin of this signal is likely a result of the modulation of the spillover of the beam between the 4K and 77K stages due to mechanical vibrations. The signal is small - approximately the same amplitude as the white noise level - but significant nonetheless. The gyro data are fit to the amplitude and phase of the $\sim$ 500 mHz signal, which is then regressed from the time ordered data. After the data are deconvolved and cleaned, the corrections for the calibration drift, as illustrated in Figure 3.5, are applied to the time-streams.

# Chapter 5

# Science Analysis

> "God does not care about our mathematical difficulties. He integrates empirically."
>
> –Albert Einstein, 1942.

While the ultimate goal of CMB experiments is to estimate the underlying power spectrum of the fluctuations in temperature and polarization of the primordial radiation, the direct observable available to us is a particular realization of that Gaussian random process, together with possible contributions from intervening structure. For single dish experiments in particular, the fundamental (that is, model independent) observable is a polarized map of temperature fluctuations projected on the sphere. We therefore begin our discussion of the science analysis with an introduction to the problem of making maps from time ordered data, and the related issue of noise estimation. Finally, we briefly address the approach to power spectrum estimation in Section 5.2.

## 5.1 An Introduction to map-making

If a receiver is operating in the linear regime then the time domain signal, $\mathbf{d}$, can be modeled as a linear function of the sky signal, $\mathbf{m}$,

$$\mathbf{d} = \mathbf{A}\mathbf{m} + \mathbf{n}$$

where in the most simple case the elements $m_p$ represent the sky signal in pixel $p$, the $A_{ip}$ are the elements of the (very sparse) matrix which maps pixels to time samples, and $n_i$ is the noise in sample $d_i$. By generalizing the definition of the matrix $\mathbf{A}$ and the vector $\mathbf{m}$, this description of the data can be extended to include any effect which is coupled linearly to the time stream. Examples of such generalizations include 1) treatment of the instrumental beam or 2) systematic effects such as the susceptibility of the COBE DMR instrument's ferrite switches to the Earth's magnetic field [172].

In the limit that the instrumental noise time stream, $\mathbf{n}$, is well described by Gaussian white noise, the optimal map is obtained by averaging all time samples $d_i$ falling in a pixel $p$. The resultant map is "optimal" in the sense that all the information in the time stream regarding the sky temperature is preserved in the estimate of the map, $\widetilde{\mathbf{m}}$. One may express this simple map-making procedure in matrix notation as,

$$\widetilde{\mathbf{m}} = (\mathbf{A}^T\mathbf{A})^{-1}\mathbf{A}^T\mathbf{d} \tag{5.1}$$

The operator $\mathbf{A}^T\mathbf{d}$ sums all TOD samples falling in a given pixel, while $(\mathbf{A}^T\mathbf{A})^{-1}$ simply divides the sum by the number of hits per pixel.

If the noise power spectrum is not white, the procedure for simple averaging results in a loss of information due to the uniform weighting of the data. The more general problem of lossless map-making in the presence of noise has been discussed extensively in the literature [76, 158, 75, 42, 17, 141, 125, 38]. The topics relevant to the BOOMERANG analysis are summarized in what follows.

## Mapffmaking in the presence of noise

The general method of making a map, $\widetilde{\mathbf{m}}$, from time ordered data $\mathbf{d}$ can be viewed as a linear problem in the data,

$$\widetilde{\mathbf{m}} = \mathbf{W}\mathbf{d}$$

Where the simple co-addition procedure described above uses $\mathbf{W}_c = (\mathbf{A}^T\mathbf{A})^{-1}\mathbf{A}^T$. A more general $\mathbf{W}_{ml}$ would be that which results in the maximum likelihood estimate

of $\widetilde{\mathbf{m}}$ in the presence of noise with non-trivial statistical properties. If the noise is Gaussian, this means that the solution, $\widetilde{\mathbf{m}} = \mathbf{W}_{ml}\ \mathbf{d}$, is that which maximizes the probability of the data given the noise.

$$P(\mathbf{d}|\mathbf{n}) \propto \mathcal{L}(\widetilde{\mathbf{m}}) = e^{-\frac{1}{2}\chi^2} \tag{5.2}$$

where,

$$\chi^2 \equiv (\mathbf{d} - \mathbf{A}\widetilde{\mathbf{m}})^T\ \mathbf{N}^{-1}\ (\mathbf{d} - \mathbf{A}\widetilde{\mathbf{m}}) \tag{5.3}$$

where $\mathbf{N}$ is the time domain noise covariance matrix of the noise time stream $\mathbf{n}$. The noise covariance matrix $\mathbf{N}$ is defined by

$$N_{tt'} \equiv \frac{1}{N}\sum_{i}^{N}(n_{i+t} - \langle\mathbf{n}\rangle)(n_{i+t'} - \langle\mathbf{n}\rangle)$$

Clearly $\mathbf{N}$ is a symmetric matrix whose diagonal elements are the variance of the noise time stream. It is usually the case that the noise has zero mean, so that $\langle\mathbf{n}\rangle = 0$. If the time domain covariance matrix is diagonal, then the noise is said to be white. If $\mathbf{N}$ depends only on the lag $\delta = (t - t')$ and not on the location in the time stream, $t$, the noise is said to be stationary. In the literature, such a matrix is called circulant or Toeplitz.

Noise stationarity implies that the statistical properties of the noise time stream are well described by a single noise power spectrum, $\widetilde{N}(f)$.[1] Under these assumptions the noise covariance matrix is simply the Fourier transform of the power spectrum,

$$N_{tt'} = \frac{1}{2\pi}\int d\omega \widetilde{N}(f)\ e^{-i\omega(t-t')}$$

The solution, $\widetilde{\mathbf{m}}$, which minimizes Equation 5.3 is determined by the system of equations,

$$\frac{\partial\chi^2}{\partial\mathbf{m}} = -2\ \mathbf{A}^T\mathbf{N}^{-1}(\mathbf{d} - \mathbf{A}\mathbf{m}). \tag{5.4}$$

[1]The following discussion assumes that non-Gaussian artifacts in the time stream have been removed, flagged, and filled with accurate signal and noise realizations during the low level analysis.

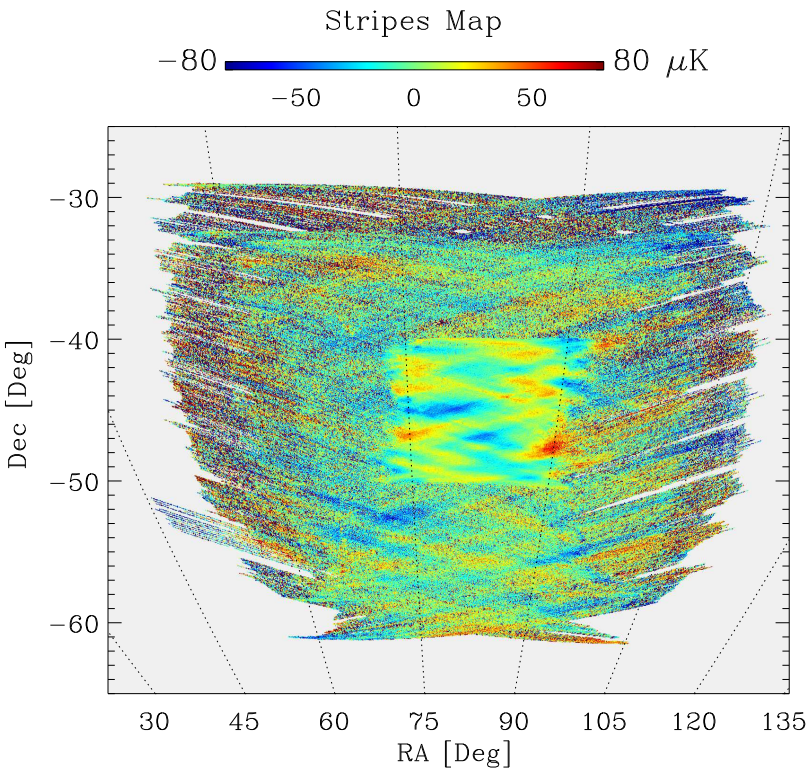


Figure 5.1: The difference between the naively co-added map (Equation 5.1) and the converged least squares solution (Equation 5.5), for the B2K data. The converged map has properly accounted for the time domain correlations in the noise, resulting in an improved recovery of the large angular scale modes in the map.

Setting the derivative to zero gives the general least squares solution,

$$\widetilde{\mathbf{m}} = (\mathbf{A}^T\mathbf{N}^{-1}\mathbf{A})^{-1}\ \mathbf{A}^T\mathbf{N}^{-1}\mathbf{d} \tag{5.5}$$

In the CMB literature, the quantity $\mathbf{C}_N \equiv (\mathbf{A}^T\mathbf{N}^{-1}\mathbf{A})^{-1}$ is referred to as the "pixel-pixel" noise covariance matrix. The $\mathrm{C}_N$ is of particular importance due to its role in the accurate estimation of the power spectrum of the underlying signal and, for extended duration experiments, the sheer numerical difficulty of its calculation.

The solution of Equation 5.5 has the attractive (and perhaps obvious) property that the error on the estimate of the signal is independent of the signal. One can show this by writing down the difference between the maximum likelihood estimate, $\widetilde{\mathbf{m}}$, and

the pure signal as observed by the experiment, $\mathbf{m}' = (\mathbf{A}^T\mathbf{N}^{-1}\mathbf{A})^{-1}\ \mathbf{A}^T\mathbf{N}^{-1}\mathbf{A}\ \mathbf{m}$, as

$$\begin{aligned}
\widetilde{\mathbf{m}} - \mathbf{m}' &= (\mathbf{A}^T\mathbf{N}^{-1}\mathbf{A})^{-1}\ \mathbf{A}^T\mathbf{N}^{-1}\ \mathbf{d} - \mathbf{m}' \\
&= \mathbf{W}_{ml}(\mathbf{s}+\mathbf{n}) - \mathbf{m}' \\
&= \mathbf{W}_{ml}(\mathbf{A}\mathbf{m}+\mathbf{n}) - \mathbf{m}' \\
&= \widetilde{\mathbf{n}}
\end{aligned}$$

where $\widetilde{\mathbf{n}} \equiv \mathbf{W}_{ml}\ \mathbf{n}$ is the noise-only map, containing no information about the sky.

Another common approach to signal estimation which does *not* satisfy the above criteria is to maximize the probability of the data given both the noise and an assumption about the statistical properties of the signal. The statistics of the signal, $\mathbf{S}$, are inserted as a prior into Equation 5.2. The linear operation which maximizes this posterior probability is called the Wiener filter, and can be shown to be given by [170]

$$\mathbf{W} = \left(\mathbf{S}^{-1} + \mathbf{A}^T\mathbf{N}^{-1}\mathbf{A}\right)^{-1}\ \mathbf{A}^T\mathbf{N}^{-1}.$$

This approach is of use when trying to discriminate, say, a CMB signal from foreground contamination, assuming you know the spectrum of both. However, when estimating power spectra it is hardly appropriate to assume one as a prior. We limit the remainder of this discussion to the application of the least squares method.

In practice, solving Equation 5.5 is non-trivial, even if one has *a priori* knowledge of the noise correlation matrix $\mathbf{N}$. There are two approaches to this solution. While an iterative solution for the maximum likelihood map is quickly and easily achieved, one needs the pixel-pixel noise correlation matrix to compute the maximum likelihood power spectrum. A brute force calculation and inversion of the $N_p \times N_p$ pixel-pixel noise correlation matrix on a dataset the size of B2K's is computationally challenging even with modern supercomputers. For B2K the number of time domain samples approaches $N_d \sim 10^9$, while the number of pixels is typically $N_p \sim 5 \cdot 10^5$. Of course, the scale of the problem is far worse for satellite missions covering the whole sky at comparable resolution. For these datasets, the brute force approach is likely to

remain intractable for some time.

The importance of the iterative method is underscored by the necessity of estimating the noise properties of the experiment from the data. All analyses, including the brute force method, require a simultaneous solution for the signal and noise. Before moving on to the treatment of polarized data, we briefly discuss the iterative solution to large matrix equations.

The fidelity of the power spectrum estimation is fundamentally limited by the accuracy achieved in the measurement of the noise properties of the instrument. Until now we have assumed that one has perfect knowledge of the statistical properties of the instrumental noise. However, noise estimation is one of the most fundamental experimental challenges in the study of the CMB , and is a topic which will be discussed at length in the following section.

### 5.1.1 Signal estimation

For most ground based telescopes, the time stream is dominated by noise, so that a good approximation to the noise covariance matrix appearing in Equation 5.5 is the covariance of the raw data itself. For orbital and sub-orbital CMB experiments like BOOMERANG, the time ordered data are not completely noise dominated, greatly complicating an accurate determination of the noise. In general, an in-situ estimation of the noise is required due to the influence of atmospheric emission, unpredictable backgrounds, and scan-synchronous effects. As a result, the simultaneous estimation of both the signal and noise is required.

An iterative solution for both $\mathbf{N}$ and $\widetilde{\mathbf{m}}$ is possible by using an adaptation of the Jacobi method. The Jacobi method is an iterative approach to the solution of a general linear system of equations, such as Equation 5.5, which does not require the inversion of large matrices. The application to the solution of Equation 5.5 is derived in Appendix C.2. This algorithm is naturally suited to the problem of noise estimation, as the signal subtraction is an integral part of the iterative procedure.

By iterating on the noise covariance matrix, $\mathbf{N}$, as well as the signal $\widetilde{\mathbf{m}}$, one ap-

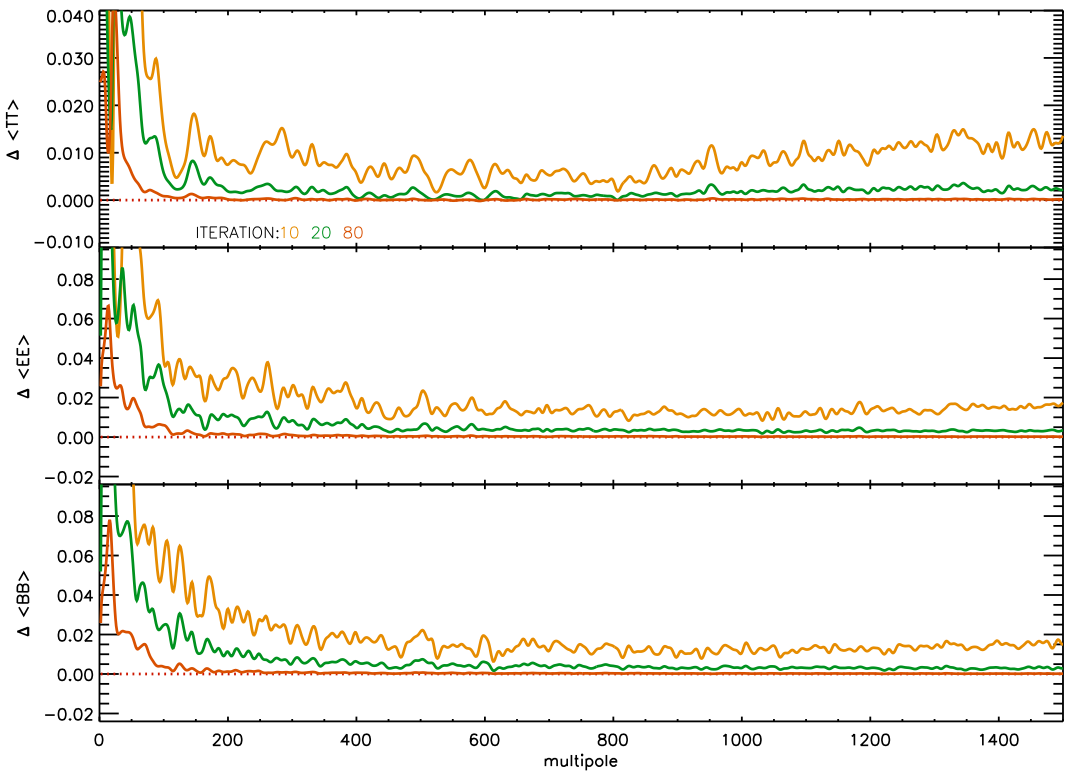


Figure 5.2: The *fractional change* in the cut-sky angular power spectrum (pseudo-$C_\ell$) from iteration to iteration of the map-maker. The largest scales take the longest to converge, and polarization takes longer to converge than does temperature.

proaches a general least squares solution for both. This procedure has been used in the noise estimation of previous experiments which probed the CMB temperature anisotropies[172, 141]. In this application, the procedure has been successfully extended to a polarized dataset.

As described in Appendix C.2, each subsequent iteration on the solution to Equation 5.5, $\widetilde{\mathbf{m}}_{k+1}$, is calculated from the previous solution according to the procedure,

$$\widetilde{\mathbf{m}}_{k+1} = \widetilde{\mathbf{m}}_k + \delta\widetilde{\mathbf{m}}_{k+1}$$

where,

$$\delta\widetilde{\mathbf{m}}_{k+1} \equiv \ \alpha \ \cdot \ \mathrm{diag}(\mathbf{A}^T\mathbf{N}_k^{-1}\mathbf{A})^{-1}\mathbf{A}^T\mathbf{N}_k^{-1}(\mathbf{d} - \mathbf{A}\ \widetilde{\mathbf{m}}_k).$$

and the relaxation parameter, $\alpha \lesssim 1$, is tuned to optimize the speed of convergence.

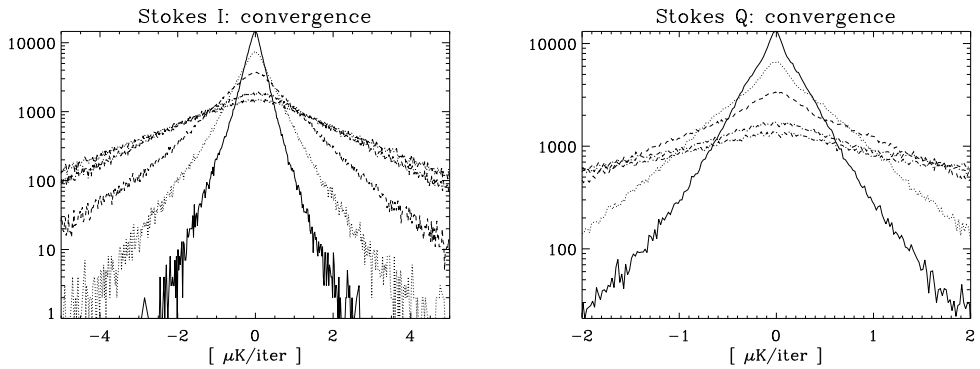


Figure 5.3: The convergence criteria for the iterative procedure is determined by a threshold on the *rms* amplitude of the correction. Histograms of the corrections to the I and Q maps (change in pixel value between subsequent iterations) are shown for 5, 10, 20, 40 and 80 iterations.

Recall that, in the case of polarized data, the quantity $\mathbf{d}$ represents the left hand side of Equation 5.12. Therefore, the calculation of the matrix $\mathrm{diag}(\mathbf{A}^T\mathbf{N}_k^{-1}\mathbf{A})^{-1}$ involves the inversion of the polarization decorrelation matrix on the right hand side of Equation 5.12. The great advantage of this method is that the convolution of the data with the inverse noise correlation matrix,

$$\mathbf{n}_{k+1} \equiv \mathbf{N}_k^{-1}(\mathbf{d} - \mathbf{A}\ \mathbf{m}_k)$$

can be efficiently calculated in the Fourier domain, without needing to invert the time domain correlation matrix, $\mathbf{N}$.

$$\mathbf{n}_{k+1} = \mathrm{FFT}^{-1}\left(\widetilde{N}_k^{-1}(f) \cdot \mathrm{FFT}(\mathbf{d} - \mathbf{A}\ \mathbf{m}_k)\right) \tag{5.6}$$

where the estimate of the noise power spectrum is taken from the previous signal estimate,

$$\widetilde{N}_{k+1}(f) = \mathrm{PSD}(\mathbf{d} - \mathbf{A}\ \mathbf{m}_k).$$

Clearly, this operation is simply the application of a Fourier filter to the noise-only time stream, using the inverse of the noise power spectrum as a kernel. Therefore, a single iteration of the process scales as $N_d \log(N_d)$, which is as fast as the calculation

of a filtered and naively co-added map.

### 5.1.2 Polarization formalisms

To extend the the map-making procedure described above to polarized data, it is first necessary to describe the correspondence between the incident polarized radiation and the detected signal. The two most commonly used conventions for handling polarized radiation are the Jones and the Stokes/Mueller formalisms. In the former, optical components are modeled with matrix operations on the (complex) electric field vectors, while the latter convention involves matrix operations on the Stokes vectors [124, 54, 79, 80, 81, 62].

The primary difference between the two approaches is that the Stokes/Mueller formalism manipulates irradiances, and therefore is applicable only to incoherent radiation. The Jones formalism works directly with the field amplitudes, making it the appropriate approach for coherent analysis. While the Jones formalism is rather intuitive, the Stokes formalism is more naturally suited to CMB analysis. In the following we introduce both approaches at an elementary level, and describe the correspondence between the two.

The general action of linear optical elements can be described in terms of the relationship between the input and output electric field vectors. The Jones matrix of an optical element is defined in terms of its action on the incident fields,

$$\mathbf{e}_f = \mathbf{J}\ \mathbf{e}_i$$

Where the Jones matrix, $\mathbf{J}$, of the system is a general product of the matrices describing individual components in the system.

$$\begin{pmatrix} E_x \\ E_y \end{pmatrix}_f = \begin{bmatrix} J_{xx} & J_{xy} \\ J_{yx} & J_{yy} \end{bmatrix}_0 \cdots \begin{bmatrix} J_{xx} & J_{xy} \\ J_{yx} & J_{yy} \end{bmatrix}_n \begin{pmatrix} E_x \\ E_y \end{pmatrix}_i$$

Of course, all such components may be rotated with respect to one another with the

usual rotation matrices,

$$\mathbf{J'} = \mathbf{R}\ \mathbf{J}\ \mathbf{R}^T$$

with

$$R \equiv \begin{pmatrix} \cos\psi & -\sin\psi \\ \sin\psi & \cos\psi \end{pmatrix}$$

This formalism allows a fairly complicated optical system to be described by a single matrix which need only be derived once from the constituent components.

As an example we describe an imperfect polarizer oriented at an angle $\psi$ with respect to the basis in which the fields are defined. Such an object may be represented by the Jones matrix

$$\begin{aligned} \mathrm{J}_p &\equiv \mathbf{R} \begin{bmatrix} \eta & 0 \\ 0 & \delta \end{bmatrix} \mathbf{R}^T \\ &= \begin{bmatrix} \eta\cos^2\psi + \delta\sin^2\psi & (\eta-\delta)\cos\psi\sin\psi \\ (\eta-\delta)\cos\psi\sin\psi & \eta\sin^2\psi + \delta\cos^2\psi \end{bmatrix} \end{aligned}$$

Where $\eta > \delta$. A perfect polarizer would have $\eta = 1$ and $\delta = 0$. After generous application of trigonometric identities, one recovers the general Jones matrix

$$\mathrm{J}_p = \frac{1}{2} \begin{bmatrix} (\eta+\delta) + (\eta-\delta)\cos 2\psi & (\eta-\delta)\sin 2\psi \\ (\eta-\delta)\sin 2\psi & (\eta+\delta) - (\eta-\delta)\cos 2\psi \end{bmatrix} \tag{5.7}$$

Each detector in polarization sensitive bolometer pair acts as just such a partial polarizer, followed by a total power detector.

The Stokes parameters are defined in terms of the electric field as follows,

$$\begin{aligned} \mathbf{I} &\equiv \langle E_x E_x^* + E_y E_y^* \rangle &&= \langle |E_x|^2 \rangle + \langle |E_y|^2 \rangle \\ \mathbf{Q} &\equiv \langle E_x E_x^* - E_y E_y^* \rangle &&= \langle |E_x|^2 \rangle - \langle |E_y|^2 \rangle \\ \mathbf{U} &\equiv \langle E_x E_y^* + E_y E_x^* \rangle &&= 2\,\langle |E_x E_y| \cos(\phi_x - \phi_y) \rangle \\ \mathbf{V} &\equiv i\langle E_x E_y^* - E_y E_x^* \rangle &&= 2\,\langle |E_x E_y| \sin(\phi_x - \phi_y) \rangle \end{aligned}$$

where the brackets, $\langle\ \rangle$, represent a time average and the fields are specified in a coordinate system fixed with respect to the instrument. For Thomson scattering of

electrons in a quadrupolar radiation field there is no mechanism for the introduction of a relative phase between the two polarizations. Therefore, the cosmological Stokes **V** parameter is presumed to be zero.

The action of linear optical elements on a Stokes vector,**s**, can be described in terms of the elements' Mueller matrix,

$$\mathbf{s}_f = \mathbf{M}\ \mathbf{s}_i.$$

Given the definition of the Stokes parameters, one can derive the relationship between a Jones matrix, and the corresponding Mueller matrix. Following Born and Wolf we find [16]

$$M_{ij} = \frac{1}{2}\mathrm{tr}\left(\sigma_{\mathbf{i}}\mathbf{J}\sigma_{\mathbf{j}}\mathbf{J}^{\dagger}\right) \tag{5.8}$$

where the $\sigma_i$ are the usual pauli matrices

$$\begin{aligned} \sigma_{\mathbf{I}} = \sigma_0 \equiv \begin{pmatrix} 1 & 0 \\ 0 & 1 \end{pmatrix} \quad \sigma_{\mathbf{Q}} = \sigma_3 \equiv \begin{pmatrix} 1 & 0 \\ 0 & -1 \end{pmatrix} \\ \sigma_{\mathbf{U}} = \sigma_1 \equiv \begin{pmatrix} 0 & 1 \\ 1 & 0 \end{pmatrix} \quad \sigma_{\mathbf{V}} = \sigma_2 \equiv \begin{pmatrix} 0 & -i \\ i & 0 \end{pmatrix} \end{aligned} \tag{5.9}$$

Applying a moderate amount of algebra to Equations 5.8 and 5.7, we find the first row of the Mueller matrix $\mathbf{M}_p$ for a partial polarizer. This defines the total power detected as a function of the incident **I**, **Q**, **U**, and **V** parameters

$$\begin{aligned} M_{II} &= \frac{1}{2}\left(\eta^2 + \delta^2\right) \\ M_{IQ} &= \frac{1}{2}\left(\eta^2 - \delta^2\right)\ \cos 2\psi \\ M_{IU} &= \frac{1}{2}\left(\eta^2 - \delta^2\right)\ \sin 2\psi \\ M_{IV} &= 0 \end{aligned}$$

The signal from a total power detector is proportional to the Stokes **I** parameter

of the incident radiation. Modeling a polarization sensitive bolometer as a partial polarizer followed by a total power detector, we find (ignoring, for the moment, the effects of finite beam size and frequency passband) the data can be expressed,

$$d_i = \frac{s}{2}\left[(1+\epsilon)\cdot\mathbf{I} + (1-\epsilon)\cdot(\mathbf{Q}\cos(2\psi_i) + \mathbf{U}\sin(2\psi_i))\right] + n_i \tag{5.10}$$

where we have defined the polarization leakage term, $\epsilon$, such that $(1-\epsilon)$ is the polarization efficiency[2], $\psi$ is the orientation of the axis of sensitivity of the PSB, and $s$ is the voltage responsivity of the detector. The term $n$ is the noise contribution to the time ordered sample. For BOOMERANG, the value of the cross polar leakage is typically $\sim 5\%$, and less than 3% for second generation devices designed for the *Planck* HFI , BICEP, and QUAD. We now return to the problem of making maps from time ordered data, now including a full treatment of the polarization.

### 5.1.3 Polarized beams

The angular response of an instrument can be characterized by co-polar and cross-polar power response functions $P_{\|}(r,\theta,\phi)$ and $P_{\perp}(r,\theta,\phi)$. In the time reversed sense these can be thought of as the normalized power at any point in space resulting from a linearly polarized excitation produced by the feed element in the focal plane. That is, for a given polarization $p = (\|, \perp)$,

$$P_p(r,\theta,\phi) \equiv \frac{|E_p(r,\theta,\phi)|^2}{|E_{\|}(r,0,0)|^2}.$$

For a single moded system, $P_p$ has absolutely nothing to do with the detector – it only depends on the feed and optical elements of the system. The polarized beam patterns can be considered separately from the detector due to the single-moded segment of waveguide at the throat of the feed-horn.

The exact definitions used for the polarizations on the sphere $p = (\|, \perp)$ vary in

[2]That is, in terms of the elements of the Jones matrix for an imperfect polarizer, the leakage $\epsilon \equiv \delta^2/\eta^2$. This is the ratio between the minimum and peak power response to a pure linearly polarized source, which is a directly observable property of the PSB.

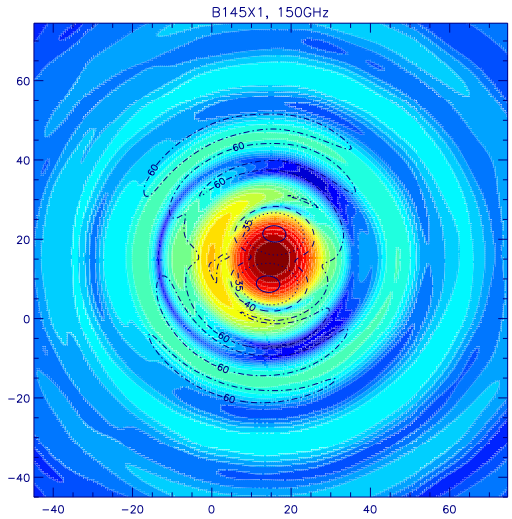


Figure 5.4: One of BOOMERANG's full beam patterns. The contours of the cross-polar beam pattern, $P_{\perp}(\theta, \phi)$, are overlaid on the co-polar beam, $P_{||}(\theta, \phi)$. The elevation axis is increasing to the right.

the literature, but the standard is Ludwig's Third definition [109]. In any case, for small angles away from the beam centroid, they are very nearly equal to the Cartesian definition.

Qualitatively, $P_{||}$ is similar to an Airy pattern; a Gaussian near the beam centroid, with a series of side-lobes. $P_{\perp}$ is zero on axis for most optical systems and, for on-axis systems, is also zero along the E and H planes. The peak of cross-polar the distribution is typically at the half power point of the co-polar beam, and the peak amplitude relative to the co-polar beam is fundamentally related to the *asymmetry* of the co-polar beam, as in Figure 5.4. For an azimuthally symmetric system, such as a feed horn antenna, this produces lobes in the 45° plane in all four quadrants of the beam. For an off-axis reflector such as the BOOMERANG telescope, the azimuthal symmetry is lost and the lobes are bimodal. It is worth noting that the polarized beams generally depend on frequency as well as on the field distance $r$, and angular position.

A PSB detects the convolution of the polarized sky with the polarized beam, integrated over the frequency bandpass, and subject to the polarization efficiency of

the detector.[3] In the flat sky approximation, the general expression for the signal from a single bolometer in a PSB pair is,

$$\begin{aligned} d_i(\hat{x}) &= \frac{s'}{2}\int d\nu \frac{\lambda^2}{\Omega_b} F_\nu \int d\Omega \\ &\quad \Big[ P_\parallel(\nu,\hat{x})\Big((1+\epsilon)\ \mathbf{I}(\nu,\hat{x}) + (1-\epsilon)(\mathbf{Q}(\nu,\hat{x})c_i\ +\ \mathbf{U}(\nu,\hat{x})s_i)\Big) \\ &\quad + P_\perp(\nu,\hat{x})\Big((1+\epsilon)\ \mathbf{I}(\nu,\hat{x}) - (1-\epsilon)(\mathbf{Q}(\nu,\hat{x})c_i\ +\ \mathbf{U}(\nu,\hat{x})s_i)\Big)\Big] + n_i \end{aligned}$$

where we have abbreviated the trigonometric functions and define the beam solid angle $\Omega_b = \int d\Omega\ (P_\parallel + P_\perp)$. Rearranging and dropping both the explicit spatial and frequency dependencies, the relation can be written more intuitively,

$$d_i \simeq \frac{s}{2}\int d\nu\ \lambda^2\ F_\nu \int d\Omega\ [\ \mathbf{I} +\ \gamma\ \mathcal{P}\ (\ \mathbf{Q}c_i +\ \mathbf{U}s_i)] + n_i \tag{5.11}$$

where we have defined the parameters,

$$\gamma = \frac{(1-\epsilon)}{(1+\epsilon)}$$

and,

$$\mathcal{P} = \frac{(P_\parallel - P_\perp)}{(P_\parallel + P_\perp)}$$

and we have used the approximation, which is exact in the flat sky approximation, that the cross polar beam, $P_\perp$, is sensitive to the Stokes parameters *rotated* by $\pi/2$ on the sky

We have also made the simplifying assumption that we may remove the beam and polarization efficiencies from the integral over the sky, and then absorb the beam and polarization efficiency pre-factors into a re-definition of the calibration constant,

[3] This treatment is actually more general; it holds for any receiver which can be characterized as a total power detector preceded by an imperfect polarizer. That is, any receiver which is well described by a Jones matrix of the type,

$$J_p = \begin{bmatrix} \eta & 0 \\ 0 & \delta \end{bmatrix}.$$

In the discussion that follows, keep in mind that $\epsilon \equiv \frac{\delta^2}{\eta^2}$.

$s = s' \int d\nu \ (1 + \epsilon)$.

We now extend the map-making discussion of the previous section to polarized data. In what follows, we do not explicitly treat the details of the beam, and instead keep in mind that the observed stokes parameters represent the convolution of the sky signal with the beam.

### 5.1.4 Polarized mapffmaking

Estimates of the **I**, **Q**, and **U** parameters can be recovered by generating orthogonal linear combinations of the data. For a given sample, $i$, from a single detector and a measurement of the projection of the orientation of that detector on the sky, $\psi_i$, one can construct the polarization decorrelation matrix defined by,

$$\begin{pmatrix} d_i \\ d_i\gamma_j c_i \\ d_i\gamma_j s_i \end{pmatrix} = \begin{pmatrix} 1 & \gamma_j c_i & \gamma_j s_i \\ \gamma_j c_i & \gamma_j^2 c_i^2 & \gamma_j^2 s_i c_i \\ \gamma_j s_i & \gamma_j^2 c_i s_i & \gamma_j^2 s_i^2 \end{pmatrix} \begin{pmatrix} \mathbf{I} \\ \mathbf{Q} \\ \mathbf{U} \end{pmatrix} \tag{5.12}$$

where $\gamma \equiv \frac{(1-\epsilon)}{(1+\epsilon)}$, is a parameterization of the polarization efficiency, and for simplicity we have abbreviated the trigonometric functions, whose argument is $2\psi_i$.

In the limit that the instrumental noise time stream, **n**, is stationary, Gaussian, and is well characterized by a white frequency spectrum, the optimal map is obtained by summing all time samples $d_i$ and decorrelation matrix elements falling in a pixel $p$. Assuming that the scan strategy, instrument, or channel combination provides modulation of the angle $\psi$, the matrix is non-singular and the best estimates for **I**, **Q**, and **U** are then obtained by inverting the co-added (3x3) decorrelation matrix at each pixel. This is the polarized analog to a naively co-added temperature map.

The situation becomes markedly more difficult in the presence of noise with non-trivial statistics. The solution which is optimal in the least squares sense is again given by Equation 5.5, with the understanding that now the data consist of the linear combinations defined by Equation 5.12.

We now find ourselves in the uncomfortable position of having to solve Equation

5.5 for polarized data, in the presence of noise with unknown statistical properties, using channels of varying sensitivity and polarization efficiency. In this general case, the data are treated in the following way; Estimates of the left hand side of the *noise only* version Equation 5.12 and the Stokes' decorrelation matrix are generated for each pixel,

$$\hat{n}_p = \sum_j^{\mathrm{NCH}} w_j \sum_{i \in p} \begin{pmatrix} n_i \\ n_i\ \gamma_j\ c_i \\ n_i\ \gamma_j\ s_i \end{pmatrix} \tag{5.13}$$

where the $n_i$ are the elements of $\mathbf{n}$ appearing in Equation 5.6. Likewise, for the decorrelation matrix we calculate

$$\hat{M}_p = \sum_j^{\mathrm{NCH}} w_j \sum_{i \in p} \begin{pmatrix} 1 & \gamma_j c_i & \gamma_j s_i \\ - & \gamma_j^2 c_i^2 & \gamma_j^2 c_i s_i \\ - & - & \gamma_j^2 s_i^2 \end{pmatrix} \tag{5.14}$$

One then obtains an estimate of the *corrections* to the Stokes parameters **I**,**Q**, and **U** maps for an iteration $k$, by inverting $\hat{M}$ at each pixel,

$$\mathbf{S}_{k+1} - \mathbf{S}_k = \hat{\mathbf{M}}_k^{-1} \hat{\mathbf{n}}_k \tag{5.15}$$

allowing one to iteratively obtain a solution for the maximum likelihood maps of each Stokes parameter.

The CMB dipole produces a $\sim$ 1.5mK gradient (increasing with increasing right ascension) across BOOMERANG's field. This signal, which for BOOMERANG appears as a triangle wave at the scan period (see Figure 3.6), is subtracted directly from the time streams using the WMAP measurement of the dipole amplitude and direction.[4]

[4]WMAP measures the CMB dipole to be $\simeq$ 370m/s toward RA,Dec (J2000) [167.845,-6.883], which is a slightly more precise determination than that provided by COBE [90].

### 5.1.5 Direct differences

A less general approach can be useful when either the cross-linking or the modulation of the polarization angles is not sufficient to constrain the entries in Equation 5.14. This approach operates on the sum and difference of the signals from a PSB pair instead of on the individual time streams. This has the numerical advantage of isolating the temperature and polarization terms from the numerical inversion of Equation 5.14 which, in signal-only simulations, is found to be useful where the pixel cross-linking is limited and where the decorrelation matrix is poorly conditioned. Differencing the signals has the additional advantage of removing common mode atmospheric or scan synchronous signals which might remain in the time domain data.

These benefits are obtained at the cost of sub-optimal noise weighting of the channels within a pair. The two approaches represent a tradeoff between optimal treatment of statistical and systematic errors.

We may represent a sample, $i$, of a single detector as the linear combination of the sort,

$$s_i = \mathbf{I} + \gamma_i \left( \mathbf{Q} \cos(2\psi_i) + \mathbf{U} \sin(2\psi_i) \right)$$

Assuming that we have properly calibrated the two channels, the sum and difference of the signals (as, say, from a PSB pair) may be written as,

$$^{+}s_i \equiv \frac{1}{2}(s_1 + s_2)_i = \mathbf{I} + \frac{1}{2}(^{+}\alpha_i \mathbf{Q} + {}^{+}\beta_i \mathbf{U})$$

$$^{-}s_i \equiv \frac{1}{2}(s_1 - s_2)_i = \frac{1}{2}(^{-}\alpha_i \mathbf{Q} + {}^{-}\beta_i \mathbf{U})$$

where we have defined the angular coefficients

$$\begin{aligned} ^{\pm}\alpha_i &= \gamma_1 \cos(2\psi_{1i}) \pm \gamma_2 \cos(2\psi_{2i}) \\ ^{\pm}\beta_i &= \gamma_1 \sin(2\psi_{1i}) \pm \gamma_2 \sin(2\psi_{2i}) \end{aligned}$$

in terms of the independent variables, $\psi_{ki}$, where $k = \{1, 2\}$ identifies the channel.

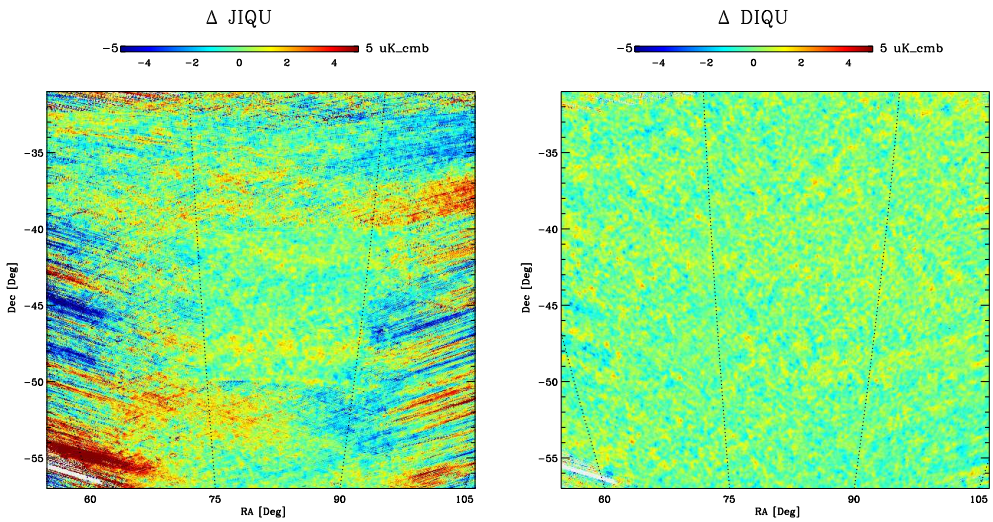


Figure 5.5: A signal only simulation, showing the residuals between the observed and input polarization (in this case, Stokes Q). While the differencing method (Section 5.1.5) is more robust than the more general case when the cross-linking is bad, it does no better when the cross linking is good.

Recall that for a PSB pair the angular separation of the channels is $\Delta \simeq 90 \pm 2°$, however this treatment in no way requires that to be the case.

Following the prescription of Section 5.1.1, one generates linear combinations of the differenced data,

$$\begin{pmatrix} {}^{-}s_i {}^{-}\alpha_i \\ {}^{-}s_i {}^{-}\beta_i \end{pmatrix} = \frac{1}{2} \begin{pmatrix} {}^{-}\alpha_i^2 & {}^{-}\alpha_i {}^{-}\beta_i \\ {}^{-}\alpha_i {}^{-}\beta_i & {}^{-}\beta_i^2 \end{pmatrix} \begin{pmatrix} \mathbf{Q} \\ \mathbf{U} \end{pmatrix} \tag{5.16}$$

As before, one builds up information about the Q,U decorrelation matrix through the combination of channel pairs, as well as modulation of the angular coverage, $\psi$. In this regard we have

$${}^{-}\hat{n}_p = \sum_{j}^{N_{pairs}} w_j \sum_{i \in p} \begin{pmatrix} {}^{-}n_i {}^{-}\alpha_i \\ {}^{-}n_i {}^{-}\beta_i \end{pmatrix} \tag{5.17}$$

where the time-streams ${}^{-}n_i$ represent the polarization subtracted difference data. The

$2 \times 2$ decorrelation matrix is therefore,

$$ {}^{-}\hat{M}_p = \frac{1}{2} \sum_{j}^{N_{pairs}} w_j \sum_{i \in p} \begin{pmatrix} {}^{-}\alpha_i^2 & {}^{-}\alpha_i {}^{-}\beta_i \\ {}^{-}\alpha_i {}^{-}\beta_i & {}^{-}\beta_i^2 \end{pmatrix} \tag{5.18} $$

and we note that we are now using sub-optimal weighting of the *pairs* to generate corrections to the polarization map. Note that, for $\Delta \simeq 90°$, the quantities ${}^{-}\alpha$ (${}^{-}\beta$) have positive (negative) parity, so that when averaged over a large sampling of $\psi$, the off-diagonals of Equation 5.18 tend to zero. Once the corrections to Q and U are obtained, one may substitute them in the sum for ${}^{+}s$ to solve self consistently for I.

This method provides an alternate approach to solve for the Stokes Q and U parameters which, for an idealized dataset, is equivalent to the more general method in the limit of equal sensitivity per channel. Generally speaking, the correlations induced by the combination of the scan and time domain filtering introduce a path dependence to the *observed* I,Q, and U parameters. If the cross-linking is sufficiently well distributed, and the pixels are observed isotropically, the effect will necessarily average out.[5] However, for rarely observed pixels and/or for those with poor cross-linking, the differencing method may help to cancel the common-mode correlation, thereby preventing aliasing between the I, Q and U terms.

### 5.1.6 Noise estimation

In order to obtain (either via direct methods or monte-carlo simulations) an unbiased estimate of the angular power spectrum of the signal, one must first obtain an accurate statistical description of the instrumental noise in the time domain. The role of noise bias in the estimation of the angular power spectrum will be investigated in more detail in Section 5.2, here we discuss how the noise power spectra of the time ordered B2K data are obtained.

In the discussion of Section 5.1.1, stationarity of the statistical properties of the

[5] By cross-linking, we mean orientation of the pixel crossing. More generally, cross linking can be thought of as the history of pixel crossings prior to a particular pass through a pixel. When time domain correlations are introduced to the data (time domain filtering), the value of the observed Stokes parameter depends, in general, on the history of pixel crossings.

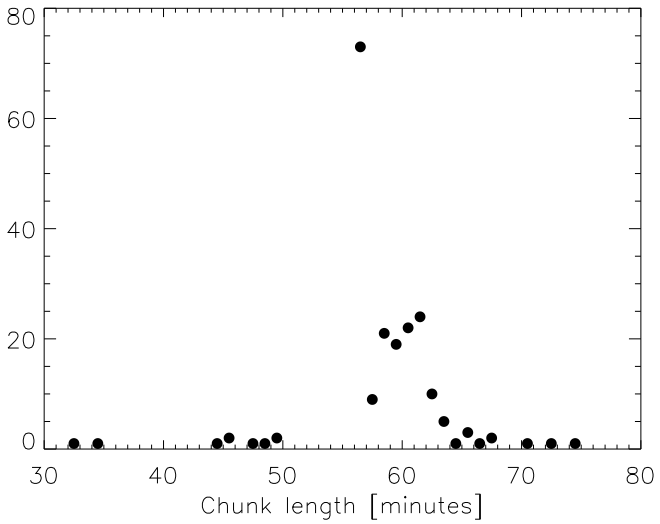


Figure 5.6: A histogram of the lengths of B2K's noise-stationary subsets ("chunks") used in the analysis. The length of the chunks determine the sample-variance limit to the precision with which the noise can be determined, and therefore play a crucial role in the noise estimation process.

noise contribution to the time ordered data is assumed. For B2K, the noise is found to be stationary only so long as the rate of the azimuth scans remain constant, which generally holds for the ∼hour periods, or "chunks", between elevation changes (see Figure 5.6). In addition, there is a diurnal and elevation dependence to the $1/f$ knee, presumably due to residual atmospheric affects (see Figure 5.8). While the noise is not stationary over the whole flight, the noise properties are piecewise stationary, allowing the application of the methods discussed in Section 5.1.1 on a chunk by chunk basis.

Once the iterative solutions for the signal, Equation 5.15, and therefore the noise, $\mathbf{n} = \mathbf{d} - \mathbf{A}\,\widetilde{\mathbf{m}}$, have converged, the noise power spectra of the TOD must be calculated. In practice, there are two factors which fundamentally limit the accuracy with which the power spectrum of the noise can be determined, sample variance and sensitivity.

Sample variance, resulting from the finite length of the noise-stationary subsets, limits both the accuracy and resolution with which features in the noise spectrum may be recovered. By smoothing and binning the power spectra, a compromise is made between the resolution and the error in the estimate. For the B2K analysis, a

logarithmic binning scheme is implemented, in which the spectra are first smoothed using a variable width kernel, and then stored in logarithmically spaced bins. This approach preserves sensitivity to lines in the extremes of our signal band, while also minimizing the error due to sample variance.

The raw sensitivity ultimately determines the signal to noise ratio of the time ordered data and, combined with the distribution of observing time on the sky, the fidelity of the recovered signal estimate, $\hat{\mathbf{m}}$. The noise in $\hat{\mathbf{m}}$ results in a frequency dependent bias in the estimate noise power spectrum do to the fact that in the time domain the signal bandwidth is generally less than the noise bandwith. The bias in the noise estimation varies from chunk to chunk as a result of the variation in signal to noise ratio achieved on different parts of the sky.

The only way to estimate and correct for this bias is to generate an ensemble of signal and noise simulations from an input noise power spectrum, and run the noise estimation procedure on each realization. The transfer function of the noise estimation procedure may then be obtained by comparing the ensemble average of the estimated noise power spectra to the input power spectra. The size of the ensemble is determined by the necessary reduction in the sample variance limit. This bias transfer function, calculated from 50 signal plus noise simulations, is then used to correct the spectra obtained from each subset of the B2K data individually. A comparison of the bias transfer functions typical of noise stationary subsets in the high and low signal to noise regimes is shown in Figure 5.7.

For reasons which will be discussed in Section 5.2.4, we require a framework in which to treat noise correlations in the time domain. Noise correlations in the data are expected both from fundamental considerations (see Appendix B.3), as well as from the practical limitations of noise and cross-talk in the readout electronics. The measured noise from a given channel, $\widetilde{n}^k$, is modeled as the sum of an intrinsic (uncorrelated) component, $n^k$, and the contributions from the intrinsic noise of the other

channels, filtered through a (frequency dependent) cross talk transfer function $\xi_{ik}$.

$$\widetilde{n}^k = n^k + \sum_{i \neq k} \xi_{ik} n^i$$

where, by definition, the intrinsic noise at each frequency are distributed as uncorrelated Gaussian distributions,

$$\langle n^i n^k \rangle \equiv \delta_{ik} P_{ik}.$$

The observable quantities,

$$\langle \widetilde{n}^i \widetilde{n}^k \rangle = \widetilde{P}_{ik}$$

are the $(N_{ch}(N_{ch} - 1)/2 + N_{ch})$ auto and cross-correlations of the noise only time-streams which are estimated directly from the $N_{ch}$ channels.

The Monte Carlo based approach to power spectrum estimation relies on the ability to accurately model the noise properties of the instrument. Therefore, in order to treat the noise in a self-consistent fashion as a realization of a Gaussian random process, it is necessary to measure and store the observed auto *and* cross correlations for all the channels, for each chunk of the data. This corresponds the calculation and storage of 36 spectra for each of the 215 noise stationary subsets, each of which must be corrected for the bias, as previously discussed. Having obtained estimates of the signal and the noise properties from the time ordered data, we are prepared to proceed with the estimation of the angular power spectra.

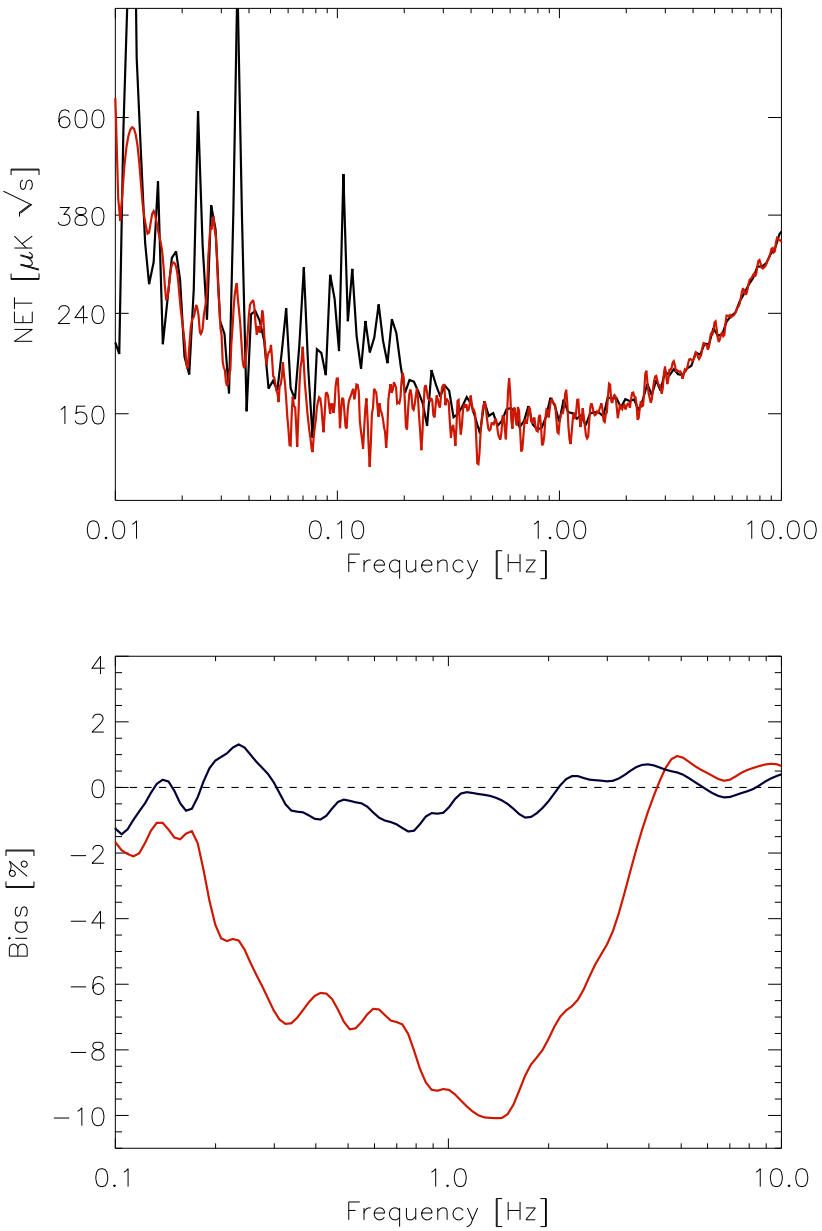


Figure 5.7: The upper panel shows the power spectral density, in CMB units, of the noise for a representative chunk of the time ordered data. The black line is derived from the raw (signal plus noise) data, whereas the red line is the estimate of the noise only PSD. The scan frequency for this chunk appears at 12 mHz, and the CMB dipole (which appears as a triangle wave at the scan frequency) has been subtracted from the TOD prior to the noise estimation. The lower panel shows the amplitude of the noise bias as determined from an ensemble of signal plus noise simulations. The blue line is representative of the bias in a typical high signal to noise chunk, whereas the red line is the most extreme example found in the low signal to noise regime.

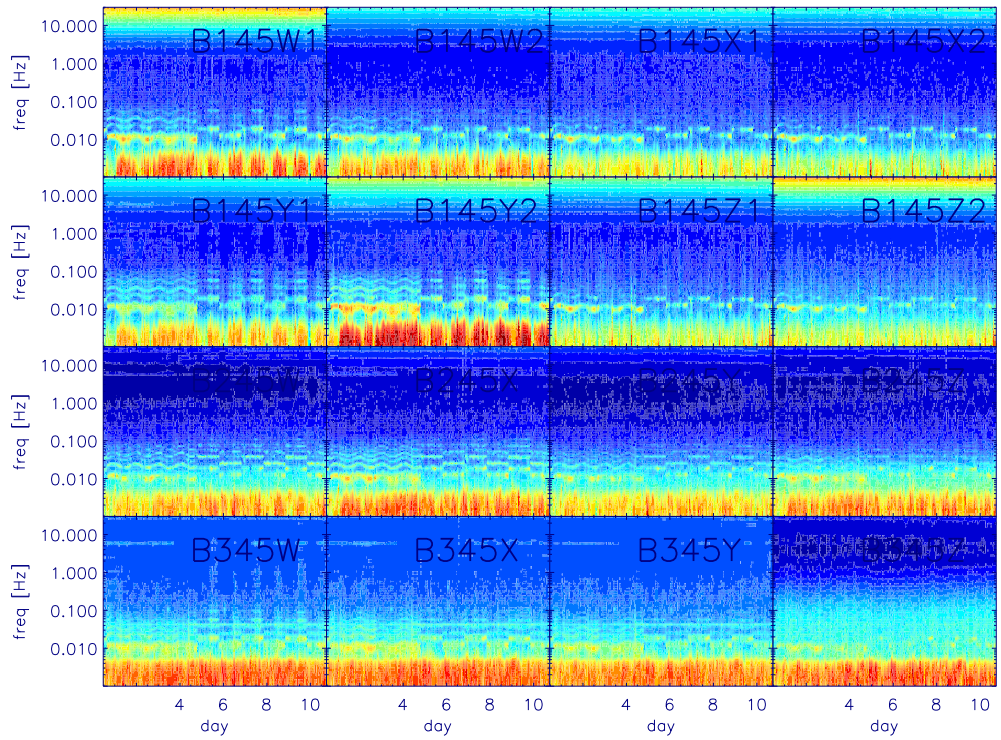


Figure 5.8: The time dependence of the (signal subtracted) noise power spectra of the BOOMERANG science channels as determined from the in-flight data. Each frame shows the power spectrum of each noise stationary subset (chunk) from a particular channel. The series of lines above 10 mHz correspond to the harmonics of the scan frequency. The signal band extends from 0.05 to 5 Hz. The diurnal dependence of the $1/f$ knee is evident. The B345Z channel exhibited noise whose properties were neither stationary nor Gaussian, which is manifest in the low frequency contribution.

## 5.2 CMB power spectrum estimation

### 5.2.1 Formalism

In this section, we briefly summarize the formalism required to treat the description of linearly polarized emission on the sphere. As before, the Stokes parameters are defined in terms of the electric field,

$$\begin{aligned}
\mathbf{I} &\equiv \langle E_x E_x^* + E_y E_y^* \rangle &&= \langle |E_x|^2 \rangle + \langle |E_y|^2 \rangle \\
\mathbf{Q} &\equiv \langle E_x E_x^* - E_y E_y^* \rangle &&= \langle |E_x|^2 \rangle - \langle |E_y|^2 \rangle \\
\mathbf{U} &\equiv \langle E_x E_y^* + E_y E_x^* \rangle &&= 2 \langle |E_x E_y| \cos(\phi_x - \phi_y) \rangle \\
\mathbf{V} &\equiv i\langle E_x E_y^* - E_y E_x^* \rangle &&= 2 \langle |E_x E_y| \sin(\phi_x - \phi_y) \rangle
\end{aligned}$$

where the brackets, $\langle\ \rangle$, represent an average over many periods of the wave. For Thomson scattering of electrons in a quadrupolar radiation field there is no mechanism for the introduction of a relative phase between the two linear polarizations. Therefore, the cosmological Stokes **V** parameter is presumed to be zero.

Any scalar quantity defined on the sphere (including the Stokes **I** parameter) can be decomposed into the spherical harmonic basis,

$$\Delta T(\hat{\mathbf{n}}) = \sum_{\ell > 0} \sum_{m=-\ell}^{\ell} a_{\ell m}^T Y_{\ell m}(\hat{\mathbf{n}}) \tag{5.19}$$

where the expansion coefficients are determined by the integrals over the sphere,

$$a_{\ell m}^T = \int d\Omega\ \Delta T(\hat{\mathbf{n}}) Y_{\ell m}^*(\hat{\mathbf{n}}) \tag{5.20}$$

If we assume that the fluctuations have zero mean and are isotropic, then $\langle a_{\ell m} \rangle = 0$ and the azimuthal averages vanish,

$$\langle a_{\ell m} a_{\ell' m'}^* \rangle = \delta_{\ell \ell'} \delta_{m m'} \langle C_\ell \rangle.$$

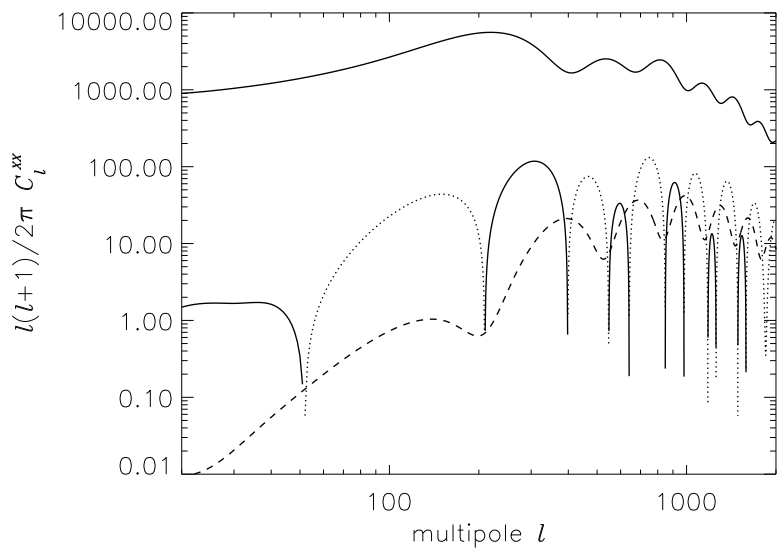


Figure 5.9: The predicted CMB power spectra corresponding to a fiducial ΛCDM cosmology. The topmost curve is the power spectrum of the unpolarized emission, $\mathcal{C}_\ell^{\rm TT}$, the alternating solid and dotted lines represent the temperature-polarization cross correlation, $\mathcal{C}_\ell^{\rm TE}$, (which goes negative when shown as a dotted line), and the lowest of the signals is the gradient mode polarization, $\mathcal{C}_\ell^{\rm EE}$. The spectra are in units of $[\mu K^2_{\rm CMB}]$. Note that the polarization power is a factor of 20 less than the unpolarized signal.

In this limit the $m$-averaged power spectrum contains all the information,

$$C_\ell = \frac{1}{(2\ell+1)} \sum_{m=-\ell}^{\ell} |a_{\ell m}|^2 \tag{5.21}$$

It has become the usual practice to display the quantity,

$$\mathcal{C}_\ell \equiv \frac{\ell(\ell+1)}{2\pi} C_\ell \tag{5.22}$$

which is roughly flat in $\ell$, and which is therefore more amenable to simple binning.

Unlike the temperature anisotropies, the Stokes Q and U parameters are not invariant under rotation of the coordinate system. A set of invariant quantities may be defined on the sky [85, 177, 176],

$$(Q+iU)(\hat{\mathbf{n}}) = \sum_{\ell>0} \sum_{m=-\ell}^{\ell} {}_{+2}a_{\ell m}\ {}_{+2}Y_{\ell m}(\hat{\mathbf{n}}) \tag{5.23}$$

$$(Q - iU)(\hat{\mathbf{n}}) = \sum_{\ell>0} \sum_{m=-\ell}^{\ell} {}_{-2}a_{\ell m}\ {}_{-2}Y_{\ell m}(\hat{\mathbf{n}}) \tag{5.24}$$

Where we have introduced the spin-weighted spherical harmonics, ${}_{\pm 2}Y_{\ell m}(\hat{\mathbf{n}})$, which satisfy the usual orthogonality requirements. These functions are defined according to the conventions in Appendix A of Reference [177],

$$\begin{aligned} {}_{s}Y_{\ell m} &= e^{im\phi} \left[ \tfrac{(\ell+m)!(\ell-m)!}{(\ell+s)!(\ell-s)!} \tfrac{(2\ell+1)}{4\pi} \right]^{1/2} \sin^{2\ell}(\theta/2) \cdot \\ & \sum_{r=0}^{\ell-s} \begin{pmatrix} \ell-s \\ r \end{pmatrix} \begin{pmatrix} \ell+s \\ r+s-m \end{pmatrix} (-1)^{\ell-r-s+m} \cot^{2r+s-m}(\theta/2) \end{aligned} \tag{5.25}$$

The expansion coefficients may be obtained in the usual way

$${}_{\pm 2}a_{\ell m} = \int d\Omega\ \Delta(Q \pm iU)(\hat{\mathbf{n}})\ {}_{\pm 2}Y^{*}_{\ell m}(\hat{\mathbf{n}}) \tag{5.26}$$

The usual practice is to introduce the so-called E-mode and B-mode (or gradient and curl) coefficients,

$$a^{E}_{\ell m} = -\left({}_{2}a_{\ell m} + {}_{-2}a_{\ell m}\right)/2 \tag{5.27}$$

$$a^{B}_{\ell m} = i\ \left({}_{2}a_{\ell m} - {}_{-2}a_{\ell m}\right)/2 \tag{5.28}$$

and the rotationally invariant power spectra,

$$C^{\mathrm{XY}}_{\ell} = \frac{1}{2\ell+1} \sum_{m=-\ell}^{\ell} a^{\mathrm{X}*}_{\ell m}\ a^{Y}_{\ell m} \tag{5.29}$$

where $X, Y$ represent any of $T, E$, or $B$. Occasionally in the literature other quantities are plotted to highlight a particular range of multipoles. For instance, some authors prefer to display the quantities $\mathcal{C}^{\mathrm{TT}}_{\ell} \equiv \ell(\ell+1)/2\pi\ C^{\mathrm{TT}}_{\ell}$ for the temperature anisotropies, $(\ell+1)/2\pi\ C^{\mathrm{TE(B)}}_{\ell}$ for the temperature-polarization cross correlation and simply, $C^{\mathrm{EE(BB)}}_{\ell}$ for the polarization auto-power spectra.

### 5.2.2 The Likelihood

Our approach to power spectrum estimation, as in many other astrophysical applications [77], is a Bayesian one [14, 6, 15]. The expression for the likelihood of the data is the convolution of the probability distribution of underlying temperature fluctuations, $s$, given the covariance of the theoretical power spectrum, $\mathbf{C}_s$, with the likelihood of the map, $\mathbf{m}$, given the covariance of the noise, $\mathbf{C}_N$, *and* the underlying signal, $s$. Clearly, we are ignorant of the true signal $s$, and so we must integrate (or marginalize) the likelihood over all values of $s$,

$$\mathcal{L}(\varpi) = \int_{-\infty}^{\infty} d\mathbf{s}\ P(\mathbf{s}|\mathbf{C}_\mathbf{s})\ P(\widetilde{\mathbf{m}}|\mathbf{C}_N, \mathbf{s})$$

Where the cosmological parameters, $\varpi$ enter by means of the signal covariance $\mathbf{C}_S$ implied by the predicted power spectrum $C_\ell$. The parameters therefore enter the likelihood in a highly nontrivial fashion. We then have an expression for the likelihood,

$$\mathcal{L}(\varpi) = \int_{-\infty}^{\infty} \frac{d^{N_p}s}{(2\pi)^{N_p/2}|\mathbf{C}_S|^{1/2}} e^{-\frac{1}{2}\ \mathbf{s}^T\mathbf{C}_S^{-1}\mathbf{s}} \frac{1}{(2\pi)^{N_p/2}|\mathbf{C}_N|^{1/2}} e^{-\frac{1}{2}\ (\widetilde{\mathbf{m}}-\mathbf{s})^T\mathbf{C}_N^{-1}(\widetilde{\mathbf{m}}-\mathbf{s})} \quad (5.30)$$

After completing the square and integrating over $\mathbf{s}$, one is left with a likelihood which is a multivariate Gaussian in the data,

$$\mathcal{L}(\varpi) \equiv P(\widetilde{\mathbf{m}}|\varpi) = \frac{1}{(2\pi)^{N_p/2}\ |\mathbf{C}|^{1/2}}\ e^{-\frac{1}{2}\ \widetilde{\mathbf{m}}^T\cdot\ \mathbf{C}^{-1}\cdot\ \widetilde{\mathbf{m}}} \quad (5.31)$$

where the noise and signal are assumed to be uncorrelated and Gaussian distributed, such that

$$\mathbf{C} = \mathbf{C}_N + \mathbf{C}_S \quad (5.32)$$

Where the signal covariance $\mathbf{C}_S$ is related to the underlying power spectrum

$$\mathbf{C}_S(\theta) = \frac{1}{4\pi}\sum_{\ell=0}^{\infty} P_\ell(\cos\theta) \sum_{m=-\ell}^{\ell} |B_{\ell m}a_{\ell m}|^2 \quad (5.33)$$

and $\theta$ is simply the angle between the two pixels represented by each element in the $N_p \times N_p$ covariance matrix $\mathbf{C}_S$. The signal covariance matrix is band limited in practice by the beam window function $B_{\ell m}$, even if the signal, $a_{\ell m}$, is not. The function $B_{\ell m}$ is the spherical harmonic transform of the effective instrumental beam, which in most cases is isotropic (has no $m$ dependence). In this case, $B_{\ell m} = B_\ell$, which is just the Legendre transform of the effective beam. For a Gaussian beam, $B_\ell = e^{-\frac{1}{2}\ell(\ell+1)\sigma_b^2}$, where $\sigma_b = \theta_{FWHM}/\sqrt{8\ln 2}$. Even in cases where the physical beam is *not* symmetric this is often an excellent approximation due to symmetrization of the effective beam on the sky resulting from the scan strategy or, pointing error.

It is worth emphasizing that while Equation 5.31 is Gaussian in the data, $\mathbf{m}$, the likelihood is most certainly *not* Gaussian in the signal covariance $\mathbf{C}_S$, much less the power spectrum $C_\ell$ . Maximizing the likelihood will therefore result in an estimate of the signal covariance, but estimating the errors on those values requires an exact treatment of the (non-trivial) shape of the likelihood function in the vicinity of the maximum likelihood estimates.

Following Dodelson, it is instructive to consider the the case when the covariance matrix takes the simple form $\mathbf{C} = (C_S + C_N) \cdot \mathbf{I}$. The maximum likelihood solution is readily obtained as a function of the signal covariance [37],

$$\frac{\partial \ln \mathcal{L}}{\partial C_S} = \frac{1}{2}\frac{\widetilde{\mathbf{m}}^T\widetilde{\mathbf{m}}}{(C_S + C_N)^2} - \frac{N_p}{2(C_S + C_N)} = 0$$

Solving for $C_S$ we find

$$C_S = \sigma^2_{\widetilde{\mathrm{m}}} - C_N$$

Which indicates the signal variance is simply the difference between the total variance of the map, $\sigma^2_{\widetilde{\mathrm{m}}}$, and the variance of the instrumental noise (see, for instance, Figure 6.3). Furthermore, one can estimate the error on this parameter by measuring the width of the likelihood function around its maximum value,

$$\sigma^2_{C_S} = -\frac{\partial^2 \ln \mathcal{L}}{\partial C_S^2} = \sqrt{\frac{2}{N_p}}(C_S + C_N)$$

A more general treatment yields an approximate error on the power spectrum $C_\ell$, by replacing the number of pixels $N_p$, by the number of independent modes measured,

$$\sigma^2_{C_\ell} = \sqrt{\frac{2}{(2\ell+1)f_{sky}}}(C_\ell + N_\ell)$$

where $f_{sky}$ is the fraction of sky covered, and $N_\ell$ is the projection instrumental noise. While this treatment is an oversimplification, it illustrates the fundamental limitation to our ability to infer the underlying power spectrum from observations of our Universe. Even a noiseless observation will suffer uncertainties due to the "cosmic variance" limit posed by the appearance of the $C_S$ term in the second derivative of the likelihood.

Following Knox, this procedure may be generalized to provide a rough estimate of the experimental sensitivity to any of the CMB observables [88, 89, 13],

$$\Delta C_b^{\rm XY} \simeq \sqrt{\frac{1}{(2\ell+1)\ f_{sky}\ \Delta\ell}}\left[(C_b^{\rm XY}+N_b^{\rm XY})^2 + (C_b^{\rm XX}+N_b^{\rm XX})(C_b^{\rm YY}+N_b^{\rm YY})\right]^{1/2} \quad (5.34)$$

where $X, Y$ are any of $T, E$, or $B$, for bands of width $\Delta\ell$, and instrumental noise power spectra may be roughly estimated given,

$$N_l = w^{-1}\ e^{\ \sigma_b^2\ \ell(\ell+1)}$$

where the weighting indicates the statistical power of the survey,

$$w^{-1} \equiv \left(\frac{\rm NET}{\tau}\right)^2 4\pi\ N_{pix}\ f_{sky}$$

with $\tau$ equal to the total duration of the observation consisting of $N_{pix}$ resolution elements, determined loosely by the beam width $\sigma_b$. It should be emphasized that the achieved sensitivity is always less than this crude estimate for a number of reasons, for example, non-white noise in the signal band,correlations between bins resulting from the geometry of the sky coverage, and the loss of spatial modes due to filtering,

to name just a few.

In reality, neither the signal nor the noise covariance matrix are anything resembling diagonal. As a result, the calculation of the complete likelihood function is extremely costly and methods to compress the data and/or accelerate the minimalization are required. One approach is to find a basis in which the signal and noise covariance are diagonal,[6] and treat only those modes which carry appreciable signal. In addition, instead of a direct solution to the exceedingly formidable Equation 5.31, a numerical method (usually iterative, employing a variant on the Newton-Raphson method for finding the roots of an equation ) is used to find the maximum likelihood solution for the signal covariance. Often, both methods are employed to speed the process. A variant of the compression method is the Karhunen-Loève, or $\Delta$signal-to-noise' eigenmode, technique.

### 5.2.3 Monte Carlo methods

Our approach extends the pseudo-power spectrum approach (which was originally proposed by Peebles in the context of clustering [133, 61]) to the analysis of linearly polarized data. First, we briefly outline the application of the Monte Carlo method to un-polarized data described in Hivon, et al.[66, 126] The approach is based on the assumption that the transform of the observed partial sky, the pseudo-power spectrum, may be expressed as the sum of a signal and a noise term,

$$\widetilde{C}_\ell^{\mathrm{TT}} = \sum_{\ell'} M_{\ell\ell'} F_{\ell'}^{\mathrm{TT}} B_{\ell'}^2 C_{\ell'}^{\mathrm{TT}} + \widetilde{N}_\ell^{\mathrm{TT}}. \tag{5.35}$$

Here, $C_\ell$ is the underlying power spectrum of the full sky. The coupling kernel, $M_{ll'}$, accounts for the incomplete sky coverage and (if desired) the weighting scheme applied to the data. The transfer function, $F_\ell$, is an approximate, symmetrized treatment of the (extremely complicated) effects of the scan strategy and the time domain filtering on the signal. The beam window function, $B_\ell^2$, is the transform of the effective beam,

[6] That is, a rotation (or series of rotations) in the pixel domain which diagonalizes the noise and signal covariance, *assuming* a fiducial signal power spectrum. The resultant eigenmodes are assumed to not depend strongly on the details of the signal power spectrum.

as shown in Figure 3.15. The noise term, $\widetilde{N}_\ell$, is the transform of the projection of the instrumental noise on the sky.

In the spherical harmonic domain, the effect of multiplying the full sky by a window is simply a convolution. The coupling kernel, $M_{\ell\ell'}$, is simply the normalized power spectrum of the (heuristically weighted) mask which is applied to the full sky,

$$M_{\ell\ell'} \equiv \frac{(2\ell'+1)}{4\pi}\sum_{\ell''}(2\ell''+1)\begin{pmatrix} \ell & \ell' & \ell'' \\ 0 & 0 & 0 \end{pmatrix}^2 \mathcal{W}_{\ell'} \tag{5.36}$$

where $\mathcal{W}_{\ell'}$ is the angular power spectrum of the mask.

The remaining two terms are determined via the analysis of ensembles of signal-only and noise-only Monte Carlos. The form of the transfer function is obtained by comparing the ensemble average of the signal only simulations with the input spectra. Similarly, the average of the noise realizations provides the noise pseudo-power spectrum, $\widetilde{N}_\ell$.

The binned power spectrum is obtained by inverting and binning Equation 5.35, using the ensemble averaged estimate of the noise power spectrum,

$$\widehat{C}_b = K^{-1}_{bb'} P_{b'\ell}\left(\widetilde{C}_\ell - \langle\widetilde{N}_\ell\rangle\right) \tag{5.37}$$

where the binning operator, $P_{b\ell}$, simply represents an average over a specified range of $\ell$. Here, and in the remainder of the discussion, repeated indices imply their summation. The reciprocal operator, $Q_{b\ell}$, simply interpolates back to the un-binned power spectrum, $C_\ell = Q_{b\ell}C_b$. With these definitions, the binned coupling matrix, $K_{bb'}$, is then easily calculated,

$$K_{bb'} = P_{b\ell}M_{\ell\ell'}F_{\ell'}B^2_{\ell'}Q_{\ell' b}.$$

The importance of accurate noise estimation is manifest in Equation 5.37; the estimate of the noise is subtracted directly from the raw harmonic transform of the data (see, for instance, Figure 5.10). Any systematic mis-estimate of the noise will result in a

bias of the estimate of the binned power spectrum; over estimation of the noise pulls the power spectrum down, while underestimation biases the estimated power high.

In order to compare with theoretical models, one requires the covariance of the binned power spectrum estimates. In one approach, a third set of signal *plus* noise simulations are generated, and the covariance of the binned power spectrum estimates is obtained via the distribution of the ensemble,

$$C_{bb'} = \left\langle \left( \widehat{C}_b - \langle \widehat{C}_b \rangle \right) \left( \widehat{C}_{b'} - \langle \widehat{C}_{b'} \rangle \right)^* \right\rangle \tag{5.38}$$

where the brackets, $\langle\rangle$, indicate averages over the Monte Carlo ensemble. As usual, the diagonal elements of the covariance may be interpreted as an estimate of the uncertainty on the estimator,

$$\Delta \widehat{C}_b = C_{bb}^{1/2}.$$

An alternative approach, which is both computationally more efficient and, in some cases, more optimal, is an adaptation of the quadratic estimator in Equation 5.31. In principle, one can solve for the maximum likelihood band-powers by guessing an initial solution (say, that of Equation 5.37), and iterating on the estimator and signal covariance using the Newton-Raphson method (see Appendix C.1).

In practice, the need to invert the noise covariance matrices of large ($\sim$mega-pixel) maps make this approach untenable for current datasets and contemporary computational capabilities. The calculation becomes trivial, however, if one neglects the off-diagonal terms. This approximation is essentially identical to that of the previous approach, where the band power estimator is corrected for a diagonal noise term derived from the Monte Carlo simulations. However, the quadratic estimator does not require the generation of an ensemble of signal plus noise simulations to recover an estimate of the covariance, resulting in a distinct speed advantage.

### Polarization spectra

The generalization of the procedure outlined above to the analysis of polarization power spectra on the cut sky is conceptually straightforward. An additional set

of three polarized coupling matrices must be defined, through which the pseudo-spectra of the $E$ and $B$ mode auto power spectra are found to be coupled [26]. This geometrical leakage is unavoidable on the cut sky, or when the noise is not evenly distributed and the data are noise weighted. A detailed description of the formalism, and a derivation of the coupling kernel algebra, can be found in Lewis, et al.[107, 21].

In addition to Equation 5.35, the observables for linearly polarized emission on the cut sky are,

$$\widetilde{C}_\ell^{\mathrm{EE}} = \sum_{\ell'} \left[ {}_+K_{\ell\ell'} F_{\ell'}^{\mathrm{EE}} C_{\ell'}^{\mathrm{EE}} + {}_-K_{\ell\ell'} F_{\ell'}^{\mathrm{BB}} C_{\ell'}^{\mathrm{BB}} \right] B_{\ell'}^2 + \widetilde{N}_\ell^{\mathrm{EE}}, \tag{5.39}$$

$$\widetilde{C}_\ell^{\mathrm{BB}} = \sum_{\ell'} \left[ {}_+K_{\ell\ell'} F_{\ell'}^{\mathrm{BB}} C_{\ell'}^{\mathrm{BB}} + {}_-K_{\ell\ell'} F_{\ell'}^{\mathrm{EE}} C_{\ell'}^{\mathrm{EE}} \right] B_{\ell'}^2 + \widetilde{N}_\ell^{\mathrm{BB}}, \tag{5.40}$$

$$\widetilde{C}_\ell^{\mathrm{TE}} = \sum_{\ell'} {}_\times K_{\ell\ell'} F_{\ell'}^{\mathrm{TE}} B_{\ell'}^2 C_{\ell'}^{\mathrm{TE}} + \widetilde{N}_\ell^{\mathrm{TE}}, \tag{5.41}$$

$$\widetilde{C}_\ell^{\mathrm{TB}} = \sum_{\ell'} {}_\times K_{\ell\ell'} F_{\ell'}^{\mathrm{TB}} B_{\ell'}^2 C_{\ell'}^{\mathrm{TB}} + \widetilde{N}_\ell^{\mathrm{TB}}, \tag{5.42}$$

$$\widetilde{C}_\ell^{\mathrm{EB}} = \sum_{\ell'} \left( {}_+K_{\ell\ell'} - {}_-K_{\ell\ell'} \right) F_{\ell'}^{\mathrm{EB}} B_{\ell'}^2 C_{\ell'}^{\mathrm{EB}} + \widetilde{N}_\ell^{\mathrm{EB}}. \tag{5.43}$$

As with the temperature power spectrum the kernels, ${}_{\pm,\times}K_{\ell\ell'}$ are calculated from the sky coverage and weighting which is applied to the whole sky, and the $F_\ell^{\mathrm{XY}}$ and $N_\ell^{\mathrm{XY}}$ are obtained through signal and noise Monte Carlos, respectively.

### 5.2.4 Practical considerations

The degree of accuracy required in the treatment of the noise is evident from the raw pseudo-power spectra obtained from B2K's deep region, as shown in Figure 5.10. While the $TT$ spectrum is signal dominated out to $\ell \sim 1000$, the polarization spectra are noise dominated at all multipoles. A great deal of care must be taken to properly estimate the projection of the time domain noise on the sky. In order to properly treat the noise in the Monte Carlo simulations, we must make use of our knowledge of the noise correlations in the time domain to produce a a set of properly correlated noise realizations.

The noise is generated in the frequency domain, with each Fourier component

constructed from the product of the (complex) $N_{ch} \times N_{ch}$ noise correlation matrix $\widetilde{P}_{ik}$ (from Section 5.1.6) with a vector of $N_{ch}$ randomized phases, g.

$$\widetilde{n} = FFT^{-1}\left(\frac{1}{\sqrt{2}}\,\widetilde{\mathrm{P}}^{1/2}(f)\;\mathrm{g}(f)\right)$$

where $\widetilde{\mathrm{P}}^{1/2}(f)$ is the Cholesky decomposition (matrix square root) of the noise correlation matrix in the frequency domain [146, 147]. The contributions from each frequency add, providing a fake noise time-stream with the same statistical properties as the real data. These fake time-streams are run through the pointing model and signal estimator, and the $\widetilde{N}_\ell^{XY}$ are calculated from the resultant I, Q and U maps.

The geometric coupling between the $E$ and $B$ mode polarization is evident in Equations 5.39 and 5.40. While the individual spectra are corrected for the leakage in a self consistent manner, the coupling represents a problem similar to that of noise estimation. The cosmological $B$ mode signal, if present, is expected to be orders of magnitude smaller than the $E$ mode signal. The precision of the $C_\ell^{\mathrm{EE}}$ measurement which is required to achieve a given sensitivity to $C_\ell^{\mathrm{BB}}$ depends directly on the amount of sky covered in the survey. For polarization measurements probing the $B$ mode spectrum, the geometric leakage of $E$ to $B$ represents a compelling motivation to cover as much area as possible.

The pseudo-power spectrum approach presented here results in sub-optimal error bars due to the failure to account for the complete off-diagonal structure of the full signal and noise covariance matrix appearing in Equation 5.31. In the Monte Carlo approach, the weighting of the temperature and polarization maps is heuristic; in the signal dominated regime, uniform weights should be applied to the data, whereas in the noise dominated regime the maps should be noise weighted. In the event that the integration time or sensitivity are not uniformly distributed on the sky, it is inevitable such a heuristic approach will achieve sub-optimal errors over some portion of the multipole range.

For B2K, where the noise contribution varies greatly between the shallow and deep CMB fields, the non-optimality of the heuristic weighting represents a significant

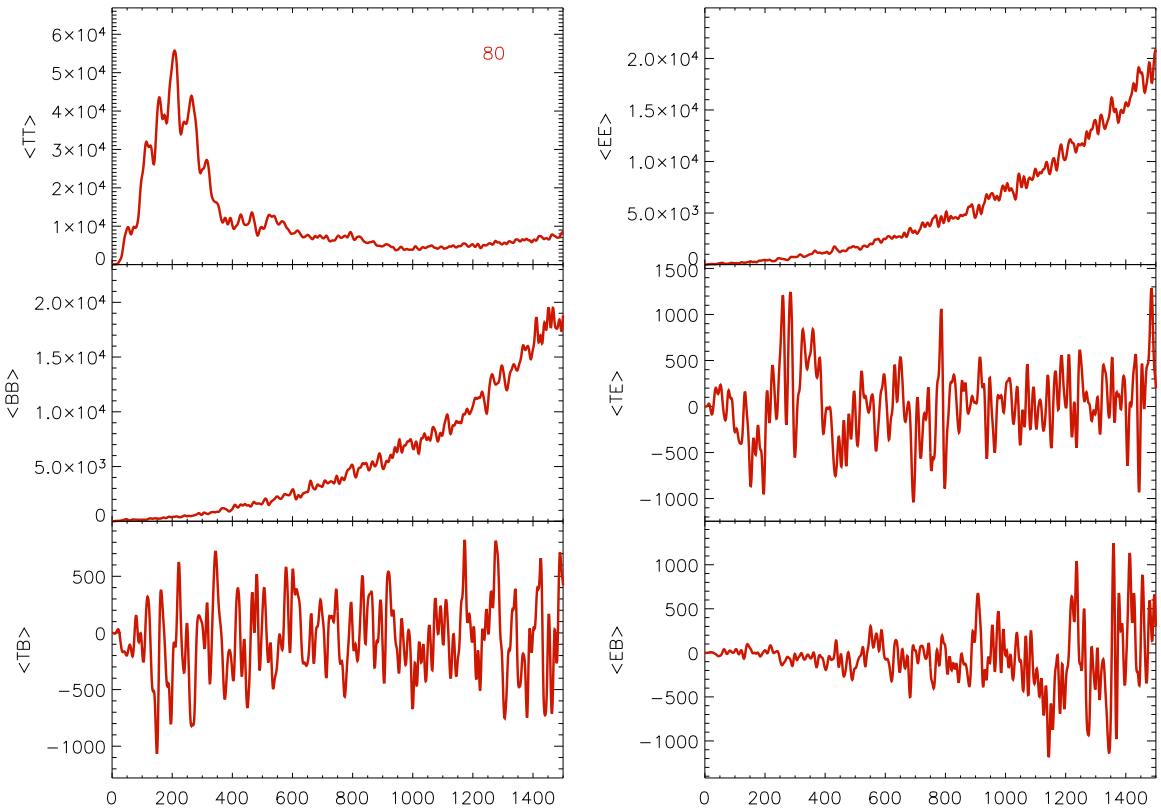


Figure 5.10: The raw pseudo-power spectra derived from the B2K deep region for each of the spectra defined in Equation 5.35 and Equations 5.39 through 5.43. The quantities displayed are $\widetilde{\mathcal{C}}_\ell^{\mathrm{XX}} \equiv \frac{\ell(\ell+1)}{2\pi}\widetilde{C}_\ell^{\mathrm{XX}}$. The first three acoustic peaks of the temperature power-spectrum are clearly evident in the upper left panel, as is the degree angular scale $TE$ correlation in the middle right. In the white noise approximation the noise power spectrum appears as quadratic, as is evident in the noise dominated $\widetilde{\mathcal{C}}_\ell^{\mathrm{EE(BB)}}$. Note that while the parabolic noise contribution is present as well in the $TT$ spectrum, the signal to noise ratio is much greater than unity below multipoles of $\ell \sim 1000$. For the polarization spectra, the noise estimation clearly must be extremely accurate to avoid introducing a bias much greater than the signal.

obstacle to the analysis. Noise weighting results in an improved measurement of the higher multipoles, while uniform weighting provides a better estimate of the larger scale features due to the larger effective area of the mask. [7] In order to address this problem, a cross-correlation method was developed to combine the two regions in the frequency domain, allowing the covariance of the noise-weighted masks to appropriately weight the two data sets over the entire range multipoles [29].

## Cross correlation

The cross correlation method enjoys two distinct advantages over the traditional Monte Carlo approach. First, and most important for B2K, it allows a nearly optimal treatment of the (highly non-uniform) noise properties in the map. Second, the method lessens the sensitivity of the analysis to the estimation of the noise in the time-domain *in proportion to the number of noise-independent data subsets.* We briefly describe the application to the B2K data.

The data are first divided into two subsets such that the noise per pixel *within* each subset is uniform. For the B2K analysis, one subset consists of the first four days of data, which encompasses the shallow field, while the other set consists of the remainder of the observations, which cover only the deep field. Stokes parameter maps are generated for each of the data subsets, as are signal and noise realizations.One of the primary benefits of the approach is the ability to calculate the covariance matrix for the cross power spectra from the cross spectra of the masks. Since the noise is roughly uniform within the shallow and deep fields, the cross correlation allows nearly optimal weighting of the combined data.

Due to the overlapping coverage of the two fields, the pseudo-cross power spectrum of the two fields is well defined. We identify the two noise-independent subsets as the $s$ (shallow) and $d$ (deep) fields. As in Equation 5.35, the psuedo-cross spectrum is

[7] The approach taken by the WMAP team is to compute three sets of spectra using uniform, noise weighted, and a transitionally weighted mask, and then generating a unified spectrum using the individual spectra with the lowest errors at a given multipole.

given by,

$$\widetilde{C}_\ell^{sd} = \sum_{\ell'} M_{\ell\ell'}^{sd} B_{\ell'}^2 F_{\ell'}^{sd} C_{\ell'}^{sd} + \widetilde{N}_\ell^{sd} \tag{5.44}$$

where,

$$\widetilde{C}_\ell^{sd} = \frac{1}{(2\ell+1)} \sum_{m=-\ell}^{\ell} a_{\ell m}^{s} a_{\ell m}^{d\star}$$

and similar to Equation 5.36, the coupling kernel here is calculated from cross power spectra of the weighted masks. One expects that $\widetilde{N}_\ell^{sd} = 0$ for statistically independent data, such as those obtained from a series of temporally distinct observations. When there are a sufficient number of independent maps, this method is a useful probe of the instrument's noise properties, representing a distinct advantage over data characterized by less redundancy.

It is often the case that a large number of channels make simultaneous observations of a given field. Time-domain correlations of the noise between channels will generally result in a non-zero noise cross power spectrum. These correlations must be measured and the cross power spectrum estimated from Monte Carlo ensembles in order to correct for the resultant noise bias. For a polarimeter which, like B2K, relies on the combination of different detectors to determine the Stokes parameters, such channel-based cross correlations are not practical. However, a method of modulating the polarization signal removes this co-dependency, enabling the cross correlation of the I, Q and U maps generated from individual channels.

The power spectra we present in this work are derived from the auto and cross spectra of the shallow and deep subsets, applying a uniform weight to each. As for the auto-power spectra, the band-power estimates and errors are obtained by solving for the (binned) least squares solution using the full correlation matrix of the auto and cross power spectra,

$$C_{bb'}^{XY,X'Y'} = \left\langle \left( \widehat{C}_b^{XY} - \langle \widehat{C}_b^{XY} \rangle \right) \left( \widehat{C}_{b'}^{X'Y'} - \langle \widehat{C}_{b'}^{X'Y'} \rangle \right)^* \right\rangle$$

which is the generalization of Equation 5.38. The result is an unbiased estimate of the power spectrum with nearly optimal errors over the entire multipole range [29, 161].

# Chapter 6

# Primary Science and Discussion

> "The search will continue. Not until the empirical resources are exhausted, need we pass on to the dreamy realms of speculation."
>
> –Edwin Hubble, *The Realm of the Nebulae*, 1930.

The primary data products resulting from the B2K analysis are calibrated maps of the Stokes I, Q and U parameters generated from the analysis of all the channels within each of the three frequency bands. A combined analysis of the three frequencies, including pixel-based foreground separation, is underway but has not been completed. A preliminary set of power spectra have been estimated from the 145 GHz data in the CMB field. In the first section of this chapter, we discuss the single frequency maps obtained from all $\sim 180$ hours spent observing CMB field. The temperature and polarization power spectra derived from these maps are discussed in the second section. Finally, a preliminary set of Galactic plane maps may be found in Appendix A.

## 6.1 CMB maps

Using the approach described in Section 5.1.1, we have generated polarized maps of the CMB which cover $\sim$2% of the sky at a $3.4'$ pixellization (Figure 6.1). The central portion of this map has an error $\langle \mathrm{diag}(\mathbf{C}_N^{1/2}) \rangle \simeq 25\mu$K, and represents the highest signal to noise image of the surface of last scattering published to date (Figure 6.2).

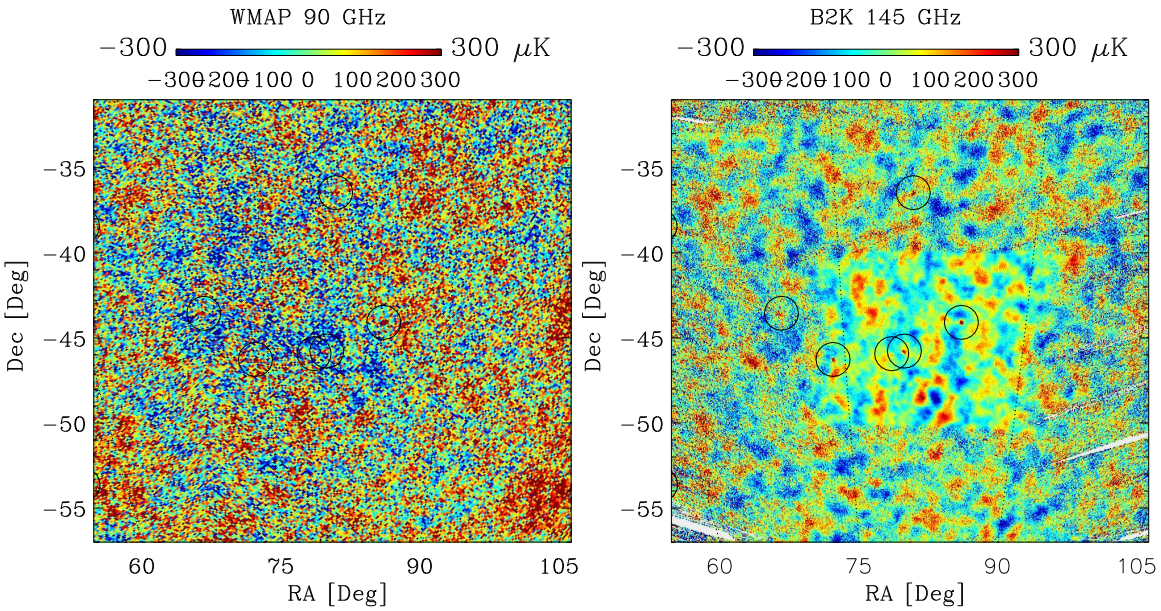


Figure 6.1: The CMB temperature anisotropy as observed by WMAP (left) and B2K (right). The WMAP data are pixellized at $7'$, whereas the B2K data are shown with $3.4'$ pixels. While the WMAP data cover nearly the whole sky, the signal to noise on the sky is quite low on angular scales of a degree or less. In the deep field, the B2K data have signal to noise in excess of 2 for features as small as $12'$, and $s/n \sim 100$ at the degree angular scales which correspond to the acoustic peak. The locations of known extra-Galactic sources are indicated with circles (see Table 3.5).

Although they cover the whole sky, the WMAP data have ∼40 times the noise per pixel of the B2K deep field. A comparison of the WMAP W-band (90 GHz) and B2K (145 GHz) maps is shown in Figure 6.1. The WMAP image is pixelized at $7'$, whereas the B2K image is shown at the full $3.4'$ resolution. Although the low signal to noise of the WMAP map makes a visual comparison difficult, the correspondence on degree angular scales is evident.

While the signal to noise on the temperature anisotropies is high, at $3.4'$ resolution the signal to noise on the polarization is less than unity. As a consistency check, the data are divided (temporally) into subsets with roughly equal statistical weight. The resultant maps are then summed and differenced. A histogram of the sum and difference maps for each of the three Stokes parameters is shown in Figure 6.3. While the temperature detection is visibly robust, the excess power of the sum for the Q

and U maps is not readily evident.

We can maximize the signal to noise ratio by applying a Wiener filter, as described in Equation 5.1. Figure 6.2 is a Wiener filtered map of the temperature and polarization anisotropies in which we approximate the kernel with a band pass matched to the ($\sim 12'$) angular scale of the $E$-mode polarization for a $\Lambda$CDM concordance model. It should be emphasized that the filtered map is used as a visual aid only - no such cosmological prior is assumed in the estimation of the power spectra.

Full resolution maps of the deep field obtained from the combined analysis of all functional channels[1] within each of the three frequencies are shown in Figures 6.4, 6.5, and 6.6. The right side of the map corresponds to a Galactic latititude of approximately $b \simeq -25$ degrees. The CMB, which dominates the 145 GHz image, is also apparent in the 245 and 345 GHz maps, as is the quasar, [PKS]0537-441, which is marked at the center right. To the author's knowledge, these maps represent the first images of the CMB anisotropies at frequencies above 150 GHz. While the CMB is the dominant feature, there are several features which are consistent with thermal emission of Galactic dust. Furthermore, these patches are well correlated with the $100\mu$m IRAS maps.

The spectrum of the emission in these regions is not in particularly good agreement with the model of Finkbeiner [43]. Therefore, in order to quantify the contribution of this dust emission at 145 GHz, the dust model of [20] is used to extrapolate the 345 GHz emission to 145 GHz. This scaling suggests that the brightest dust-correlated features have a 145 GHz brightness which is less than $10\mu K$, well below the level of the sample variance and statistical uncertainty, as is consistent with the findings reported in Ruhl,*et al.* [145]. Although the polarization fraction of the diffuse dust emission is not known, it is expected to be at the $\sim 5\%$ level, which is well below our sensitivity. As an additional check on the foregrounds, the brightest features in the 345 GHz map are masked out of the 145 GHz data prior to the power spectrum estimation. The spectra are found to be insensitive to the inclusion or exclusion of these areas.

[1] The 345Z channel is not included, due to its non-stationary and non-Gaussian noise properties.

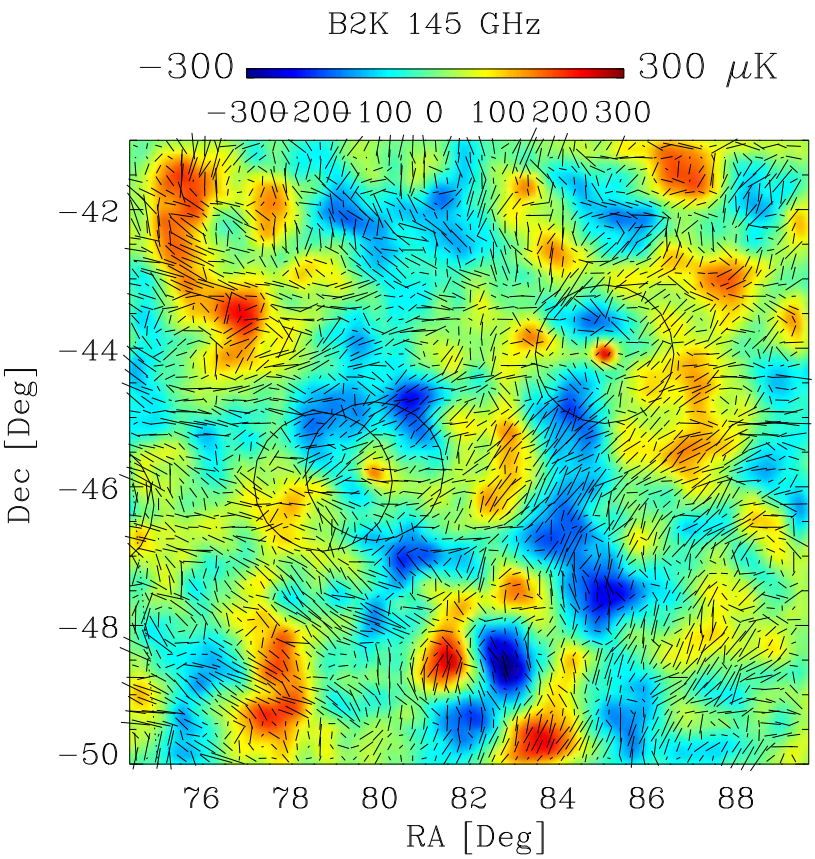


Figure 6.2: A Wiener-filtered temperature map with the polarization vectors overlaid. The kernel, which is very close to that of a 0.2° low-pass filter, has been applied to increase the signal to noise relative to the full resolution image. The median length polarization vector corresponds to $(\sqrt{Q^2+U^2}) = 14\mu$K.

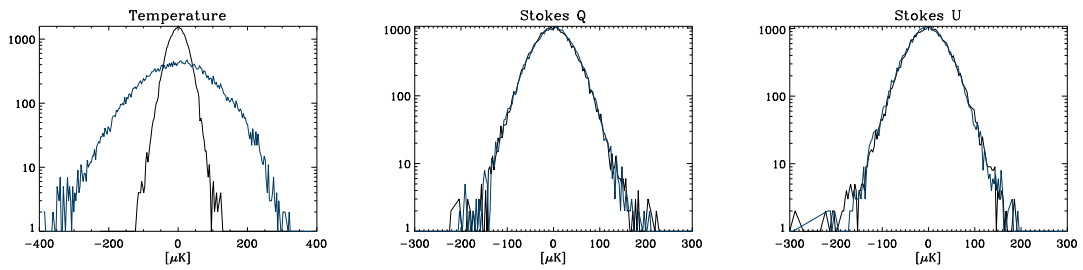


Figure 6.3: The deep field data are divided (temporally) into two halves. Separate I,Q, and U maps are generated at full (3.4′) resolution from the data subsets, and histograms of are generated for the sum (blue) and difference (black) maps. The high signal to noise is evident in the temperature map (at left), as is the noise domination of the Q (center) and U (right) maps.

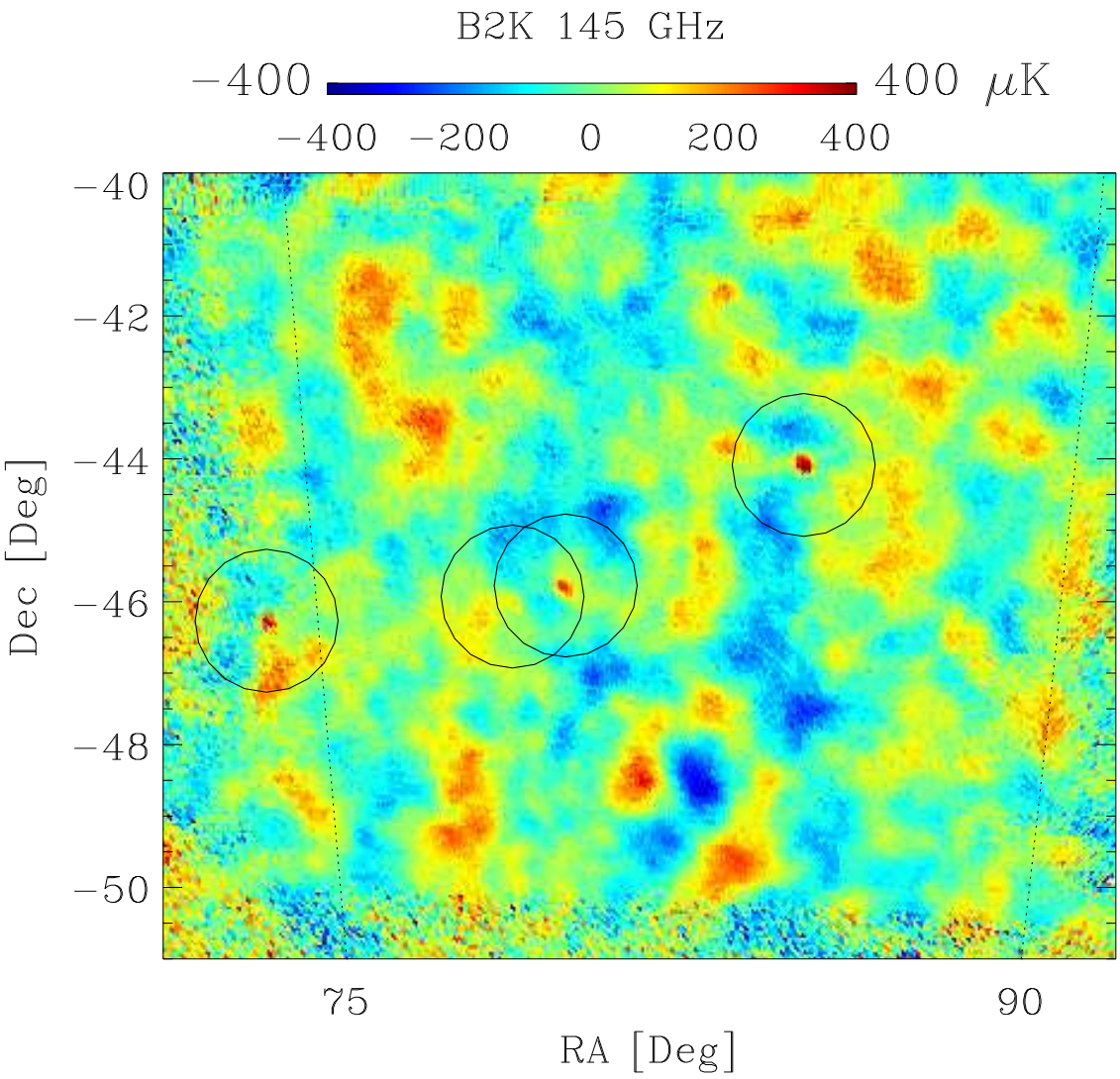


Figure 6.4: A full resolution map of the deep field obtained from the 145 GHz data.

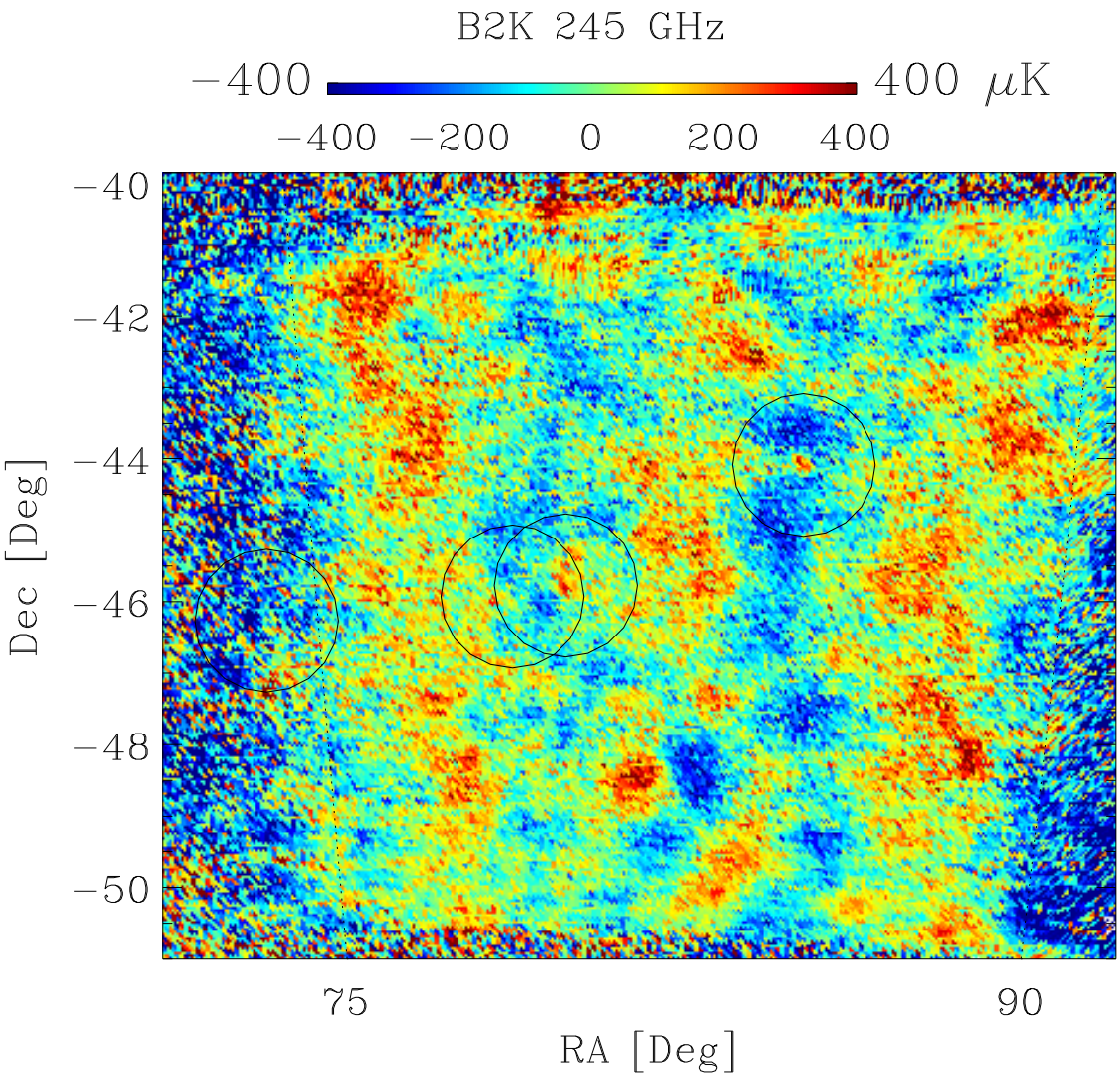


Figure 6.5: A full resolution map of the deep field obtained from the 245 GHz data.

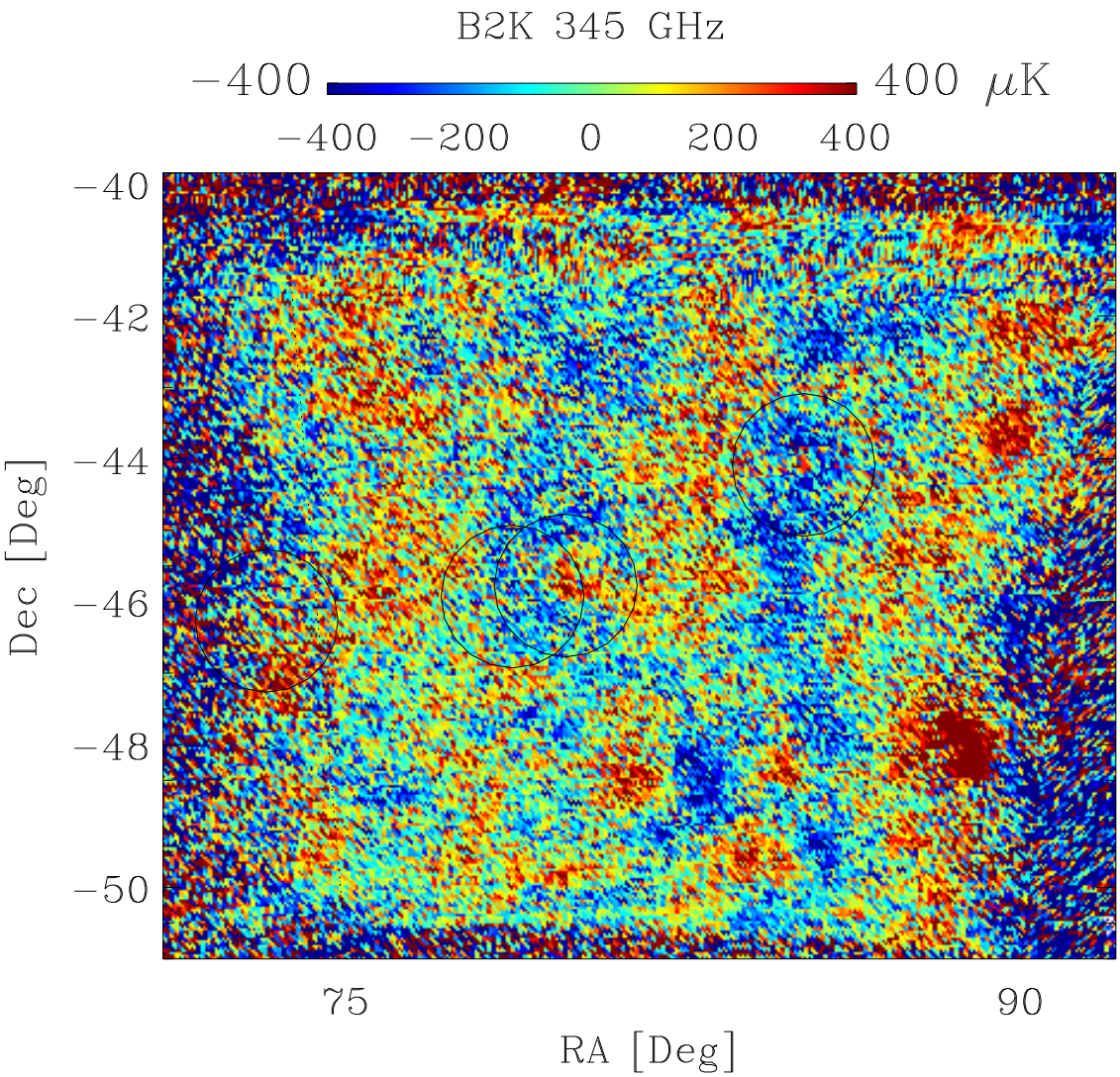


Figure 6.6: A full resolution map of the deep field obtained from the 345 GHz data.

## 6.2 Spectra

In this section we discuss the preliminary spectra derived from the 145 GHz data, which are obtained according to the prescription of Section 5.2. These spectra are derived from maps which are generated using the general signal estimator of Section 5.1.4, as well as the sum and difference method of Section 5.1.5. The spectra obtained from each method are found to be consistent with one another in the deep field.

Two full (TOD $\rightarrow$ spectra) consistency tests are performed, one of which is based on a temporal division of the data, the other on a channel-based division. In each case, the statistical weight of the data subsets are roughly equal. The temporal jackknife divides the data into a first half and second half, in which the shallow and deep scans are separately divided to provide roughly equal coverage of the sky in each subset. The channel jackknives are defined as B145W/X and B145Y/Z, which are complementary pairs of PSBs, in that the axis of sensitivity of the W/X (Y/Z) channels are rotated by 45° with regard to one another[2].

Maps are generated from both the data and the signal/noise ensembles for each subset, and the spectra are estimated from both the sum and difference of these maps. The results are compared with the analysis of the complete data set. In all cases, the "summed" spectra are consitent with the spectra derived from the full dataset. However, due to the non-optimal statistical weighting of the "summed" spectra, the errors are marginally larger than those obtained via the joint analysis of the full data set. The spectra shown are thus those obtained using the full analysis.

The noise properties of the various channels, and therefore the time domain filtering, vary slightly due to differences in the transfer functions between the channels (see Figure 4.1). This asymmetry results in a non-zero difference spectrum even in a noiseless observation free of systematics, when processed in the time domain according to Equation 5.5. The same is true of the temporal test; the scan is not symmetric for the two halves, which will result in subtle differences in the signal processing. These effects are easily incorporated into the Monte Carlo analysis by performing the

[2]Each pairing therefore provides independent measurements of both the $Q$ and $U$ parameters.

same consistency test on the simulations. The ensemble average of these difference spectra are directly subtracted from the spectra obtained from the differenced data.

### 6.2.1 Temperature

The temperature power spectrum derived from the B2K data (Figure 6.1) is shown in Figure 6.7. Two spectra are generated using staggered binnings (shown in blue and red) which are highly correlated in order to show independence of the result on the binning used. The window functions for the $\langle TT \rangle$ spectrum are shown in Figure 6.10; the bin-to-bin correlations are $\sim 15\%$ in $\mu\mathrm{K}^2$. The staggered binning is shown without error bars, in order to avoid the inference of undue statistical significance relative to the nominal binning. The B2K $\langle TT \rangle$ power spectrum is sample variance limited at multipoles of $\ell \lesssim 900$. The contribution of the beam uncertainty reported in Table 3.5 to the total (statistical plus sample variance) uncertainty is shown bracketing the errorbars in Figure 6.7.

The signal to noise with which the temperature anisotropies are detected is evident in the spectra of the differenced data, which are shown in the lower two panels. The first is the spectrum of the difference generated from the B145W/X and B145Y/Z data, the second is the temporal test. While the former (with a $\chi^2 = 20.8$ for 24 degrees of freedom) passes the test, the latter clearly fails ($\chi^2 = 73.4$). The failure of the first-half/second-half consistency test, though significant, is small compared to the uncertainties from instrumental noise and sample variance. This failure of this jackknife is believed to be due to atmospheric contamination as a result of the $\sim 8$ km decrease in altitude between the first and second halves of the flight (see Figure 3.4).

The B2K coverage is a subset of the area observed in the 1998 flight, and therefore the signal in the two data sets is completely correlated. While the high signal to noise and the signal correlation limit the value of a joint analysis, the complete independence of the pipelines provides an interesting check on the consistency of each of the results. A comparison of the BOOMERANG98 $\langle TT \rangle$ spectrum of Ruhl, et al. [145],

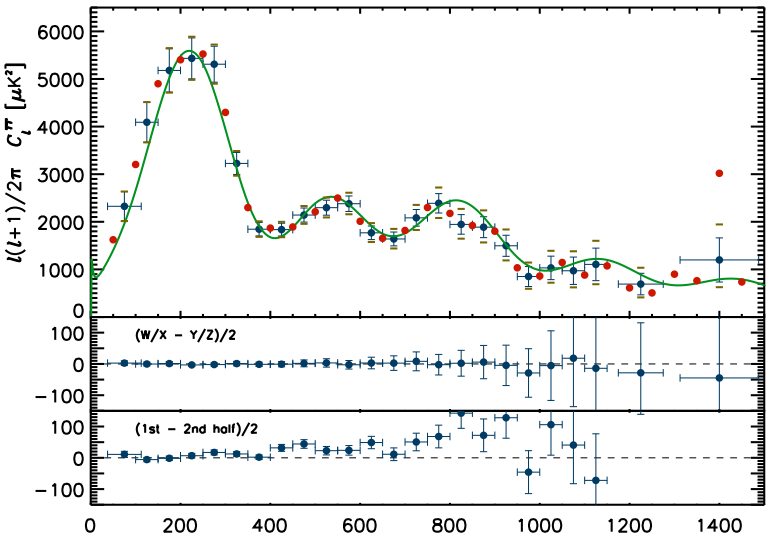


Figure 6.7: The temperature angular power spectrum, $\mathcal{C}_\ell^{\rm TT}$, derived from the B2K data. The red points represent an alternate binning, and should not be interpreted as having statistical weight beyond that of the nominally binned data, which are shown with errorbars. The beam uncertainty is indicated by the olive ticks bracketing the bandpower estimates. The continuous line is the WMAP best fit ΛCDM model, not the best fit to the B2K data, as the parameter estimation has not yet been completed. The power spectra of the consistency checks described in the text are shown in the lower two panels. The failure of the second test, which is believed to be due to atmospheric contamination in the latter half of the flight, is highly significant but appears at a very low amplitude. The systematic error associated with this failure contributes negligibly to the total (sample variance plus instrumental) uncertainty (see Table 6.1).

and the spectrum derived from the B2K data are shown in Figure 6.9. The degree of agreement suggests a good understanding of the statistical and systematic errors for each result.

The series of acoustic peaks is readily apparent in the power spectrum. As has become the common practice (see, for example, [33, 145, 130]) we characterize the location, amplitude and significance of the features in the power spectrum in a model dependent way through a comparison of the goodness of fit of a parabola (or Gaussian) to each set of five contiguous bins [3]. In this case, we fit a Gaussian in the vicinity of

[3]While the result is relatively insensitive to the number of bins that are fit, as the subsets get larger than the characteristic size of the features in the spectrum, the reduced $\chi^2$ clearly will degrade. Five bins is found to be the largest set which does not result in a poor goodness of fit statistic over the full range in $\ell$.

the first peak, and parabolas to the other features.

As is well known, the likelihoods of the band powers are not Gaussian distributed [14]. We therefore transform to the "offset log-normal" variables whose likelihood distributions are better approximated by a Gaussian [6, 15]. The transformation is a simple one,

$$Z_b \equiv \ln(\mathcal{C}_b + x_b)$$

where the noise offsets, $x_b$, are determined from the $N_\ell$ from Equation 5.35. The inverse Fisher (covariance) matrix must similarily be transformed,

$$(F^Z)^{-1}_{bb'} = \frac{F^{-1}_{bb'}}{(\mathcal{C}_b + x_b)(\mathcal{C}_{b'} + x_{b'})}.$$

In addition, the models to be fit are windowed according to Figure 6.10, namely

$$\mathcal{C}^{\rm XX}_b \equiv \frac{\mathcal{I}\left[W^b_\ell \mathcal{C}^{\rm XX}_\ell\right]}{\mathcal{I}\left[W^b_\ell\right]}$$

where,

$$\mathcal{I}\left[f_\ell\right] \equiv \sum_\ell \frac{(\ell + \frac{1}{2})}{\ell(\ell+1)} f_\ell.$$

The parabolic model,

$$\mathcal{C}^m_\ell = \mathcal{C}_c(\ell - \ell_0)^2 + \mathcal{C}_0$$

is similarily transformed, and the three dimensional likelihoods are calculated directly on a grid about each of the best fit locations. The $\Delta\chi^2$ contours for the curvature-marginalized likelihoods are shown in Figure 6.11. In previously published works, the significance of a detection has been determined by the curvature of the likelihood at the peak of the distribution [33, 145]. However, as is evident in Figure 6.8, the distributions are highly non-Gaussian. We therefore determine the significance of the detections from the amplitude of the marginalized likelihood at zero curvature.

The first three peaks and three dips in the power spectrum are detected with high confidence, whereas the fourth feature is consistent with zero curvature. For comparison, the same analysis was applied to the BOOMERANG98 data from the

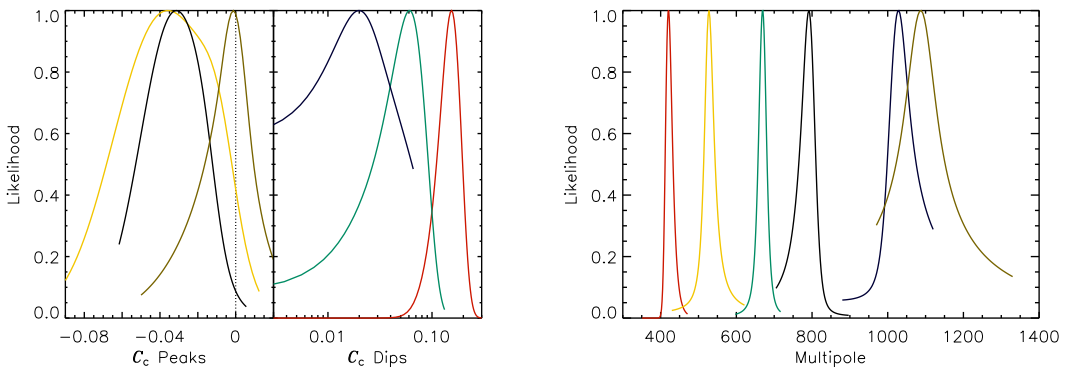


Figure 6.8: The marginalized likelihoods for the curvature parameter, $\mathcal{C}_c$, (at left) and the multipole, $\ell_0$, (at right) of each feature in the temperature power spectrum. All three dips in the power spectrum are detected with high confidence, whereas only the first three peaks are detected with curvature significantly different than zero.

Ruhl, et al. release [145], as well as the binned first-year WMAP data [11]. The results of all three analyses are compared in Table 6.2, and indicate a remarkable degree of consistency between the three independent experiments.

The degree of concordance in temperature observations is further illustrated in Figure 6.12, which shows a compilation of the power spectrum estimates from four experiments which apply three very different experimental approaches, with observations probing nearly a decade in electromagnetic frequency.

The joint cosmological parameter analysis of this dataset is currently underway, but not yet complete. The B2K temperature data, rather than the polarization spectra, will drive the statistical significance of the dataset. In particular, the statistical power to constrain parameters will derive from the data covering the multipole range from $600 \lesssim \ell \lesssim 1000$, over which the B2K data represent the most precise measurements to date.

The most important results from B2K, if not in terms of their power to constrain parameters then in their ability to confirm models, are the results of the analysis of the polarization data. We turn to this analysis in the following section.

Consistency Tests

| $\ell_b$ | $\mathcal{C}_b$ | $\Delta\mathcal{C}_b$ | (WX-YZ)/2 | (1st-2nd)/2 |
|---|---|---|---|---|
| 75 | 2325 | 310 | 11 ± 7 | 11 ± 10 |
| 125 | 4091 | 418 | -1 ± 6 | -6 ± 7 |
| 175 | 5180 | 455 | 5 ± 6 | -2 ± 7 |
| 225 | 5433 | 431 | -13 ± 5 | 7 ± 7 |
| 275 | 5310 | 378 | -8 ± 5 | 17 ± 8 |
| 325 | 3226 | 231 | 5 ± 7 | 12 ± 8 |
| 375 | 1845 | 142 | -5 ± 7 | 2 ± 7 |
| 425 | 1836 | 134 | -3 ± 8 | 32 ± 11 |
| 475 | 2142 | 148 | 7 ± 11 | 44 ± 14 |
| 525 | 2297 | 158 | 13 ± 13 | 23 ± 14 |
| 575 | 2380 | 163 | -11 ± 14 | 24 ± 15 |
| 625 | 1769 | 142 | 12 ± 19 | 49 ± 20 |
| 675 | 1640 | 145 | 11 ± 23 | 11 ± 20 |
| 725 | 2083 | 175 | 33 ± 30 | 51 ± 28 |
| 775 | 2388 | 204 | -10 ± 33 | 68 ± 36 |
| 825 | 1945 | 206 | 9 ± 41 | 143 ± 48 |
| 875 | 1887 | 220 | 24 ± 53 | 72 ± 52 |
| 925 | 1496 | 221 | -18 ± 65 | 128 ± 66 |
| 975 | 851 | 210 | -115 ± 78 | -46 ± 69 |
| 1025 | 1032 | 247 | -21 ± 111 | 106 ± 97 |
| 1075 | 972 | 287 | 73 ± 155 | 41 ± 123 |
| 1125 | 1105 | 342 | -56 ± 190 | -72 ± 149 |
| 1225 | 692 | 226 | -113 ± 160 | 273 ± 134 |
| 1400 | 1199 | 463 | -179 ± 451 | 746 ± 313 |

Table 6.1: The temperature power spectra and consistency test results. The ensemble average of the spectra of the simulated difference maps has been subtracted from the spectra derived from the data. The tests return a $\chi^2 = 20.8(73.4)$ to zero for 24 degrees of freedom, for the channel (temporal) difference power spectra. While the significance of the first-half/second-half failure is high, the amplitude of the failure is small compared to the combined uncertainty due to sample variance and instrumental error.

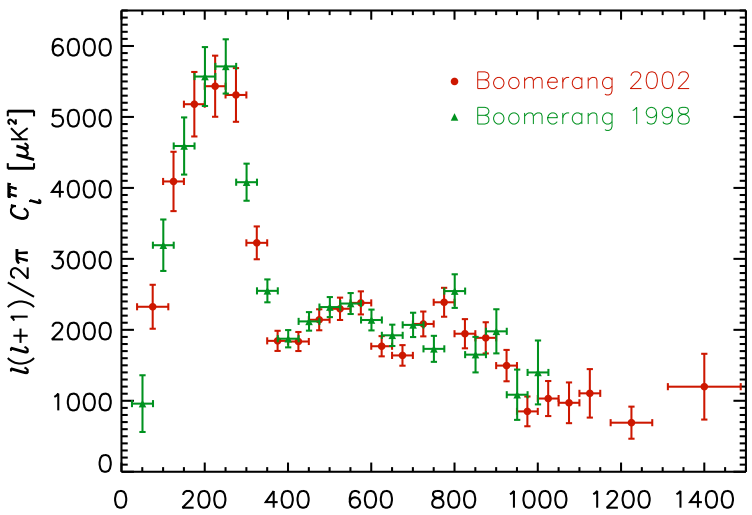


Figure 6.9: A comparison of the spectra derived from the BOOMERANG98 and B2K data sets. While the sky coverage is common, and therefore the signal is correlated, the experiments and analysis are completely independent. The consistency of the spectra suggest a good understanding of systematics and noise in both experiments.

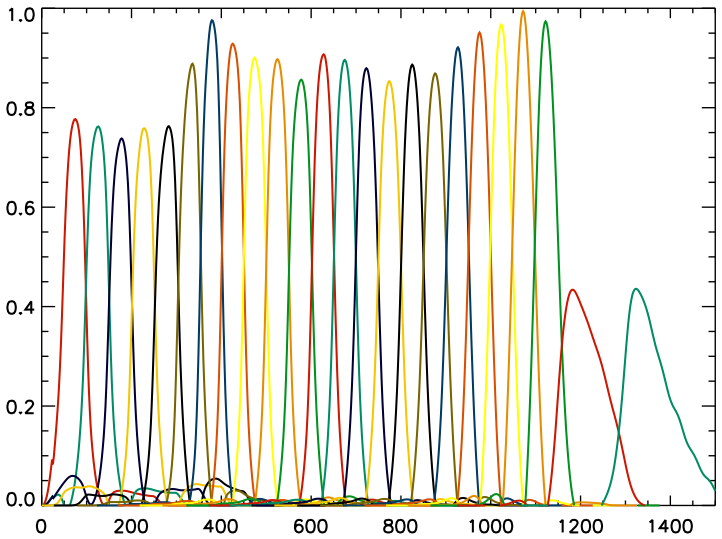


Figure 6.10: The normalized window functions, $W_\ell^b$, corresponding to the bandpowers in Figure 6.7 and Table 6.1.

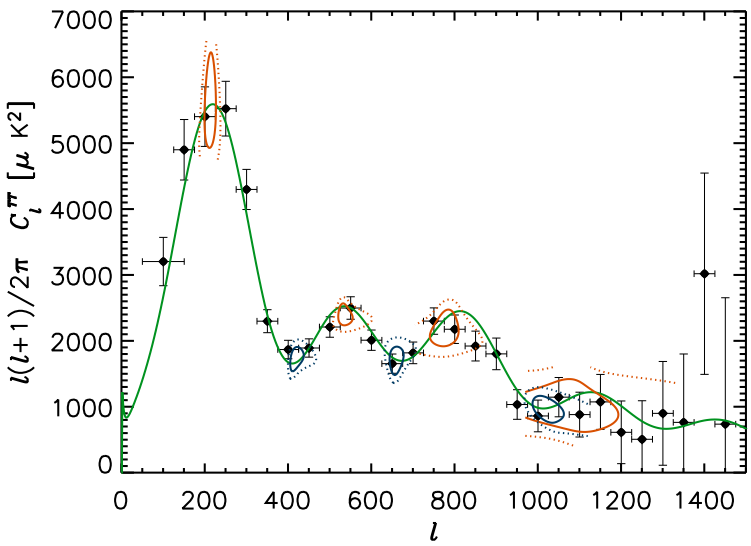


Figure 6.11: The CMB spectrum with the one and two-sigma $\Delta\chi^2$ contours for the fits shown in red (blue) for the features determined to have negative (positive) curvature. The likelihoods have been marginalized over the curvature parameter. The fourth "peak" only marginally favors negative curvature over a flat bandpower, and is not considered a detection.

Features in the Temperature Power Spectrum

| feature | $\ell_{\rm B2K}$ | $\Delta T^2_{\rm B2K}$ | $\ell_{\rm B98}$ | $\Delta T^2_{\rm B98}$ | $\ell_{\rm WMAP}$ | $\Delta T^2_{\rm WMAP}$ |
|---|---|---|---|---|---|---|
| Peak 1 | $214\ ^{+8}_{-9}$ | $5550\ ^{+498}_{-476}$ | $217\ ^{+10}_{-10}$ | $5551\ ^{+477}_{-443}$ | $222\ ^{+3}_{-2}$ | $5385\ ^{+147}_{-157}$ |
| Valley 1 | $416\ ^{+12}_{-7}$ | $1730\ ^{+120}_{-105}$ | $411\ ^{+9}_{-7}$ | $1870\ ^{+136}_{-120}$ | $418\ ^{+5}_{-4}$ | $1660\ ^{+62}_{-62}$ |
| Peak 2 | $534\ ^{+10}_{-9}$ | $2382\ ^{+100}_{-119}$ | $526\ ^{+17}_{-14}$ | $2316\ ^{+119}_{-121}$ | $530\ ^{+15}_{-8}$ | $2404\ ^{+89}_{-64}$ |
| Valley 2 | $659\ ^{+10}_{-10}$ | $1725\ ^{+147}_{-137}$ | $(677)\ ^{+65}_{-29}$ | $(1958)\ ^{+200}_{-170}$ | — | — |
| Peak 3 | $783\ ^{+15}_{-20}$ | $2146\ ^{+180}_{-188}$ | $(766)\ ^{+42}_{-43}$ | $(2080)\ ^{+261}_{-227}$ | — | — |
| Valley 3 | $1033\ ^{+39}_{-23}$ | $911\ ^{+194}_{-187}$ | — | — | — | — |
| Peak 4 | $(1090)\ ^{+44}_{-49}$ | $(1020)\ ^{+190}_{-198}$ | — | — | — | — |

Table 6.2: A comparison of the locations and amplitudes of the features in the temperature power spectrum derived from the B2K, BOOMERANG98, and WMAP datasets. The values and ($1\sigma$) errors are obtained from the marginalized likelihood distributions directly. Values in parenthesis indicate a curvature parameter consistent with zero at $2\sigma$ level, or greater (that is, a marginalized likelihood for the curvature parameter for which $\mathcal{L}(\mathcal{C}_c = 0) \geq 2\sigma$). Note that this analysis has been performed on the binned WMAP data, instead of on the full dataset, for better comparison with the BOOMERANG window functions. The full resolution WMAP constraints on the first peak and dip locations are stronger than (but also consistent with) those reported here. For the full resolution analysis of the first year WMAP data, see [130].

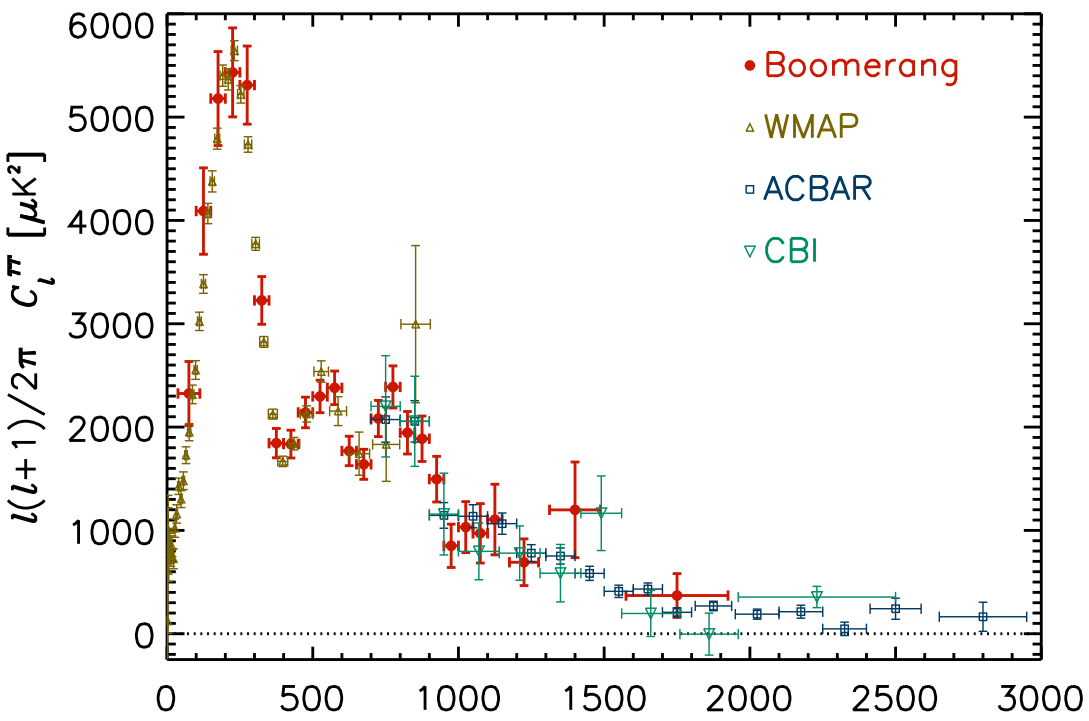


Figure 6.12: A comparison of the current state of observations of the angular power spectrum of the CMB temperature fluctuations. The temperature power spectrum is now well characterized at multipoles of $2 < \ell \lesssim 3000$, although the resolution (in $\ell$) of the measurements beyond $\ell \gtrsim 1500$ are not sufficiently high to resolve any features. Remarkably, the experiments are in good agreement with one another over the entire range of angular scale.

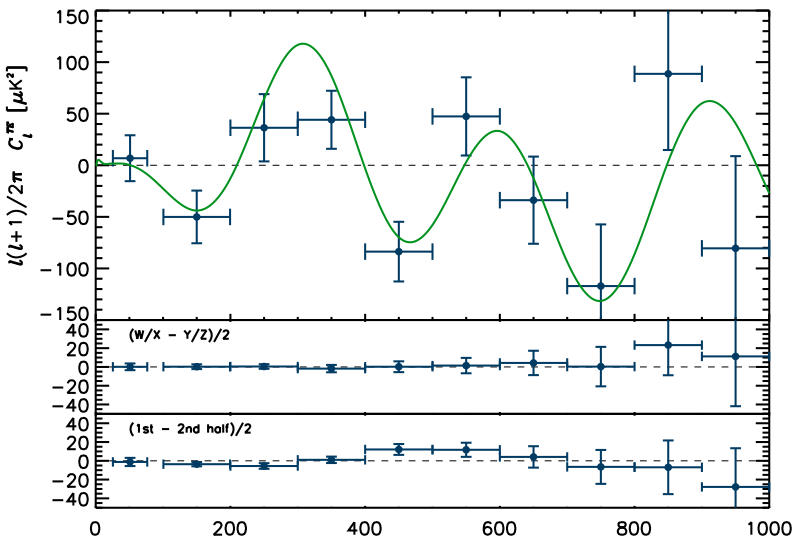


Figure 6.13: The correlation between the temperature anisotropies and the $E$-mode polarization. The correlation is seen to be out of phase with the acoustic peaks in the temperature power spectrum, as expected from polarized emission due to quadrupole anisotropies sourced by velocity gradients in the optically thin plasma present during the epoch of last scattering.

### 6.2.2 Polarization

The first statistical detection of polarization in the CMB was reported by the DASI team in 2002 [94, 102], followed by the WMAP measurement of the $\langle TE \rangle$ correlation in the release of the first year data [130]. Recently, the CBI and CAPMAP experiments have published detections of an $E$-mode polarization in the CMB [142, 4]. Both DASI and the CBI are interferometers operating at 20 GHz [103], while WMAP is a coherent (HEMT-based) instrument with radiometers operating in five bands between 20 and 90 GHz [10], and CAPMAP is a 90 GHz heterodyne correlation polarimeter [3]. B2K is the first bolometric instrument to measure CMB polarization, and is the first detection made at frequencies above 90 GHz.

The PSB receivers flown on B2K are particularly well suited to measure the temperature-polarization cross correlation, as it measures the polarized and unpolarized components of the radiation field through identical optical and filter elements. B2K's measurement of the $\langle TE \rangle$ power spectrum is shown in Figure 6.13, along with

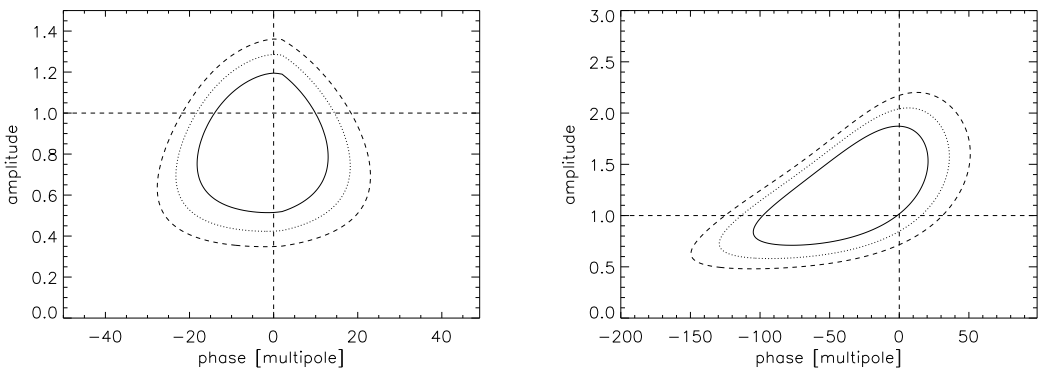


Figure 6.14: The 1,2, and $3\sigma$ likelihood contours for a scaling in amplitude and phase of a fiducial $\langle TE \rangle$ spectrum (left) and $\langle EE \rangle$ spectrum (right).

the difference spectra. Both the channel and first-half/second-half jackknife tests are easily passed by the polarization spectra. The failure of the temperature power spectrum to pass the first-half/second-half test is thought to be due to atmospheric effects. The atmosphere is expected to be almost entirely unpolarized (linearly), and therefore is expected to impact the polarization less than the total intesity data.

B2K measures the $\langle TE \rangle$ angular power spectrum (Figure 6.13) over a wide range of $\ell$, extending the WMAP result at $\ell \lesssim 400$ with modest $\ell$ resolution to a multipole $\ell \sim 1000$. The measurement of the $\langle EE \rangle$ angular power spectrum (Figure 6.15) extends to a multipole $\ell \lesssim 800$. The BOOMERANG data confirm the expected phase relationship between the polarization and temperature anisotropies, providing support, independent of the temperature anisotropies alone, for the scenario in which CMB features are sourced by acoustic oscillations in the primordial plasma. B2K detects no $B$-mode polarization (Figure 6.16), and provide an upper limit to the $B$-mode amplitude to $\leq 2\mu\mathrm{K}^2$ over a broad band from $100 < \ell < 600$ in $\ell(\ell+1)/2\pi\ C_\ell^{\mathrm{BB}}$.

The amplitude of the detections are consistent with the level of polarization expected in the context of the standard cosmological models, namely that of (dominantly) adiabatic initial conditions for a $\Lambda$CDM concordance model [110]. The significance of the detection can be characterized in terms of the relative likelihood of this concordance model versus alternate possiblities, including the null hypothesis.

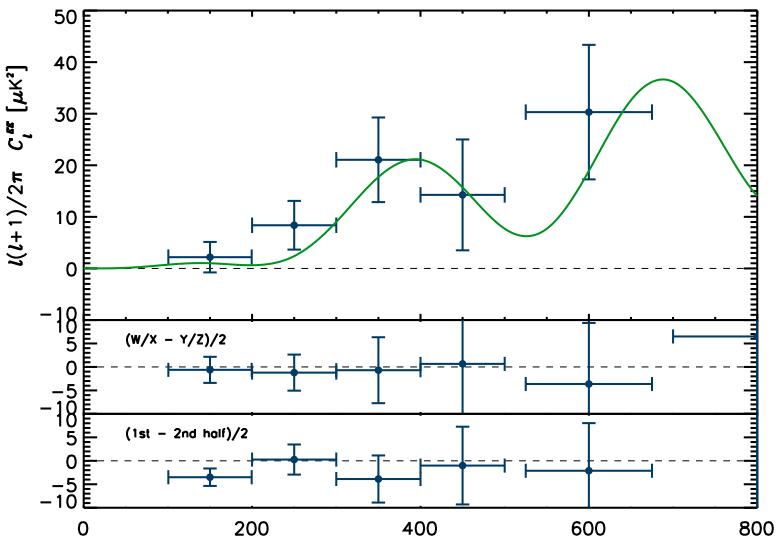


Figure 6.15: The $E$-mode polarization power spectrum derived from the B2K dataset. The detection is consistent with the signal expected from adiabatic ΛCDM concordance models.

We investigate this likelihood by paramterizing the $\langle TE \rangle$ and $\langle EE \rangle$ spectra predicted from the best fit adiabatic concordance model with an amplitude and phase. The parameterization is arbitrary - a multiplicative factor in amplitude, and a shift of the fiducial spectrum in $\ell$ for the phase - and is not representative of any particular underlying physical model. Given that the data are consistent with a concordance model, this excersize enables a model independent statement to be made regarding the significance of a positive detection.

The results of this analysis are shown in Figure 6.14. The one, two and three sigma likelihood contours are shown for the amplitude and phase of the $\langle TE \rangle$ spectrum (at left) and the $\langle EE \rangle$ spectrum (at right). Both the cross correlation and the $E$-mode spectrum are inconsistent with the null hypothesis at greater than the $5\sigma$ level. While both the $E$-mode spectrum and the cross correlation are consistent with the nominal phase, the $E$-mode spectrum in particular allows a shift to lower multipoles. In the joint analysis of the $\langle TE \rangle$ and $\langle EE \rangle$ spectra, the cross-correlation carries more statistical weight, and dominates the likelihood.

The power spectra, window functions, and covariance (inverse Fischer) matrices

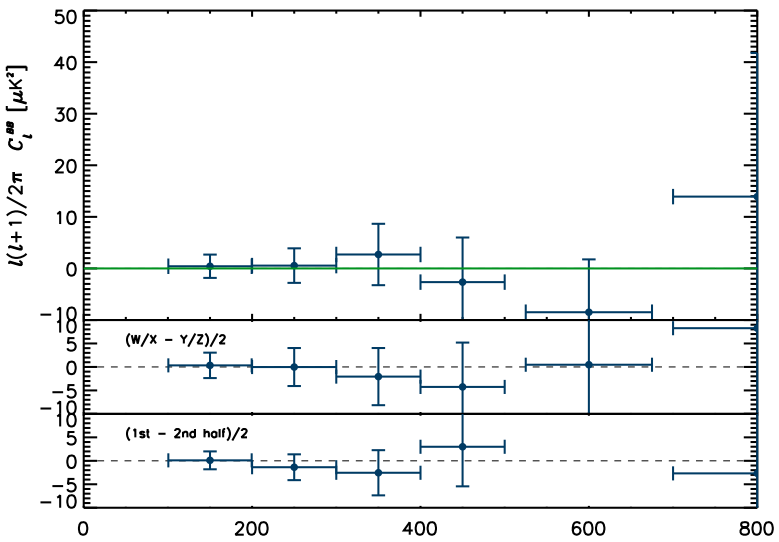


Figure 6.16: The $B$-mode polarization power spectrum derived from the B2K dataset. No power is seen in the $B$-mode spectrum which is constrained by an upper limit of $\sim$ $2\mu$K over a broad band from $100 < \ell < 600$.

for all the spectra will be made publicly avaliable in the B2K publications [84, 139, 123].

## 6.3 Conclusion

In addition to making a precise measurement of the unpolarized power spectrum, the B2K experiment has measured the $E$-mode polarization in the CMB, confirming the recent detections reported by the DASI and CBI teams, as well as the temperature-polarization cross correlation reported by the WMAP team [102, 142, 130]. The polarization power spectrum is consistent with that expected from a $\Lambda$CDM concordance cosmology characterized by adiabatic initial conditions, as would be expected from the most simple Inflationary models.

From an experimental point of view, the B2K results serve as an important proof of concept for the second generation of CMB polarimeters which are now being deployed (such as QUAD and BICEP), as well as for *Planck* HFI, all of which are based around receivers identical to the ones designed for, and flown on, B2K [83, 19, 87, 157, 156].

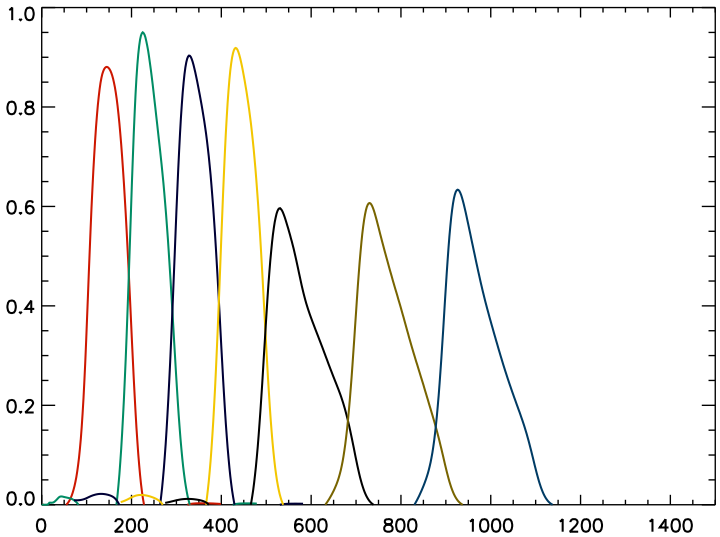


Figure 6.17: The window funtions for the polarization power spectra. The bin-to-bin correlations are at the 10% level.

Both the experimental procedures and the analytical methods employed by B2K are directly applicable to these experiments.

The field of CMB polarization is rapidly maturing. As can be seen in Figure 6.18, a variety of experiments, applying widely varying experimental approaches and susceptible to different systematic effects, have produced broadly consistent detections. The second generation of polarization experiments which are now coming on line are likely to produce sample variance limited measurements of the temperature and polarization anisotropies induced by scalar fluctuations over a broad range of angular scales. However, it is likely that an experiment with sufficient sensitivity and sky coverage to make a definitive measurement of the $B$-mode signal is still a number of years away. The imprint of primordial gravitational waves on the microwave background provides a direct probe of Inflation. As such, a measurement of this tensorial component represents one of the most important goals for fundamental physics in the decade to come.

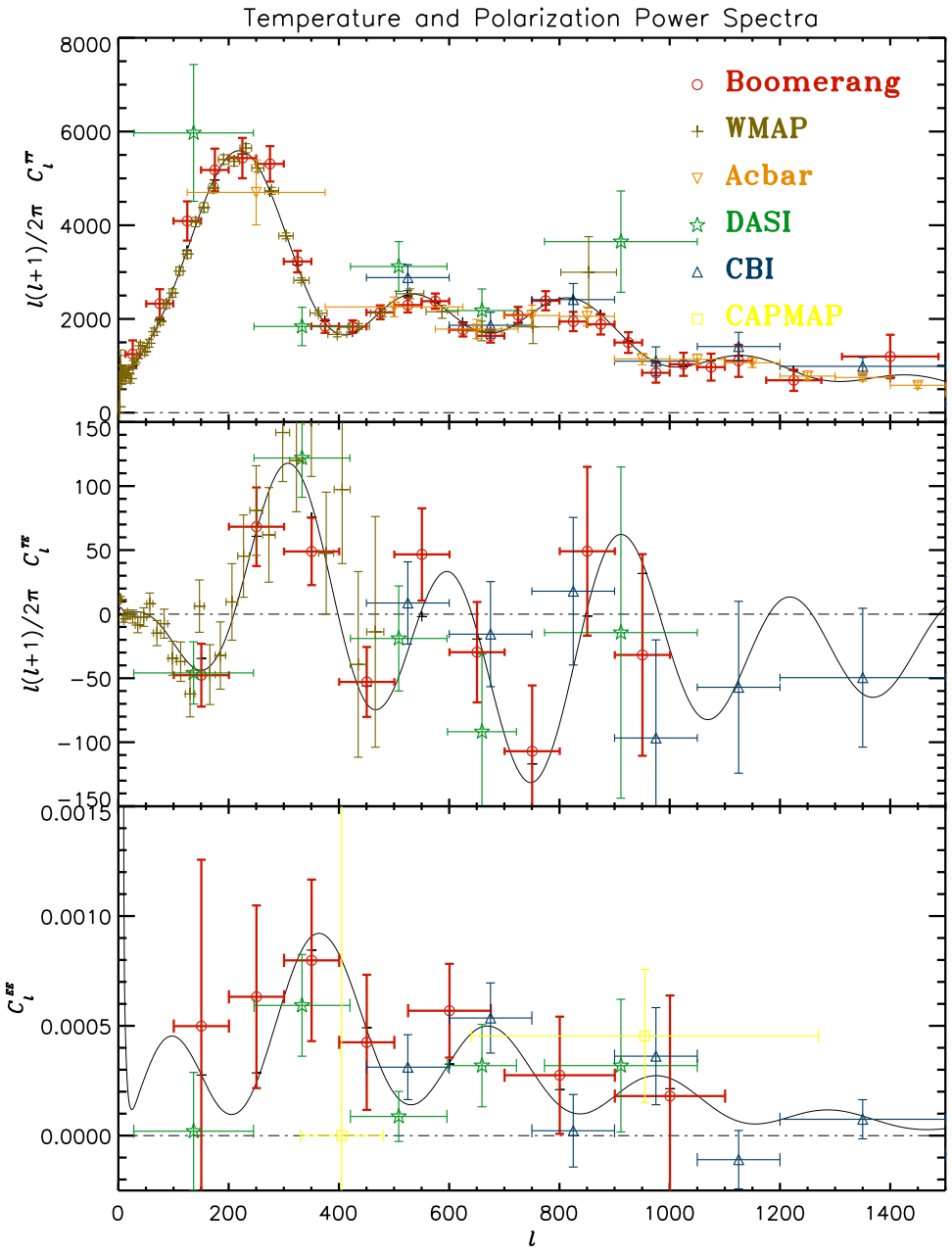


Figure 6.18: A compilation of the most recent measurements of the temperature and polarization power spectra of the CMB, including B2K, CBI [142], WMAP [130], DASI [102], and CAPMAP [4]. The observational field has progressed quickly, particularly in polarization, with the spectra becoming well characterized less than three years after the first reported detection. The results shown here are derived from data obtained with orbital (WMAP), terrestrial (CBI,DASI,CAPMAP) and balloon-borne instruments (B2K) using coherent interferometric receivers (CBI, DASI), and both coherent (WMAP,CAPMAP) and bolometric (2kn) single dish telescopes. The experiments span more than a decade in electromagnetic frequency. △

# Bibliography

[1] R. A. Alpher, R. Herman, and G. A. Gamow. Thermonuclear Reactions in the Expanding Universe. *Physical Review*, 74:1198–1199, November 1948.

[2] R. Anthes, C. Rocken, and Y. H. Kuo. Applications of cosmic to meteorology. *Terrestrial Atmospheric and Oceanic Sciences*, 11(1):115–156, March 2000.

[3] D. Barkats. The CAPMAP instrument and its first season. *New Astronomy Review*, 47:1077–1081, December 2003.

[4] D. Barkats, C. Bischoff, P. Farese, L. Fitzpatrick, T. Gaier, J. O. Gundersen, M. M. Hedman, L. Hyatt, J. J. McMahon, D. Samtleben, S. T. Staggs, K. Vanderlinde, and B. Winstein. First measurements of the polarization of the cosmic microwave background radiation at small angular scales from capmap. *preprint*, September 2004.

[5] C. Barnes, M. Limon, L. Page, C. Bennett, S. Bradley, M. Halpern, G. Hinshaw, N. Jarosik, W. Jones, A. Kogut, S. Meyer, O. Motrunich, G. Tucker, D. Wilkinson, and E. Wollack. The MAP Satellite Feed Horns. *Astrophysical Journal Supplement Series*, 143:567–576, December 2002.

[6] J. G. Bartlett, M. Douspis, A. Blanchard, and M. Le Dour. An approximation to the likelihood function for band-power estimates of cmb anisotropies. *Astronomy and Astrophysics*, pages astro–ph/9903045.

[7] R. Bean, A. Melchiorri, and J. Silk. Recombining WMAP: Constraints on ionizing and resonance radiation at recombination. *Physical Review D*, 68(8):083501, October 2003.

[8] J. Beeman. http://www.haller-beeman.com.

[9] C. L. Bennett, A. J. Banday, K. M. Gorski, G. Hinshaw, P. Jackson, P. Keegstra, A. Kogut, G. F. Smoot, D. T. Wilkinson, and E. L. Wright. Four-Year COBE DMR Cosmic Microwave Background Observations: Maps and Basic Results. *Astrophysical Journal Letters*, 464:L1, June 1996.

[10] C. L. Bennett, M. Bay, M. Halpern, G. Hinshaw, C. Jackson, N. Jarosik, A. Kogut, M. Limon, S. S. Meyer, L. Page, D. N. Spergel, G. S. Tucker, D. T. Wilkinson, E. Wollack, and E. L. Wright. The Microwave Anisotropy Probe Mission. *Astrophysical Journal*, 583:1–23, January 2003.

[11] C. L. Bennett, M. Halpern, G. Hinshaw, N. Jarosik, A. Kogut, M. Limon, S. S. Meyer, L. Page, D. N. Spergel, G. S. Tucker, E. Wollack, E. L. Wright, C. Barnes, M. R. Greason, R. S. Hill, E. Komatsu, M. R. Nolta, N. Odegard, H. V. Peiris, L. Verde, and J. L. Weiland. First-Year Wilkinson Microwave Anisotropy Probe (WMAP) Observations: Preliminary Maps and Basic Results. *Astrophysical Journal Supplement Series*, 148:1–27, September 2003.

[12] A. Benoît, P. Ade, A. Amblard, R. Ansari, É. Aubourg, S. Bargot, J. G. Bartlett, J.-P. Bernard, R. S. Bhatia, A. Blanchard, J. J. Bock, A. Boscaleri, F. R. Bouchet, A. Bourrachot, P. Camus, F. Couchot, P. de Bernardis, J. Delabrouille, F.-X. Désert, O. Doré, M. Douspis, L. Dumoulin, X. Dupac, P. Filliatre, P. Fosalba, K. Ganga, F. Gannaway, B. Gautier, M. Giard, Y. Giraud-Héraud, R. Gispert, L. Guglielmi, J.-C. Hamilton, S. Hanany, S. Henrot-Versillé, J. Kaplan, G. Lagache, J.-M. Lamarre, A. E. Lange, J. F. Macías-Pérez, K. Madet, B. Maffei, C. Magneville, D. P. Marrone, S. Masi, F. Mayet, A. Murphy, F. Naraghi, F. Nati, G. Patanchon, G. Perrin, M. Piat, N. Ponthieu, S. Prunet, J.-L. Puget, C. Renault, C. Rosset, D. Santos, A. Starobinsky, I. Strukov, R. V. Sudiwala, R. Teyssier, M. Tristram, C. Tucker, J.-C. Vanel, D. Vibert, E. Wakui, and D. Yvon. Cosmological constraints from Archeops. *Astronomy and Astrophysics*, 399:L25–L30, March 2003.

[13] J. R. Bond, G. Efstathiou, and M. Tegmark. Forecasting cosmic parameter errors from microwave background anisotropy experiments. *Mon. Not. R. Astron. Soc.*, 291:L33–L41, November 1997.

[14] J. R. Bond, A. H. Jaffe, and L. Knox. *Physical Review D*, 57:2117–2137, February 1998.

[15] J. R. Bond, A. H. Jaffe, and L. Knox. Radical Compression of Cosmic Microwave Background Data. *Astrophysical Journal*, 533:19–37, April 2000.

[16] M. Born and E. Wolf. *Principals of Optics, sixth edition.* Pergammon, 1980.

[17] J. Borrill. In *Proceedings of the 5th European SGI/Cray MPP Workshop, Bologna, Italy*, 1999.

[18] A. Boscaleri *et al.*. *Measurement Science and Technology*, 5:190, 1994.

[19] M. Bowden, A. N. Taylor, K. M. Ganga, P. A. R. Ade, J. J. Bock, G. Cahill, J. E. Carlstrom, S. E. Church, W. K. Gear, J. R. Hinderks, W. Hu, B. G. Keating, J. Kovac, A. E. Lange, E. M. Leitch, B. Maffei, O. E. Mallie, S. J. Melhuish, J. A. Murphy, G. Pisano, L. Piccirillo, C. Pryke, B. A. Rusholme, C. O'Sullivan, and K. Thompson. Scientific optimization of a ground-based cmb polarization experiment. *Monthly Notices RAS*, 349(1):321–321, 2004.

[20] W. N. Brandt, C. R. Lawrence, A. C. S. Readhead, J. N. Pakianathan, and T. M. Fiola. Separation of foreground radiation from cosmic microwave background anisotropy using multifrequency measurements. *Astrophysical Journal*, 424:1–21, March 1994.

[21] M. L. Brown, P. G. Castro, and A. N. Taylor. CMB temperature and polarization pseudo-$C_\ell$ estimators and their covariances. *submitted to MNRAS*, pages astro–ph/0410394, October 2004.

[22] M. Bucher, K. Moodley, and N. Turok. General primordial cosmic perturbation. *Physical Review D*, 62(8):083508, October 2000.

[23] M. Bucher, K. Moodley, and N. Turok. Constraining Isocurvature Perturbations with Cosmic Microwave Background Polarization. *Physical Review Letters*, 87(19):191301, November 2001.

[24] M. Bucher, K. Moodley, and N. Turok. Constraining Isocurvature Perturbations with Cosmic Microwave Background Polarization. *Physical Review Letters*, 87, November 2001.

[25] M. Bucher, K. Moodley, and N. Turok. Primordial Isocurvature Perturbations: Testing the Adiabaticity of the CMB Anisotropy. In *AIP Conf. Proc. 555: Cosmology and Particle Physics*, page 313, 2001.

[26] E. F. Bunn, M. Zaldarriaga, M. Tegmark, and A. de Oliveira-Costa. E/B decomposition of finite pixelized CMB maps. *Physical Review D*, 67, January 2003.

[27] N. Caderni *et al.*. *Phys. Rev. D.*, 17, 1978.

[28] K. Coble, P. A. R. Ade, J. J. Bock, J. R. Bond, J. Borrill, A. Boscaleri, C. R. Contaldi, B. P.Crill, P. de Bernardis, K. Ganga, M. Giacometti, E. Hivon, V. V. Hristov, A. Iacoangeli, A. H. Jaffe, W. C. Jones, A. E. Lange, L. Martinis, S. Masi, P. Mason, P. D. Mauskopf, A. Melchiorri, T. Montroy, C. B. Netterfield, L. Nyman, E. Pascale, F. Piacentini, D. Pogosyan, G. Polenta, F. Pongetti, S. Prunet, G. Romeo, J. E. Ruhl, and F. Scaramuzzi. Observations of Galactic and Extra-galactic Sources From the BOOMERANG and SEST Telescopes. *Astrophysical Journal Supplement*, 2003.

[29] C. R. Contaldi, J. R. Bond, B. .P. Crill, E. Hivon, W. C. Jones, C. MacTavish, T. Montroy, C. .B. Netterfield, D. Pogosyan, and S. Prunet. XFASTER: A Faster Monte-Carlo CMB Power Spectrum Estimator for Multiple Polarization Observations. *in preparation*, 2005.

[30] R. Cowen. Cosmology Solved? *Science News*, 154(25):392, December 1998.

[31] B. P. Crill, P. A. R. Ade, Artusa D. R., R. S. Bhatia, J. J. Bock, A. Boscaleri, P. Cardoni, S. E. Church, K. Coble, P. de Bernardis, G. De Troia, P. Farese, K. M. Ganga, M. Giacometti, C. V. Haynes, E. Hivon, V. V. Hristov, A. Iacoangeli, W. C. Jones, A. E. Lange, L. Martinis, S. Masi, P. V. Mason, P. D. Mauskopf, L. Miglio, T. Montroy, C. B. Netterfield, C. G. Paine, E. Pascale, F. Piacentini, D. Pogosyan, F. Pongetti, G. Polenta, F. Pongetti, G. Romeo, J. E. Ruhl, F. Scaramuzzi, D. Sforna, and A. D. Turner. BOOMERANG: A Balloon-borne Millimeter Wave Telescope and Total Power Receiver for Mapping Anisotropy in the Cosmic Microwave Background. *Astrophysical Journal Supplement*, page 527, 2002.

[32] Brendan P. Crill. PhD thesis, 2000.

[33] P. de Bernardis, P. A. R. Ade, J. J. Bock, J. R. Bond, J. Borrill, A. Boscaleri, K. Coble, C. R. Contaldi, B. P. Crill, G. De Troia, P. Farese, K. Ganga, M. Giacometti, E. Hivon, V. V. Hristov, A. Iacoangeli, A. H. Jaffe, W. C. Jones, A. E. Lange, L. Martinis, S. Masi, P. Mason, P. D. Mauskopf, A. Melchiorri, T. Montroy, C. B. Netterfield, E. Pascale, F. Piacentini, D. Pogosyan, G. Polenta, F. Pongetti, S. Prunet, G. Romeo, J. E. Ruhl, and F. Scaramuzzi. Multiple Peaks in the Angular Power Spectrum of the Cosmic Microwave Background: Significance and Consequences for Cosmology. *Astrophysical Journal*, 564:559–566, January 2002.

[34] P. de Bernardis, P. A. R. Ade, J. J. Bock, J. R. Bond, J. Borrill, A. Boscaleri, K. Coble, B. P. Crill, G. De Gasperis, P. C. Farese, P. G. Ferreira, K. Ganga, M. Giacometti, E. Hivon, V. V. Hristov, A. Iacoangeli, A. H. Jaffe, A. E. Lange, L. Martinis, S. Masi, P. V. Mason, P. D. Mauskopf, A. Melchiorri, L. Miglio, T. Montroy, C. B. Netterfield, E. Pascale, F. Piacentini, D. Pogosyan, S. Prunet, S. Rao, G. Romeo, J. E. Ruhl, F. Scaramuzzi, D. Sforna, and N. Vittorio. A flat Universe from high-resolution maps of the cosmic microwave background radiation. *Nature*, 404:955–959, April 2000.

[35] J. Delabrouille. Measuring CMB polarisation with the Planck mission. *Astrophysics and Space Science*, 290:87–103, 2004.

[36] R. H. Dicke, P. J. E. Peebles, P. G. Roll, and D. T. Wilkinson. Cosmic Black-Body Radiation. *Astrophysical Journal*, 142:414–419, July 1965.

[37] S. Dodelson. *Modern Cosmology*. Academic Press, Elsevier Science, San Diego, 2003.

[38] O. Doré, R. Teyssier, F. R. Bouchet, D. Vibert, and S. Prunet. MAPCUMBA: A fast iterative multi-grid map-making algorithm for CMB experiments. *Astronomy and Astrophysics*, 374:358–370, July 2001.

[39] A. G. Doroshkevich and I. D. Novikov. Mean Density of Radiation in the Metagalaxy and Certain Problems in Relativistic Cosmology. *Soviet Physics-Doklady*, 9(2):111–113, August 1963.

[40] A. Einstein. *The special and general theory*. Henry Holt and Company, New York, 1916.

[41] K. Enqvist, H. Kurki-Suonio, and J. Väliviita. Limits on isocurvature fluctuations from Boomerang and MAXIMA. *Physical Review D*, 62, November 2000.

[42] P. G. Ferreira and A. H. Jaffe. Simultaneous Estimation of Noise and Signal in CMB Experiments. *Mon. Not. R. Astron. Soc.*, 312:89–102 (astro–ph/9909250), September 2000.

[43] D.P. Finkbeiner, M. Davis, and D.J. Schlegel. *Astrophysical Journal*, 524:2, 1999.

[44] M. L. Fischer, D. C. Alsop, E. S. Cheng, A. C. Clapp, D. A. Cottingham, J. O. Gundersen, T. C. Koch, E. Kreysa, P. R. Meinhold, A. E. Lange, P. M. Lubin, P. L. Richards, and G. F. Smoot. A bolometric millimeter-wave system for

observations of anisotropy in the cosmic microwave background radiation on medium angular scales. *Astrophys. J.* , 388:242–252, April 1992.

[45] W. L. Freedman, B. F. Madore, B. K. Gibson, L. Ferrarese, D. D. Kelson, S. Sakai, J. R. Mould, R. C. Kennicutt, H. C. Ford, J. A. Graham, J. P. Huchra, S. M. G. Hughes, G. D. Illingworth, L. M. Macri, and P. B. Stetson. Final Results from the Hubble Space Telescope Key Project to Measure the Hubble Constant. *Astrophysical Journal*, 553:47–72, May 2001.

[46] M. Frigo and S. G. Johnson. The Design and Implementation of FFTW3. *Proceedings of the IEEE*, 93:216–231, 2005.

[47] G. Gamow. The Origin of Elements and the Separation of Galaxies. *Physical Review*, 74:505, 1948.

[48] G. Gamow. On Relativistic Cosmogony. *Reviews of Modern Physics*, 21:367–373, July 1949.

[49] E. Gawiser and G. F. Smoot. Contribution of Extragalactic Infrared Sources to Cosmic Microwave Background Foreground Anisotropy. *Astrophysical Journal Letters*, 480:L1+, May 1997.

[50] K. Grainge *et al.*. The CMB power spectrum out to l=1400 measured by the VSA. *Monthly Notices of the Royal Astronomical Society*, in press, astro-ph/0212495, 2002.

[51] J. E. Gunn and B. A. Peterson. On the Density of Neutral Hydrogen in Intergalactic Space. *Astrophysical Journal*, 142:1633–1636, November 1965.

[52] A. H. Guth. Inflationary universe: A possible solution to the horizon and flatness problems. *Physical Review D*, 23:347–356, January 1981.

[53] N. W. Halverson, E. M. Leitch, C. Pryke, J. Kovac, J. E. Carlstrom, W. L. Holzapfel, M. Dragovan, J. K. Cartwright, B. S. Mason, S. Padin, T. J. Pearson, A. C. S. Readhead, and M. C. Shepherd. Degree Angular Scale Interferometer

First Results: A Measurement of the Cosmic Microwave Background Angular Power Spectrum. *Astrophysical Journal*, 568:38–45, March 2002.

[54] J. P. Hamaker and J. D. Bregman. Understanding radio polarimetry. III. Interpreting the IAU/IEEE definitions of the Stokes parameters. *Astronomy and Astrophysics*, 117:161–165, May 1996.

[55] S. Hanany, P. Ade, A. Balbi, J. Bock, J. Borrill, A. Boscaleri, P. de Bernardis, P. G. Ferreira, V. V. Hristov, A. H. Jaffe, A. E. Lange, A. T. Lee, P. D. Mauskopf, C. B. Netterfield, S. Oh, E. Pascale, B. Rabii, P. L. Richards, G. F. Smoot, R. Stompor, C. D. Winant, and J. H. P. Wu. MAXIMA-1: A Measurement of the Cosmic Microwave Background Anisotropy on Angular Scales of $10' - 5°$. *Astrophysical Journal Letters*, 545:L5–L9, December 2000.

[56] R. Hanbury Brown and R. Q. Twiss. Correlation between photons in two coherent beams of light. *Nature*, 177:27–29, January 1956.

[57] R. Hanbury Brown and R. Q. Twiss. The question of correlation between photons in coherent light rays. *Nature*, 178:1447–1448, November 1956.

[58] R. Hanbury Brown and R. Q. Twiss. Interferometry of the Intensity Fluctuations in Light. I. Basic Theory: The Correlation between Photon in Coherent Beams of Radiation. *Proc. Royal Soc. London., Series A*, 242:300–324, November 1957.

[59] R. Hanbury Brown and R. Q. Twiss. The question of correlation between photons in coherent beams of light. *Nature*, 179:1128–1129, 1957.

[60] E. R. Harrison. *Physical Review D*, 1:2726, 1970.

[61] M. G. Hauser and P. J. E. Peebles. Statistical analysis of catalogs of extragalactic objects. ii. the abell catalog of rich clusters. *Astrophysical Journal*, 185:757–785, November 1973.

[62] E. Hecht. *Optics, third edition.* Addison Wesley Longman, Inc., Reading, MA, 1998.

[63] G. Herzberg. *Molecular Spectra and Molecular Structure, Vol. I. Spectra of Diatomic Molecules.* D. Van Nostrand Co., New York, 1950.

[64] G. Hinshaw, C. Barnes, C. L. Bennett, M. R. Greason, M. Halpern, R. S. Hill, N. Jarosik, A. Kogut, M. Limon, S. S. Meyer, N. Odegard, L. Page, D. N. Spergel, G. S. Tucker, J. L. Weiland, E. Wollack, and E. L. Wright. First-Year Wilkinson Microwave Anisotropy Probe (WMAP) Observations: Data Processing Methods and Systematic Error Limits. *Astrophysical Journal Supplement Series*, 148:63–95, September 2003.

[65] G. Hinshaw, D. N. Spergel, L. Verde, R. S. Hill, S. S. Meyer, C. Barnes, C. L. Bennett, M. Halpern, N. Jarosik, A. Kogut, E. Komatsu, M. Limon, L. Page, G. S. Tucker, J. L. Weiland, E. Wollack, and E. L. Wright. First-Year Wilkinson Microwave Anisotropy Probe (WMAP) Observations: The Angular Power Spectrum. *Astrophysical Journal Supplement Series*, 148:135–159, September 2003.

[66] E. Hivon, K. M. Górski, C. B. Netterfield, B. P. Crill, S. Prunet, and F. Hansen. MASTER of the Cosmic Microwave Background Anisotropy Power Spectrum: A Fast Method for Statistical Analysis of Large and Complex Cosmic Microwave Background Data Sets. *Astrophysical Journal*, 567:2–17, March 2002.

[67] W. S. Holland. Design and Development of Bolometric Detector Systems. *Ph.D. Thesis*, 1991.

[68] W. Holmes, J. M. Gildemeister, and P. L Richards. Measurement of thermal transport in low stress silicon nitride films. *Applied Physics Letters*, 72(18):2250–2252, 1998.

[69] W. L. Holzapfel, T. M. Wilbanks, P. A. R. Ade, S. E. Church, M. L. Fischer, P. D. Mauskopf, D. E. Osgood, and A. E. Lange. The Sunyaev-Zeldovich

Infrared Experiment: A Millimeter-Wave Receiver for Cluster Cosmology. *Astrophys. J.* , 479:17–+, April 1997.

[70] M. Hoskin. *Cambridge Illustrated History of Astronomy*. Cambridge University Press, Cambridge, 1996.

[71] W. Hu, N. Sugiyama, and J. Silk. The Physics of Microwave Background Anisotropies. *Nature*, 386:37–43, 1997.

[72] W. Hu and M. White. A CMB Polarization Primer. *New Astronomy*, 2:323–344, September 1997.

[73] W. T. Hu. *Wandering in the Background: a Cosmic Microwave Background Explorer*. PhD thesis, January 1995.

[74] A. H. Jaffe, P. A. Ade, A. Balbi, J. J. Bock, J. R. Bond, J. Borrill, A. Boscaleri, K. Coble, B. P. Crill, P. de Bernardis, P. Farese, P. G. Ferreira, K. Ganga, M. Giacometti, S. Hanany, E. Hivon, V. V. Hristov, A. Iacoangeli, A. E. Lange, A. T. Lee, L. Martinis, S. Masi, P. D. Mauskopf, A. Melchiorri, T. Montroy, C. B. Netterfield, S. Oh, E. Pascale, F. Piacentini, D. Pogosyan, S. Prunet, B. Rabii, S. Rao, P. L. Richards, G. Romeo, J. E. Ruhl, F. Scaramuzzi, D. Sforna, G. F. Smoot, R. Stompor, C. D. Winant, and J. H. Wu. Cosmology from MAXIMA-1, BOOMERANG, and COBE DMR Cosmic Microwave Background Observations. *Physical Review Letters*, 86:3475–3479, April 2001.

[75] A. H. Jaffe, J. R. Bond, P. G. Ferreira, and L. E. Knox. CMB Likelihood Functions for Beginners and Experts. *3K Cosmology, Proceedings of the EC-TMR Conference held in Rome, Italy*, 476:249 (astro–ph/0306506), October 1999.

[76] M. A. Janssen and S. Gulkis. in the infrared and submillimeter sky after cobe. 1992.

[77] B. B. Jones. *A Search for Gamma-Ray Bursts and Pulsars, and the Application of Kalman Filters to Gamma-Ray Reconstruction*. PhD thesis, 1998.

[78] B. J. T. Jones and R. F. G. Wyse. The ionisation of the primeval plasma at the time of recombination. *Astronomy and Astrophysics*, 149:144–150, August 1985.

[79] R. Jones. *J. Opt. Soc. Am.*, 31:448, 1941.

[80] R. Jones. *J. Opt. Soc. Am.*, 31:500, 1941.

[81] R. Jones. *J. Opt. Soc. Am.*, 32:446, 1942.

[82] R. C. Jones. *J. Opt. Soc. Am.*, 43(1):1–14, January 1953.

[83] W. C. Jones, R. S. Bhatia, J. J. Bock, and A. E. Lange. A Polarization Sensitive Bolometric Receiver for Observations of the Cosmic Microwave Background. *Proc. SPIE Int. Soc. Opt. Eng.*, 4855, 2003.

[84] W. C. Jones *et al.*. A Measurement of the Temperature Power Spectum by B2K . *...in preparation.*

[85] M. Kamionkowski, A. Kosowsky, and A. Stebbins. Statistics of cosmic microwave background polarization. *Physical Review D*, 55:7368–7388, June 1997.

[86] J. Kaplan and J. Delabrouille. Some sources of systematic errors on CMB polarized measurements with bolometers. In *AIP Conf. Proc. 609: Astrophysical Polarized Backgrounds*, pages 209–214, March 2002.

[87] B. G. Keating, P. A. R. Ade, J. J. Bock, E. Hivon, W. L. Holzapfel, A. E. Lange, H. Nguyen, and K. Yoon. BICEP: a large angular scale CMB polarimeter. In *Polarimetry in Astronomy. Edited by Silvano Fineschi . Proceedings of the SPIE, Volume 4843, pp. 284-295 (2003).*, pages 284–295, February 2003.

[88] L. Knox. Determination of inflationary observables by cosmic microwave background anisotropy experiments. *Physical Review D*, 52:4307–4318, October 1995.

[89] L. Knox and M. S. Turner. Detectability of tensor perturbations through anisotropy of the cosmic background radiation. *Physical Review Letters*, 73:3347–3350, December 1994.

[90] A. Kogut, A. J. Banday, C. L. Bennett, K. M. Gorski, G. Hinshaw, P. D. Jackson, P. Keegstra, C. Lineweaver, G. F. Smoot, L. Tenorio, and E. L. Wright. Calibration and Systematic Error Analysis for the COBE DMR 4 Year Sky Maps. *Astrophysical Journal*, 470:653, October 1996.

[91] A. Kogut, A. J. Banday, C. L. Bennett, K. M. Gorski, G. Hinshaw, G. F. Smoot, and E. I. Wright. Microwave Emission at High Galactic Latitudes in the Four-Year DMR Sky Maps. *Astrophysical Journal Letters*, 464:L5, June 1996.

[92] E. W. Kolb and M. Turner. *The Early Universe*. Addison-Wesley, New York, 1990.

[93] A. Kosowsky. Introduction to Microwave Background Polarization. *New Astronomy Review*, 43:157–168, July 1999.

[94] J. M. Kovac, E. M. Leitch, C. Pryke, J. E. Carlstrom, N. W. Halverson, and W. L. Holzapfel. Detection of polarization in the cosmic microwave background using DASI. *Nature*, 420:772–787, December 2002.

[95] C. L. Kuo, P. A. R. Ade, J. J. Bock, C. Cantalupo, M. D. Daub, J. H. Goldstein, W. L. Holzapfel, A. E. Lange, Lueker M., M. Newcomb, J. B. Peterson, D. Pogosyan, J. E. Ruhl, M. C. Runyan, and E. Torbet. High Resolution Observations of the CMB Power Spectrum with ACBAR. *Astrophysical Journal*, submitted, astro-ph/0212289, 2002.

[96] A. E. Lange, P. A. Ade, J. J. Bock, J. R. Bond, J. Borrill, A. Boscaleri, K. Coble, B. P. Crill, P. de Bernardis, P. Farese, P. Ferreira, K. Ganga, M. Giacometti, E. Hivon, V. V. Hristov, A. Iacoangeli, A. H. Jaffe, L. Martinis, S. Masi, P. D.

Mauskopf, A. Melchiorri, T. Montroy, C. B. Netterfield, E. Pascale, F. Piacentini, D. Pogosyan, S. Prunet, S. Rao, G. Romeo, J. E. Ruhl, F. Scaramuzzi, and D. Sforna. Cosmological parameters from the first results of Boomerang. *Physical Review D*, 63:42001, February 2001.

[97] A. E. Lange, M. M. Freund, S. Sato, T. Hirao, T. Matsumoto, and T. Watabe. The Far-Infrared Photometer on the Infrared Telescope in Space. *Astrophys. J.* , 428:384–392, June 1994.

[98] H. S. Leavitt and E. C. Pickering. Periods of 25 Variable Stars in the Small Magellanic Cloud. *Harvard College Observatory Circular*, 173:1–3, March 1912.

[99] A. T. Lee, P. Ade, A. Balbi, J. Bock, J. Borrill, A. Boscaleri, P. de Bernardis, P. G. Ferreira, S. Hanany, V. V. Hristov, A. H. Jaffe, P. D. Mauskopf, C. B. Netterfield, E. Pascale, B. Rabii, P. L. Richards, G. F. Smoot, R. Stompor, C. D. Winant, and J. H. P. Wu. A High Spatial Resolution Analysis of the MAXIMA-1 Cosmic Microwave Background Anisotropy Data. *Astrophysical Journal Letters*, 561:L1–L5, November 2001.

[100] C. Lee, P. A. R. Ade, and C. V. Haynes. Self Supporting Filters for Compact Focal Plane Designs. *ESA SP-388*, 1996.

[101] S. Lee, J. Gildemeister, W. Holmes, A. T. Lee, and P. L. Richards. Voltage biased superconducting transition-edge bolometer with strong electrothermal feedback operated at 370mK. *Applied Optics*, 37:3391–3397, June 1998.

[102] E. M. Leitch, J. M. Kovac, N. W. Halverson, J. E. Carlstrom, C. Pryke, and M. W. E. Smith. Dasi three year cmb polarization results. *submitted to the Astrophysical Journal*, September 2004.

[103] E. M. Leitch, J. M. Kovac, C. Pryke, J. E. Carlstrom, N. W. Halverson, W. L. Holzapfel, M. Dragovan, B. Reddall, and E. S. Sandberg. Measurement of polarization with the Degree Angular Scale Interferometer. *Nature*, 420:763–771, December 2002.

[104] G. Lemaître. Expansion of the universe, A homogeneous universe of constant mass and increasing radius accounting for the radial velocity of extra-galactic nebul&aelig. *Monthly Notices of the Royal Astronomical Society*, 91:483–490, March 1931.

[105] G. Lemaître. Expansion of the universe, The expanding universe. *Monthly Notices of the Royal Astronomical Society*, 91:490–501, March 1931.

[106] A. Lewis and A. Challinor. Evolution of cosmological dark matter perturbations. *Physical Review D*, 66(2):023531, July 2002.

[107] A. Lewis, A. Challinor, and N. Turok. Analysis of CMB polarization on an incomplete sky. *Phys. Rev. D.*, 65(2):023505, January 2002.

[108] A. R. Liddle and D. H. Lyth. *Cosmological Inflation and Large-Scale Structure.* Cambridge University Press, Cambridge, UK, 2000.

[109] A. Ludwig. *IEEE Trans. Ant. Prop.*, AP-21:116, 1973.

[110] C. MacTavish *et al.*. Cosmological Parameter Estimates from B2K . *...in preparation.*

[111] S. Masi *et al.*. *Cryogenics*, 38:319, 1998.

[112] S. Masi *et al.*. *Cryogenics*, 39:217, 1999.

[113] B. Mason, T. J. Pearson, A. C. S. Readhead, M. C. Shepherd, J. H. Sievers, P. S. Udomprasert, J. K. Cartwright, A. J. Farmer, S. Padin, S. T. Meyers, J. R. Bond, C. R. Contaldi, U. L. Pen, D. Pogosyan, Prunet S., J. E. Carlstrom, J. Kovac, E. M. Leitch, C. Pryke, N. W. Halverson, W. L. Holzapfel, P. Altamirano, L. Bronfman, S. Casassus, J. May, and M. Joy. The Anisotropy of the Microwave Background to l = 3500: Deep Field Observations with the Cosmic Background Imager. *Astrophysical Journal*, in press, astro-ph/0205384, 2002.

[114] J. C. Mather. Bolometer Noise: nonequilibrium theory. *Applied Optics*, 21:1125–1129, 1982.

[115] J. C. Mather. *Applied Optics*, 23:584–588, 1984.

[116] J. C. Mather, E. S. Cheng, D. A. Cottingham, R. E. Eplee, D. J. Fixsen, T. Hewagama, R. B. Isaacman, K. A. Jensen, S. S. Meyer, P. D. Noerdlinger, S. M. Read, L. P. Rosen, R. A. Shafer, E. L. Wright, C. L. Bennett, N. W. Boggess, M. G. Hauser, T. Kelsall, S. H. Moseley, R. F. Silverberg, G. F. Smoot, R. Weiss, and D. T. Wilkinson. Measurement of the cosmic microwave background spectrum by the COBE FIRAS instrument. *Astrophysical Journal*, 420:439–444, January 1994.

[117] P. D. Mauskopf, P. A. R. Ade, P. de Bernardis, J. J. Bock, J. Borrill, A. Boscaleri, B. P. Crill, G. DeGasperis, G. De Troia, P. Farese, P. G. Ferreira, K. Ganga, M. Giacometti, S. Hanany, V. V. Hristov, A. Iacoangeli, A. H. Jaffe, A. E. Lange, A. T. Lee, S. Masi, A. Melchiorri, F. Melchiorri, L. Miglio, T. Montroy, C. B. Netterfield, E. Pascale, F. Piacentini, P. L. Richards, G. Romeo, J. E. Ruhl, E. Scannapieco, F. Scaramuzzi, R. Stompor, and N. Vittorio. Measurement of a Peak in the Cosmic Microwave Background Power Spectrum from the North American Test Flight of Boomerang. *Astrophysical Journal Letters*, 536:L59–L62, June 2000.

[118] P. D. Mauskopf *et al.*. *Applied Optics*, 36:765, 1997.

[119] A. D. Miller, R. Caldwell, M. J. Devlin, W. B. Dorwart, T. Herbig, M. R. Nolta, L. A. Page, J. Puchalla, E. Torbet, and H. T. Tran. A Measurement of the Angular Power Spectrum of the Cosmic Microwave Background from L = 100 to 400. *Astrophys. J. Lett.* , 524:L1–L4, October 1999.

[120] P. Molaro, S. A. Levshakov, M. Dessauges-Zavadsky, and S. D'Odorico. The cosmic microwave background radiation temperature at $z_{abs} = 3.025$ toward QSO 0347-3819. *Astronomy and Astrophysics*, 381:L64–L67, January 2002.

[121] T. Montroy and the Boomerang collaboration. Measuring CMB Polarization with Boomerang. *New Astronomy Reviews*, The Cosmic Microwave Background and its Polarization, astro-ph/0305593, September 2003.

[122] Thomas E. Montroy. PhD thesis, 2002.

[123] T. Montroy *et al.*. A Measurement of the Polarization Power Spectum by B2K . *...in preparation.*

[124] H. Mueller. *J. Opt. Soc. Am.*, 38:661, 1948.

[125] P. Natoli, G. de Gasperis, C. Gheller, and N. Vittorio. A Map-Making algorithm for the Planck Surveyor. *Astronomy and Astrophysics*, 372:346–356, June 2001.

[126] C. B. Netterfield, P. A. R. Ade, J. J. Bock, J. R. Bond, J. Borrill, A. Boscaleri, K. Coble, C. R. Contaldi, B. P. Crill, P. de Bernardis, P. Farese, K. Ganga, M. Giacometti, E. Hivon, V. V. Hristov, A. Iacoangeli, A. H. Jaffe, W. C. Jones, A. E. Lange, L. Martinis, S. Masi, P. Mason, P. D. Mauskopf, A. Melchiorri, T. Montroy, E. Pascale, F. Piacentini, D. Pogosyan, F. Pongetti, S. Prunet, G. Romeo, J. E. Ruhl, and F. Scaramuzzi. A Measurement by BOOMERANG of Multiple Peaks in the Angular Power Spectrum of the Cosmic Microwave Background. *Astrophysical Journal*, 571:604–614, June 2002.

[127] C. B. Netterfield, M. J. Devlin, N. Jarolik, L. Page, and E. J. Wollack. A Measurement of the Angular Power Spectrum of the Anisotropy in the Cosmic Microwave Background. *Astrophysical Journal*, 474:47, January 1997.

[128] C. W. O'dell, B. G. Keating, A. de Oliveira-Costa, M. Tegmark, and P. T. Timbie. CMB Polarization at Large Angular Scales: Data Analysis of the POLAR Experiment. astro-ph/0212425, 2002.

[129] E. A. Ohm. Project Echo, Receiving System. *The Bell System Technical Journal*, pages 1065–1094, July 1961.

[130] L. Page, M. R. Nolta, C. Barnes, C. L. Bennett, M. Halpern, G. Hinshaw, N. Jarosik, A. Kogut, M. Limon, S. S. Meyer, H. V. Peiris, D. N. Spergel, G. S. Tucker, E. Wollack, and E. L. Wright. First-Year Wilkinson Microwave Anisotropy Probe (WMAP) Observations: Interpretation of the TT and TE Angular Power Spectrum Peaks. *Astrophysical Journal Supplement Series*, 148:233–241, September 2003.

[131] Ricardo Paniagua. private communication, 2005.

[132] P. J. E. Peebles. *Principles of Physical Cosmology*. Princeton University Press, Princeton, 1966.

[133] P. J. E. Peebles. Statistical analysis of catalogs of extragalactic objects. i. theory. *Astrophysical Journal*, 185:413–440, October 1973.

[134] P. J. E. Peebles, S. Seager, and W. Hu. Delayed Recombination. *Astrophysical Journal Letters*, 539:L1–L4, August 2000.

[135] P. J. E. Peebles and J. T. Yu. *Astrophysical Journal*, 162:815, 1970.

[136] A. A. Penzias and R. W. Wilson. The Measure of Excess Antenna Temperature at 4080 mc/s. *Astrophysical Journal*, 142:419, 1965.

[137] W. J. Percival, W. Sutherland, J. A. Peacock, C. M. Baugh, J. Bland-Hawthorn, T. Bridges, R. Cannon, S. Cole, M. Colless, C. Collins, W. Couch, G. Dalton, R. De Propris, S. P. Driver, G. Efstathiou, R. S. Ellis, C. S. Frenk, K. Glazebrook, C. Jackson, O. Lahav, I. Lewis, S. Lumsden, S. Maddox, S. Moody, P. Norberg, B. A. Peterson, and K. Taylor. Parameter constraints for flat cosmologies from cosmic microwave background and 2dFGRS power spectra. *Monthly Notices of the Royal Astronomical Society*, 337:1068–1080, December 2002.

[138] S. Perlmutter, G. Aldering, G. Goldhaber, R. A. Knop, P. Nugent, P. G. Castro, S. Deustua, S. Fabbro, A. Goobar, D. E. Groom, I. M. Hook, A. G. Kim,

M. Y. Kim, J. C. Lee, N. J. Nunes, R. Pain, C. R. Pennypacker, R. Quimby, C. Lidman, R. S. Ellis, M. Irwin, R. G. McMahon, P. Ruiz-Lapuente, N. Walton, B. Schaefer, B. J. Boyle, A. V. Filippenko, T. Matheson, A. S. Fruchter, N. Panagia, H. J. M. Newberg, W. J. Couch, and The Supernova Cosmology Project. Measurements of Omega and Lambda from 42 High-Redshift Supernovae. *Astrophysical Journal*, 517:565–586, June 1999.

[139] F. Piacentini *et al.*. A Measurement of the Temperature-Polarization Cross-Power Spectum by B2K . *...in preparation.*

[140] W. H. Press, S. A. Teukolsky, W. T. Vetterling, and B. P. Flannery. *Numerical Recipes*. Cambridge University Press, Cambridge, 2 edition, 1997.

[141] S. Prunet, P. A. R. Ade, J. J. Bock, J. R. Bond, J. Borrill, A. Boscaleri, K. Coble, B. P. Crill, P. de Bernardis, G. de Gasperis, G. de Troia, P. C. Farese, P. G. Ferreira, K. Ganga, M. Giacometti, E. Hivon, V. V. Hristov, A. Iacoangeli, A. H. Jaffe, A. E. Lange, L. Martinis, S. Masi, P. Mason, P. D. Mauskopf, A. Melchiorri, L. Miglio, T. Montroy, C. B. Netterfield, E. Pascale, F. Piacentini, D. Pogosyan, F. Pongetti, S. Prunet, S. Rao, G. Romeo, J. E. Ruhl, F. Scaramuzzi, D. Sforna, and N. Vittorio. Noise Estimation in CMB Time-Streams and Fast Iterative Map-Making. In *Mining the Sky*, page 421, 2001.

[142] A. C. S. Readhead, S. T. Myers, T. J. Pearson, J. L. Sievers, B. S. Mason, C. R. Contaldi, J. R. Bond, R. Bustos, P. Altamirano, C. Achermann, L. Bronfman, J. E. Carlstrom, J. K. Cartwright, S. Casassus, C. Dickinson, W. L. Holzapfel, J. M. Kovac, E. M. Leitch, J. May, S. Padin, D. Pogosyan, M. Pospieszalski, C. Pryke, R. Reeves, M. C. Shepherd, and S. Torres. Polarization Observations with the Cosmic Background Imager. *Science*, 306:836–844, October 2004.

[143] A. G. Riess, A. V. Filippenko, P. Challis, A. Clocchiatti, A. Diercks, P. M. Garnavich, R. L. Gilliland, C. J. Hogan, S. Jha, R. P. Kirshner, B. Leibundgut,

M. M. Phillips, D. Reiss, B. P. Schmidt, R. A. Schommer, R. C. Smith, J. Spyromilio, C. Stubbs, N. B. Suntzeff, and J. Tonry. Observational Evidence from Supernovae for an Accelerating Universe and a Cosmological Constant. *Astronomical Journal*, 116:1009–1038, September 1998.

[144] C. Rocken, Y. H. Kuo, W. Schreiner, D. Hunt, S. Sokolovskiy, and C. McCormick. Cosmic system description. *Terrestrial Atmospheric and Oceanic Sciences*, 11(1):21–52, March 2000.

[145] J. E. Ruhl, P. A. R. Ade, J. J. Bock, J. R. Bond, J. Borrill, A. Boscaleri, C. R. Contaldi, B. P. Crill, P. de Bernardis, G. De Troia, K. Ganga, M. Giacometti, E. Hivon, V. V. Hristov, A. Iacoangeli, A. H. Jaffe, W. C. Jones, A. E. Lange, S. Masi, P. Mason, P. D. Mauskopf, A. Melchiorri, T. Montroy, C. B. Netterfield, E. Pascale, F. Piacentini, D. Pogosyan, G. Polenta, F. Pongetti, S. Prunet, and G. Romeo. Improved Measurement of the Angular Power Spectrum of Temperature Anisotropy in the CMB from Two New Analyses of BOOMERANG Observations. *Astrophysical Journal*, 2002.

[146] M. C. Runyan. *A Search for Galaxy Clusters Using the Sunyaev-Zel'dovich Effect*. PhD thesis, December 2002.

[147] M. C. Runyan, P. A. R. Ade, R. S. Bhatia, J. J. Bock, M. D. Daub, J. H. Goldstein, C. V. Haynes, W. L. Holzapfel, C. L. Kuo, A. E. Lange, J. Leong, M. Lueker, M. Newcomb, J. B. Peterson, C. Reichardt, J. Ruhl, G. Sirbi, E. Torbet, C. Tucker, A. D. Turner, and D. Woolsey. ACBAR: The Arcminute Cosmology Bolometer Array Receiver. *Astrophysical Journal Supplement*, 149:265–287, December 2003.

[148] J. Ruze. Antenna tolerance theory – a review. *Proc. of the IEEE*, 54:633–640, April 1966.

[149] R. Sancisi and T. S. van Albada. Dark matter. In *IAU Symp. 124: Observational Cosmology*, pages 699–710, 1987.

[150] R. H. Sanders. Observational Cosmology. *Proceedings of the Second Aegean Summer School on the Early Universe*, astro-ph/0402065, February 2004.

[151] U. Seljak and M. Zaldarriaga. A Line-of-Sight Integration Approach to Cosmic Microwave Background Anisotropies. *Astrophysical Journal*, 469, October 1996.

[152] D. N. Spergel, L. Verde, H. V. Peiris, E. Komatsu, M. R. Nolta, C. L. Bennett, M. Halpern, G. Hinshaw, N. Jarosik, A. Kogut, M. Limon, S. S. Meyer, L. Page, G. S. Tucker, J. L. Weiland, E. Wollack, and E. L. Wright. First-Year Wilkinson Microwave Anisotropy Probe (WMAP) Observations: Determination of Cosmological Parameters. *Astrophysical Journal Supplement Series*, 148:175–194, September 2003.

[153] D. Spiga *et al.*. Cmb observations: improvements of the performance of correlation radiometers by signal modulation and synchronous detection. *astro-ph/0202292*, 2002.

[154] R. A. Stokes, P. E. Boynton, and D. T. Wilkinson. A Measurement of the Cosmic Microwave Background at $\lambda$=3.3 mm. *Bulletin of the American Astronomical Society*, 1:206, March 1969.

[155] R. A. Sunyaev and Y. B. Zeldovich. Small Scale Entropy and Adiabatic Density Perturbations - Antimatter in the Universe. *Astrophysics and Space Science*, 9:368, 1970.

[156] J. A. Tauber. Prospects for Polarimetry of the Interstellar Medium with the Planck Satellite. In *The Magnetized Interstellar Medium*, pages 191–199, February 2004.

[157] J. A. Tauber. The Planck mission. *Advances in Space Research*, 34:491–496, 2004.

[158] M. Tegmark. How to Make Maps from Cosmic Microwave Background Data without losing Information. *Astrophysical Journal Letters*, 480, 1997.

[159] M. Tegmark, M. R. Blanton, M. A. Strauss, F. Hoyle, D. Schlegel, R. Scoccimarro, M. S. Vogeley, D. H. Weinberg, I. Zehavi, A. Berlind, T. Budavari, A. Connolly, D. J. Eisenstein, D. Finkbeiner, J. A. Frieman, J. E. Gunn, A. J. S. Hamilton, L. Hui, B. Jain, D. Johnston, S. Kent, H. Lin, R. Nakajima, R. C. Nichol, J. P. Ostriker, A. Pope, R. Scranton, U. Seljak, R. K. Sheth, A. Stebbins, A. S. Szalay, I. Szapudi, L. Verde, Y. Xu, J. Annis, N. A. Bahcall, J. Brinkmann, S. Burles, F. J. Castander, I. Csabai, J. Loveday, M. Doi, M. Fukugita, J. R. I. Gott, G. Hennessy, D. W. Hogg, Ž. Ivezić, G. R. Knapp, D. Q. Lamb, B. C. Lee, R. H. Lupton, T. A. McKay, P. Kunszt, J. A. Munn, L. O'Connell, J. Peoples, J. R. Pier, M. Richmond, C. Rockosi, D. P. Schneider, C. Stoughton, D. L. Tucker, D. E. Vanden Berk, B. Yanny, and D. G. York. The Three-Dimensional Power Spectrum of Galaxies from the Sloan Digital Sky Survey. *Astrophysical Journal*, 606:702–740, May 2004.

[160] T. Timusk and P. L. Richards. *Applied Optics*, 20:1355–1360, 1981.

[161] M. Tristram, J. F. Macías-Pérez, C. Renault, and D. Santos. XSPECT, estimation of the angular power spectrum by computing cross-power spectra with analytical error bars. *Monthly Notices of the Royal Astronomical Society*, 358:833–842, April 2005.

[162] M. S. Turner. Dark Matter and Dark Energy: The Critical Questions. In *To appear in "Hubble's Science Legacy: Future Optical-Ultraviolet Astronomy from Space", eds. K.R. Sembach, J.C. Blades, G.D. Illingworth, and R.C. Kennicutt, ASP Conference Series, astro-ph/0207297*, 2003.

[163] D. Tytler, J. M. O'Meara, N. Suzuki, and D. Lubin. Review of Big Bang Nucleosynthesis and Primordial Abundances. *Physica Scripta Volume T*, 85:12, 2000.

[164] R. Ulrich. *Infrared Physics*, 7:37, 1967.

[165] J. Väliviita and V. Muhonen. Correlated Adiabatic and Isocurvature Cosmic Microwave Background Fluctuations in the Wake of the Results from the Wilkinson Microwave Anisotropy Probe. *Physical Review Letters*, 91(13):131302, September 2003.

[166] G. Ventura, M. Barucci, E. Monticone, M. Pasca, and M Rajteri. Development of Ti based Transition Edge Sensors for Cryogenic Detectors. *World Scientific*, 2002.

[167] A. D. Walker, M. Harwood, F. Lowater, W. Fleming, A. J. Cannon, H. S. Leavitt, and E. C. Pickering. Periods of 22 Variable Stars. *Harvard College Observatory Circular*, 170:6–8, February 1912.

[168] S. Weinberg. *The First Three Minutes.* Basic Books, New York, 1977.

[169] J. Wickert *et al.*. *Geophysical Research Letters*, 28(17):3263–3266, 2001.

[170] N. Wiener. *Extrapolation and Smoothing of Stationary Time Series.* Wiley, New York, 1949.

[171] D. T. Wilkinson. A Measurement of the Cosmic Microwave Background at 8.56-mm Wavelength. *Phys. Rev. Lett.*, 19, November 1967.

[172] E. L. Wright, G. Hinshaw, and C. L. Bennett. Producing megapixel cmb maps from differential radiometer data. *Astrophysical Journal*, 458:L53–L55, February 1996.

[173] Y. Yamada, A. Mitsuishi, and H. Yoshinaga. *J. Opt. Soc. Am.*, 52:17, 1962.

[174] M. et al Yun. Bolometric detectors for the planck surveyor. *Proc. SPIE Int. Soc. Opt. Eng.*, 4855:136, 2003.

[175] O. Zahn and M. Zaldarriaga. Probing the Friedmann equation during recombination with future cosmic microwave background experiments. *Physical Review D*, 67(6):063002, March 2003.

[176] M. Zaldarriaga. Nature of the E-B decomposition of CMB polarization. *Physical Review D*, 64:103001, November 2001.

[177] M. Zaldarriaga and U. Seljak. All-sky analysis of polarization in the microwave background. *Physical Review D*, 55:1830–1840, February 1997.

[178] J. Zhang, W. Cui, M. Juda, D. McCammon, R. L. Kelley, S. H. Moseley, C. K Stahle, and A. E. Szymkowiak. Non-ohmic effects in hopping conduction in doped silicon and germanium between 0.05 and 1 k. *Physical Review B*, 57(8):4472, 1998.

[179] X. Zhang. *IEEE Trans. Microwave Theory and Techniques*, 41:1263, 1993.

[180] J. Zmuidzinas. Thermal noise and correlations in photon detection. *Applied Optics*, 42(25):4989–5008, September 2003.

# Appendix A

# Galactic Plane Maps

The following are the total intensity maps of the Galactic plane derived from the B2K observations. The polarization maps which follow are generated at a degraded resolution and spacially low-pass filtered, in order to mitigate persistant pointing errors which remain in the Galactic data. For these images, the scale of the polarization vectors are such that the median length vector corresponds to a polarized brightness $\sqrt{Q^2 + U^2} \simeq 14\mu\mathrm{K}_{\mathrm{CMB}}$, or 5.4, 6.5, and 4.5 $\cdot 10^{-3}$ MJy/sr, at 145, 245 and 345 GHz, respectively. While work is under way to correct these errors, a considerable amount of work remains to be done. Nevertheless, these images give the general impression of the quality of the Galactic data obtained by B2K.

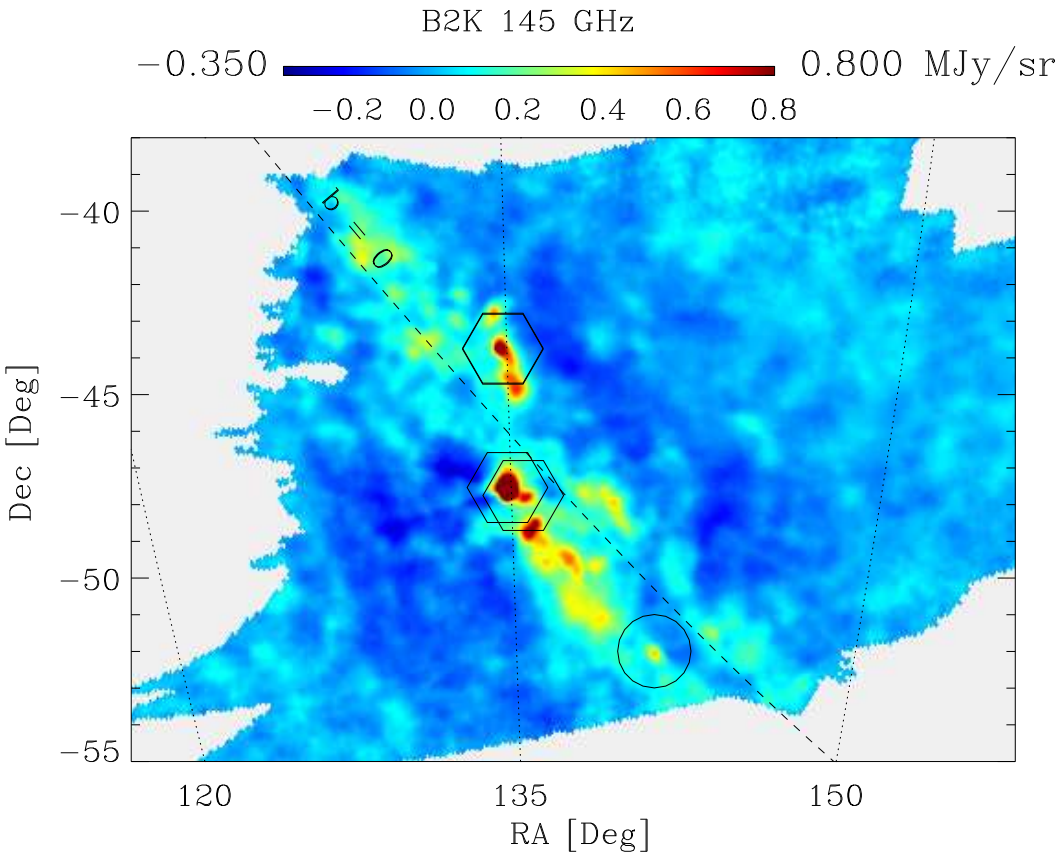


Figure A.1: The 145 GHz B2K data.

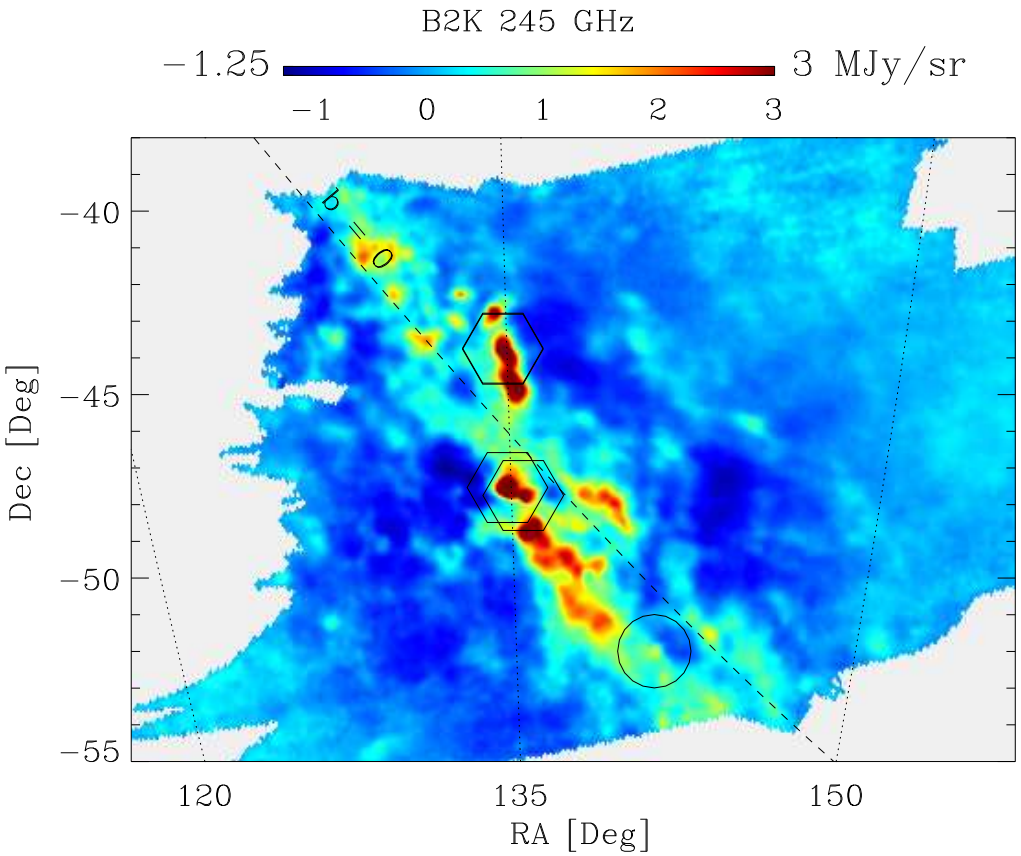


Figure A.2: The 245 GHz B2K data.

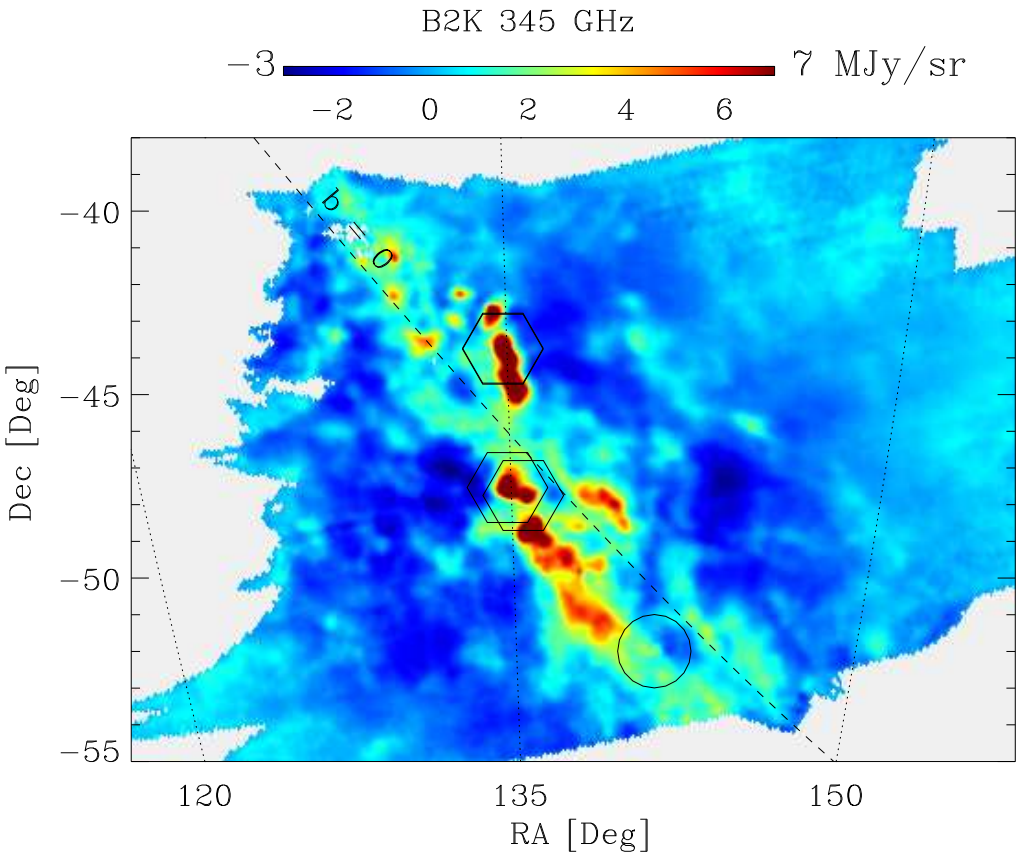


Figure A.3: The 345 GHz B2K data.

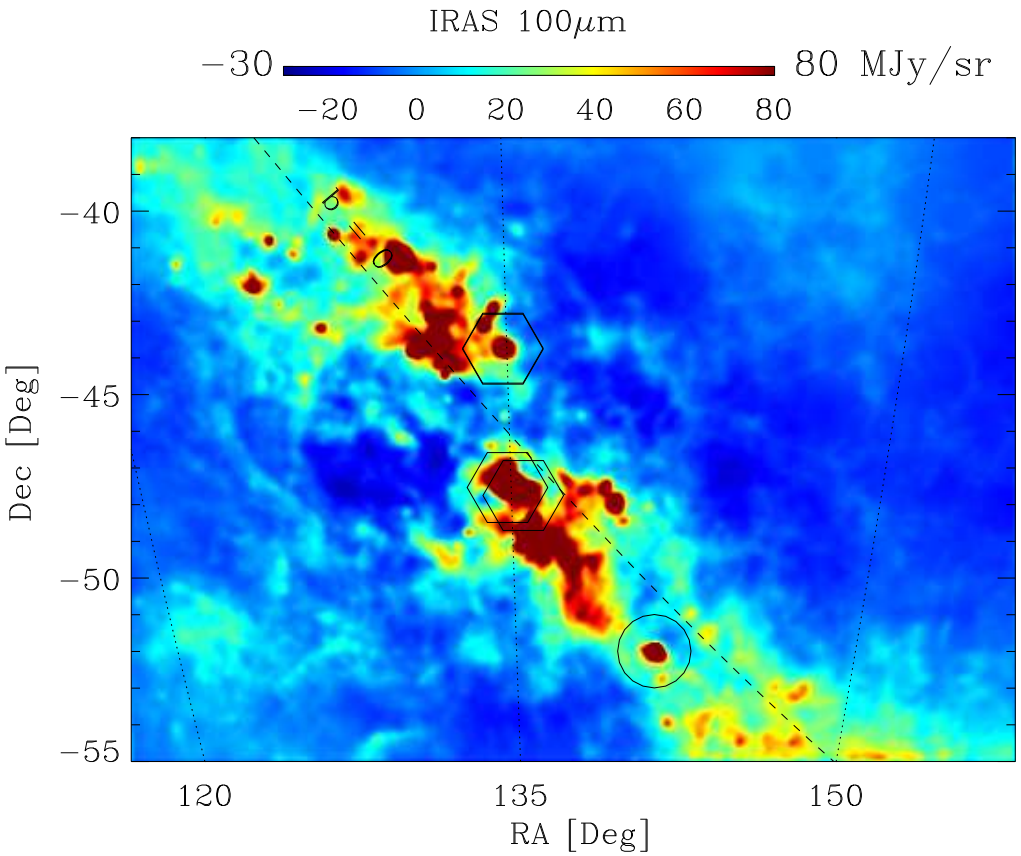


Figure A.4: The IRAS 100$\mu$m data.

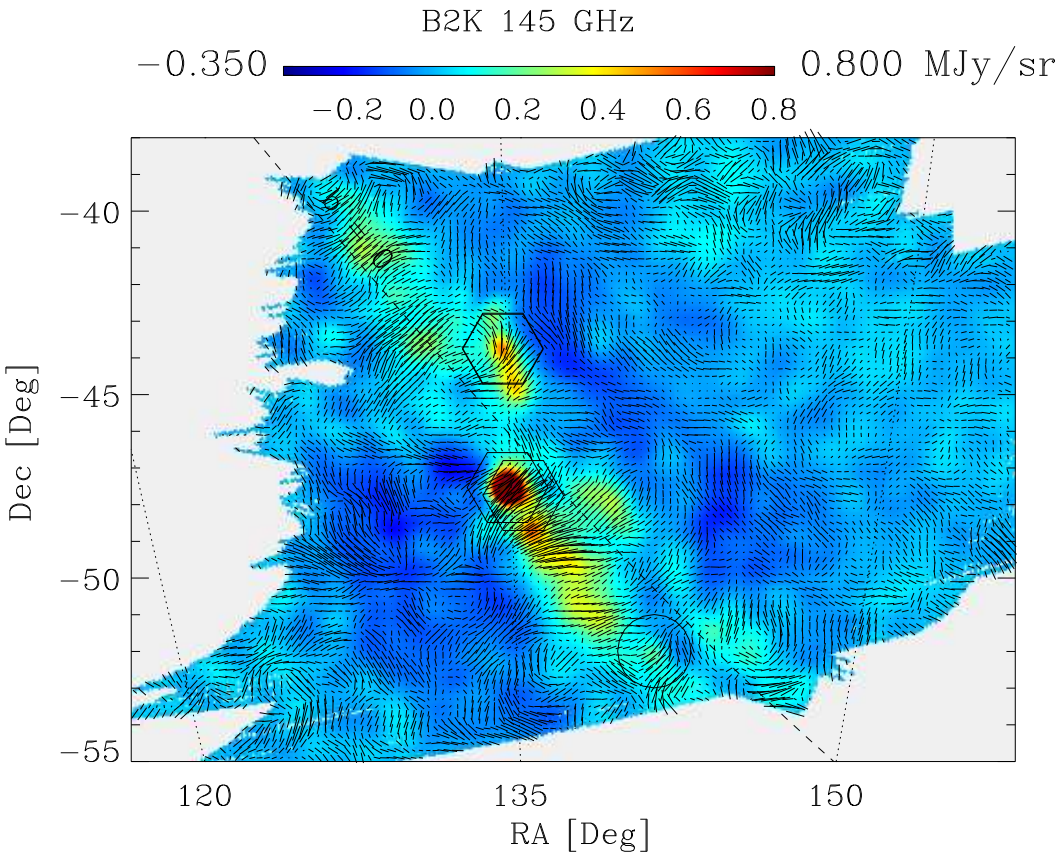


Figure A.5: The 145 GHz B2K data.

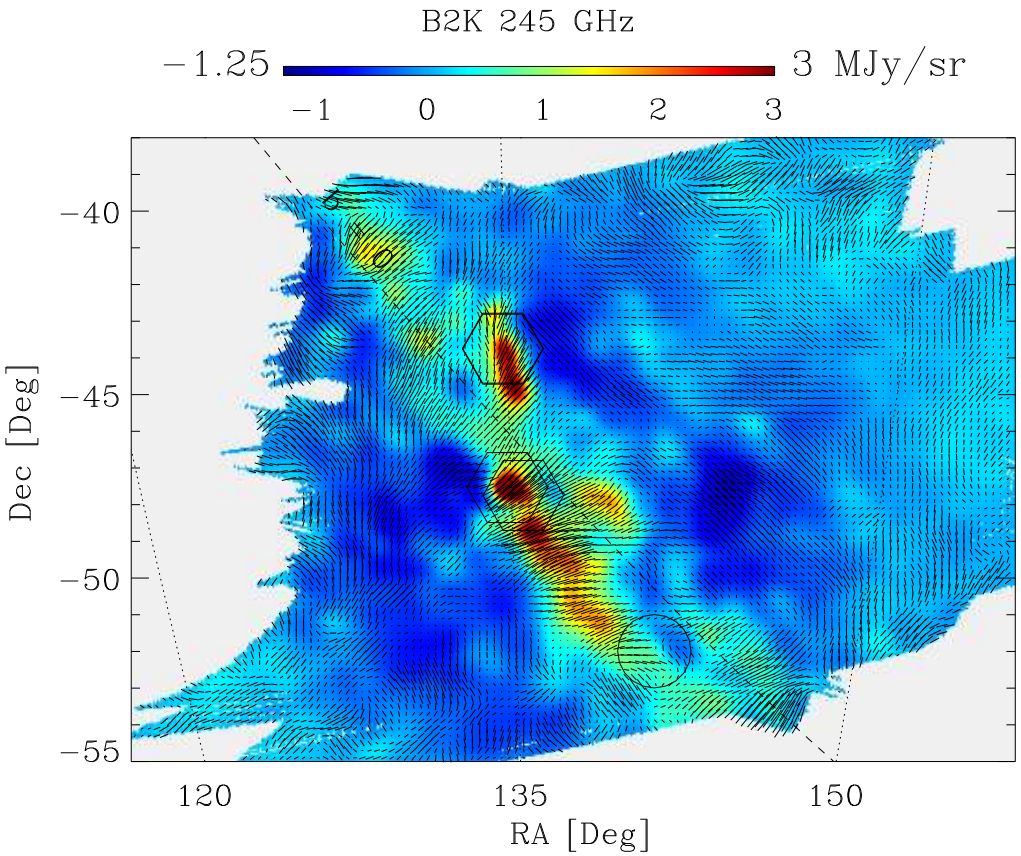


Figure A.6: The 245 GHz B2K data.

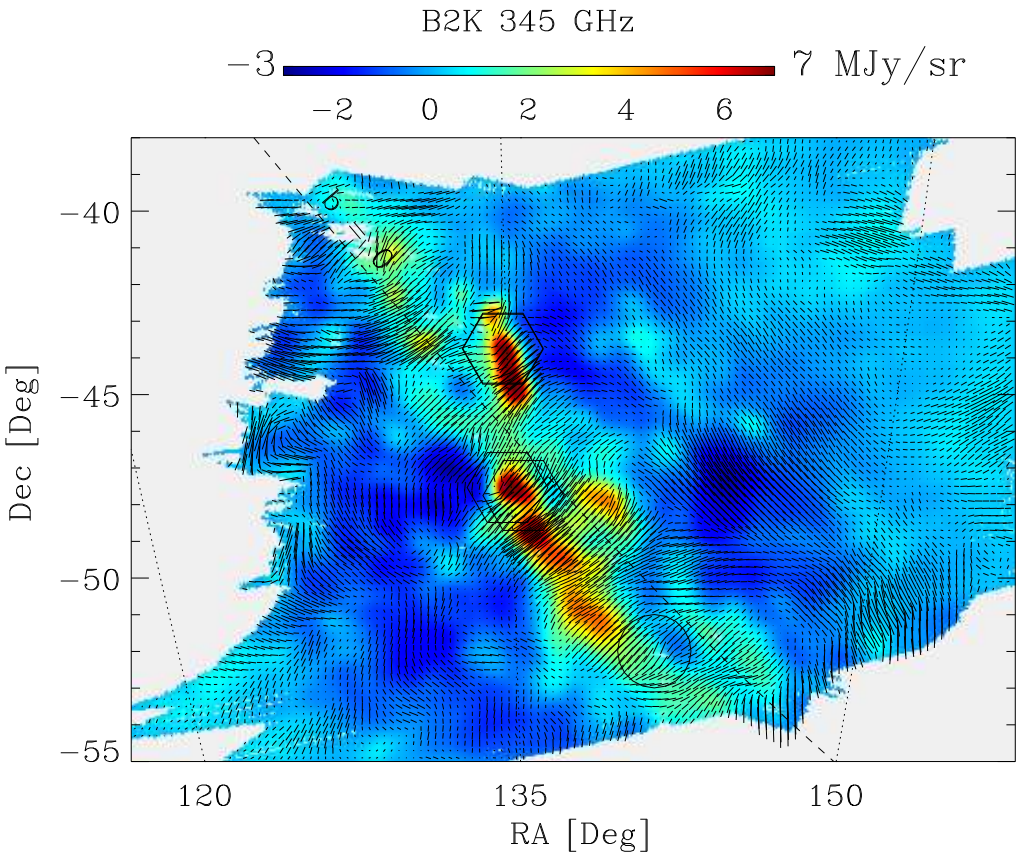


Figure A.7: The 345 GHz B2K data.

# Appendix B

# Numerical Modeling of Bolometric Receivers

## B.1 Bolometers 101

The performance of a bolometric detector can be understood analytically based on the detailed balance between the total power dissipated in the device and the thermal conductance to the temperature bath. This can be expressed by the power balance equation for equilibrium,

$$P_{ele} + Q = \int_{T_{base}}^{T} G(T)dT \tag{B.1}$$

where $P_{ele}$ represents the electrical power dissipated in the device and, for the purposes of astrophysical instrumentation, Q is the optical power on the bolometer, and $G(T)$ is the thermal conductance characterizing to the temperature bath.

For a simple system described by a single thermal conductance to a temperature bath and a heat capacity $C(T)$, the differential relationship between power and temperature fluctuations is determined,

$$\delta P_{ele} + \delta Q = G(T)\delta T + C(T)\delta\dot{T} \tag{B.2}$$

### B.1.1 Semiconductor bolometers

For the circuit shown in Figure B.1, equations B.1 and B.2, together with parametric models of the thermistor resistance and the thermal conductance to the bath allow

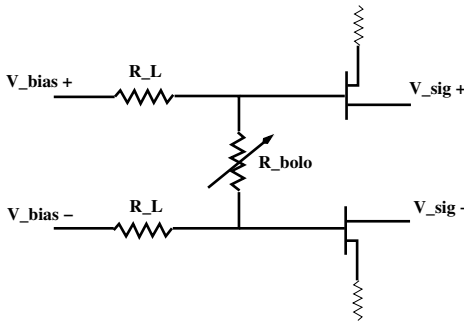


Figure B.1: A typical NTDGe bolometer readout circuit. The circuit is usually AC biased, with the bolometer held at a virtual ground. The impedence transformers (usually JFETs) must be maintained at a temperature above freezeout (usually $\sim$ 100K), where the voltage noise is minimized. The signals are then sent to a warm synchronous demodulation circuit.

one to numerically determine all aspects of the receiver performance.

In particular, if we assume the following functional forms for the temperature dependence of the thermistor resistance, thermal conductance[1], and heat capacities [178, 68],

$$R(T) = R_0 e^{\left(\sqrt{\frac{\Delta}{T}} - \frac{\lambda(T)}{L}\frac{eV}{kT}\right)} \tag{B.3}$$

$$\begin{aligned} G(T) &= G_1\left(\frac{T}{T_0}\right) + G_2\left(\frac{T}{T_0}\right)^3 \\ &\simeq G_0\left(\frac{T}{T_0}\right)^\beta \end{aligned} \tag{B.4}$$

and

$$C(T) = C_1\left(\frac{T}{T_0}\right) + C_2\left(\frac{T}{T_0}\right)^3 \tag{B.5}$$

then equation B.1 can be solved to provide the bolometer properties (such as signal voltage, bolometer impedance, thermal conductance, responsivity, time constants, etc.), parameterized by the set $\{R_0, \Delta, T_{\rm base}, Q, R_L, G_0, \beta, C_i, \lambda\}$ as a function of bias voltage.

The linear and cubic terms in Equations B.4 and B.5 arise from the electrical and

[1]Here, and in what follows, I use the terms "conductance" and "conductivity" loosely and usually interchangeably. Here, it has units [Watts/Kelvin] rather than [Watts/meter·Kelvin].

lattice contributions of the system, respectively. It is standard practice to approximate the behavior in both cases by a power law index, $1 \geq \beta \leq 3$, as in Equation B.4. However, it should be understood that this approximation remains valid only over a limited range of temperature.

The amplitude second term in the argument of the exponential of Equation B.3, the electric field effect, depends crucially on the temperature and the properties of the thermistor employed [67]. The parameter $\lambda(T)$ is related to the mean free path for scattering of electrons, and is generally temperature dependent. $L$ is the physical length of the chip. For NTDGe chips at 300 mK, this term is rarely important as the voltage levels are small and the chips are relatively large[178].

Equation B.2 can be used to derive the voltage responsivity $[V/W]$ of the receiver as follows. The electrical power dissipated in the device is

$$P_{ele} \equiv I_{\text{bias}}^2 R = \frac{V_b^2}{(R_L + R)^2} R$$

giving, for small variations in power,

$$\delta P_{ele} = \delta R \frac{V_b^2}{(R_L + R)^2} \cdot \left(1 - \frac{2R}{(R_L + R)}\right)$$

We would like to express $\delta P_{ele}$ in terms of the temperature fluctuation, so we use the functional form for $R(T)$ given above to find,

$$\delta R = -\delta T \frac{R}{2T} \sqrt{\frac{\Delta}{T}}$$

Therefore, the temperature fluctuation resulting from a variation in optical power is determined by the equation,

$$\delta Q = \left[ G(T) + \frac{R}{2T} \sqrt{\frac{\Delta}{T}} \frac{V_b^2}{(R_L + R)^2} \cdot \left(1 - \frac{2R}{(R_L + R)}\right) \right] \delta T + C(T) \dot{\delta T} \qquad \text{(B.6)}$$

For a sinusoidal fluctuation in optical power at a frequency $\omega = 2\pi f$, the temperature response must also be a phase offset sinusoidal $\delta T(t) \propto e^{i[wt + \phi(C)]}$ where the

constant of proportionality is determined by equation B.6. Explicitly, the constant of proportionality for a given Fourier component of the temperature fluctuation is simply,

$$\widetilde{\delta Q} = \left( \left[ G(T) + \frac{R}{2T}\sqrt{\frac{\Delta}{T}}\frac{V_b^2}{(R_L+R)^2} \cdot \left(1 - \frac{2R}{(R_L+R)}\right)\right] + i\omega C(T) \right) \widetilde{\delta T} \qquad \text{(B.7)}$$

One can define the effective thermal conductance by the system's response to a sinusoidal optical signal. In this case it is useful to define $G_{eff}$ to be the physical thermal conductance plus the effect of electro-thermal feedback,

$$G_{eff} \equiv G(T) + \frac{R}{2T}\sqrt{\frac{\Delta}{T}}\frac{V_b^2}{(R_L+R)^2} \cdot \left(1 - \frac{2R}{(R_L+R)}\right)$$

$$G_{eff} = G(T) + \alpha \cdot I_{\text{bias}}^2 \left|\frac{\partial R}{\partial T}\right| \qquad \text{(B.8)}$$

where,

$$\alpha \equiv \left(1 - \frac{2R}{(R_L+R)}\right). \qquad \text{(B.9)}$$

The effective thermal conductance describes the (complex) amplitude of the thermal response to the optical signal

$$\widetilde{\delta T} = \frac{\widetilde{\delta Q}}{G_{eff} + i\omega C} \qquad \text{(B.10)}$$

It is important to note the effect of the term resulting from a variation in the electrical power dissipation in equation B.8. This electro-thermal feedback mechanism serves to increase the device's speed of response to optical power variations over and above that which you would expect for a given thermal conductance and fixed-impedance load. So long as $|\frac{dR}{dT}|$ is appreciable and the device is fairly well current biased, the electro-thermal feedback term is comparable in magnitude to the value of $G(T)$. Note, however, that when $R = R_L$, the electro-thermal feedback term vanishes. When the bolometer impedance exceeds that of the load resistor the sign of the electro-thermal feedback reverses, resulting in a further degradation in thermal relaxation time.

The *rms* voltage response to the optical excitation is the responsivity, $S(\omega)$ of the bolometer,

$$S(\omega) \equiv \langle \frac{\delta V_s(t)}{\delta Q(t)} \rangle = \sqrt{\left(\frac{\delta V_s(\omega)}{\delta Q(\omega)}\right)\left(\frac{\delta V_s(\omega)}{\delta Q(\omega)}\right)^*}$$

We can use Equation B.10 together with the expression for signal voltage,

$$V_s = R\frac{V_b}{R_L + R} \tag{B.11}$$

and variations in signal for small changes in bolometer impedance,

$$\delta V_s = \delta R \frac{V_b}{R_L + R} \cdot \left(1 - \frac{R}{R_L + R}\right)$$

to relate temperature fluctuations to signal fluctuations

$$\delta V_s = -\delta T \frac{R}{2T}\sqrt{\frac{\Delta}{T}}\frac{V_b}{(R_L + R)} \cdot \left(1 - \frac{R}{R_L + R}\right)$$

and therefore the responsivity.

$$S(\omega) = -\frac{1}{\sqrt{1 + (\omega\tau)^2}}\frac{1}{G_{eff}}\frac{R}{2T}\sqrt{\frac{\Delta}{T}}\frac{V_b}{(R_L + R)} \cdot \left(1 - \frac{R}{R_L + R}\right) \tag{B.12}$$

where we have used $\tau \equiv \frac{C(T)}{G_{eff}}$.

In many cases it is convenient to be able to produce signal voltages, bolometer impedances, or other measurable parameters given a set of bolometer parameters. For example, when performing likelihood analysis of bolometer data in order to obtain estimates of the device parameters, a rapid method of generating load curves is necessary. This is accomplished by integrating equation B.1,

$$P_{ele} + Q = \frac{G_0 T_0}{(\beta + 1)}\left[\left(\frac{T}{T_0}\right)^{\beta+1} - \left(\frac{T_{\text{base}}}{T_0}\right)^{\beta+1}\right] \tag{B.13}$$

and expanding $P_{ele}$ in terms of the desired parameter, taking $T$ as the independent

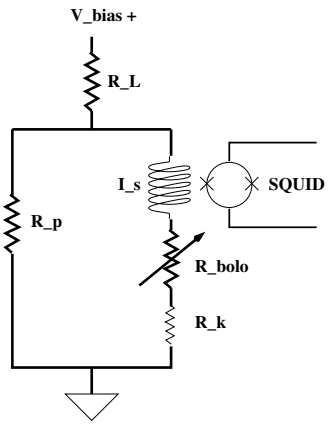


Figure B.2: A typical TES readout circuit with a SQUID current amplifier. Typical component values are, for the load resistor $R_L \sim 2\ k\Omega$, the parallel impedence $R_p \sim 16\ m\Omega$, the TES impedence range $0 \geq R_b \lesssim 10\ \Omega$, and a contact resistance $R_k \sim 0.5\ \Omega$.

variable. This equation can then be calculated numerically for a set of parameter values. For example, a model load curve can be efficiently generated by producing a vector of bolometer temperatures $\mathbf{T}$

$$V_s = \sqrt{R_0 e^{\sqrt{\frac{\Delta}{\mathbf{T}}}} \left( \frac{G_0 T_0}{(\beta+1)} \left[ \left( \frac{\mathbf{T}}{T_0} \right)^{\beta+1} - \left( \frac{T_{\text{base}}}{T_0} \right)^{\beta+1} \right] - Q \right)} \tag{B.14}$$

and the corresponding bias points are obtained by inverting equation B.11. It then remains only to interpolate the model values to the exact bias points of the measurement.

### B.1.2 TES bolometers

While not yet in widespread use for far-infrared detection, transition-edge superconducting (TES) devices are the clear successor to semiconductor bolometers due to their ease of manufacture, ease of multiplexing, low heat capacity, and wide dynamic range. These benefits come at the cost of relatively poor 1/f stability, more difficult operational requirements, and prohibitively large power requirements for the warm electronics.

TES devices are simply thermistors, so an analysis similar to the above may be

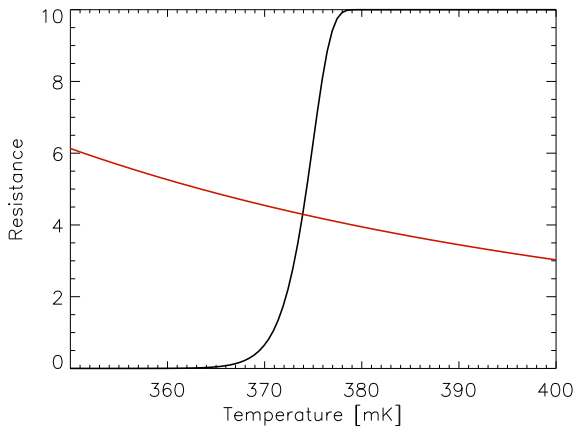


Figure B.3: A comparison of the resistance versus temperature for a typical semiconductor and TES bolometer. The much steeper $d\log R/d\log T$ of the TES bolometer is what makes the electrothermal feedback qualitatively different from a NTDGe thermistor.

applied with minimal modification. A typical TES readout circuit is shown in Figure B.2. While Equations B.1 and B.2 still apply, the temperature dependence of a superconductor operating near its transition temperature has a functional form which differs greatly from that of a semiconductor bolometer. A TES thermistor typically consists of a Ti bilayer evaporated onto a $Si_3N_4$ substrate. By varying the relative thickness of the layers, it is possible tune the transition temperature, $T_c$, with fairly high accuracy [166, 101]. As illustrated in Figure B.3, the TES transitions from a superconductor to a normal metal over a very narrow, $sim$10mK, temperature range. The temperature dependence of a TES is much more steep, and has the opposite sign from that of an NTDGe thermistor. Therefore, a TES device requires a much different bias/readout circuit than that of a semiconductor bolometer.

$$R(T) = R_0 \left(1 - e^{-x^n}\right) \tag{B.15}$$

where $x \equiv T/T_c$.

$$\delta R = \delta T \; R_0 \; e^{-x^n} \; \frac{n x^{n-1}}{T_c} \tag{B.16}$$

and

$$R_{EQ} = R_L + \left(R_p^{-1} + (\widetilde{Z}_s)^{-1}\right)^{-1}.$$

In the interest of simplicity the complex impedance of the TES and SQUID, $\widetilde{Z}_s$, is taken to be purely real. We do consider a boundary resistance, so we take $\widetilde{Z}_s \simeq R(T) + R_k$.

$$R_{EQ} = R_L + \left(R_p^{-1} + (R + R_k)^{-1}\right)^{-1}$$

The current detected by the SQUID is therefore,

$$I_s = \frac{V_b}{(R + R_k)} \left(1 - \frac{R_L}{R_{EQ}}\right).$$

It is convenient to introduce the parameter,

$$\gamma \equiv (1 - R_L/R_{EQ}).$$

The relationship between SQUID current and film resistance is,

$$\begin{aligned} \delta I_s &= \frac{V_b}{(R + R_k)} \left[ \delta R_{EQ} \, \frac{R_L}{R_{EQ}^2} - \frac{\delta R}{(R + R_k)} \, \gamma \right] \\ &= -\frac{\delta R}{(R + R_k)} \, I_s \left( 1 - \frac{R_L}{(R + R_k)} \, \gamma \right) \end{aligned} \tag{B.17}$$

where we have used

$$\delta R_{EQ} = \delta R \, \left(\frac{R_{EQ} - R_L}{R + R_k}\right)^2$$

and

$$I_s = \frac{V_b}{(R + R_k)} \gamma.$$

From Equation B.2 we have,

$$\begin{aligned} \delta\widetilde{Q}(\omega) + \delta\widetilde{P}_{ele}(\omega) &= (\, G(T) + i\omega C(T) \,) \; \delta\widetilde{T}(\omega) \\ &= (\, G(T) + i\omega C(T) \,) \; \frac{\partial R}{\partial I_s} \, \frac{\partial T}{\partial R} \, \delta\widetilde{I}_s(\omega). \end{aligned} \tag{B.18}$$

Dropping the explicit frequency dependence, we can write the relationship between

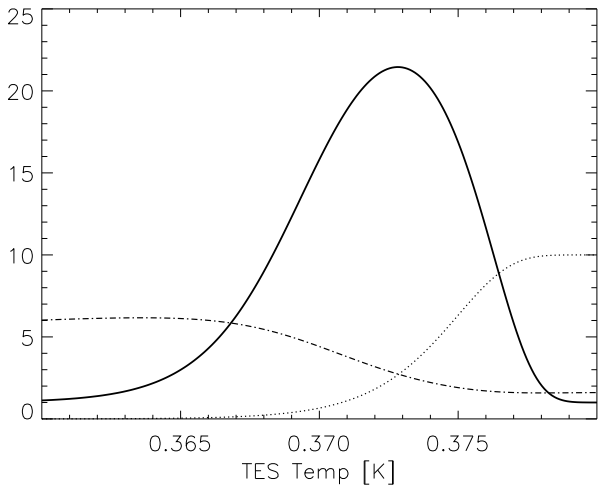


Figure B.4: The behavior of a typical TES bolometer with temperature. Solid line is the ratio of $G_{eff}/G(T)$, often referred to as loop gain, $\mathfrak{L}$, in the TES literature. This quantity is between 1.5 and 2 for an NTD Ge system. Dashed line is the SQUID current, in $\mu$A, dotted line is the TES resistance, in $\Omega$.

variations in optical power and TES current,

$$\delta Q = \left( G(T) - 2I_s(R+R_k)\frac{\partial I_s}{\partial R}\frac{\partial R}{\partial T} - I_s^2\frac{\partial R}{\partial T} + i\omega C(T) \right) \frac{\partial R}{\partial I_s}\frac{\partial T}{\partial R}\,\delta I_s \qquad \text{(B.19)}$$

Comparison with the semiconductor bolometers is simplified by using Equation B.17 to rearrange the frequency independent terms inside the parenthesis in Equation B.19,

$$\begin{aligned} G_{eff} &\equiv G(T) - I_s^2\frac{\partial R}{\partial T} + 2I_s^2\frac{\partial R}{\partial T}\left(1 - \frac{R_L}{(R+R_k)}\,\gamma\right) \\ &= G(T) + \alpha\cdot I_s^2\,\frac{\partial R}{\partial T} \end{aligned} \qquad \text{(B.20)}$$

where

$$\alpha \equiv \left(2\left[1 - \frac{R_L}{(R+R_k)}\,\gamma\right] - 1\right) \qquad \text{(B.21)}$$

Under normal operating conditions, a TES will have $\alpha \sim 0.95$, whereas for an NTDGe bolometer Equation B.9 gives $\alpha \sim 0.75$.

The current responsivity of a TES sensor to an optical signal takes the familiar

form,

$$|S(\omega)| \equiv \left|\frac{\partial I_s}{\partial Q}\right| = \frac{1}{\sqrt{1+(\omega\tau)^2}}\frac{1}{G_{eff}}\ \frac{\partial R}{\partial T}\ \left|\frac{\partial I_s}{\partial R}\right| \tag{B.22}$$

In the TES literature, the quantity $G_{eff}/G(T)$ is often referred to as the loop gain, $\mathfrak{L}$ [101, 166], and has a peak value of $> 20$ for a typical TES, as shown in Figure B.4. Recall that this ratio monotonically increases with bias for an NTDGe bolometer, Equation B.8, but only approaches a value of $\sim 2$ when heavily biased.[2] The much stronger electro-thermal feedback, coupled with the relatively small heat capacity of the TES compared to an NTDGe chip, is the origin of the high bandwidth of TES detectors.

As in the previous discussion regarding NTDGe bolometers, given a set of system parameters, $R_0, n, T_c, R_L, R_p, R_k, Q$, one may take the TES temperature, $T$, as the independent variable. All other observable properties of the system (eg $I_s, R, V_b$) may be derived from Equation B.13. One may then use the above equations to numerically solve for the dynamic properties of the system, such as the loop gain, $G_{eff}/G$, or the current responsivity, $S(\omega)$ (Equation B.22), and therefore the noise equivalent power (NEP) without resorting to *any* approximations. Alternatively, the parametric dependence of the observed TES properties on the system parameters enables one to calculate the full likelihood of some or all of the parameters.

## B.2 Bolometer parameter estimation

Given the analytic expressions derived in Section B.1, one can attempt to deduce bolometer parameters directly from measurements of loadcurves and optical time constants. Parameter fitting from loadcurves is straightforward, and can be very useful for a general determination of bolometer properties and loading conditions. One must use caution, however, as the model parameters are highly degenerate, and accurate determinations of the parameters requires a careful treatment of their

[2] It is often stated (without justification) that the responsivity of a TES is simply the inverse of bias voltage. This is neither obvious nor, strictly speaking, correct. It is true, however, that the responsivity is very close to the inverse of the voltage across the TES, over a limited range of TES temperature.

covariance. Many of the degeneracies may be alleviated by simultaneous fitting of data taken at different base temperatures and/or under controlled optical loading conditions. An example of a major degeneracy in NTDGe systems is illustrated in Figure B.5.

It is often helpful to constrain one or more of the parameters prior to fitting the model to the load curve data. For example, the NTDGe parameters, $R_0$ and $\Delta$, are easily determined from controlled measurements of the bolometer impedance as a function of base temperature, $R(T)$, in an environment with an optical background sufficiently low that the temperature gradient from the bath to the bolometer is negligible. Given a measurement of $R(T)$, the functional form of the thermal conductivity may be obtained by differentiating Equation B.1 with respect to the bolometer temperature. This quantity is independent of the optical background, $Q$, and allows a simple fit for the parameters of interest,

$$\log\left(\frac{\partial P_{ele}}{\partial T_{bolo}}\right) = \log G_0 + \beta \log\left(\frac{T_{bolo}}{T_0}\right).$$

The slope gives the effective spectral index, $\beta$, while the offset provides the nominal thermal conductance $G_0$. This method is very robust to systematic uncertainties in the optical load and base temperature.

Given measurements of the various bolometer parameters described above, load curve fitting can be a very useful method of estimating optical loading. Such a determination of the optical power can be used to calculate optical efficiencies as well as an estimate of the parasitic loading originating from thermal emission within the cryostat or optical chain. That said, a more robust measure of the optical efficiency may be obtained by taking loadcurves with temperature controlled loads filling the throughput of the detector. At a given bolometer impedance, the difference in electrical power dissipation between two or more load temperatures determines the difference in the optical power between the two loads. This allows an accurate measurement of the optical efficiency of the system which is completely independent of any other system parameters.

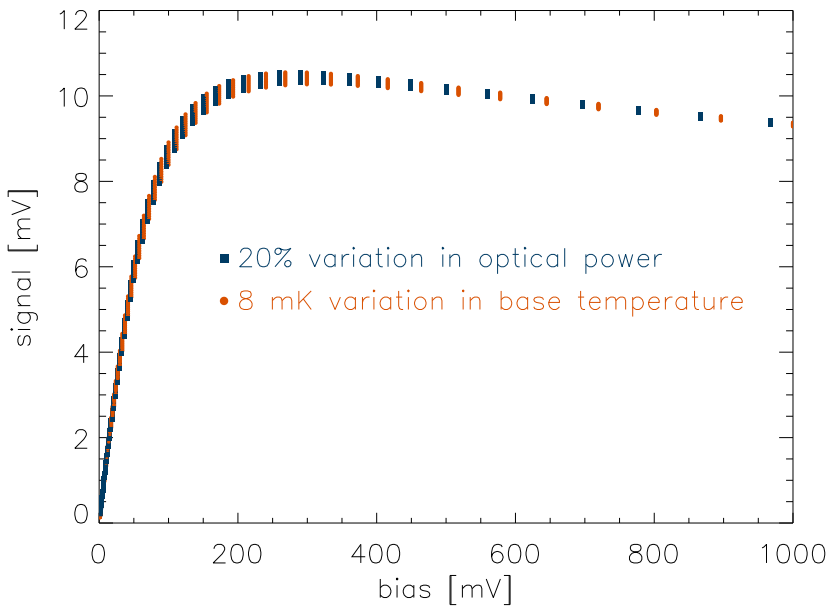


Figure B.5: An illustration of one of the primary parameter degeneracies entering the analysis of NTDGe bolometer loadcurves. A few percent variation in bath temperature is degenerate with a $\sim 20\%$ variation in the optical background. This (and other) parameter degeneracies make accurate parameter determination difficult.

The only remaining parameter needed to fully describe the bolometer is the heat capacity of the device. This is trivially accomplished by measuring the optical transfer function of the detector under various loading conditions and base temperatures with a high bandwidth readout, as in the left panel of Figure 2.15.

## B.3 Noise in bolometric receivers

Given the receiver parameters and an accurate model of the optical loading in a bolometric system, one can accurately calculate the receiver sensitivity. The ability to quickly and accurately probe the impact of loading and various receiver parameters on sensitivity is an invaluable tool for the instrument designer. Not only is one able to use such a tool to optimize design parameters, but one may also quantify and control the exposure to risk arising from variations in optical loading, system temperature, and detector properties.

Noise in bolometric receivers originates from several independent sources. An accurate treatment of the noise must include the effects of the amplifiers, the detector, and that due to the intrinsic fluctuations of the optical background. These noise sources are, to a good approximation, independent processes. As such, their contributions to the NEP add in quadrature,

$$\mathrm{NEP}^2_{total} = \mathrm{NEP}^2_{photon} + \mathrm{NEP}^2_{Johnson} + \mathrm{NEP}^2_{phonon} + \mathrm{NEP}^2_{readout}.$$

The derivation of the detector responsivity from the previous section provides a parametric representation of the responsivity, $S$, allowing the conversion of voltage or current fluctuations to equivalent incident power fluctuations. In what follows, we summarize the salient aspects of each of these noise contributions.

## Photon noise

A fundamental limitation to the sensitivity of any receiver (band-gap, coherent, or bolometric) derives from the intrinsic temporal fluctuations in the optical, often thermal, background radiation. The noise properties of thermal background radiation, or photon noise, differ greatly between radio, sub-millimeter, infrared, and optical instrumentation due to their vastly different operational regimes of photon occupation number. Photons satisfy Bose-Einstein statistics, and therefore the occupation of a mode of frequency $\nu$ is

$$n(\nu, T) = \frac{1}{e^{h\nu/kT} - 1} \tag{B.23}$$

for a thermal background of temperature, $T$.

The ratio $k/h = 20.8$ [GHz/K] sets, for a given background temperature, the frequency for which average occupancy is above or below unity. At radio wavelengths astronomical instruments typically enjoy background levels of order 10K, with the minimum background limited by the CMB monopole at 2.73K. At higher frequencies, atmospheric loading and thermal emission from the instrument tend to dominate the background, and are typically $\sim 30 - 100$K for terrestrial telescopes. Therefore, in-

struments operating at frequencies above $\sim$ 100 GHz have occupation numbers of order unity, while receivers at lower frequencies tend to have very large occupation numbers, $n \simeq kT/h\nu$. In the low $n$ regime, photons can be thought of as arriving at the detector sporadically. The photon noise in high frequency ($\gtrsim$ 100 GHz) instruments with low backgrounds can therefore be expected to largely satisfy Poisson statistics, where one expects fluctuations on the mean to scale roughly as $\sqrt{N}$.

Hanbury Brown and Twiss were the first to complete a rigorous analysis of noise correlations in photons [56, 56, 57, 58, 59]. The topic has been continually revisited in the fifty years since the first published work, and is still relatively un-advertised among many instrumentalists and observers alike. Therefore, we go through the analysis in detail.

Following Zmuidzinas, we can write the covariance matrix describing detector outputs in all generality [180],

$$\sigma_{ij}^2 = \frac{1}{\tau} \int d\nu B_{ij} \left( B_{ji} + \delta_{ij} \right) \tag{B.24}$$

where we define the power coupling matrix,

$$B_{ij} \equiv h\nu \sum_k S_{ik} S_{jk}^* n_k + C_{ij} \tag{B.25}$$

and the internal noise term,

$$C_{ij} \equiv (I - S\ S^\dagger)_{ij}\ \frac{h\nu}{2} \frac{e^x + 1}{e^x - 1}. \tag{B.26}$$

Here, $S_{ij}$ is the standard scattering matrix which couples an output amplitude to the inputs at each port of a network, as in Figure B.6. It is defined by $a_i = \sum_j S_{ij} b_j$. In Equation B.26, $x \equiv h\nu/kT_S$, where $T_S$ is the thermodynamic temperature of the system $S$, and the $n_k$ in Equation B.25 are the occupation numbers of the modes at port $k$. We take ports 0 and 1 to label the two input polarization states, and let ports 2 and 3 label the two bolometers in a PSB pair. For simplicity, we assume that $n_2 = n_3 = 0$ (ie, the detectors are extremely cold with respect to the background),

and that the input populations $n_0 = n_1 = n(\nu, T_{\rm load})$ imply no net polarization in the background.

The internal noise term, $C_{ij}$ arises as a result of losses in the system. Any mechanism causing loss implies a thermal noise contribution, $c_i$, to the outgoing signals

$$a_i = \Sigma_j S_{ij} b_j + c_i$$

which depends on the temperature of the lossy component.

In an ideal lossless network, the system's thermal noise term will vanish since $S$ is unitary, $(I - S\ S^\dagger)_{ij} = 0$. In this case, the only nonzero terms in the scattering matrix are $S_{20} = S_{31} = 1$. Since the only nonzero populations are $n_{0,1} = n$, the covariance matrix contains only terms with $B_{20} = B_{31} = n \cdot h\nu$. Under this assumption the detectors' noise is uncorrelated, and the auto-correlations satisfy,

$$\sigma_{ii}^2 = \frac{(h\nu)^2}{\tau} \int d\nu n(n+1). \tag{B.27}$$

Therefore the $1\sigma$ uncertainty in the incident power due to intrinsic background fluctuations is,

$$\sigma_{photon} = \frac{h\nu}{\eta} \sqrt{\frac{\Delta\nu}{\tau}} \sqrt{\eta n(\eta n + 1)}\ . \tag{B.28}$$

Note that in the above we have explicitly included the optical efficiency, $\eta \equiv |S_{20}|^2 = |S_{31}|^2$. This result differs from the familiar Dicke radiometer equation describing coherent receivers,

$$\sigma_{photon} = \frac{h\nu}{\eta} \sqrt{\frac{\Delta\nu}{\tau}} (\eta n + 1). \tag{B.29}$$

While Equation B.29 is the limiting form of Equation B.28 for large occupation number $n$, it is instructive to derive Equation B.29 from Equation B.24.

**Example 1: The Dicke radiometer equation**

The scattering matrix for an idealized coherent receiver with perfect isolation contains a single nonzero term, $|S_{10}|^2 = G$, where $G$ is the gain of the system. An amplifier

can be thought of as a population characterized by an inverted distribution of energy levels, such as that found in a maser or laser. Such systems are conveniently described in terms of a negative temperature. As $T \rightarrow {}^{-}0$, the sign of the $C_{ij}$ from Equation B.26 is reversed. The only nonzero element of $\mathbf{C}$ is $C_{11} = G - 1$, and therefore $B_{11} = Gn + G - 1$. Applying Equation B.24 gives,

$$\begin{aligned} \sigma_{11}^2 &= \frac{(h\nu)^2}{\tau} \int d\nu \; G^2 \left[ n + 1 - (G)^{-1} \right] [n+1] \\ &= \Delta\nu \; \frac{(h\nu)^2}{\tau} \; G^2 \left[ (n+1)^2 - \frac{(n+1)}{G} \right]. \end{aligned}$$

In the limit that $G$ is significantly larger than unity, the second term becomes negligible. Referencing the noise to the input, we recover the (lossless) Dicke radiometer equation, Equation B.29,

$$\sigma_{11} = h\nu \sqrt{\frac{\Delta\nu}{\tau}} (n+1).$$

**Example 2: Polarization sensitive bolometers**

A dual polarized, single moded receiver (coherent or bolometric) is completely described by a four port network. Polarization sensitive bolometers and coherent receivers using orthogonal mode transducers (OMTs) are two examples of such systems. We now derive the photon noise properties of a PSB pair.

The action of the network, $S$, is that of an imperfect polarized beam splitter, with two inputs and two detectors. The PSBs (two of the four ports, labeled say, as numbers 2 and 3) are assumed to be at cryogenic temperatures, and therefore contribute negligibly to the photon occupation number. Therefore, the entries in the scattering matrix relevant to the observed photon noise are limited to the lower left quadrant, namely $S_{20} = \gamma$, $S_{31} = \gamma'$, $S_{21} = \delta$, and $S_{30} = \delta'$. Here the parameters $\gamma$ and $\delta$ describe the efficiency of transmission of the co-polar amplitude and the cross-polar amplitude, respectively, and in practice $\gamma >> \delta$.

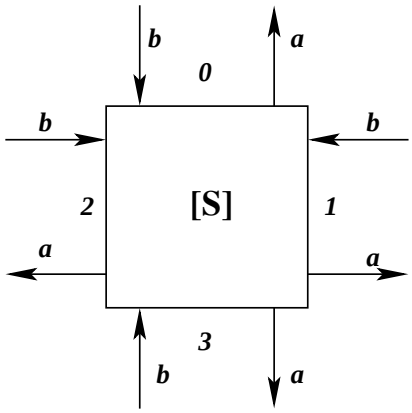


Figure B.6: The scattering matrix of a four port network. A polarization sensitive bolometer can be modeled by such a network.

Only the lower right quadrant of $SS^\dagger$ is nonzero,

$$(SS^\dagger)_{22} = \gamma^2 + \delta\delta' \quad (SS^\dagger)_{23} = \delta\ (\gamma + \gamma')$$
$$(SS^\dagger)_{32} = \delta'\ (\gamma + \gamma') \quad (SS^\dagger)_{33} = \gamma'^2 + \delta\delta'$$

The power coupling terms, $B_{ij}$, of interest are given by,

$$\begin{aligned} B_{22} &= \left(|S_{20}|^2\ n_0 + |S_{21}|^2\ n_1\right)\ h\nu + C_{22} \\ &= \left(\gamma^2\ n_0 + \delta^2\ n_1 + [1 - (\gamma^2 + \delta\delta')]\ n_c\right)\ h\nu \\ B_{23} &= (S_{20}S_{30}\ n_0 + S_{21}S_{31}\ n_1)\ h\nu + C_{22} \\ &= (\gamma\delta'\ n_0 + \gamma'\delta\ n_1 - \delta\ (\gamma + \gamma')\ n_c)\ h\nu \end{aligned}$$

where we have written the thermal contribution of the network

$$n_c \equiv \frac{1}{2}\frac{e^x + 1}{e^x - 1}.$$

In the case of PSBs, the origin of the modal couplings are the detectors themselves and/or the optics. In the case of the detectors, they are extremely cold compared to the background. For BOOMERANG, the re-imaging optics and filters are also cooled, and have low emissivity. Therefore, we assume the thermal noise contribution of the

network, $n_c$, is very small compared to the background populations, $n_i$. Furthermore, we assume that the background is isotropic, ie $n_0 = n_1 = n$. The covariance of the photon noise is then fully described by

$$\sigma_{ii}^2 = (h\nu)^2 \frac{\Delta\nu}{\tau} \left[ \left(\gamma^2 + \delta^2\right)^2 n^2 + \left(\gamma^2 + \delta^2\right) n \right] \tag{B.30}$$

$$\sigma_{ij}^2 = (h\nu)^2 \frac{\Delta\nu}{\tau} \left[ \left(2\gamma\delta\right)^2 n^2 \right]. \tag{B.31}$$

The autocorrelation, Equation B.30, contains terms proportional to both $n^2$ and $n$. The former is commonly referred to as the Bose contribution, or as a "photon bunching" term. Equation B.31 shows that correlations between devices are proportional only to the Bose contribution, implying that PSBs operating under higher background loading conditions will exhibit a higher proportion of correlated noise than the same instrument operating in a lower background. For an idealized system, in which the polarization leakage $\delta$ is zero, the covariance between detectors vanishes since the two linear polarization states are statistically independent of one another.

In practice, we estimate the total optical background power, $Q$, arising from the CMB, atmosphere, the telescope, and emission from within the cryostat. For simplicity, this optical background is treated as having originated from a single thermal source at an effective temperature $T_{RJ} = Q/\eta k_B \Delta\nu$. The noise equivalent power from the background fluctuations is then given by Equation B.30,

$$\mathrm{NEP}_{photon}^2 \simeq 2h\nu\, Q\, \left(1 + \eta\, n(T_{RJ})\right). \tag{B.32}$$

This is, of course, only approximate as we do not treat the background sources independently. It is often the case, however, that a single thermal source contributes the majority of the background optical power.

## Johnson, phonon, and amplifier noise

A detailed discussion of the proper treatment of Johnson, phonon, and amplifier noise may be found in the literature, particularly in original 1953 work of Jones [82]. The

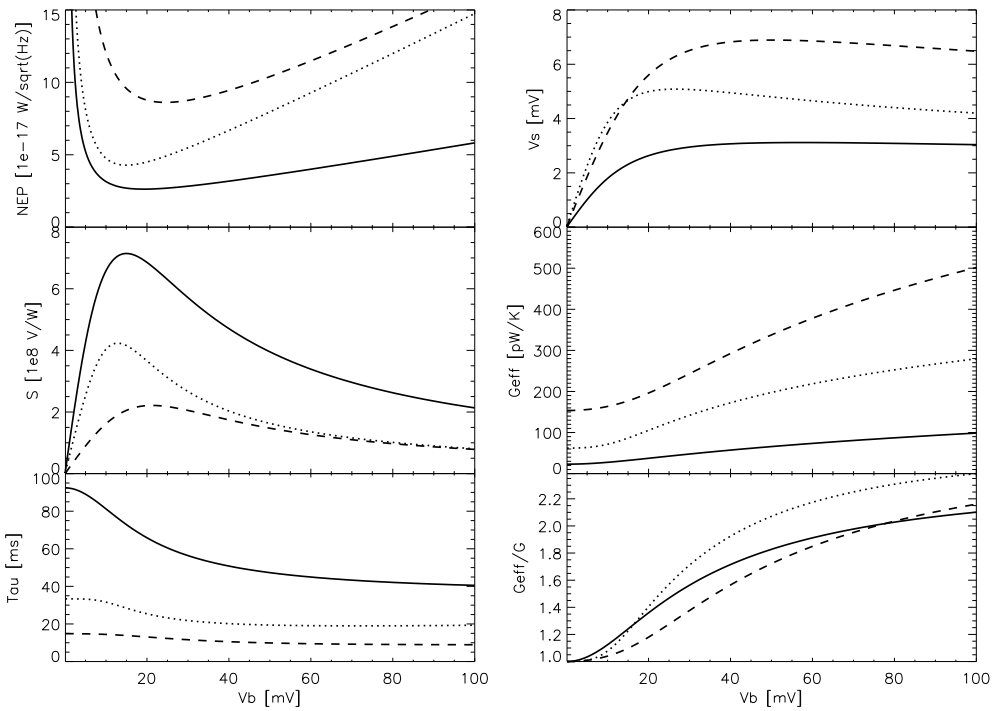


Figure B.7: The NTDGe receiver model, applied to B2K's three bands, as used to determine Table 3.4. The model accurately predicts the NEP and responsivity to $\sim 10\%$, consistent with the uncertainties on the loading and bolometer parameters.

same material is covered in the baffling prose of Mather[114]. We leave the derivation of the results to those references, and here only briefly summarize the various contributions, providing convenient expressions for each. Here, we consider the NTDGe bolometers, such as those used by BOOMERANG, for which the responsivity, $|S|$ (Equation B.12), has units of $[V/W]$. The expressions are easily extended to the TES circuit by converting voltage fluctuations to current fluctuations using Equation B.22.

Johnson noise is the one dimensional analog to thermal blackbody radiation. Thermodynamic arguments lead to the standard expression for the voltage noise of a circuit element, $|v_n|^2 = 4k_BTR$. The presence of the load resistors and the dynamic thermal conductance modifies the contribution to the detector NEP,

$$\mathrm{NEP}^2_{johnson} = \frac{4k_BTR}{|S|^2}\,\frac{G(T)}{G_{eff}}\,\frac{R_L}{R+R_L} \tag{B.33}$$

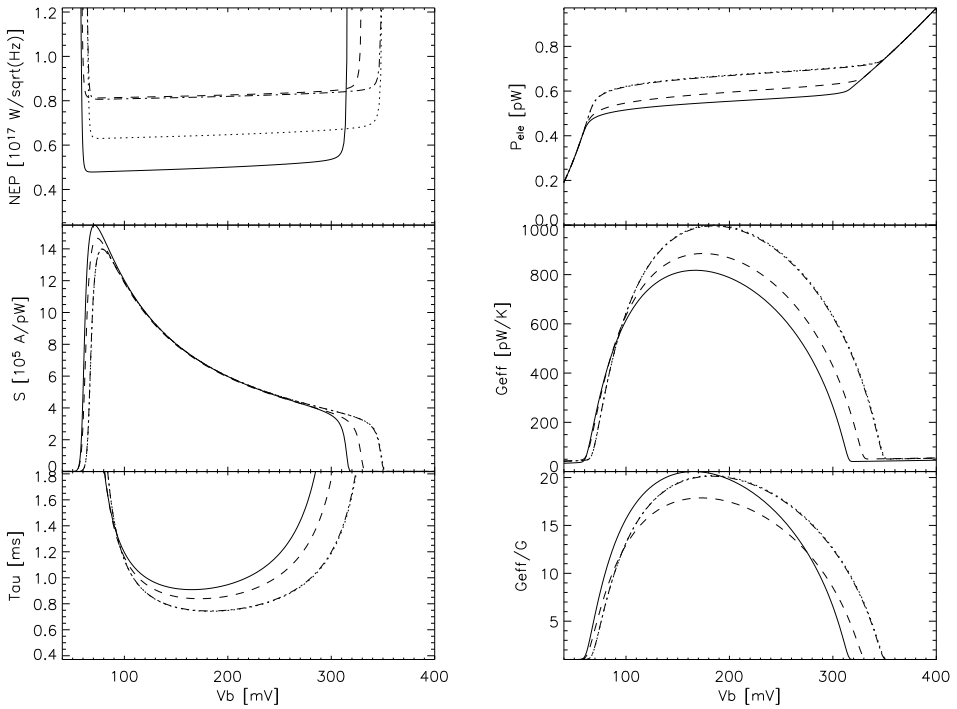


Figure B.8: The same as Figure B.7, but applied to a TES circuit. Note in particular the upper right panel, which shows the optical loading margin. The dynamic range of the TES is very high, but when driven above the transition temperature the device simply turns off. Variations in the background level can be offset to some degree by changing the electrical power dissipation, which is shown in the upper right.

Note that in the limit that $R_L >> R$ and $G(T) \rightarrow \infty$, we recover the result for a normal resistor. At low frequencies, the thermal feedback of the bolometer reduces the effective noise power relative to a resistor at the same temperature. At frequencies above the bolometer's thermal time constant, one can show that the Johnson voltage noise approaches that of a standard resistor as well [82].

The readout circuit contributes both voltage and current noise from the amplifier and from the load resistors, which act as a current noise source for the bolometer,

$$\mathrm{NEP}^2_{amp} = \frac{1}{|S|^2}\left(v_n^2 + (i_n^2 + 4k_B T_L/R_L)\left[\frac{ZR_L}{Z+R_L}\right]^2\right) \tag{B.34}$$

where we have used $Z \equiv \partial V_s/\partial I_{bias}$, and $T_L$ is the temperature of the load resistor.

Finally, thermal lattice fluctuations contribute to the noise power at the bolome-

ter. The thermal noise power from a differential element with thermal conductance, $G$, at a temperature, $T$, is simply $4k_BTG$. For a bolometer, the temperature dependence of the thermal conductance results in thermal phonon noise determined by an effective temperature which is the conductance weighted average over the temperature gradient.

$$\mathrm{NEP}^2_{phonon} = 4\ k_B\ G(T)\ \frac{\int T'\ G(T')\ dT'}{\int G(T')\ dT'} \tag{B.35}$$

where the integral runs from the bath temperature to the equilibrium temperature of the bolometer, as determined by Equation B.1.

# Appendix C

# Numerical procedures

## C.1 The Newton-Raphson method

The Newton-Raphson method is so widely used in analysis that is merits a brief discussion. The Newton-Raphson algorithm is an elegant method of finding the roots of nonlinear equations with finite first derivatives. Consider the one dimensional case, where one desires to find the roots of the (generally nonlinear) equation $f(x) = 0$. One can Taylor expand $f$ about a trial solution, $x_0$, keeping only the linear terms,

$$f(x_0 + \delta x) \simeq f(x_0) + \delta x \left.\frac{\partial f}{\partial x}\right|_{x_0}$$

If we assume that the step $\delta x$ brings us to the solution, $f(x_0 + \delta x) = 0$, we can solve for our improved estimate,

$$x_i = x_0 - \frac{f(x_0)}{\partial f/\partial x|_{x_0}}.$$

In the limit that $f(x)$ is linear in $x$, the first iteration gives us an exact solution.

This algorithm can be trivially extended to multiple dimensions. Given a function, $F(\vec{\lambda})$, where the $N$ values $\{\lambda_i\}$ are the free parameters ($C_\ell$'s, for instance), suppose one would like to minimize $F$ with respect to the $\lambda_i$. The desired values $\vec{\lambda}$ must provide the roots of the partial derivatives of $F$,

$$\mathbf{f}' \equiv \left\{\frac{\partial F}{\partial \lambda_i}\right\} = 0.$$

The Taylor expansion of the functions $\mathbf{f}'$ provide $N$ equations of the form

$$\frac{\partial F(\vec{\lambda_0} + \delta\vec{\lambda})}{\partial \lambda_i} \simeq \frac{\partial F(\vec{\lambda_0})}{\partial \lambda_i} + \sum_j^N \delta\lambda_j \, \frac{\partial^2 F(\vec{\lambda_0})}{\partial \lambda_i \partial \lambda_j}$$

This linear system of equations can be written

$$\mathbf{f}'(\vec{\lambda_0} + \delta\vec{\lambda}) \simeq \mathbf{f}'(\vec{\lambda_0}) + \mathbf{H}(F)|_{\lambda_0} \cdot \delta\vec{\lambda}$$

where the matrix of partial derivatives, $\mathbf{H}$, is the Hessian of $F$ in the parameters $\{\lambda_i\}$. Assuming the function $F$ is sufficiently well behaved, we can iteratively recover estimates of the parameters by inverting the Hessian,

$$\vec{\lambda}_{i+1} = \vec{\lambda}_i - \mathbf{H}^{-1}(F)|_{\vec{\lambda}_i} \cdot \mathbf{f}'(\vec{\lambda}_i). \tag{C.1}$$

In the literature, the matrix of second derivatives is occasionally referred to as the Jacobian of the vector $\mathbf{f}'$. Truth be told, the terminology gets even more muddled. Recall that for the purposes of CMB analysis, the likelihood function $F$ depends on the estimate of the sky signal, $\widetilde{\mathbf{m}}$. Rather than rely on these estimates, one typically replaces the product $\langle \widetilde{\mathbf{m}}\widetilde{\mathbf{m}}^T \rangle$ appearing in the matrix $\mathbf{H}$ with their ensemble average. If the estimator $\widetilde{\mathbf{m}}$ is unbiased, this is just the signal covariance matrix. It turns out that this significantly simplifies the algebra. This is effectively taking the ensemble average of the matrix $\mathbf{H}$ over many realizations of the signal and noise which, in statistical parlance is referred to as the Fisher matrix.

The Newton-Raphson algorithm is an extremely efficient method of finding the maximum of the likelihood. Computationally, it requires the inversion of the Fisher matrix, whose size is determined by the number of independent band-powers going into the analysis. Even for an analysis of the full sky, the number of independent band-powers number less than a few thousand.

While extremely efficient, the Newton-Raphson algorithm converges to the nearest local minimum, and one should check that the solution is a global minimum of the

function. A standard approach is to require that the scalar product $(\mathbf{f}' \cdot \mathbf{f}')$ decrease from the previous iteration before accepting a given step, $\delta\vec{\lambda}$. It is often the case that a root finding algorithm employs a convergence parameter, $0 < \alpha \leq 1$, as a prefactor to $\delta\vec{\lambda}$. This takes advantage of the fact that $\mathbf{H}^{-1}$ may indicate the optimal direction to follow in parameter space, even if it overestimates the optimal step size.

## C.2 The Jacobi method

The Jacobi method is a robust numerical method of solving a set of linear equations, $\mathbf{Ax} = \mathbf{b}$, for which the matrix $A$ is (or can be arranged to be) diagonally dominant. The great strength of this method is that, subject to this requirement, it is guaranteed to converge, although it may do so relatively slowly. The procedure is straightforward. One may estimate a new solution without inverting the matrix $\mathbf{A}$ simply by solving for each component, $x_i^{k+1}$, given an estimate of the values $\{x_i^k\}$,

$$x_i^{k+1} = A_{ii}^{-1}\left(b_i - \sum_{j\neq i} A_{ij}x_j^k\right).$$

It is often convenient, and advantageous from a numerical point of view, to write the above in terms of a correction to the previous iteration,

$$x_i^{k+1} = x_i^k + \delta x_i^{k+1}$$

where

$$\delta x_i^{k+1} \equiv \eta\ A_{ii}^{-1}\left(b_i - \sum_{j} A_{ij}x_j^k\right). \tag{C.2}$$

Here we have inserted a convergence parameter $\eta \lesssim 1$, which may be tuned to aid the convergence of the algorithm. In the limit that $\mathbf{A}$ is diagonal, the optimal value is $\eta = 1$. Generally speaking, the larger the off diagonal terms become, the lower the optimal value of $\eta$. Clearly the diagonals of $\mathbf{A}$ must not be near zero. Furthermore, as can be seen from Equation C.2, the solution will diverge if the absolute value of the sum of the off-diagonals is greater than the diagonal element of each row.

As an example, consider the following linear system.

$$\begin{pmatrix} 5 & -2 & 1 \\ 5 & -7 & 1 \\ -2 & 1 & 6 \end{pmatrix} \mathbf{x} = \begin{pmatrix} -1 \\ 0 \\ 1 \end{pmatrix} \tag{C.3}$$

Setting $\eta = 1$, and using the above procedure results in the following sequence of solutions.

$$\begin{aligned} x_0 &= (\ 0.000,\ 0.000,\ 0.000) \\ x_1 &= (-0.200,\ 0.000,\ 0.167) \\ &\vdots \\ x_5 &= (-0.291, -0.187,\ 0.102) \\ &\vdots \\ x_\infty &= (-0.300, -0.200,\ 0.100) \end{aligned}$$

This example converges to twelve significant digits after 40 iterations, largely independent of $\mathbf{x}_0$, the trial solution. The rate of convergence does not scale strongly with the array size, so the solution is an efficient way of solving large systems of equations.

A minor modification to the above procedure results in the Gauss-Seidel algorithm, in which for the estimate for each value $x_i^{k+1}$ incorporates the most recent estimate previous parameters $\{x_j^{k+1}\}_{j<i}$ instead of the set of values from the previous iteration. This procedure is less numerically robust, but tends to converge more rapidly than Jacobi iteration.

The application to Equation 5.5 is clear. The Jacobi method provides a robust method of solving for the general least squares map, Equation 5.5. Equating Equa-

tions 5.5 and Equation C.2 we find the correspondence,

$$\begin{aligned} \mathbf{A} &\rightarrow \mathbf{C}_N^{-1} \equiv (\mathbf{A}^T\mathbf{N}^{-1}\mathbf{A}) \\ \mathbf{x} &\rightarrow \widetilde{\mathbf{m}} \\ \mathbf{b} &\rightarrow \mathbf{A}^T\mathbf{N}^{-1}\mathbf{d} \end{aligned}$$

Recall that the matrix $\mathbf{A}$ which appears on the right hand side is the pointing matrix, and should not be confused with the general linear system described in Equation C.2. The general algorithm we use for calculating the correction to an estimate of the least squares map, $\widetilde{\mathbf{m}}^k$, is therefore

$$\delta\widetilde{\mathbf{m}}^{k+1} \propto \mathrm{diag}(\mathbf{A}^T\mathbf{N}^{-1}\mathbf{A})^{-1}\mathbf{A}^T\mathbf{N}^{-1}(\mathbf{d} - \mathbf{A}\widetilde{\mathbf{m}}^k)$$

In practice, one must simultaneously solve for the noise covariance matrix of the data, $\mathbf{N}$. This typically results in slightly slower convergence of the algorithm than for the case of known noise.

# Appendix D

# The BOOMERANG Readout

The BOOMERANG receiver employs a highly stable AC bias and a single phase digital switching multiplier. While the digital switching multiplier provides a much larger dynamic range than an analog multiplier, noise from odd harmonics of the bias is mixed with the signal. Therefore the signal bandwidth is limited to $\sim 20$ Hz prior to demodulation by a bi-quad bandpass filter, and extensive low pass filtering, including a 4-pole Butterworth, is applied to the demodulated output.

In a typical quasi-total power AC biased readout, the situation is a bit different from the DC biased situation described in the previous section. AC biased systems are arranged so that there is a virtual ground at the center of the bolometer. In this case, the steady state *rms* bias voltage produces a current through the load resistor,

$$V_{bias} = I_L \left( R_L + \frac{R_b}{2} || Z_p \right)$$

where $Z_p \equiv \frac{1}{i\omega C_p}$. The carrier signal voltage (above virtual ground), $V$, is then determined by the current flowing through the parallel impedance of the bolometer and the parasitic capacitance.

$$I_L = I_b + I_c = \frac{2V}{R_b} + \frac{V}{Z_p} = \frac{V}{\left(\frac{R_b}{2} || Z_p\right)}$$

The transfer function, $T \equiv V/V_{bias}$, is then determined by

$$\begin{aligned} V_{bias} &= I_L \cdot \left( R_L + \frac{R_b}{2} || Z_p \right) \\ &= V \left( R_L + \frac{R_b}{2} || Z_p \right) \left( \frac{2}{R_b} + i\omega C_p \right) \\ &= V \left( 1 + \frac{2R_L}{R_b} + i\omega R_L C_p \right) \end{aligned}$$

If we then define $\eta \equiv (1 + 2\frac{R_L}{R_b})$, we have for the transfer function

$$T = \frac{1}{\eta + i\omega R_L C_p}$$

In the following discussion it is convenient to introduce the ratio

$$\epsilon \equiv \frac{\omega R_L C_p}{\eta}.$$

For an applied voltage bias, $V_{bias}$, we obtain a signal amplitude of

$$|V| = \frac{V_{bias}}{\sqrt{\eta^2 + (\omega R_L C_p)^2}} = \frac{V_{bias}}{\eta\sqrt{1+\epsilon^2}}$$

with phase shift (with respect to the reference signal) given by $\phi = \tan^{-1}(\epsilon)$, and a bias current which is less than the equivalent DC circuit, namely

$$I_{bias} = \frac{V_{bias}}{R_b\ \eta\sqrt{1+\epsilon^2}}$$

The signal, $v(t)$, progresses through the demodulation circuit in the following way,

1. The carrier signal at frequency $\omega_c$ is phase shifted with respect to the bias generator by a phase $\phi$, and is partially modulated by the signal of interest of amplitude $\alpha \ll 1$ and frequency $\omega_s$.

$$v(t) = \cos(\omega_c t + \phi)(1 + \alpha\cos(\omega_s t)) \tag{D.1}$$

At this point, the power spectrum of the signal contains a component at the carrier frequency and components at the sum and difference frequencies of amplitude $\alpha$.

2. $\widetilde{v}(f)$ is bandpass filtered with spectral width $> 2\ \max(\omega_s)$ about $\omega_c$ to reject noise at all but the signal bandwidth.

3. The filtered $v(t)$ is multiplied by the Fourier series of a square wave at $\omega_c$. Because the odd harmonics are well above the cutoff of the low-pass filter, we only consider the effects of the multiplication by the fundamental frequency,

   (a) $\widetilde{v}(\omega_c)$ is aliased to zero frequency (DC) and $2\omega_c$

   (b) $\widetilde{v}(\omega_c + \omega_s)$ is aliased back to $\omega_s$ and $2\omega_c + \omega_s$

   (c) $\widetilde{v}(\omega_c - \omega_s)$ is aliased to $2\omega_c - \omega_s$

4. After low pass filtering well below $\omega_c$, the only components which remain are

$$v(t) = \frac{\cos\phi}{2} + \alpha\cos\phi\cos\omega_s t$$

5. The final stage of the demodulation circuit contains a single pole 5.6 mHz high-pass filter which sets the output bandwidth of the electronics from $\sim$10mHz $\rightarrow$ 18 Hz. In practice, the time constant of the bolometers further limits the signal bandwith to about 5 Hz.

In all generality, the signal at the input of the demodulator is

$$\begin{aligned} v(t) &= \cos(\omega_c t + \phi)(1 + \alpha\cos(\omega_s t)) \\ v(t) &= \cos(\omega_c t)\cos\phi - \sin(\omega_c t)\sin\phi \\ &+ \frac{\alpha}{2}\cos\phi\left(\cos(\Delta^+ t) + \cos(\Delta^- t)\right) \\ &- \frac{\alpha}{2}\sin\phi\left(\sin(\Delta^+ t) + \sin(\Delta^- t)\right) \end{aligned}$$

where $\Delta^{\pm} = \omega_c \pm \omega_s$. At the modulator, the signal is multiplied by a square wave. Considering only the fundamental we have, up to a constant factor (the leading term

in the Fourier series of the square wave),

$$\begin{aligned} v(t) &= \frac{cos\phi}{2}\left(1+\cos(2\omega_c t)\right) - \frac{sin\phi}{2}\sin(2\omega_c t) \\ &+ \frac{\alpha}{2}\cos\phi\left(\cos([2\omega_c+\omega_s]t) + \cos([2\omega_c-\omega_s]t) + 2\cos(\omega_s t)\right) \\ &- \frac{\alpha}{2}\sin\phi\left(\sin([2\omega_c+\omega_s]t) + \sin([2\omega_c-\omega_s]t)\right) \end{aligned}$$

After low pass filtering well below $\omega_c$, all that remains is the demodulated signal

$$v(t) = \cos\phi\left(\frac{1}{2} + \alpha\cos(\omega_s t)\right)$$

In most cases the phase angle, $\phi$, can be eliminated by the introduction of a compensating phase shift between the reference generator and the demodulator. However, if by some mechanism the phase $\phi$ is influenced by the signal $\alpha(t)$ the situation becomes decidedly more complicated, as we discuss below.

## Signal/Reference phase shifts

That the readout is single phase and that there is no allowance for tuning the phase of the reference in flight poses a significant limitation to the performance of the receiver. The reason for this is that the phase shift between the signal and reference depends strongly on the parasitic capacitance of each channel, and weakly on the in-flight loading via the bias amplitude and the equilibrium bolometer impedance. A dual phase analog readout or a purely digital demodulation would greatly simplify the optimization of the readout at the expense of a twice the analog circuitry or a more sophisticated analog to digital converter, respectively.

For a quasi-total power receiver, one wants to maximize ones sensitivity to signals in your optical bandwidth (which for BOOMERANG is roughly 5Hz) rather than the DC component of the demodulated carrier signal. In the presence of parasitic capacitance, a variation in the bolometer impedance due, say, to a variation in the background optical load will result in a change in the amplitude and phase of the

signal at the input to the demodulation circuit.

$$\begin{aligned}\frac{\partial V}{\partial R_b} &= \frac{2\ R_L}{R_b^2}\frac{V_{bias}}{(\eta + i\ \omega_c R_L C_p)^2} \\ &= \frac{2\ R_L}{(R_b\ \eta)^2}\frac{V_{bias}}{(1 + i\ \epsilon)^2}\end{aligned}$$

Note that this expression reduces to its analog in the previous section as $\omega$ approaches zero. As before, the variation in the signal due to a variation in optical power is given by the product,

$$\frac{dV}{dQ} = \frac{\partial V}{\partial R_b}\frac{\partial R_b}{\partial T}\frac{\partial T}{\partial Q}$$

So, the signal response of an AC biased system will depend on the carrier frequency, $\omega_c$, and the frequency of the small signal, $\omega_s$, in the following way,

$$\delta\widetilde{V} = -\delta\widetilde{Q}\frac{R_L}{R_b^2}\frac{V_{bias}}{(\eta + i\omega_c R_L C_p)^2}\frac{1}{G_{eff}} \cdot \frac{R_b}{2T}\sqrt{\frac{\Delta}{T}} \cdot \left(\frac{1}{1 + i\omega_s\tau}\right)$$

Then the signal input to the demodulation circuit is the sum of the $\omega_s$ independent component, with phase shift

$$\phi_c = \tan^{-1}\ (\epsilon)$$

and (after considerable algebra) that of the small signal component, with phase shift

$$\begin{aligned}\phi_s &= \tan^{-1}\left(-\frac{2\epsilon + \omega_s\tau(1-\epsilon^2)}{1-\epsilon^2-2\omega_s\tau\epsilon}\right) \\ &\simeq \tan^{-1}\left(-\frac{2\epsilon}{1-\epsilon^2}\right)\end{aligned}$$

Therefore, the nature of the signal input to the demodulator is significantly different

than the idealized case of Equation D.1.

$$\begin{aligned}\widetilde{v}(f) &= V_{bias}(f)\left[\frac{1}{\eta(1+i\epsilon)}+\frac{\widetilde{\alpha}(f)}{[(1-\epsilon^2)-2\epsilon\omega_s\tau]+i\,[(1-\epsilon^2)\omega_s\tau+2\epsilon]}\right] \\ &\simeq V_{bias}(f)\left[\frac{1}{\eta(1+i\epsilon)}+\frac{\widetilde{\alpha}(f)}{(1+i2\epsilon)}\right] \end{aligned} \tag{D.2}$$

Where, in terms of the receiver parameters,

$$\widetilde{\alpha} \equiv -\delta\widetilde{Q}\;\frac{1}{\eta\;G_{eff}}\frac{R_L}{R_0^2}\frac{R_{bolo}}{2T}\sqrt{\frac{\Delta}{T}}$$

For BOOMERANG, $\omega_s\tau \ll \epsilon$, and $\epsilon \simeq 0.3$, and in Equation D.2 we have only kept terms of order $\epsilon$. Tuning the reference phase based on the first term alone, as is common practice, may result in the attenuation of the signal of interest.